SEARCH FOR LONG-LIVED PARTICLES DECAYING INTO DISPLACED HADRONIC JETS IN THE MUON SPECTROMETER IN pp COLLISIONS AT $\sqrt{s} = 13$ TEV WITH THE ATLAS DETECTOR

by

Michael Louis Schott

A Dissertation Submitted to the Faculty of the

DEPARTMENT OF PHYSICS

In Partial Fulfillment of the Requirements

For the Degree of

DOCTOR OF PHILOSOPHY

In the Graduate College

THE UNIVERSITY OF ARIZONA

2024

THE UNIVERSITY OF ARIZONA
GRADUATE COLLEGE

As members of the Dissertation Committee, we certify that we have read the dissertation prepared by: Michael Louis Schott,
titled: *Search for Long-Lived Particles Decaying into Displaced Hadronic Jets in the Muon Spectrometer in pp Collisions at $\sqrt{s} = 13$ TeV with the ATLAS Detector*

and recommend that it be accepted as fulfilling the dissertation requirement for the Degree of Doctor of Philosophy.

Kenneth Johns — Date: 11/18/24

Elliott Cheu — Date: 11/18/24

John Rutherfoord — Date: 11/18/24

Shufang Su — Date: 11/18/24

Erich Varnes — Date: 11/18/24

Final approval and acceptance of this dissertation is contingent upon the candidate's submission of the final copies of the dissertation to the Graduate College.

I hereby certify that I have read this dissertation prepared under my direction and recommend that it be accepted as fulfilling the dissertation requirement.

Kenneth Johns — Date: 11/18/24
Dissertation Committee Chair
Department of Physics

ACKNOWLEDGMENTS

No man is an island,
Entire of itself;
Every man is a piece of the continent,
A part of the main.

- John Donne

No meaningful endeavor can hope to be successful without external support and guidance, and I have received much of both throughout the writing of this dissertation. While I would like to thank each and every person who has helped in any way, writing that document would compete with the rest of this dissertation in length. For every word of thanks written here, know that there are tens of thousands more left unwritten.

First and foremost, I wish to thank the generosity, in both time and patience, of my advisor, Ken Johns. Without his guidance, feedback, and support over these past several years, this dissertation would have remained a distant collection of dreams. I also want to thank Erich Varnes and Elliott Cheu, who provided valuable feedback, in the form of both answers and questions, during our weekly analysis meetings. I would also like to thank John Rutherfoord and Shufang Su for their support throughout these years, in research, in teaching, and in learning.

I would like to thank Simon Berlendis for being incredibly patient with me as I took my first clumsy steps into research, and Hao Zhou for the continuing guidance all the way through my defense.

To Jad Sardain, thank you for answering all my questions over the years, both about ATLAS and otherwise, for always assuring me when I was on the right track (and guiding me

back when I wasn't), and for helping me get across the dissertation finish line. To Zhaoyuan "Maxwell" Cui and Nick Lopez, I'd like to thank you both for being wonderful office-mates, for always being willing to help me think through any problem that I encountered, and for all the less technical conversations that we had. And to Billie Braimah and Rachel Lindley, thank you both for having an open door to any and all questions, conversations, and passing thoughts, whether about physics or not.

Thanks to Gardie Lueders, Mike Eklund, Shane Smith, and all of the other Department of Physics staff who have supported me throughout my time at the University of Arizona.

Words are insufficient to describe how thankful I am to all those who have supported me in ways beyond academics as well. Jad, Maxwell, Nick, Billie, and Rachel: though I've already thanked you once as colleagues, I'd like to thank you again for your support as friends. The casual conversations, the trips for boba-tea, the lengthy technical discussions and the deeper reflective ones have all kept me grounded during this research. I would also like to specifically thank Will Lockhart, who has helped me grow as both a scientist and as a person since day one of graduate school, and without whom I likely would never have finished this journey.

I would also like to thank my family, Mike, Martha, Thomas, and Katherine. I would not be the person I am today without their love and support - especially my parents who have always supported my curiosity and encouraged me to keep going.

And to all of my family and friends back home, who supported me from afar, and all of the friends I made in Tucson, who supported me from down the road: Thank you! I cannot name you all, but know that every offering of support or assurance helped.

I would also like to acknowledge the United States Department of Energy (DOE) for funding this work under the DOE grant number DE-SC0009913. Without this support, this dissertation would not have been possible.

LAND ACKNOWLEDGMENT

We respectfully acknowledge the University of Arizona is on the land and territories of Indigenous peoples. Today, Arizona is home to 22 federally recognized tribes, with Tucson being home to the O'odham and the Yaqui. Committed to diversity and inclusion, the University strives to build sustainable relationships with sovereign Native Nations and Indigenous communities through education offerings, partnerships, and community service.

DEDICATION

For my parents

TABLE OF CONTENTS

LIST OF FIGURES

LIST OF TABLES

ABSTRACT

A search for the decay of neutral, weakly-interacting, long-lived particles (LLPs) leaving a single displaced hadronic jet in the Muon Spectrometer (MS) using data collected by the ATLAS detector is presented in this dissertation. The analysis uses $140.1\,\text{fb}^{-1}$ of proton-proton collision data at $\sqrt{s} = 13\,\text{TeV}$ collected during Run 2 of the LHC from 2015-2018. LLPs appear in many beyond the Standard Model (BSM) theories, motivating dedicated searches for their signatures. Two benchmark signal models utilizing a Higgs portal mechanism are considered. The primary benchmark model is a Hidden Sector extension with decays to pairs of scalar LLPs, while the second is a Higgs portal baryogenesis model. A specialized trigger algorithm that targets regions of high activity in the MS is discussed. A specialized software algorithm designed for reconstructing displaced vertices is also discussed. The background for the single-vertex signature is estimated using a data-driven ABCD method. The search sensitivity is extended to higher and lower LLP lifetimes using a toy MC extrapolation technique. The observed number of events is consistent with expected backgrounds. Limits on the benchmark signal models are presented. Combined limits with previous two-vertex results are also presented. For the SM Higgs boson Hidden Sector model, constraints are placed on the process cross-section at the 95% CL in the range from 0.5-50.5 m for branching ratios above 10%, varying with LLP mass. For Higgs masses different than 125 GeV, upper limits are placed on the LLP production cross section times branching ratio.

Chapter 1

Introduction

Physics is the pursuit of an explanation of things, motivated by a desire to explain them at the most fundamental level. Particle physics is the current culmination of this attempt in the direction of what composes all things; whether there is some irreducible set of objects that join to form the complexity and dynamics observed everywhere. Today, this irreducible set of objects is called the fundamental particles, and their behavior is described by the best current model of particle physics, the Standard Model (SM).

Published in its current form in 1967 [1, 2] and completed, with the discovery of the Higgs boson in 2012 [3, 4], the Standard Model has proven to be the most successful model of fundamental particles in terms of both descriptive and predictive power. The Standard Model is a quantum field theory, meaning, in the broadest sense, that the objects it describes are particle fields and that the states of these fields are quantized. It is also a gauge theory, meaning that it has some internal symmetries that arise as conserved quantities. It is Lorentz invariant, by construction, making it a description of quantum particle fields at relativistic energy scales. Through the combination of these features, the Standard Model describes nearly all of what is known to be true regarding fundamental particles to incredible accuracy.

The Standard Model, for the incredibly successful theory that it is, has largely been accepted as an incomplete picture of fundamental particles, or an effective low-energy theory, by physicists today. Observations indicate several reasons the SM is incomplete. Among them are the lack of a dark matter candidate, the presence of a non-zero neutrino mass, the Hierarchy problem, matter-antimatter asymmetry in the universe, and the strong CP problem.

Extensions to the SM have been proposed that would address these problems. Theories

derived from Supersymmetry (SUSY), like minimal supersymmetric SM (MSSM) [5] or split SUSY [6, 7], would address the Hierarchy problem by introducing new particles, while also including explanations for dark matter or unification with gravity, depending on their formulation. Hidden Valley models [8, 9] address the hierarchy and dark matter problems using different mechanisms. There are dark matter models [10], baryogenesis models [11, 12], and many others [13].

This dissertation describes a search for new long-lived particles (LLPs) using the ATLAS detector and proton-proton (pp) collisions produced at the CERN Large Hadron Collider (LHC) [14, 15, 16]. A long-lived particle is commonly defined to be a charge neutral fundamental particle with a proper lifetime ranging from hundredths to hundreds of meters. LLPs would leave no signature in a detector until a decay occurs, which would appear to be a vertex located some distance away from the primary vertex (PV) of the event. Such a displaced vertex (DV) would look unlike any SM process, making them an appealing signature to investigate [9, 14].

Depending on the lifetime, the LLPs could leave DVs in any subdetector of ATLAS. Thus searches for LLPs could be carried out in the Inner Detector (ID), the Calorimeter, or the Muon Spectrometer (MS). Dedicated proposed detectors, such as MATHUSLA, may be constructed to probe LLP lifetimes sufficiently long that they decay outside of the ATLAS cavern [15].

This analysis uses two benchmark models, a Hidden Sector model ($H \to ss$) and a Baryogenesis model ($H \to \chi\chi$). The s particles are scalar boson LLPs and the χ particles are Majorana fermion LLPs. This analysis covers the search for a single LLP decay matching the signature predicted by the two benchmark models over a range of LLP proper lifetimes from 0.01 m to 200 m[1]. It also includes a statistical interpretation of the search results.

A background of the SM and of the benchmark BSM extensions are given in Chapter 2. This is followed by a description of the LHC accelerator and the ATLAS detector in Chapter 3. Data collection and signal Monte Carlo sample production methods are discussed in Chapter 4. Chapter 5 discusses the ATLAS trigger system, with focus on the special-

[1]This is the extrapolation range. The signal MC samples were generated with $c\tau$ between 0.127 m and 6.039 m. See Chapters 4 and 8 for details.

ized muon region-of-interest cluster trigger used in this analysis. Chapter 6 describes the reconstruction procedure for standard physics objects, including tracks found in the ID, jets found in the calorimeter, and tracks found in the MS. This chapter also provides a description of the specialized algorithm used to reconstruct the MS vertex (MSVtx) objects used in this analysis. The MS vertex identification and quality criteria are described in Chapter 7. Chapter 8 describes the process of selecting events that could contain LLPs, the strategy for estimating background contamination, and the procedure used to extrapolate expected signal sensitivity to higher and lower lifetimes. Chapter 9 describes the statistical model used to interpret the results of the analysis. The results on limits of LLP production are also given in this chapter. Chapter 10 summarizes the analysis and discuses improvements that could be made to a future search for LLPs in this detector region.

Chapter 2

Long-Lived Particles and The Standard Model

2.1 The Standard Model

The Standard Model (SM) is an $SU(3)_C \times SU(2)_L \times U(1)_Y$ gauge theory that aims to describe all of the fundamental particles and their interactions within the framework of quantum field theory and is the most comprehensive and successful theory of particles to date.

The modern incarnation of the Standard Model was first written in 1967 [1, 2] and completed in 2012 with the discovery of the Higgs Boson [3, 4]. The Standard Model is a theory composed of Lorentz-invariant fermion 4-vectors, which describe the particles that make up the matter in the universe. By enforcing local gauge symmetry, gauge fields enter the formulation. The fermion fields couple with gauge fields via interaction terms introduced in the field Lagrangian. Experimental evidence supports the existence of three generations of fermions, four gauge fields, and a single complex scalar field called the Higgs field. A diagram of all the particles present in the Standard Model can be seen in Figure 2.1 [17].

The fermions are composed of two different collections of particles: quarks and leptons. Quarks interact with all three fundamental forces represented in the Standard Model, making them the only color-charge carriers along with the gluon, g, the massless gauge boson that mediates color interactions. Leptons, along with quarks, couple with the weak force, mediated by the $W^{\pm}$ and Z^0 bosons. Of the leptons, only the charged leptons, the electron, muon, and tau, interact via the electromagnetic force. The neutrinos have no charge and do not couple to the electromagnetic field. The electromagnetic interactions are mediated by the other massless gauge boson, the photon, γ. The Higgs boson enters the Standard Model

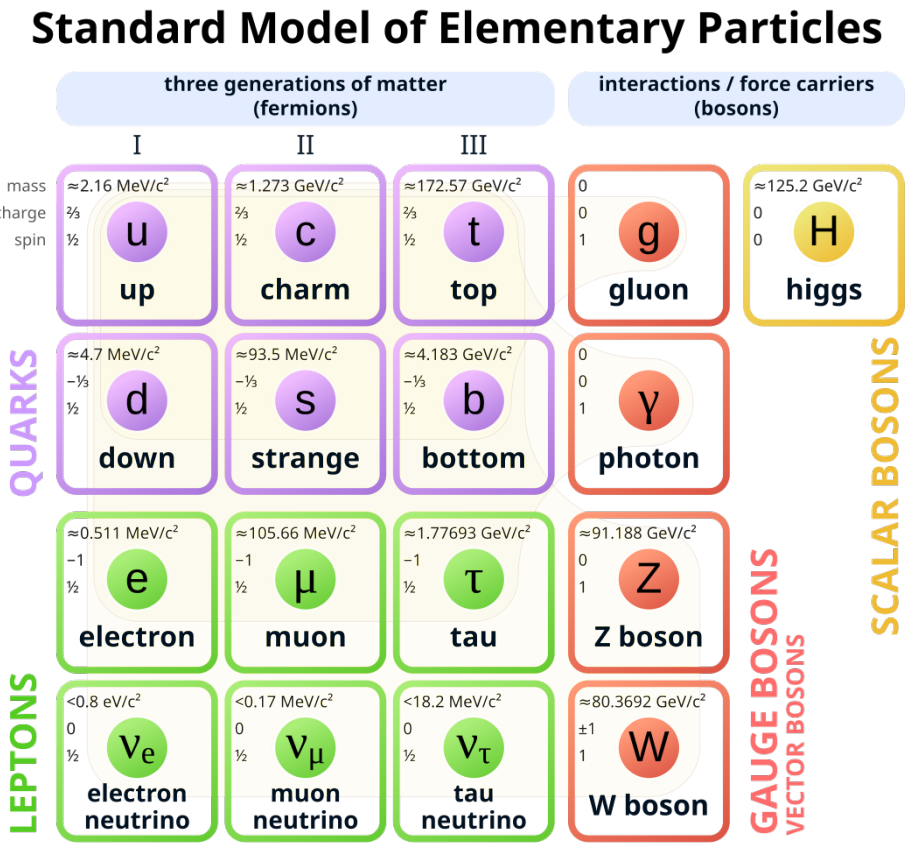

Figure 2.1: Diagram of all particles included in the Standard Model with particle mass, charge, and spin included. Fermions include quarks (purple) and leptons (green), while bosons include the gauge bosons (red) and the Higgs boson (yellow). Strong, weak, and electromagnetic interactions are indicated by the shaded boundaries surrounding the particles.

through the Higgs Mechanism, in which a complex doublet of locally gauge invariant Higgs fields is introduced into the field Lagrangian. This field causes the W and Z gauge fields to acquire a mass after spontaneous symmetry breaking. An additional Yukawa coupling results in the fermions also acquiring a mass.

Unlike what is shown in Figure 2.1, which shows all experimental values for particle masses, the Standard Model does not include any neutrino mass terms. This is one of the known shortcomings of the Standard Model, along with the mathematical structure of the Standard Model, which are described in more detail in the following sections.

2.1.1 Particles, Fields, and Gauge Invariance

The fundamental components of the Standard Model are relativistic quantum gauge fields arising from a theory of Dirac fermions. The concept of a gauge field, and gauge invariance, is familiar through its use in classical electrodynamics. Through the quantization of the field, excitations in the field become discrete and these excitations are treated as the particles, themselves. To say that a field theory is relativistic is equivalent to saying that it is Lorentz-invariant, or that Lorentz boosts are a symmetry of the system, in addition to classical symmetries of translation and rotation. To say that a field theory is gauge invariant means that there exists a symmetry in the theory that, under a specific transformation or collection of transformations, returns the same field dynamics [18].

Maxwell's equations describe the electric and magnetic fields, are Lorentz-invariant, and turn out to be necessary when building a theory of fermions that exhibit electric charge. These fermions, electrons and positrons, demonstrate an internal $U(1)$ gauge symmetry when combined with the electromagnetic field. Maxwell's equations (without charges) can be expressed as

$$\partial^{\mu} F_{\mu\nu} = 0 \tag{2.1}$$

where $F_{\mu\nu} = \partial_{\mu} A_{\nu} - \partial_{\nu} A_{\mu}$ is the covariant form of the electromagnetic field tensor, with A_{μ} representing the electromagnetic 4-potential, $A_{\mu} = \{\varphi, -\vec{A}\}$. Of particular note is the gauge freedom inherent in Eq. 2.1,

$$\vec{A} \mapsto \vec{A} + \vec{\nabla} f \tag{2.2}$$

$$\varphi \mapsto \varphi + \frac{\partial f}{\partial t} \tag{2.3}$$

where f can be any scalar function.

The Lagrangian density for the electromagnetic field can then be written as

$$\mathcal{L}_{EM} = -\frac{1}{4} F^{\mu\nu} F_{\mu\nu} \tag{2.4}$$

In this form, it's evident that this electromagnetic field Lagrangian is invariant under Lorentz transformations since the product $F^{\mu\nu}F_{\mu\nu}$ is a Lorentz scalar.

The Lagrangian for a fermion field, $\psi(x)$, comes from Dirac [19]

$$\mathcal{L}_F = \overline{\psi}(x)\left(i\gamma^\mu\partial_\mu - m\right)\psi(x) \tag{2.5}$$

A $U(1)$ transformation is represented as the introduction of a complex phase to the field,

$$\psi(x) \mapsto e^{iQ\alpha}\psi(x) \tag{2.6}$$

where Q corresponds to the generator of the transformation, the electric charge, which takes the values ± 1.

The fermion field is invariant under the $U(1)$ transformation as it is written in Eq. 2.6, which expresses a *global* symmetry. The phase, α, that is introduced is a constant phase introduced everywhere (i.e. at all values of x). A stronger constraint can be made by making the phase local, meaning that α goes to $\alpha(x)$. In this case the field dynamics should be invariant under choice of gauge *anywhere* such that two observers agree on electrodynamics, even if they both choose different gauges. Enforcing a *local* gauge invariance means the phase is made to vary with x.

$$\psi(x) \mapsto e^{i\alpha(x)}\psi(x) \tag{2.7}$$

Applying this transformation to the fermion field and taking the derivative shows that the field and, by extension, the Lagrangian are currently *not* locally gauge invariant.

$$\begin{aligned}\partial_\mu\psi'(x) &= \partial_\mu\left[e^{i\alpha(x)}\psi(x)\right] \\ &= e^{i\alpha(x)}\partial_\mu\psi(x) + \boldsymbol{ie^{i\alpha(x)}\psi(x)\partial_\mu\left(\alpha(x)\right)}\end{aligned} \tag{2.8}$$

To reclaim the symmetry, it is necessary to introduce a term to the derivative to compensate. This introduces a *gauge covariant* derivative, here called D_μ.

$$D_\mu \equiv \partial_\mu - ieA_\mu \tag{2.9}$$

The introduction of this gauge covariant derivative then permits us to eliminate the additional term introduced by enforcing local gauge invariance in Eq. 2.8 with an appropriate choice of gauge field A_μ.

$$D_\mu \left[e^{i\alpha(x)} \psi(x) \right] = e^{i\alpha(x)} D_\mu \psi(x) \tag{2.10}$$

The gauge field introduced in doing this behaves identically to the electromagnetic 4-potential, meaning that a combined Lagrangian for an EM-coupled fermion field fully describes the behavior of electrons and positrons along with their interactions mediated by the electromagnetic field. The combined Lagrangian is

$$\mathcal{L}_F = \overline{\psi}(x) \left(i\gamma^\mu \left(\partial_\mu - ieA_\mu \right) - m \right) \psi(x) - \frac{1}{4} F^{\mu\nu} F_{\mu\nu} \tag{2.11}$$

The three fermion terms in Eq. 2.11 consist of the fermion kinetic term, $\overline{\psi}(x) i\gamma^\mu \partial_\mu \psi(x)$, the fermion-photon coupling term, $\overline{\psi}\gamma^\mu e A_\mu \psi(x)$, and the fermion mass term, $m\overline{\psi}(x)\psi(x)$. The remaining term is just the Lagrangian for the electromagnetic field kinetic energy, which was introduced in Eq. 2.4. This field theory is known as quantum electrodynamics, of QED.

2.1.2 Electroweak Gauge Theory

A similar locally gauge invariant, relativistic description of the weak force can be achieved by extending the $U(1)$ symmetry of QED with the $SU(2)$ symmetry group. The full symmetry group of the combined theory, called *Electroweak Theory*, is written as $SU(2)_L \times U(1)_Y$. The subscript L stands for "left-handed" and the subscript Y stands for "weak hypercharge". These properties will be explained in more detail below.

Before the transformations in $SU(2)_L \times U(1)_Y$ are discussed, it is useful to employ an alternate notation for the fermions fields. In QED, only the electron and positron are introduced as fermions, but in electroweak theory, neutrino lepton states, ν_l for $l \in \{e, \mu, \tau\}$ must be included. For simplicity, the first generation states are shown. Second and third generations of fermions take identical form.

$$\psi_1(x) = \begin{pmatrix} \nu_e \\ e \end{pmatrix}_L, \quad \psi_2(x) = \nu_{eR}, \quad \psi_3(x) = e_R \tag{2.12}$$

where $\psi_1(x)$ is a left-handed Weyl spinor that represents the chiral left-handed weak isospin doublet and $\psi_3(x)$ is the right-handed weak isospin singlet. The fermion states for $\psi_2(x)$ do not interact with any of the other fermion fields and so do not enter the Standard Model since there have not been any observed right-handed neutrinos.

Quark interactions with the weak sector mirror the leptons and so their representation is introduced here as well.

$$\psi_1(x) = \begin{pmatrix} u \\ d \end{pmatrix}_L, \quad \psi_2(x) = u_R, \quad \psi_3(x) = d_R \tag{2.13}$$

where u and d are the up-type and down-type quark flavor states, respectively.

This notation can be compacted further, and recover the fermion field, $\psi(x)$, by introducing left and right projection operators [20]. These "Vector-minus-Axial" and "Vector-plus-Axial", or V-A and V+A, operators interact with the fermion field $\psi(x)$ in exactly the way needed to generate the left- and right-chiral states introduced in Eqs. 2.12 and 2.13, respectively.

$$\begin{gathered} \psi(x)_R = \frac{1}{2}\left(1+\gamma^5\right)\psi(x), \quad \psi(x)_L = \frac{1}{2}\left(1-\gamma^5\right)\psi(x) \\ \text{Letting} \quad \psi(x) = \begin{pmatrix} \psi_L \\ \psi_R \end{pmatrix} \end{gathered} \tag{2.14}$$

where γ^5 is the fifth gamma matrix, $\gamma^5 = i\gamma^0\gamma^1\gamma^2\gamma^3$. The V-A and V+A constructions connect the chiral Weyl spinors, used to represent the left-handed fermions and the right-handed anti-fermions, back to the Dirac spinors used in the field Lagrangian with the correct transformation properties required by experiment.

The subscripts L and R indicate the chiral handedness of the electroweak basis states. Only the left-handed fermions couple to the weak sector, and so it will be seen that all $SU(2)$ generators necessarily are 2×2 matrices since they act on the left-handed doublet states. The singlet states are unaffected by weak interactions.

There are three generators of the $SU(2)$ symmetry, which are represented as 2×2 anti-hermitian matrices. Conveniently, the set of Pauli matrices is a representation of these generators, I_1,I_2,$I_3 = \frac{\sigma_1}{2}, \frac{\sigma_2}{2}, \frac{\sigma_3}{2}$. This makes the operator for transformations in $SU(2)$ take on the following form:

$$\begin{aligned} &U_L = \exp\left\{ i\frac{\sigma_i}{2}\alpha^i(x) \right\} \quad \text{for} \quad (i = 1, 2, 3) \\ &\text{such that} \quad \psi(x) \mapsto U_L\psi(x) = \exp\left\{ i\frac{\sigma_i}{2}\alpha^i(x) \right\}\psi(x) \end{aligned} \tag{2.15}$$

where $\psi(x)$ are left-handed doublet states mentioned above, the $\alpha^i(x)$ represent the gauge parameters for each of the three isospin generators. U_L is chosen to represent this gauge transformation since it is unitary and only acts on the left-handed doublet states. The transformations for local gauge invariance involve the change from α^i to $\alpha^i(x)$. The left-handed fermions transform as weak isospin doublets and have a weak isospin (I_3) of $\pm\frac{1}{2}$, while right-handed singlets have a weak isospin (I_3) of 0.

The $U(1)_Y$ transformations are not generated by the electromagnetic charge, Q, alone but by a quantity called *weak hypercharge*, Y, which is defined as $Y \equiv 2\,(Q - I_3)$. Here Q is the electric charge and I_3 is the z-component of the weak isospin.

$$\begin{aligned} &U_Y = \exp\left\{ i\frac{Y}{2}\beta(x) \right\} \\ &\text{such that} \quad \psi(x) \mapsto U_Y\psi(x) = \exp\left\{ i\frac{Y}{2}\beta(x) \right\}\psi(x) \end{aligned} \tag{2.16}$$

where Y is the weak hypercharge, $\psi(x)$ are the fermion fields, U_Y is the unitary operator for a $U(1)_Y$ transformation, and $\beta(x)$ is the gauge parameter associated with the $U(1)_Y$ symmetry.

Because there are four gauge parameters, $\alpha^i(x)$ and $\beta(x)$, there will be four gauge fields introduced in the covariant derivatives, D_μ. These fields are typically denoted as $W^i_\mu(x)$ for $i \in \{1, 2, 3\}$ and $B^0_\mu(x)$. The following combinations of these gauge fields manifest the familiar gauge bosons $W^\pm$, Z^0, and γ.

$$
\begin{aligned}
W_{\mu}^{\pm} &= \frac{1}{\sqrt{2}}\left(W_{\mu}^{1} \mp W_{\mu}^{2}\right) \\
Z_{\mu}^{0} &= W_{\mu}^{3}\cos\left(\theta_{W}\right) - B_{\mu}^{0}\sin\left(\theta_{W}\right) \\
A_{\mu} &= W_{\mu}^{3}\sin\left(\theta_{W}\right) + B_{\mu}^{0}\cos\left(\theta_{W}\right)
\end{aligned}
\tag{2.17}
$$

The mixing that occurs between Z_{μ}^{0} and A_{μ} is parameterized by the weak mixing angle, θ_{W}. It is required by local gauge invariance that the gauge bosons, which arise from interactions between these fields and the fermion states, are necessarily massless. As a matter of fact, introducing mass terms for even the fermion fields proves problematic, as any such mass term would also break the gauge invariance. This is inconsistent with the fact that the leptons, quarks, and gauge bosons have mass. A solution is achieved through the Higgs Mechanism, which is described in the following section.

2.1.3 The Higgs Mechanism and Yukawa Coupling

In order to write down Lorentz and gauge invariant mass terms, a couple of clever changes are made. The introduction of a complex scalar field with a non-zero vacuum expectation value (v.e.v), called the Higgs Field, causes spontaneous symmetry breaking (SSB) of the electroweak theory. The Goldstone Bosons produced by SSB combine with all of the gauge bosons, except for the photon, which gives them mass. Separately, mass terms can be added for the fermions through a Yukawa-like interaction between the fermion fields and the Higgs field.

To begin, the following complex doublet field and its potential are introduced.

$$
\begin{aligned}
\phi(x) &= \begin{pmatrix} \phi_{\alpha} \\ \phi_{\beta} \end{pmatrix} = \sqrt{\frac{1}{2}}\begin{pmatrix} \phi_{1} + i\phi_{2} \\ \phi_{3} + i\phi_{4} \end{pmatrix} \\
V(\phi) &= \mu^{2}\phi^{\dagger}\phi + \lambda\left(\phi^{\dagger}\phi\right)^{2}
\end{aligned}
\tag{2.18}
$$

where μ represents the field's mass and λ is the coupling for the self-interaction. In the case where the mass is real and $\mu^{2} > 0$, the potential behaves as expected and the minimum remains at $\phi = 0$. In the case where $\mu^{2} < 0$, the potential no longer has a minimum at $\phi = 0$, but where

$$\phi^\dagger\phi = \frac{1}{2}\left(\phi_1^2 + \phi_2^2 + \phi_3^2 + \phi_4^2\right) = -\frac{\mu^2}{2\lambda} \equiv \frac{v^2}{2} \tag{2.19}$$

Because the values of the field components are under-constrained here, this corresponds to a continuum of minima. It is also invariant under $SU(2)$ transformations, so there is freedom around the representation of the vacuum state. It is convenient to choose to write $\phi(x)$ as

$$\phi^0 = \sqrt{\frac{1}{2}}\begin{pmatrix}0\\v\end{pmatrix} \xrightarrow{\text{Expand}} \phi(x) = \sqrt{\frac{1}{2}}\begin{pmatrix}0\\v+h(x)\end{pmatrix} \tag{2.20}$$

where ϕ^0 corresponds to the vacuum state and $\phi(x)$ represents the generalized scalar fields, which can be found by expanding the field around the vacuum state. The new scalar gauge field that is introduced, $h(x)$, is the Higgs scalar field. Excitations in this field correspond to the Higgs boson.

The Higgs portion of the field Lagrangian takes the form

$$\mathcal{L}_{\text{Higgs}} = \left(D_\mu\phi\right)^\dagger\left(D^\mu\phi\right) - V(\phi) \tag{2.21}$$

with the covariant derivative being the $SU(2)_L \times U(1)_Y$-invariant derivative. This is the combination of local gauge invariant transformations introduced in Eqs. 2.15 and 2.16.

$$\begin{aligned} D_\mu &= \partial_\mu - ig\frac{\sigma_a}{2}W_\mu^a - ig'\frac{Y}{2}B_\mu^0 \\ \phi(x) \mapsto \phi'(x) &= \exp\left\{i\boldsymbol{\alpha}(x)\cdot\frac{\boldsymbol{\sigma}}{2} + i\beta(x)\frac{Y}{2}\right\}\phi(x) \end{aligned} \tag{2.22}$$

where W_μ^a and B_μ^0 are the unmixed electroweak gauge fields. These fields gain a mass term in the interaction with the Higgs field ground state due to the nonzero vacuum expectation value. By evaluating Eq. 2.21 in the Higgs field ground state, the following can be written.

$$\mathcal{L}_{\text{Higgs}} = \left|\partial_\mu\phi\right|^2 + \left|\left(-ig\frac{\sigma_a}{2}W_\mu^a - ig'\frac{Y}{2}B_\mu^0\right)\phi\right|^2 + V(\phi) \tag{2.23}$$

Where the notation $|\ |^2$ is taken to mean $(\ )^\dagger(\ )$. The relevant term for boson masses is the second term, which can be expanded [21].

$$
\begin{aligned}
&\left|\left(-ig\frac{\sigma_a}{2}W_\mu^a - ig'\frac{Y}{2}B_\mu^0\right)\phi\right|^2 \\
&= \frac{1}{8}\left|\begin{pmatrix} gW_\mu^3 + g'B_\mu^0 & g\left(W_\mu^1 - iW_\mu^2\right) \\ g\left(W_\mu^1 + iW_\mu^2\right) & -gW_\mu^3 + g'B_\mu^0 \end{pmatrix}\begin{pmatrix} 0 \\ v \end{pmatrix}\right|^2 \\
&= \frac{1}{8}v^2g^2\left[\left(W_\mu^1\right)^2 + \left(W_\mu^2\right)^2\right] + \frac{1}{8}v^2\left(g'B_\mu^0 - gW_\mu^3\right)\left(g'B_\mu^0 + gW_\mu^3\right) \\
&\quad \text{recall} \;\; W^\pm = \sqrt{\frac{1}{2}}\left(W^1 \mp iW^2\right) \\
&= \left(\frac{1}{2}vg\right)^2 W_\mu^+ W^{-\mu} + \frac{1}{8}v^2\begin{pmatrix} W_\mu^3 & B_\mu^0 \end{pmatrix}\begin{pmatrix} g^2 & -gg' \\ -gg' & g'^2 \end{pmatrix}\begin{pmatrix} W^{3\mu} \\ B^{0\mu} \end{pmatrix}
\end{aligned}
\tag{2.24}
$$

The first term, $\left(\frac{1}{2}vg\right)^2 W_\mu^+ W^{-\mu}$, contains the mass of the $W^\pm$ bosons: $M_W = \frac{1}{2}vg$. The second term contains the mass of the Z^0, but to get it requires a bit more work.

$$
\begin{aligned}
\frac{1}{8}v^2\begin{pmatrix} W_\mu^3 & B_\mu^0 \end{pmatrix}\begin{pmatrix} g^2 & -gg' \\ -gg' & g'^2 \end{pmatrix}\begin{pmatrix} W^{3\mu} \\ B^{0\mu} \end{pmatrix} &= \frac{1}{8}\left[g^2\left(W_\mu^3\right)^2 - 2gg'W_\mu^3B^{0\mu} + g'^2\left(B_\mu^0\right)^2\right] \\
&= \frac{1}{8}\left[gW_\mu^3 - g'B_\mu\right] + 0\left[gW_\mu^3 + g'B_\mu\right]
\end{aligned}
\tag{2.25}
$$

where the vanishing eigenstate of the matrix is included explicitly since this term corresponds to the massless photon, γ.

Recall in Eq. 2.17 that the third component of the weak isospin gauge fields, W_μ^3, mixed with the hypercharge gauge field, B_μ^0, by a mixing angle θ_W. This mixing angle corresponds to the ratio of g and g' in the following way.

$$
\frac{g'}{g} = \tan\theta_W \tag{2.26}
$$

This lets us construct the physical Z_μ^0 and A_μ fields as

$$
\begin{aligned}
Z_\mu^0 &= W_\mu^3\cos\left(\theta_W\right) - B_\mu^0\sin\left(\theta_W\right) = \frac{g'W_\mu^3 - gB_\mu^0}{\sqrt{g^2 + g'^2}} \\
A_\mu &= W_\mu^3\sin\left(\theta_W\right) + -B_\mu^0\cos\left(\theta_W\right) = \frac{g'W_\mu^3 + gB_\mu^0}{\sqrt{g^2 + g'^2}}
\end{aligned}
\tag{2.27}
$$

Connecting this back to the solutions in Eq. 2.25, the mass of the photon is $M_\gamma = 0$ and the mass of the Z^0 is $M_{Z^0} = \frac{1}{2}v\sqrt{g^2 + g'^2}$. The ability of the Higgs mechanism to organically reproduce the massless photon is one additional advantage of the mechanism.

To give masses to the fermions, a Yukawa coupling connecting the fermions to the Higgs field is introduced. The fields of right- and left-handed fermions cannot have mass terms as currently written, as these terms would take the form $m(\bar{\psi}_L\psi_R + \bar{\psi}_R\psi_L)$, which is not a gauge invariant quantity.

With the addition of the Higgs field, it is possible to introduce a Yukawa coupling of the form $\bar{\psi}\phi\psi$, with the ψ terms as the $SU(2)$ left-handed doublet and right-handed singlet states.

$$\mathcal{L}_{\text{Yukawa}} = -G\left(\bar{\psi}_L\phi\psi_R + \bar{\psi}_R\phi^c\psi_L\right) \tag{2.28}$$

The interaction strength is given by G and ϕ^c is the conjugate-transpose of the Higgs field,

$$\phi = \sqrt{\frac{1}{2}}\begin{pmatrix} 0 \\ v + h(x) \end{pmatrix}, \qquad \phi^c = -i\sigma_2\phi = \sqrt{\frac{1}{2}}\begin{pmatrix} v + h(x) & 0 \end{pmatrix} \tag{2.29}$$

The introduction of ϕ^c is utilized in the quark field terms to couple the Higgs field to the upper doublet states. Both of these forms of the Higgs field permit the right-handed singlets to fully contract with the left-handed doublets and produce $SU(2)_L$ scalars, which makes the fermion mass terms gauge invariant.

The Yukawa terms in the field Lagrangian for the coupling between the fermions and the Higgs field are

$$\mathcal{L}_{\text{Yukawa}} = -G_e\begin{pmatrix} \bar{\nu}_e & \bar{e} \end{pmatrix}_L \phi\, e_R - G_u\begin{pmatrix} \bar{u} & \bar{d} \end{pmatrix}_L \phi\, d_R - G_d\begin{pmatrix} \bar{u} & \bar{d} \end{pmatrix}_L \phi^c\, u_R + h.c. \tag{2.30}$$

where, u, d, and e represent the quark and lepton states of all three generations, and $h.c.$ stands for "hermitian conjugate" of the terms shown. Using the Higgs field terms from Eq. 2.29, its possible to simplify this Lagrangian and write down the explicit mass terms.

$$\mathcal{L}_{\text{Yukawa}} = \frac{v + h(x)}{\sqrt{2}} \left(-G_e \bar{e}_L e_R - G_u \bar{d}_L d_R - G_d \bar{u}_L u_R \right) + h.c. \tag{2.31}$$

For each lepton, the mass is given by

$$M_f = \frac{v G_f}{\sqrt{2}} \tag{2.32}$$

While this Yukawa coupling to the Higgs field solves a lot of problems in modeling particle masses, it should be emphasized that the mass terms are not theoretically constrained. Each coupling factor G_f must be set by experimental observations. This hints to further shortcomings and potential improvements that could be made to the Standard Model, some of which are discussed in the following section.

2.2 Beyond the Standard Model

The Standard Model has been incredibly successful in its ability to correctly predict particle interactions and processes, as well as the *existence* of several fundamental particles. However, most physicists believe that the Standard Model is a low-energy effective field theory rather than the fundamental theory of particle physics. Some missing elements of the Standard Model are:

- **Neutrino Oscillations** - Observation of flavor-changing oscillations in neutrinos has demonstrated that neutrinos must have some non-zero mass. Although neutrino masses are predicted to be very small, the Standard Model does not include a neutrino mass term. The simplest inclusion of a Dirac mass via Yukawa coupling, mirroring the other lepton masses, would necessitate the inclusion of right-handed neutrinos, which have so far not been observed [22].

- **Dark Matter** - Astrophysics and Cosmology give us evidence, by way of observations of rotational motion of galaxies and gravitational lensing, of gravitational phenomena that cannot be explained by general relativity and ordinary matter alone. One explanation for these phenomena is the existence of a massive, weakly interacting particle called dark matter [23]. Neutrinos do not provide enough mass to produce the

observations, so dark matter would be a particle outside the Standard Model. Many direct searches for dark matter have been performed at the LHC and in other dedicated experiments, but no evidence has been found for these particles to date.

- **Matter-Antimatter (Baryon) Asymmetry** - Measurements of the matter-antimatter asymmetry, $(n_b - n_{\bar{b}})/n_\gamma$, (and our existence) show that the universe is predominantly composed of matter. This is difficult to explain given the understanding that the early universe was hot and had an equal mixture of the two. Sakharov described the conditions necessary to break the matter-antimatter symmetry in the early universe [24], but so far these conditions are not sufficiently met by the Standard Model. For example, while the Standard Model permits CP violation, the amount observed is insufficient to explain the matter-antimatter asymmetry [25].

- **Strong Unification** - The strong interactions are described by an $SU(3)$ symmetry, and so the Standard Model is described as an $SU(3)_C \times SU(2)_L \times U(1)_Y$ theory. Unlike the electroweak theory, which actually unifies the weak and electromagnetic forces before SSB, the strong force is added as a gauge group extension in the Standard Model. A theory that unifies all of these forces (strong, weak, and electromagnetic), or a Grand Unified Theory (GUT), would require an additional mechanism to break some higher-order symmetry into the current $SU(3)_C \times SU(2)_L \times U(1)_Y$ theory and particles associated with this symmetry breaking have not been observed [26].

- **Quantum Gravity** - The Standard Model offers a quantum framework explaining three of the four fundamental forces: the strong force, the weak force, and electromagnetism. Yet it doesn't offer any explanation for gravity. Efforts have been made to develop a theory of quantum gravity, but none so far have been renormalizable [27]. It is understood, however, that any theory of quantum gravity would necessarily couple to a spin-2 boson, called the graviton. To date, no such particle has been observed by experiment [28, 29].

In addition to the phenomena listed above, which are not described by the Standard Model, there are other theoretical shortcomings. They tend to hint at some lack of understanding

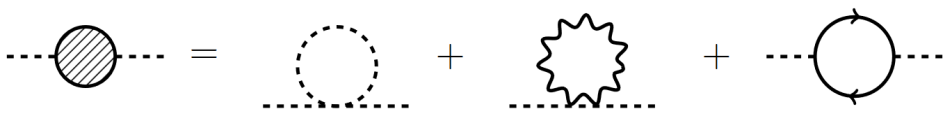

Figure 2.2: Diagrammatic description of loop-level corrections to the Higgs mass.

that may lead to the development of a more fundamental theory. Some examples of these modeling shortcomings are:

- **Hierarchy Problem** - Experimentally, the mass of the Higgs boson has been measured to be 125.25 GeV. At loop level, the Higgs mass receives corrections from self-interactions, gauge loops, and fermion loops. These corrections are shown diagrammatically in Figure 2.2. These corrections appear as

$$\delta m_H^2 = \frac{\Lambda^2}{32\pi^2}\left[6\lambda + \frac{1}{4}\left(9g^2 + 3g'^2\right) - y_t^2\right] \tag{2.33}$$

  where g and g' are the gauge boson strength factors, λ is the Higgs self-interaction strength, y_t is the Yukawa coupling strength, and Λ is the renormalization cutoff scale [30]. This quadratic dependence in Λ means that, as the Higgs mass is calculated at higher renormalization cutoffs, the Higgs corrections diverge quickly. To unify gravity, Λ must be at the plank scale, $\sim 10^{16}$ TeV. These corrections come to dominate the Higgs mass when $\Lambda \gg 10$ TeV. In order for the Higgs to have its experimentally determined mass, the strength parameters g, g', λ, and y_t all must take on exceedingly small values or cancel each other to high precision in order to assure the Higgs mass takes its experimental value. This is a type of "Fine Tuning" problem, where model parameters must be finely tuned in order to return correct physics. In order to reduce the amount of fine tuning required, BSM models can introduce new particles that would add additional terms to the loops. These additional terms could counteract contributions from those shown in Eq. 2.33.

- **Strong CP Problem** - QCD has been experimentally shown to preserve CP-symmetry, but the QCD Lagrangian in the Standard Model permits the existence of CP-violating strong interactions. This is another fine tuning problem that requires model parame-

ters to take on very specific values in order to produce the physics seen in experiment [31, 32].

- **Number of Parameters** - The Standard Model contains 19 free parameters, the values of which are set by experiment. Specifically, all of the masses present in the Standard Model rely on a free coupling parameter. This freedom, inherent to the Standard Model, means that it provides no insight into why the particle masses take the values that they have. The number of fermion generations is also not motivated aside from matching experimental observation.

2.2.1 The Hidden Sector Model of Long-Lived Particles

Theories Beyond the Standard Model (BSM) aim to address one or several of the outstanding problems in the Standard Model. From experiment, the Higgs boson has a relatively large upper limit on its branching ratio into invisible products ($H \rightarrow inv.$) of $10-15\%$ [33, 34, 35]. Some BSM models take advantage of this by predicting particles that do not directly couple with the rest of the Standard Model, but interact through effective couplings mediated by the Higgs boson. These types of models are referred to as Hidden Sector models, since the BSM particles predicted are not directly detectable (and therefore "hidden" from collider experiments). The mechanism is often called a Higgs portal.

A simple model that demonstrates this kind of an extension to the Standard Model is one that introduces a hidden $U(1)$ symmetry, $U(1)_{hid}$, and a scalar field Φ that has a non-zero v.e.v, similar to the Higgs field [36, 37, 9]. This hidden gauge sector would only interact with the Standard Model through mixing with the $U(1)_Y$ gauge group via their gauge bosons. The Φ field would also couple to the Higgs Field and the most general additional interactions would make the Higgs Lagrangian contributions take the form

$$\mathcal{L}_{Higgs} = |D_\mu \phi|^2 + |D_\mu \Phi|^2 + m_\phi^2 |\phi|^2 + m_\Phi^2 |\Phi|^2 - \lambda |\phi|^4 - \rho |\Phi|^4 + \eta |\phi|^2 |\Phi|^2 \tag{2.34}$$

where ϕ is the Standard Model Higgs field, introduced in Eq. 2.18, and Φ is the new, hidden scalar field.

In order for Φ to be uncharged in the Standard Model, it transforms as an $SU(2)_L$ singlet.

After symmetry breaking occurs, the SM Higgs and Hidden Sector "Higgs", Φ, will produce two coupled fields. This leads to two physical mass eigenstates that correspond to the SM Higgs-like boson, H, and the hidden sector scalar, s. The coupling term η in Eq. 2.34 induces the $H \to ss$ decay [36, 37, 9]. Because of the mixing of mass eigenstates, and the Yukawa coupling between the Higgs field and the fermions, the s scalars are able to decay back into SM particles as fermion-antifermion pairs. If the mass mixing angle between H and s is sufficiently small, then s would be fairly stable, leading to a macroscopic decay length in the detector frame. Their decay into fermions then could produce showers that would appear as displaced jets. The Feynman diagram in Figure 2.3 shows a pair of Hidden Sector s-decays producing displaced jets. For this analysis, the branching ratio of $s \to f\bar{f}$ is assumed to be 100%.

This model is an appealing extension since it maintains the predictive integrity of the Standard Model, while also providing an additional field which could ease the Hierarchy problem. It also permits future extensions into a Hidden Sector, which could contain other, stable particles that could serve as dark matter candidates.

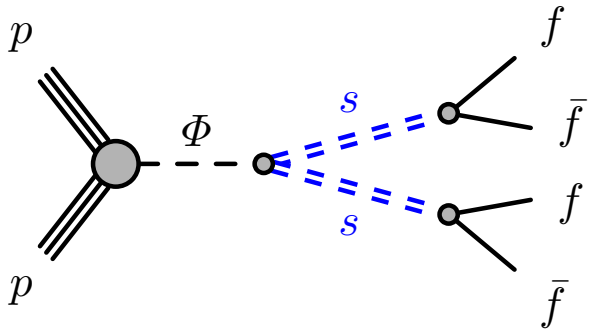

Figure 2.3: Feynman diagram of long-lived scalar s bosons decaying into displaced vertices.

2.2.2 Baryogenesis Model of Long-Lived Particles

Baryogenesis models aim to address the matter-antimatter asymmetry in the early universe by introducing a baryon(B)- or lepton(L)-number violating decay. The benchmark model used in this analysis introduces a Weakly Interacting Massive Particle (WIMP), which could

also serve as a dark matter candidate [38].[1]

Using a similar Higgs portal mechanism as the Hidden Sector model, the baryogenesis benchmark model introduces a Standard Model singlet state that mixes slightly with the Higgs boson mass eigenstate due to a weakly broken $\mathbb{Z}_2$ symmetry [38]. In order to be accessible at LHC energies, and to connect to other WIMP baryogenesis models, the Higgs portal energy is set to the electroweak scale. The resulting long-lived particle is a hidden sector Majorana fermion, χ, which produces CP-violating and B/L-number violating decays.

The Majorana fermions would be produced and annihilate in equilibrium with SM fermions in the early universe. As the universe cooled, the χ particles would cease production, as the energy density of the universe would be insufficient to produce heavy χ particles. Because the χ particles are Majorana fermions, they are their own antiparticle and could continue to annihilate. Eventually, the universe cooled and expanded to the point where the χ particles would no longer annihilate each other and freeze-out. This freeze-out temperature occurs around the electroweak scale. Below the freeze-out temperature is where the $\mathbb{Z}_2$ symmetry is broken, the Higgs and S particles involved in the Higgs portal mix their mass eigenstates, and the CP-violating B/L-number violating decays of the χ can occur.

The long-lived particle, χ, transforms as a Standard Model singlet and connects to the SM fermions through the mixing of a scalar S with the SM Higgs boson. It's through this mixing that a Yukawa coupling to the SM fermions permits the production of detectable displaced vertices. While χ production could be mediated by a resonance with S through a similar Yukawa interaction, for simplicity and to avoid overlap with the Hidden Sector model discussed in Section 2.2.1, the S boson is taken to be heavy and decoupled from the χ production, which is solely mediated by a SM Higgs after mass state mixing, ($gg \to h \to \chi\chi$). A Feynman diagram of the baryogenesis model can be seen in Figure 2.4 [39].

There are two different regions where long-lived particle production in the baryogenesis model could be investigated. One region is the on-shell region where the χ pair is produced by an on-shell SM Higgs ($m_\chi < m_H/2$). The production cross section at the LHC center-of-mass energy of 13 TeV is expected to be substantial, proportional to the coupling of the

[1] If the particle has a sufficiently long lifetime, it would leave the detector before decaying and would be a more appropriate candidate for dark matter searches.

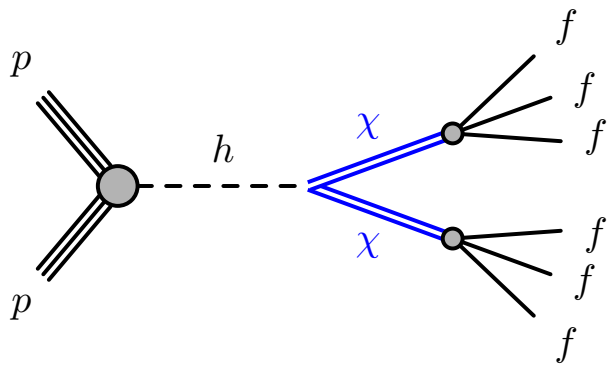

Figure 2.4: Feynman diagram of long-lived Majorana fermions χ decaying into displaced vertices. Majorana fermions are capable of having baryon- and lepton-number-violating decays, which are a necessary condition for matter-antimatter asymmetry.

Higgs and χ pair. As such, a strong constraint on the $h \to \chi\chi$ branching ratio is possible. Alternatively, there is the off-shell production region, ($m_\chi > m_H/2$), where the cross section drops quickly with increasing m_χ. While the sensitivity to this particular production region is not expected to be high, it is interesting to study it in the context of the full Run 2 luminosity.

Chapter 3

The LHC and ATLAS Detector

3.1 Introduction

One central trend of experimental particle physics over the past several decades has been to design and construct particle accelerators of increasing center-of-mass energy, $\sqrt{s}$, which permits smaller length scales to be probed. As the momentum of a particle increases, its de Broglie wavelength decreases. The de Broglie wavelength represents the characteristic scale of the particle's interactions, which makes higher-energy accelerators collisions attractive for investigating smaller-scale physics. The first circular particle accelerator was the Betatron magnetic induction accelerator, the concept of which was introduced in 1922 by J. Slepian [40]. The general concept of the Betatron was that electrons (beta particles) could be accelerated by way of a changing magnetic field [40]. While capable of accelerating electrons to around a few 10s of MeV, with the highest energy reaching 300 MeV, higher energies would be achieved by the cyclotron [41]. The first cyclotron was developed by E.O. Lawrence in 1929-1930, having been inspired by an earlier linear accelerator designed by R. Wideröe. The cyclotron's operating principal was for charged particles, immersed in a magnetic field, to be accelerated using an oscillating electric field across a gap. Due to the magnetic field, the particles trajectory would be circular, with the radius increasing as the particle's velocity increased. The highest energy cyclotron, the PSI Ring located in Switzerland, was able to reach a beam of protons with an energy of 590 MeV in 1974 [41, 42].

Most modern circular particle accelerators are designed around the synchrotron operating principle, built at a fixed radius, where the magnetic field is *synchronized* to increase alongside the particle kinetic energy. The synchrotron principle was invented by V. Veksler in

1944 and E.M. McMillan, independently, in 1945. The first proton synchrotron design based on this principle was introduced by M.O. Oliphant, which was later constructed in 1952. Since then, more powerful synchrotron particle accelerators have been constructed, with the current leading device being the LHC in Geneva, Switzerland.

3.2 The Large Hadron Collider

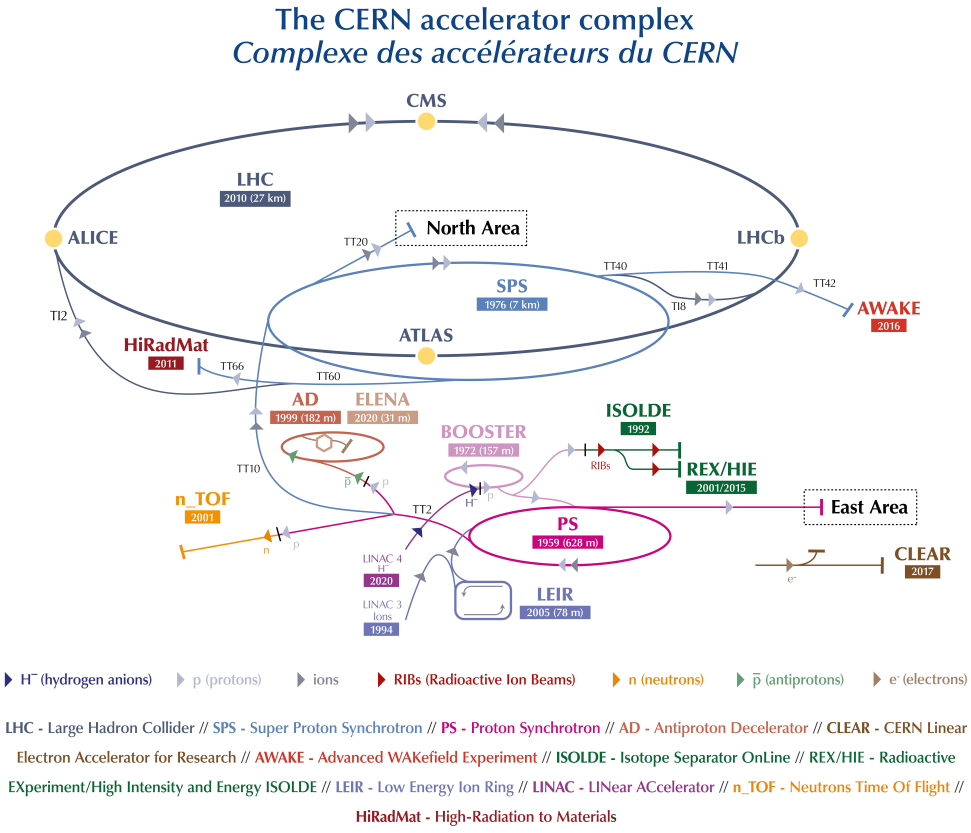

Figure 3.1: Diagram of the LHC complex, with experiments and LHC acceleration chain components labeled.

The LHC is currently the world's most energetic accelerator. The center-of-mass energy was 13 TeV during the 2015-2018 (Run 2) data collection period, and was increased to 13.6 TeV in 2022 with the beginning of Run 3. The LHC is a two-ring superconducting hadron accelerator and collider designed to use the 26.7 km tunnel, located between 45 and 170 m below the surface on the Swiss-French border, that had been occupied by the Large

Electron Positron (LEP) collider until its decommissioning in 2000. The LHC project was approved by the CERN Council in December 1994 with a plan at the time to build the machine in two steps, with the first step to reach a center-of-mass energy, $\sqrt{s}$, of 10 TeV, before later upgrading to 14 TeV. In December 1996, the CERN Council redefined the plan so the LHC was constructed with a target $\sqrt{s}$ of 14 TeV in a single step [43].

Construction on the LHC ended in 2008. The LEP tunnel it was built within had two surface structures located at Points 2 and 8, which were used for the ALICE and LHCb experiments, respectively. As part of the LHC construction, two additional surface structures were built at Points 1 and 5, which were used for the ATLAS and CMS experiments, respectively. One advantage of reusing the LEP tunnel was the existing LEP injection chain. This same injection chain was utilized for the LHC, and can be seen in Figure 3.1 [44].

The inaugural test of the LHC was held on September 10th, 2008. Only a few days later, on September 19th, an electrical fault caused a liquid helium leak, which led to the superconducting magnets in sector 3-4 rapidly becoming non-superconducting in an event called a "quench". This released much of the energy contained in the magnetic field of the superconductor as heat, which caused the increase and violent release in pressure of the liquid helium used to cool the superconducting magnets. This incident pushed back the first run of the LHC until 2009 [45, 46]

The first run (Run 1) of the LHC began in 2009 with the first circulating beam having an energy of 0.45 TeV. The energy was raised to 1.18 TeV, and a second beam was added, by the end of November of the same year. It ended 2009 having reached an energy of 2.36 TeV, and having delivered over a million bunch pairs to the LHC experiments. On March 19th, 2010, physics collisions were produced at 3.5 TeV energy per beam, or a $\sqrt{s} = 7$ TeV. Following a short break at the end of 2011, the LHC was able to achieve energies of $\sqrt{s} = 8$ TeV [47].

The period from 2013-2015, known as Long Shutdown 1 (LS1), consisted of upgrades to the LHC, which included increasing the strength of the superconducting magnets in order to support beams up to 6.5 TeV [48].

3.2.1 The LHC Injection Chain

The LHC injection chain begins with a standard cylinder of hydrogen gas. This neutral hydrogen is ionized and split into its constituent protons and electrons by a duoplasmatron [49, 50]. The proton beam is then accelerated by a **linear accelerator (LINAC)**. From 2008 through 2020, this was the LINAC 2 accelerator. LINAC 2 was able to accelerate protons to energies of 50 MeV. In 2020, LINAC 2 was replaced with LINAC 4, as part of the High Luminosity LHC (HL-LHC) upgrade, which accelerates protons to 160 MeV [51]. The protons from the LINAC are then accelerated in the **Proton Synchrotron (PS) Booster** to 1.4 GeV [52]. The **Proton Synchrotron (PS)** can accelerate both the protons from the PS Booster as well as heavy ions provided by the Low Energy Ion Ring (LEIR). The protons in this stage are accelerated from 1.4 GeV to 26 GeV [53].

The protons leaving the PS enter the **Super Proton Synchrotron (SPS)** accelerator. The SPS is the second-largest accelerator at CERN's accelerator complex in Geneva, measuring approximately 7 km in circumference. The SPS accelerates the protons up to 450 GeV from the PS for delivery to the COMPASS experiment, the NA61/SHINE and NA62 experiments and other North Area experiments using the SPS test beams [54], and the LHC [55]. The **LHC** then accelerates the protons to their final energy, 6.5 TeV (6.8 TeV after LS2), which gives the center-of-mass energy of 13 TeV (13.6 TeV after LS2).

In order to bend and focus the proton beam, dipole, quadrupole, and higher-order superconducting magnets are used. The LHC has a total of 1232 dipole magnet segments and 474 quadrupole magnet segments, with additional sextupole, octupole, and decapole magnets used in each segment to shape and focus the beam. The dipole magnets are responsible for bending the beam around the full LHC circumference. Each dipole segment is 14.3 m long and produces a magnetic field of $\sim$ 8.4 T. The quadrupole magnets come in a variety of lengths and nominal magnetic field strengths and are the primary focusing magnets, which keep the beam from dispersing and focus the beam for collisions. The higher-order magnets correct for smaller fluctuations in the beam shape. [54, 56, 57]

The protons are accelerated in the LHC by sixteen radio frequency (RF) cavities (eight per beam). Each cavity generates a longitudinal oscillating voltage of 2 MV that provides

an accelerating electric field strength of 5 MV/m and operate at a frequency of 400 MHz. In addition to providing the acceleration to the protons, the RF cavities also maintain the bunch structure of the beams. By synchronizing the RF frequency with the proton revolution frequency, the RF cavities apply a longitudinal restoring force that accelerates the protons back toward the center of each proton bunch [58, 59].

3.2.2 Detectors and Experiments

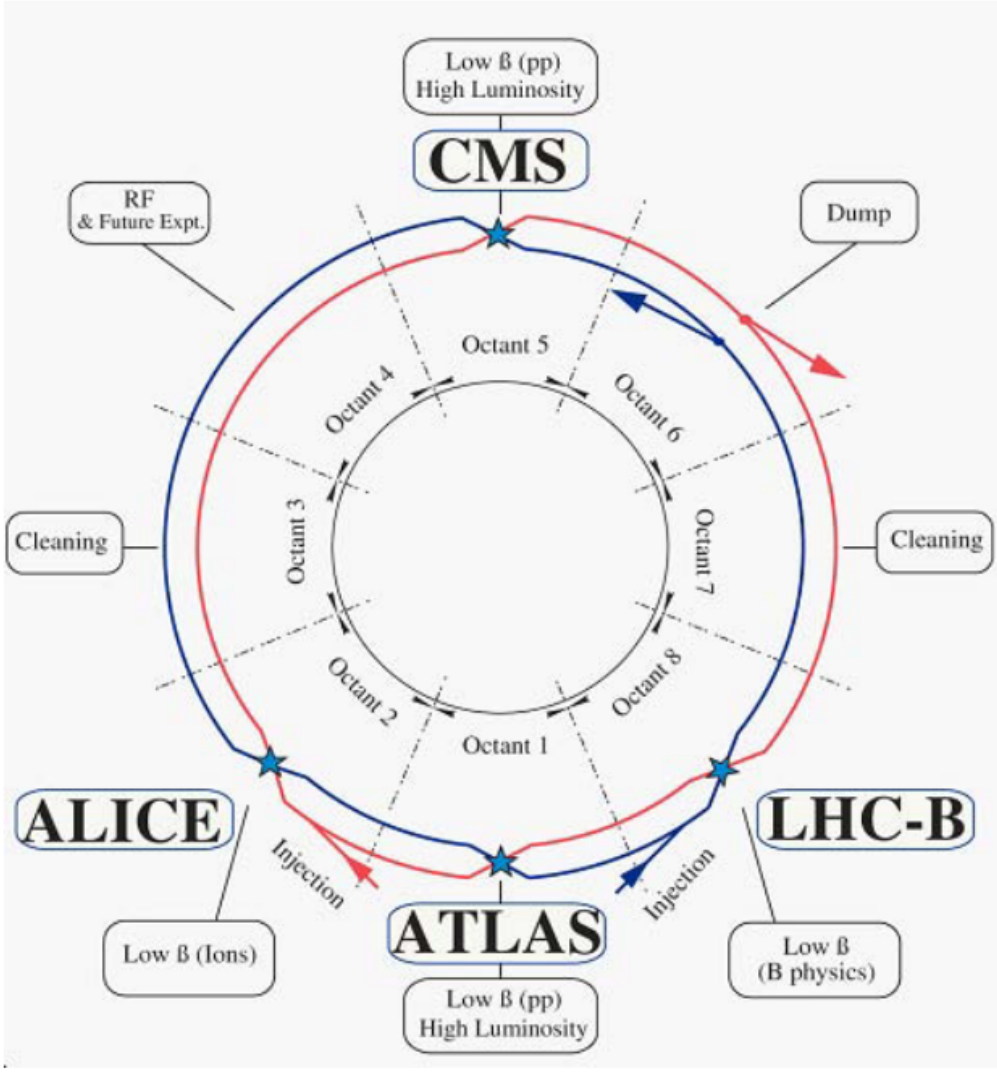

Figure 3.2: Diagram of the LHC beams. Beam 1 is in red and circles clockwise. Beam 2 is in blue and circles counterclockwise. Diagram is not to scale.

There are nine experiments installed at the LHC, four of which are installed along the beam line, which use the beams generated to probe collisions in different ways based on

their design purposes and specialties. A diagram of the beam directions and the location of the four beam line experiment locations can be seen in Figure 3.2 and descriptions of the main four experiments follow [43].

ALICE (A Large Ion Collider Experiment), located at P2, is a general-purpose heavy-ion detector. With a focus on QCD and the strong-interaction sector, ALICE was designed to probe strongly-interacting matter and quark-gluon plasma at extreme energies [60].

CMS (Compact Muon Solenoid), located at P5, is a multipurpose apparatus with the primary motivation to yield precise measurements of the momentum of charged particles [61]. Due to design goals, CMS also contains a very precise EM calorimeter for precision reconstruction of high energy photons [62].

ATLAS (A Toroidal Lhc ApparatuS), located at P1, is a multi-purpose particle detector with the capability to observe all final states expected from proton-proton (or heavy ion) collisions. It utilizes magnet systems to produce curved paths of charged particles for momentum reconstruction and a calorimeter to measure energy deposition [63]. This was the detector used to collect the data used in this analysis. More information on ATLAS is presented in Section 3.3.

LHCb, located at P8, is an LHC experiment focused on heavy flavor physics, with a primary goal to look for indirect evidence of new physics in CP violation and rare decays of hadrons with bottom and charm quarks, specifically B and D mesons [64].

3.3 The ATLAS Detector

The ATLAS detector is a cylindrical, multi-purpose particle detector located at Point 1 on the LHC. It is 46 meters long and 25 meters in diameter. It uses a right-handed coordinate system where the beam line is defined as the z-axis, with the interaction point corresponding to the point where $z = 0$. The x-y plane is orthogonal, with the positive x-axis pointing from the detector to the center of the LHC ring, and the y-axis pointing upward [65].

It is often more convenient to use cylindrical coordinates when discussing collision events. The azimuthal angle ϕ is measured in the x-y plane with $\phi = 0$ corresponding to the positive x-axis, and the polar angle θ is measured with respect to the positive z-axis. Pseudorapidity

η, is defined as

$$\eta = -\ln\left[\tan\frac{\theta}{2}\right] \tag{3.1}$$

It is often used in place of θ, because particle densities are approximately constant in this variable. Pseudorapidity is an approximation of a particle's rapidity in the limit where $E \sim p$. In terms of particle's energy, E, and the longitudinal momentum p_z, the rapidity can be expressed as

$$y = \frac{1}{2}\ln\left(\frac{E + p_z}{E - p_z}\right) \tag{3.2}$$

To recover Eq. 3.1, it's possible to expand the energy using $E = \sqrt{m^2 + p^4}$. The relationship between $|\overrightarrow{p}|$ and p_z brings θ into the equation.

In this coordinate system, the distance between two objects is often expressed as the angular separation ΔR, which is defined as

$$\Delta R = \sqrt{\Delta\eta^2 + \Delta\phi^2} \tag{3.3}$$

The ATLAS detector has a layered design, with each layer featuring a sub-detector that focuses on measuring specific quantities of a collision event. There are three sub-detectors that comprise ATLAS, the Inner Detector (ID), the Calorimeter (Calo), and the Muon Spectrometer (MS), as well as a dedicated superconducting magnet system that provides the magnetic fields for the ID and MS. A diagram of ATLAS is shown in Figure 3.3 [66].

The superconducting magnet system is comprised of the central solenoid (CS), which provides a 2 T magnetic field to the ID, the barrel toroid (BT), and the endcap toroid (ECT), which both provide a magnetic field with a peak strength of 4 T to the MS. The entire system is cooled to 4.5 K.

3.3.1 The ATLAS Inner Detector

The ATLAS Inner Detector (ID) is a cylindrical sub-detector, centered around the beam axis, with a length of 7 m and a diameter of 2.3 m. The ID is immersed in a 2 T magnetic

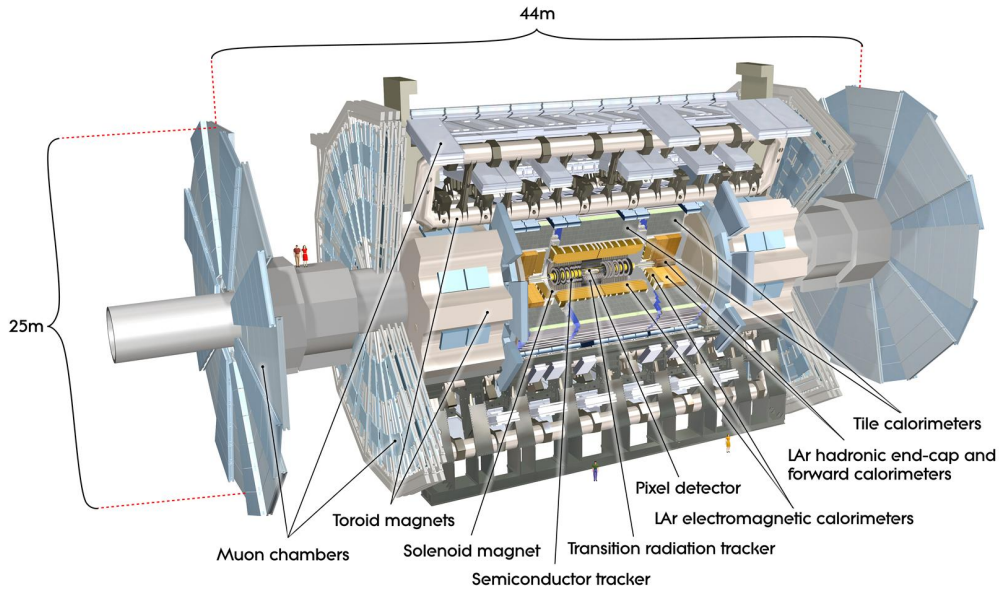

Figure 3.3: Diagram of the ATLAS detector with sub-detectors labeled.

field. The ID is composed of three main subsystems: the pixel detectors, the semiconductor tracker (SCT), and the transition radiation tracker (TRT). A figure with each ID subsystem labeled can be seen in Figure 3.4 [67].

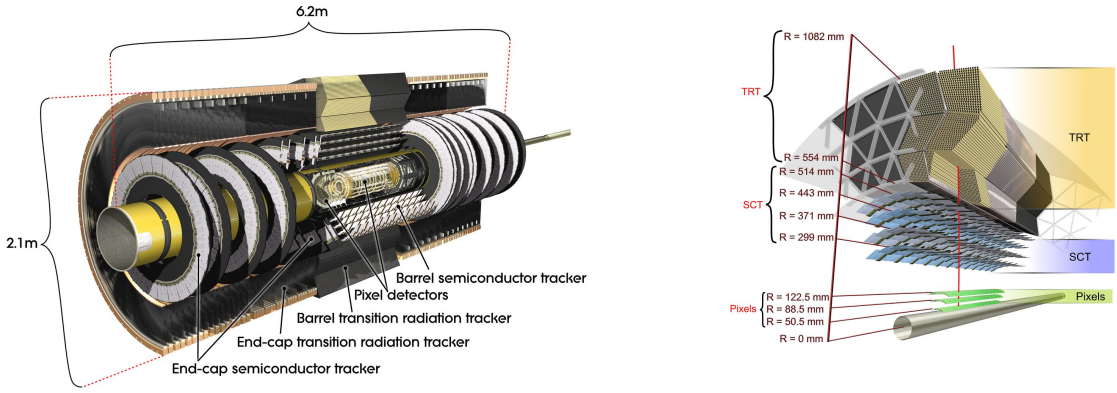

(a) **(b)**

Figure 3.4: (a) Diagram of the ID with subsystems labeled, (b) Cross-sectional diagram of the barrel portion of the ID

The Pixel Detector is designed to provide high-granularity, high-precision measurements as close to the beam line as possible. It is composed of two barrel layers, five disks in each endcap, and one removable barrel layer (B-layer). In the barrel, the inner radius is

approximately 4 cm from the beam line and the outer radius is about 13 cm. In the endcap, the disks are between 11 cm and 20 cm from the beam line. The resolution of the B-layer and the two additional barrel layers is 12 μm in the azimuthal ϕ direction and 66 μm in the longitudinal z direction [65].

The Semiconductor Tracker (SCT) is designed to provide precision track measurements at larger radii, which helps improve measurements of incident particle momentum. Track information collected in the SCT is also used in reconstructing the primary interaction impact parameter and vertex position. The SCT is composed of four barrel layers and nine wheels in each endcap, for a total of eighteen wheels. The barrel layers have an inner radius of 30.0 cm and an outer radius of 52.0 cm, while the endcap wheels have a varying inner radii such that they cover a region with $|\eta| \leq 2.5$ and a maximum outer radius of 56.0 cm [68]. The resolution for both the barrel SCT layers and the endcap SCT disks is 16 μm in the azimuthal direction ϕ and 580 μm along the longitudinal axis z [65].

The Transition Radiation Tracker (TRT) provides tracking at large radius using a technology different from that of the SCT: proportional drift tube detectors. Each drift tube (straw) is a 4 mm diameter cylinder with a 30 μm diameter gold-plated tungsten wire running along its central axis, for the full straw length of 144 cm in the barrel and approximately 37 cm in the endcap [69]. Both the barrel and endcap TRT straws have a resolution of 170 μm per straw [65].

3.3.2 The ATLAS Calorimeter

The ATLAS Calorimeter is designed primarily to measure the energy of particles that are absorbed by it. The calorimeter features two sections: an electromagnetic calorimeter (ECal) covering a pseudorapidity range of $|\eta| < 3.2$ and a hadronic calorimeter (HCal) covering $|\eta| < 1.7$ in the barrel and $1.5 < |\eta| < 3.2$ in the endcaps [70]. It also has full ϕ symmetry and coverage around the beamline. The ECal is a lead/liquid-argon (LAr) detector. The ECal LAr calorimeters are divided between a cylindrical barrel section and two endcap sections. The ECal barrel forms a cylinder with an inner radius of 1.15 m and outer radius of 2.25 m with a length of 13.3 m, centered at $z = 0$ along the beam axis [71]. The ECal endcaps cover the region of $1.375 < |\eta| < 3.2$ with an inner radius of $\sim$ 300 mm

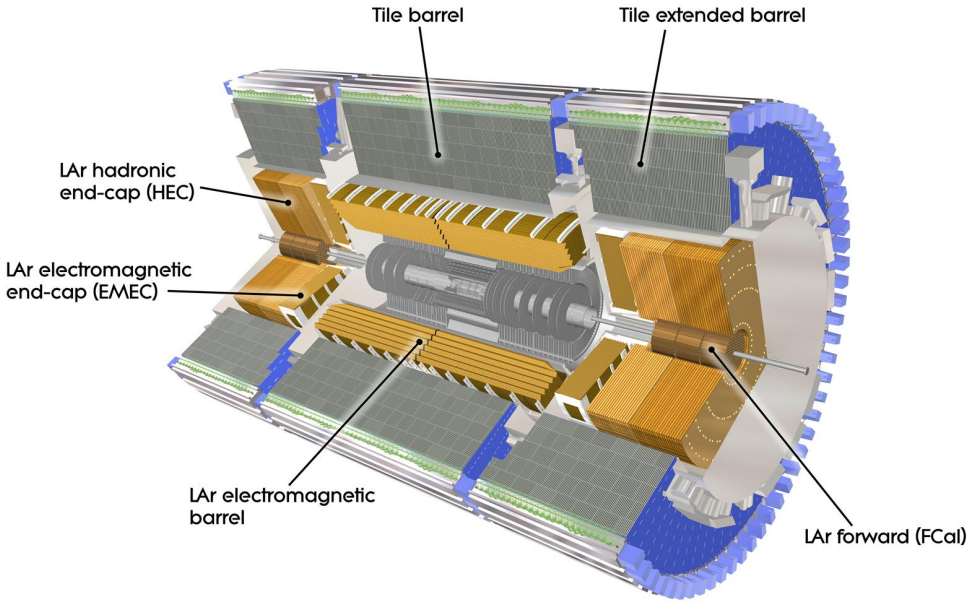

Figure 3.5: Diagram of the ATLAS calorimeter with sections labeled.

and an outer radius of $\sim 2\,\text{m}$ [72]. The HCal is divided between the barrel and endcap sections. The endcaps are an LAr calorimeter and the barrel is covered by a scintillator-tile calorimetry system. The outer radius of the HCal scintillator-tile calorimeter is 4.25 m and its length, centered along the beam axis, is 12.20 m [65]. A diagram of the ATLAS calorimeter can be seen in Figure 3.5 [73].

The ECal is designed to measure the energy of particles that produce electromagnetic showers. These particles are electrons, positrons, and photons, which are either produced directly or through the decay of neutral pions produced in hadronic showers. The decay products can then ionize the LAr, generating a response proportional to the energy of the particles passing through. The total thickness in the LAr EM calorimeter is > 24 radiation lengths, X_0, in the barrel and > 26 X_0 in the endcap [65]. The barrel ECal consists of two wheels of 1024 lead absorbers interleaved with readout electrodes in an accordion configuration. There are a total of 3424 readout cells for each of the 16 barrel LAr modules. The endcap ECal is composed of two concentric wheels in each endcap. There are 256 absorbers on the inner wheel and 768 absorbers on the outer wheel [71, 74]. The ECal covers $|\eta| < 1.475$ in the barrel and $1.375 < |\eta| < 3.2$ in the endcap. In the barrel, there are three sampling

layers, with ($\Delta\eta \times \Delta\phi$) resolutions of (0.003 $\times$ 0.1), (0.025 $\times$ 0.025), and (0.05 $\times$ 0.025), respectively [65].

The HCal is designed to measure the energy of particles that produce hadronic showers and reduce shower punch-through into the muon spectrometer. The HCal covers a pseudorapidity range of $|\eta| < 4.9$ using a combination of lead/LAr calorimeters, copper/LAr calorimeters, and iron/scintillating-tile (Tile) calorimeter systems [65, 75]. The Tile calorimeter covers the region $|\eta| < 1.7$ in the barrel and extended barrel regions. The lead/LAr and copper/LAr calorimeters cover the range from $\sim 1.5 < |\eta| < 4.9$, with the endcap HCal extending to $|\eta| < 3.2$ and a specialized forward calorimeter (FCal) covering the range $3.1 < |\eta| < 4.9$.

The Tile calorimeter is composed of two segments called the central barrel segment, which is 5.64 m long, and two extended barrel segments, each 2.91 m long. The segments extend from a radius of 2.28 m to 4.25 m, the pseudorapidity range of $|\eta| < 1.7$, and are split into three layers. The layers have thicknesses of 1.4, 4.0, and 1.8 interaction lengths, λ, respectively, yielding a total tile calorimeter depth of 7.2 λ. The first two sampling layers have an ($\Delta\eta \times \Delta\phi$) granularity of (0.1 $\times$ 0.1), while the third has a granularity of 0.2 $\times$ 0.1. The barrel segment covers the pseudorapidity range of $|\eta| < 1.0$, with a slight gap (6 mm) between them centered at $\eta = 0$. The extended barrel covers $0.8 < |\eta| < 1.7$ [65, 75].

The endcap HCal is a copper/LAr calorimeter composed of two wheels, with an outer radius of 2.03 m, at each end. The wheel closer to $z = 0$ has a minimum inner radius of 0.372 m while the outer wheel has an inner radius of 0.475 m [71]. It covers the pseudorapidity region of $1.5 < |\eta| < 3.2$ and the longitudinal location is 4.26 m $< |z| <$ 6.12 m with four sampling layers [71]. In the pseudorapidity range $1.5 < |\eta| < 2.5$, the ($\Delta\eta \times \Delta\phi$) granularity is (0.1 $\times$ 0.1), while in the range $2.5 < |\eta| < 3.2$ it is (0.2 $\times$ 0.2) [65].

The FCal covers a region of the detector with high particle multiplicity, and so special consideration was taken in its design to accommodate the higher activity. One such design accommodation was assuring the FCal has more stopping power than the rest of the endcap calorimeter in order to reduce background radiation levels in the muon system. The FCal is composed of three sections. The first section is a copper/LAr calorimeter, while the other two are tungsten/LAr calorimeters. The FCal has a minimum inner radius of 72.3 mm and an outer radius of 449.4 mm, which corresponds to a pseudorapidity range of $3.1 < |\eta| < 4.9$

[76]. It sits longitudinally between 4.7 m $< |z| <$ 6.1 m, which is longitudinally recessed by 1.2 m from the start of the endcap calorimeter. This recess is to reduce neutron albedo in the ID [65]. The first section has a depth of 2.7 λ, while the second and third sections have a depth of 3.7 λ and 3.6 λ, respectively, making the total depth 10 λ. The FCal ($\Delta\eta \times \Delta\phi$) granularity across all three sections is ($\sim 0.2 \times 0.2$). In the FCal, there are 1762 readout channels across all modules on a single side [77]. Across all LAr calorimeters, there are 182,468 readout channels.

The tile calorimeter has an energy resolution of $\sigma_E/E = 52.9\%/\sqrt{E} \oplus 5.7\%$ for hadrons [78]. The LAr calorimeter has an energy resolution of $\sigma_E/E = 10\%/\sqrt{E} \oplus 0.7\%$ for the EM calorimeter, $\sigma_E/E = 50\%/\sqrt{E} \oplus 3\%$ for the endcap HCal, and $\sigma_E/E = 100\%/\sqrt{E} \oplus 10\%$ for the FCal [79].

3.3.3 The ATLAS Muon Spectrometer

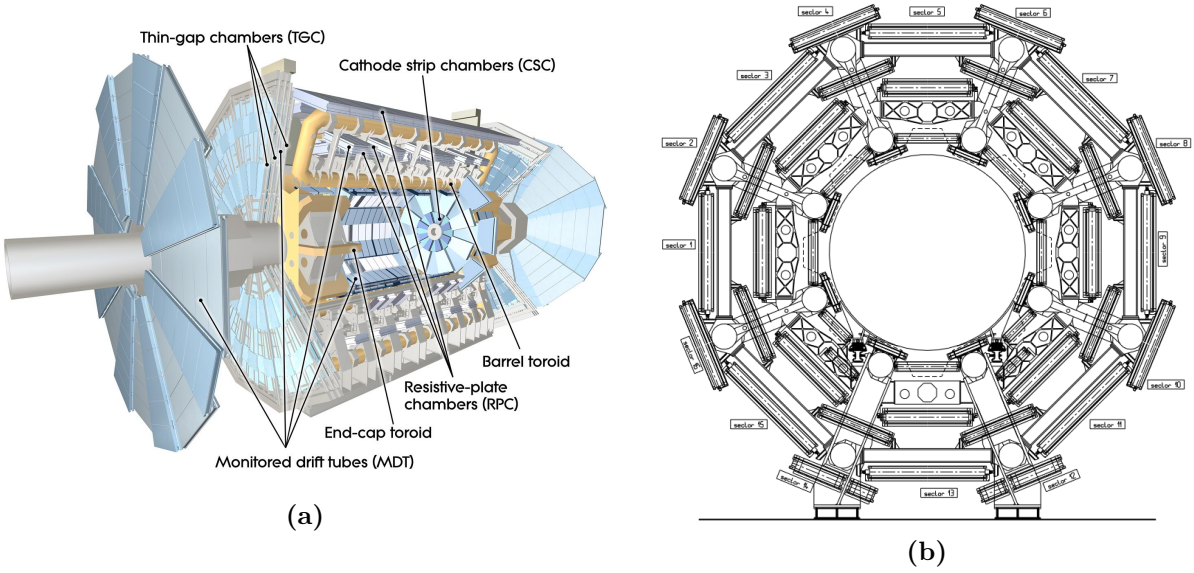

Figure 3.6: (a) Labeled diagram of ATLAS Muon Spectrometer, (b) Azimuthal cross section of the ATLAS Muon Spectrometer with sectors labeled

The Muon Spectrometer (MS) is designed to produce high-resolution measurements of muon position and momentum over a large range of transverse momenta, p_T, and a wide range of pseudorapidity, η. It contains the barrel and endcap toroidal magnets, which immerse the barrel in a peak magnetic field of 4 T and the endcap in a peak magnetic field of 2 T,

respectively [65]. These magnetic fields are mostly orthogonal to muon trajectories and provide the bending required to get high-precision p_T measurements. A labeled diagram of the MS can be seen in Figure 3.6 [80].

The MS is composed of several sub-components, separated by barrel and endcap region. Both regions feature a 16-fold segmentation along ϕ to match the 8-fold symmetry of the toroidal magnets. The segments that cover the spaces between the magnet coils are "large" segments and the segments covering the same azimuthal range as the magnet coils are called "small" segments.

The barrel region covers a pseudorapidity range of $|\eta| < 1$ and is composed of three layers (stations) located at radii of about 5, 7.5, and 10 m. Each station uses Monitored Drift Tube (MDT) chambers for precision measurement of muon tracks. The trigger function for the MS barrel is provided by Resistive Plate Chambers (RPCs) located on both sides of the middle MDT station and above or below the outer MDT station. The barrel chambers, both MDT and RPC, are rectangular with sizes between 2-10 m^2 for each individual chamber module. Special consideration is made for the MDT and RPC systems around the barrel toroid support feet, located around $\phi \approx 247.5°, 292.5°$ and $|\eta| \lesssim 1.7$ [81].

The endcap region covers a pseudorapidity range of $1.0 < |\eta| < 2.7$ and has four disks arranged at distances of 7, 10, 14, and 21-23 m from the point $z = 0$. All endcap chambers combined provide almost complete coverage of the pseudorapidity range $1.0 < |\eta| < 2.7$ [81]. All four disks feature precision MDT chambers for measurement of muon tracks, except the innermost ring of the first disk, where Cathode Strip Chambers (CSCs) are used. The trigger function is provided by Thin Gap Chambers (TGCs), which are located near the middle MDT station. The endcap chambers are trapezoidal with tapering angles of 8.5° for "small" chambers and 14° for large chambers with sizes ranging from 1-10 m^2 for individual chamber modules [81].

The MDTs have a spacial resolution of $81.7 \pm 2.2\,\mu$m radially outward from the central wire and a maximum drift time of ~ 500 ns [82]. The CSCs have a spacial resolution of $\sim 60\,\mu$m and a maximum drift time of ~ 30 ns [81]. The RPCs have a time resolution of 1 ns while the TGCs have a $> 99\%$ efficiency within a 25 ns window [81].

Chapter 4

Data and Monte Carlo Samples

This analysis utilizes data collected during Run 2 of the LHC. It also uses Monte Carlo (MC) samples to simulate collision events containing LLPs consistent with the BSM models being tested. These signal MC samples are used to develop selection criteria, systematic uncertainties, and expected yields. The primary background comes from punch-through jets (PT jets), which are jets where part of the hadronic shower escapes the calorimeter and continues into the muon spectrometer (MS) [83]. Because this background is not well modeled by MC simulation, this analysis uses a data-driven background technique described in Section 8.3.

Signal MC is used alongside blinded data samples from Run 2 to develop the selection criteria and estimate backgrounds, uncertainties, and expected yields. The data are blinded by ensuring the region expected to be rich in signal events is not analyzed immediately. Selection criteria are used to divide the data into two regions. One region contains a large fraction of possible signal events and is excluded from the analysis until after all pieces of the analysis have been developed and validated. This region is called the signal region (SR). The other region contains a smaller fraction of possible signal and is where most background events are expected to occur. This region is used to optimize the analysis by maximizing signal sensitivity and minimizing background sensitivity.

4.1 Data Samples

[1]Figure 4.1(a) was produced prior to the 2022 Run 2 luminosity recalculation and an equivalent figure has not yet been produced with updated luminosity values. The total physics-usable luminosity collected by ATLAS during Run 2 is $140.1 \pm 1.2\,\text{fb}^{-1}$ [84].

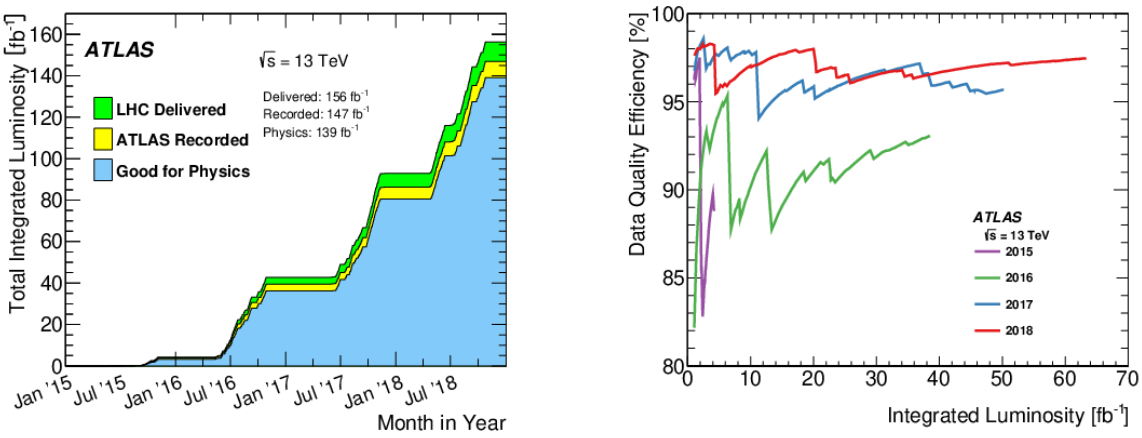

(a) **(b)**

Figure 4.1: (a) Cumulative integrated luminosity delivered to ATLAS (Green), recorded by ATLAS (Yellow), and used for physics (Blue) for all of Run 2, (b) Cumulative data quality efficiency per Run 2 data-taking years[1].

This analysis uses the full set of Run 2 data collected by ATLAS at $\sqrt{s} = 13\,\text{TeV}$ between July 2015 and October 2018 [85, 86, 87]. The peak luminosity of Run 2 began at $\mathcal{L}_{\text{peak}} = 5 \times 10^{33}\,\text{cm}^{-2}\text{s}^{-1}$ and ended at $\mathcal{L}_{\text{peak}} = 1.9 \times 10^{34}\,\text{cm}^{-2}\text{s}^{-1}$. The bunch-averaged peak number of inelastic collisions per bunch crossing, $\langle\mu\rangle$, increased from 16 in 2015 to 55 in 2018, with the luminosity-weighted mean number of collisions being 13 in 2015 and 36 in 2018 [84].

The data collected at ATLAS is synchronized with the LHC fill cycle and is organized into runs. These runs roughly correspond to one LHC fill, which lasts around 12 hours, and each is assigned a unique integer called a run number. These runs are then further subdivided into luminosity blocks, or LumiBlocks (LBs), which are periods of $\sim 60\,\text{s}$ during which the beam instantaneous luminosity and detector conditions, such as trigger configuration and data quality, are the same. Each LumiBlock also gets its own LumiBlock number.

To assure that the results can be trusted, a detailed process of data acquisition (DAQ) and data quality (DQ) assurance is performed for collecting live *pp* collision at ATLAS. The ATLAS DQ group maintains and manages the ATLAS defect database, which contains a list of all defects present in each LB [88]. If a LumiBlock passes data quality criteria and is deemed to be good for physics, then its LB number is added to a Good Run List (GRL). A GRL is compiled by querying the ATLAS defect database, and only those LBs without major defects are added to the GRL. The data used in this analysis were taken from the

GRLs listed in Table 4.1.

List of GRLs	
2015	data15_13TeV:physics_25ns_21.0.19.xml
2016	data16_13TeV:physics_25ns_21.0.19.xml
2017	data17_13TeV:physics_25ns_Triggerno17e33prim.xml
2018	data18_13TeV:physics_25ns_Triggerno17e33prim.xml

Table 4.1: List of GRLs used for this analysis, separated by year.

The luminosity at ATLAS is measured by the LUCID (LUminosity Cherenkov Integrating Detector) Cherenkov detector. LUCID was upgraded to LUCID2 prior to Run 2 to account for the increase in $\langle\mu\rangle$ that was expected to occur between the end of Run 1 and the beginning of Run 2 [89]. LUCID2 is composed of several small Cherenkov detectors positioned around the beamline, which measure the Cherenkov radiation generated by inelastic pp scattering [90, 77].

Measurements of the luminosity delivered to ATLAS were complemented by beam condition measurements from the ATLAS beam conditions monitor (BCM) diamond detectors, as well as from offline measurements of charged particle multiplicities. The amount of data collected, per data-taking year, can be seen in Figure 4.2 [88]. The amount of data is expressed in terms of integrated luminosity. The average pileup, $\langle\mu\rangle$, per data-taking year is also shown.

The total integrated luminosity delivered to ATLAS over the course of Run 2 was $140.1 \pm 1.2\,\text{fb}^{-1}$, which is an uncertainty of 0.83% [84]. Luminosity calculations involve measurements of the transverse distribution of the protons (or heavy ions) in the colliding beams. This is done in ATLAS through a van der Meer (vdM) scan, where the beams are shifted with respect to each other and the change in number of interactions is measured. The beams are displaced both vertically and horizontally. The primary contribution to the luminosity uncertainty comes from the vdM calibration [84, 90, 91].

4.1.1 Late Stream Data

In addition to the Main Stream data, which are used for the bulk of physics analyses at ATLAS, additional specialized data streams are collected. One of these specialized streams,

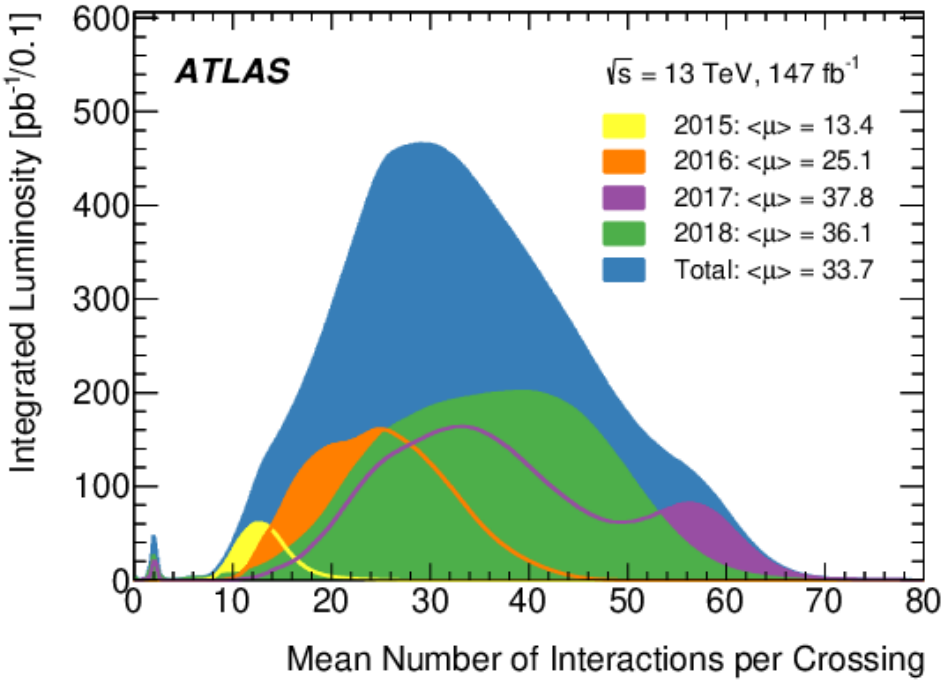

Figure 4.2: Distribution of the integrated luminosity delivered versus average number of interactions per crossing, $\langle\mu\rangle$.

called the Late Stream, collects data from ATLAS during an empty or half-filled bunch crossing. Data from this stream can be used to estimate the background contribution coming from non-collision sources, such as cavern radiation, beam halo, and cosmic ray radiation. The Late Stream data collected during Run 2 was used for this purpose in this analysis.

4.2 Monte Carlo Samples

Monte Carlo (MC) simulation is used in high energy physics to study the detector response to, and reconstruction algorithms efficiency for, specific physics processes. For particle search analyses, signal MC samples are typically produced, which simulate the data that would be produced in ATLAS if the signal process were to occur. Many analyses also employ MC samples to study physics-based background processes so better selection criteria can be developed. In this analysis, several signal MC samples were generated. These samples simulate the decay of a Higgs Boson or Higgs-like boson into a pair of scalar bosons. Each of these scalar bosons then decay to fermions which would appear in ATLAS as displaced

jets.

As described in Sections 2.2.1 and 2.2.2, two distinct benchmark models were used: a Hidden Sector model ($H \to ss$) and a Baryogenesis model ($H \to \chi\chi$). The $H \to ss$ model had some samples generated with the SM Higgs mass and some with non-SM Higgs masses. All of the baryogenesis samples were generated using a SM Higgs mass. The branching ratios used for each of the $H \to ss$ samples are described in Table 4.3. Separate MC samples were generated for each baryogenesis decay channel, so the branching ratio into a given final state was 100% for that sample. A list of the different mass parameters and lifetimes of these samples can be seen in Table 4.2.

Modeling how particles like LLPs appear in the ATLAS detector involves two steps: producing the events from pp interactions that contain LLPs, and then simulating the interactions of the produced particles with the ATLAS detector. This first step is often called event generation, and the second step is called detector simulation.

Signal LLP events were generated at leading order using the MadGraph5_aMC@NLO [92] version 2.6.2 event generator for the primary pp interaction and the resulting hard scatter. The Higgs p_{T} distribution was then reweighted to match that obtained in next-to-leading-order (NLO) Higgs samples. For the BSM process of interest, a Higgs decaying to a pair of LLPs, the model `HAHM_variableMW_v3_UFO` is used. Pythia 8 [93] is used to model the parton shower and hadronization of the resulting particles. Pythia 8 has different sets of tuned parameters, referred to as the tune, which dictate the details of how partons will hadronize and interact within the parton showers. The signal MC used in this analysis used the ATLAS A14 tune [94]. Showers coming from b- and c-hadrons can be improved by using the EvtGen package as an "afterburner", which specializes in simulating b- and c-decays. The EvtGen 1.2.0 program was used for this analysis.

In order to properly model the pp hard scatter, the probability distributions of the parton momenta must be specified. These values are determined by theory and experimental data. The collections of these probabilities are expressed as parton distribution functions (PDFs).

For this analysis, the NNPDF31LO PDF set was chosen [95, 96]. NNPDF31LO is version 3.1 of the PDF set produced by the NNPDF Collaboration evaluated at leading order (LO). The truth-level particles produced by MadGraph5 and Pythia 8 are used by Geant4,

Model	m_H [GeV]	m_s [GeV]	N events	Lifetime $c\tau$ [m]
$H \to ss$	125	5	150k	0.127
			600k	0.411
		16	500k	0.580
		35	700k	1.310
			500k	2.630
		55	1000k	1.050
			450k	5.320
	60	5	600k	0.217
		16	300k	0.0661
	200	50	200k	1.255
	400	100	200k	1.608
	600	50	300k	0.590
		150	300k	1.840
			150k	3.309
		275	1000k	4.288
	1000	50	300k	0.406
		275	300k	2.399
			150k	4.328
		475	1000k	6.039
	m_χ [GeV]	χ Decay Channel	N events	Lifetime $c\tau$ [m]
$H \to \chi\chi$	10	$\tau^+\tau^-\nu$, cbs, $b\bar{b}\nu$	400k	0.920
	55		400k	5.550
	100		400k	3.500

Table 4.2: Table of signal MC Samples used in this analysis. Columns show the sample model, Higgs/Higgs-like mass, scalar mass, number of events, and the proper decay length $c\tau$. All three baryogenesis decay channels were produced for each χ mass.

which is a toolkit for simulating the passage of particles through matter, to simulate the interactions with the ATLAS detector [97].

Pileup refers to the other pp interactions that occur within the same and neighboring bunch crossings that contribute to the underlying event. Pileup is modeled by overlaying simulated inelastic pp interactions with the hard-scatter events. These inelastic collisions are generated with Pythia 8.2 using the `NNPDF2.3NLO` PDF set and the A3 tune.

MC events that have been simulated, but have yet to have detector simulation or reconstruction algorithms run are called truth-level samples. The true positions, momenta, child particles, and decay positions are known at this level. Truth-level samples are typically useful for calibrating or analyzing reconstruction algorithms. In this analysis, truth-level signal MC is generated and used in the lifetime extrapolation procedure described in Section 8.4. Distributions of some truth-level characteristics of the LLPs are shown in Figures 4.3 and 4.4. The bimodal distribution seen in the samples with a higher LLP mass in Figure 4.3(c) comes from the generally lower boost these LLPs tend to have. Because the LLPs are back-to-back in the Higgs rest frame, the more highly boosted LLPs tend to have a larger p_{T} component making their decay locations more central in η.

The events from detector simulation are saved in the Raw Data Object (RDO) format, which is used as input in the reconstruction step [98]. Reconstruction is a software-based process run in the `Athena` framework [99], which is a collection of packages built upon the `Gaudi` framework [100], designed to analyze particle data. `Athena` Release 21 was used to reconstruct both the signal MC samples and the Run 2 data samples in this analysis. The reconstruction process saves all relevant particle data in the Analysis Object Data (xAOD) format. The xAOD format contains reconstructed physics object information and is readable by `ROOT` [101]. Different caches of Athena are used to reconstruct data from different data-taking years. The 2015 and 2016 data are reconstructed using the `AtlasOffline_21.0.20` cache, `Athena_21.0.53` is used for 2017 data, and `Athena_21.0.77` is used for 2018 data. The xAOD files can then be further processed by the Athena Derivation Framework to produce an xAOD file that contains analysis-specific objects. This is useful for analyses, as the xAOD files are quite large and often include information about objects not required for the analysis. The derived files are referred to a DAODs or derivations. The derivation definition used for this analysis was `EXOT15`. The derivation for signal MC is produced by `AthDerivation_21.2.56.0`. For data derivations, a different cache, `AthDerivation_21.2.108.0`, was used since it contained a single jet trigger necessary for the scale factor studies, described later. The DAODs were processed into `ROOT` ntuples with analysis code developed by the analysis team. The analysis procedures described in Chapter 8 were primarily applied to these ntuples.

m_s [GeV]	$s \to \tau\overline{\tau}$	$s \to c\bar{c}$	$s \to b\bar{b}$	$s \to t\bar{t}$
5	25%	75%	-	-
16	7%	13%	80%	-
35	5%	9%	86%	-
55	4%	8%	87%	-
100	4%	8%	87%	-
150	4%	8%	88%	-
275	4%	8%	88%	-
475	0%	0%	0%	100%

Table 4.3: Branching ratios for the different scalar masses, m_s, used in the signal MC samples for this analysis.

4.2.1 Background Samples

Data-driven methods of background estimation are used in this analysis. However, some QCD multi-jet MC simulations were used to give insight into this process. The QCD multi-jet samples are arranged in slices. Each slice is generated such that the leading jet p_T distribution is approximately flat. Weights are then applied to each event to match the expected leading jet p_T distribution. The calculation to get these weights is given in Eq. 4.1.

$$w = (\text{mcEventWeight}) \cdot \epsilon_{filter} \cdot \sigma \cdot \mathcal{L}/N_{evt} \tag{4.1}$$

where σ is the cross section of the given slice, mcEventWeight is the event weight applied at the event-generation level, ϵ_{filter} is the filtering efficiency which comes from filters applied after event generation, and $\mathcal{L}$ is the integrated luminosity [102, 103, 104]. The samples used for this analysis were generated by Pythia 8 using the NNPDF23LO PDF with the set of A14 tunes. The A14 tunes (ATLAS 2014 tunes) are a series of tuned event generation and showering parameters produced using Run 1 data and a collection of different parton distribution functions [105, 94]. More detailed information can be found in [94].

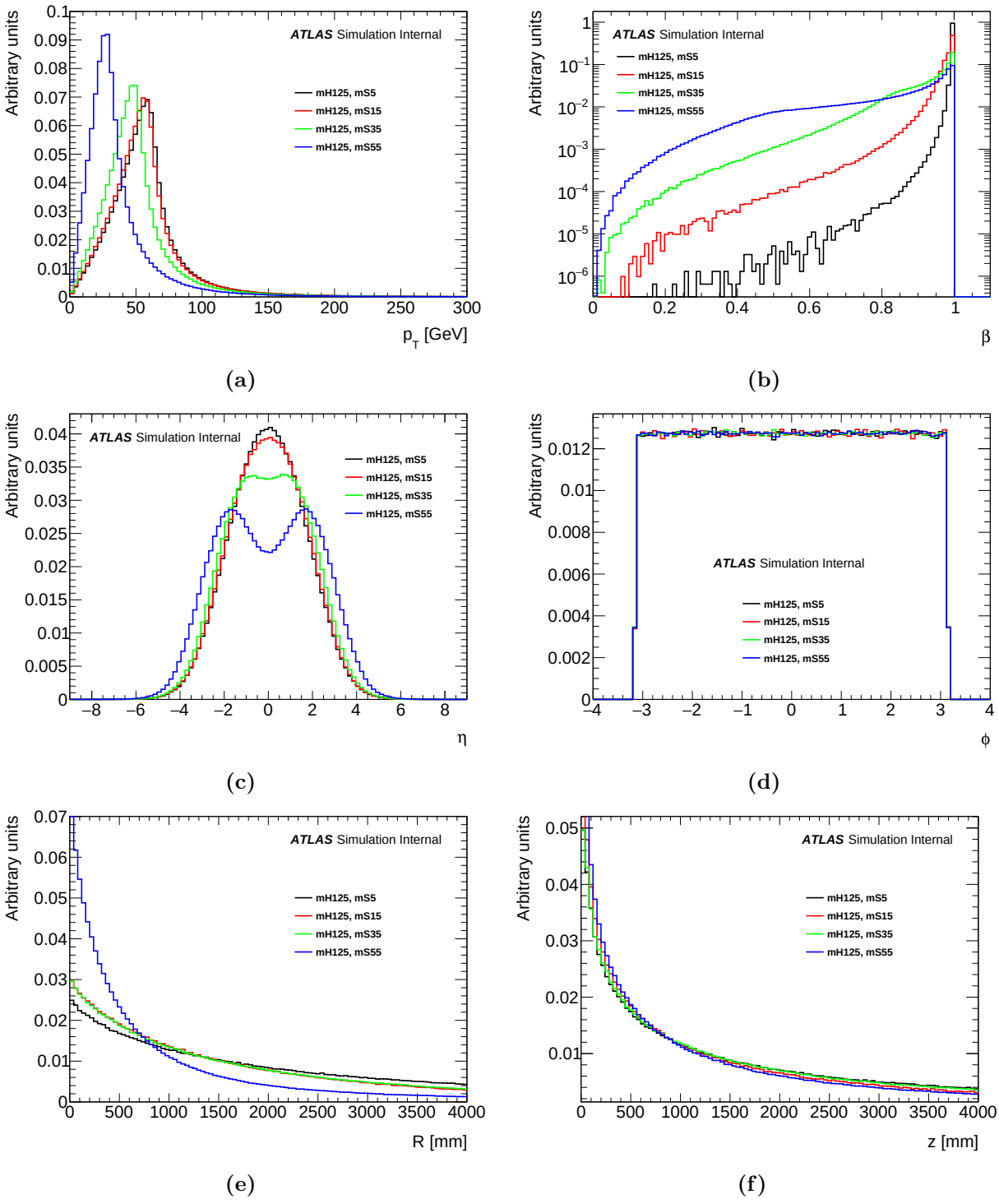

Figure 4.3: Truth-level distributions of the p_{T}, β, ϕ, R, and L_z of the LLPs from the $H \to ss$ signal MC samples with a SM Higgs mass. Each line corresponds to a different scalar mass. The distributions in each plot have the same normalization.

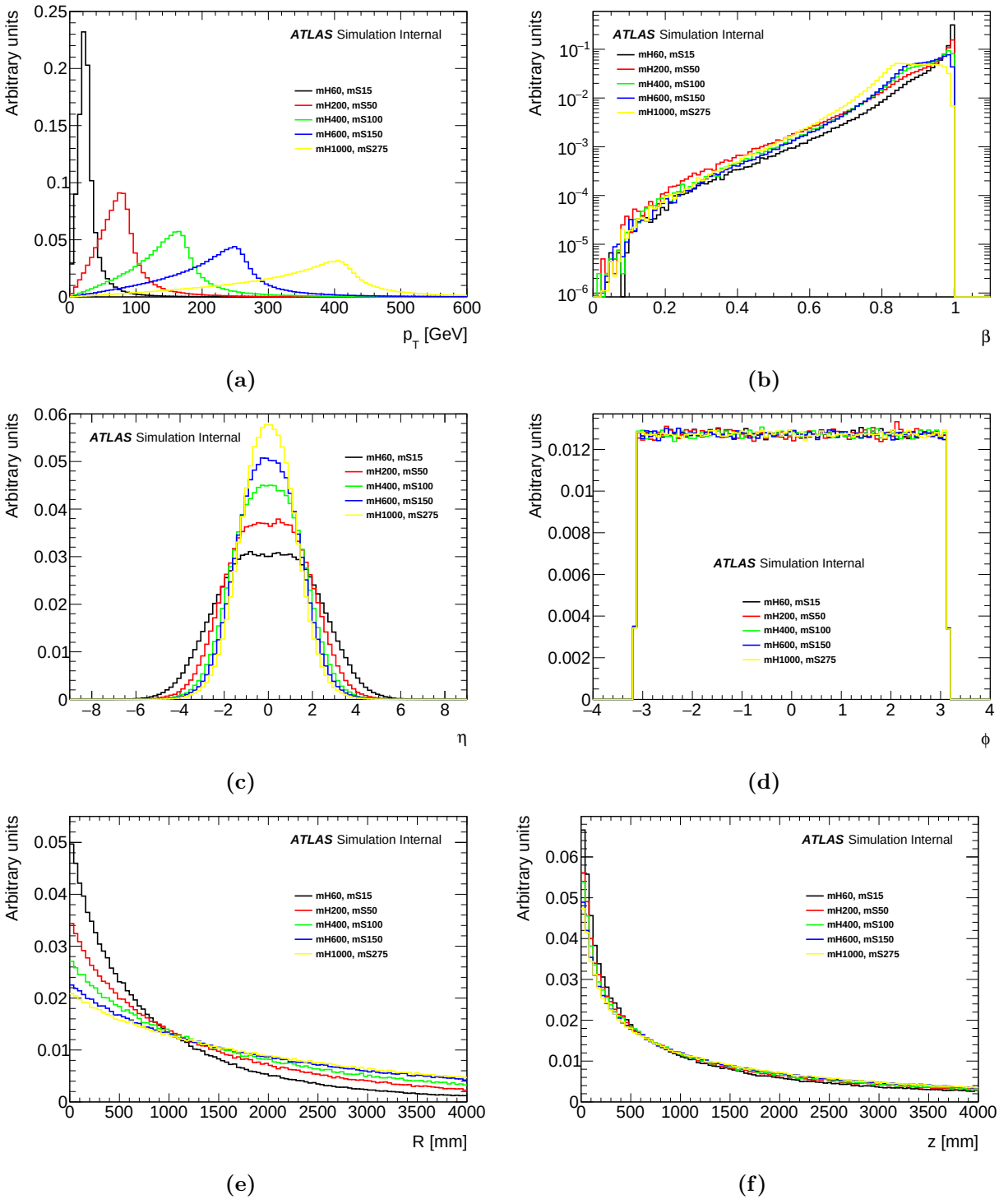

Figure 4.4: Truth-level distributions of the p_{T}, β, ϕ, R, and L_z of the LLPs from the $H \to ss$ signal MC samples with a non-SM Higgs mass. Each line corresponds to a different scalar mass. The distributions in each plot have the same normalization.

Chapter 5

The ATLAS Trigger System

The LHC delivers pp bunch-crossings every 25 ns (40 MHz) to ATLAS. Due to the amount of data the detector creates for each collision (~ 1.6 MB [106]), it's not possible to save every event. There are also many collision events that do not generate any interactions of interest and are not worth saving. The solution to both of these problems is the development of a multi-level trigger system that screens each bunch crossing for signatures of interesting interactions and only saves the collision data for those that pass this screening. This system is called the ATLAS Trigger and Data Acquisition (TDAQ) system. The ATLAS trigger system in Run 2 employs a two-level system that brings the rate of recorded collisions down to an average of ~ 1 kHz. A diagram of the Run 2 TDAQ system is shown in Figure 5.1.

The Level 1 (L1) trigger, is a hardware-based system that uses custom electronics to evaluate the event features based on lower-granularity information coming from the calorimeter and muon detectors. The L1 trigger can accept events at a rate up to the ATLAS readout maximum rate of 100 kHz, with a trigger latency after collision of 2.5 μs. The L1 trigger digitizes the analog signals and uses them to identify electron, photon, muon, τ-lepton, and jet candidates along with estimates of the total- (E_{T}) and missing- ($E_{\mathrm{T}}^{\mathrm{miss}}$) transverse energy [108].

The high-level trigger (HLT) is a software-based trigger that runs on a dedicated computing farm. Approximately 40,000 selection applications, called Processing Units (PUs), run the online HLT triggers, which apply slower, more precise reconstruction algorithms and make trigger decisions based on these more robust physics objects. The HLT further reduces the L1 trigger rate of 100 kHz down to around 1 kHz [108].

Each of the L1 and high level triggers can be combined into a chain of algorithms that

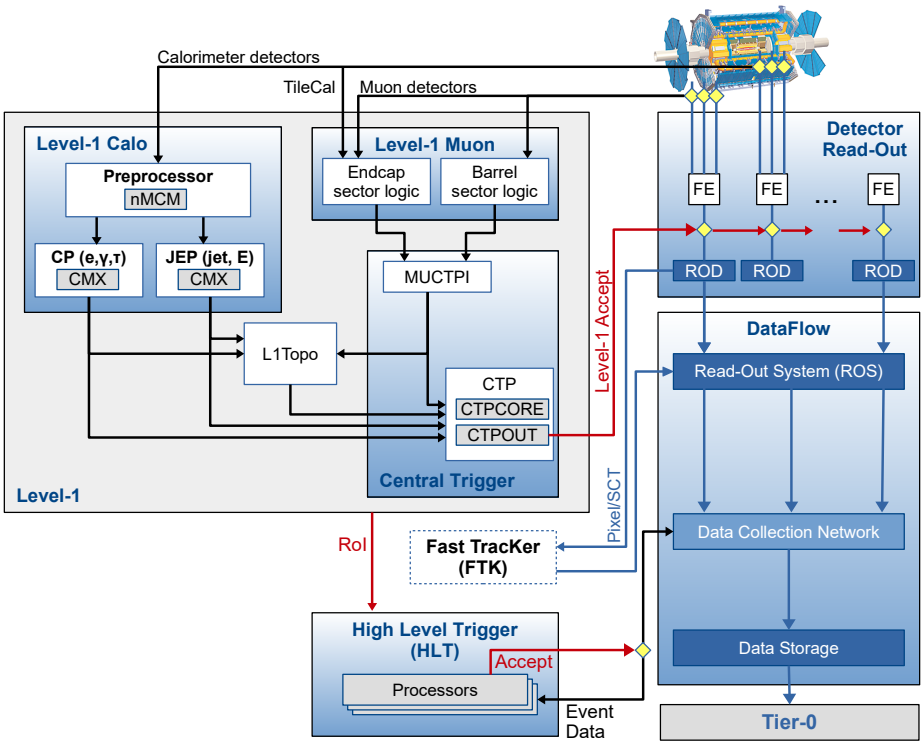

Figure 5.1: Run 2 diagram of the ATLAS Trigger and Data Acquisition (TDAQ) system [107].

will run together called a *trigger chain*. The collection of all such trigger chains, along with a "prescale" factor that can be set to reduce the rate at which the chain fires, are referred to as the *trigger menu*. Analyses typically begin by identifying the appropriate trigger chains that would meet the needs of their signal signature from the trigger menu. Alternatively, as is the case for this analysis, a signature-specific trigger chain is developed [109, 110].

5.1 The Level-1 Trigger

The L1 trigger is composed of three main trigger subsystems: the L1 calorimeter (L1Calo) trigger, the L1 muon system (L1Muon) trigger, and a topological trigger (L1Topo). These trigger subsystems are responsible for deciding whether an "L1 Accept" signal is sent to the detector readout system to buffer the event data and pass it to the HLT trigger. The L1 trigger system also converts the analog detector signals into digital signals. The L1Calo information is calibrated in a preprocessor before being sent to the Cluster Processor (CP) and Jet/Energy-sum Processor (JEP). All L1 decisions are handled by the Central Trigger

Processor (CTP) after receiving information from the trigger subsystems [108].

The L1Calo trigger is responsible for several hardware-implemented trigger algorithms such as the electron/photon and tau/hadron trigger algorithms. These algorithms, which are specifically handled by the CP, accept inputs from a set of ~ 7200 trigger towers. These towers, shown in Figure 5.2(a), mostly have a granularity of 0.1×0.1 in $\Delta\eta \times \Delta\phi$, though some towers in the endcaps are larger, and cover the region $|\eta| < 2.5$. These sets of algorithms produce E_{T} sums for EM and hadronic showers, define 2×2 tower cluster Regions of Interest (RoIs), and produce isolation measurements [111].

The main jet trigger, handled by the JEP, uses "jet elements". Jet elements are formed by first summing over each 2×2 trigger tower cluster, then summing in depth over both the EM and hadronic calorimeters. The trigger towers, shown in Figure 5.2(b), have a granularity of 0.2×0.2 in $\Delta\eta \times \Delta\phi$. The jet elements, therefore, cover a region of 0.4×0.4 in $\Delta\eta \times \Delta\phi$. These jet elements are created in the region $|\eta| < 3.2$. Algorithms use jet elements to provide E_{T} estimates and RoI clusters for jet objects [111]. The L1Calo trigger system additionally manages a forward calorimeter (FCAL) trigger, also handled by the JEP, which covers the η range $|\eta| < 4.9$ for jet and calorimeter energy triggers. The L1Calo trigger's JEP system also estimates the total E_{T} and $E_{\mathrm{T}}^{\mathrm{miss}}$ for the entire event [111].

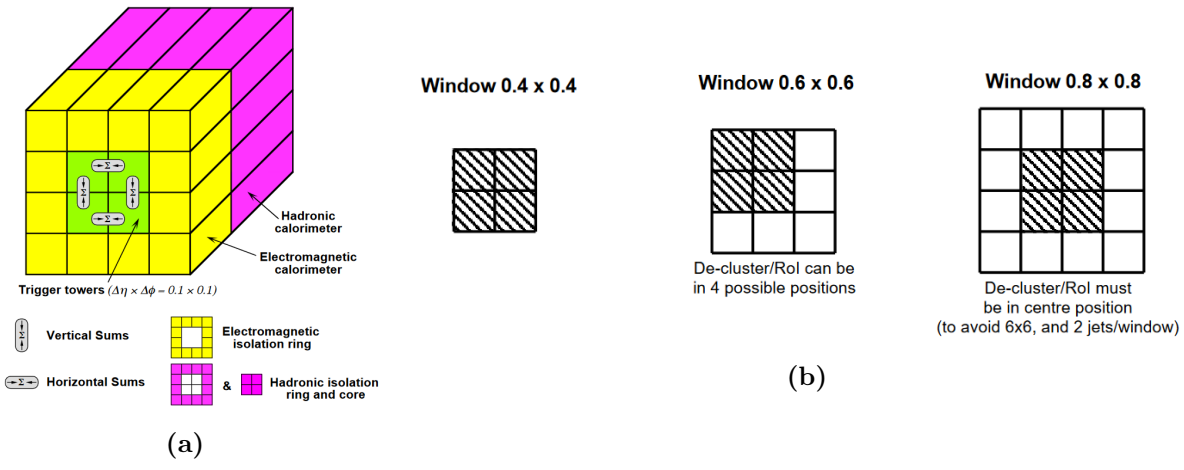

Figure 5.2: (a) Diagram of an L1Calo trigger tower, separated into EM (yellow) and hadronic (magenta) sections. (b) Diagram of jet windows used in the L1Calo jet triggers.

The L1Muon trigger uses RPC and TGC hits in the barrel and endcap regions, respectively, for its trigger logic. The main algorithm of the L1Muon trigger uses the amount of deviation

in the hit pattern between what is measured and what is expected from a muon with infinite momentum in order to estimate the muon p_{T}. This p_{T} is used to determine which of six p_{T} thresholds are exceeded. These thresholds then determine which L1 accept is fired in a given event. There are three high-p_{T} thresholds and three low-p_{T} thresholds. Only the high-p_{T} thresholds are used for single-muon triggers, whereas the low-p_{T} thresholds are used for multi-object triggers, including multi-muon triggers. The p_{T} thresholds are reflected in the L1 trigger names, which all have the form "`L1_MU20`", where the number following the "`MU`" is the threshold p_{T} in GeV. The L1Muon trigger used for this analysis is called `L1_2MU10`, which requires events to contain at least two muons with $p_{\mathrm{T}} > 10\,\mathrm{GeV}$. For each muon that passes an L1 threshold, the location of the region surrounding the associated hit pattern is also marked as a Region of Interest (RoI) in the MS. These muon RoIs are then tagged based on which thresholds they passed, along with other information such as their p_{T} estimate. The muon RoIs are sent to the CTP for the L1 accept decision and can be forwarded to HLT triggers for further consideration [112].

The L1Muon RoIs are typically 0.1×0.1 in $\Delta\eta \times \Delta\phi$ in the RPCs and 0.3×0.3 in the TGCs and have geometric coverage over $\approx 80\%$ of the barrel and $\approx 99\%$ of the endcaps [112]. Due to low-p_{T} muons originating from beam halo protons interactions with the endcap toroid magnets and beam shielding, additional background mitigation techniques had to be applied in the endcaps ($1.05 < |\eta| < 2.4$) for Run 2 in order to reduce the L1 trigger rate and preserve low trigger prescales. In Run 2, an additional coincidence between the TGC Forward/Endcap Inner chambers and the middle layer of TGC chambers (the Big Wheel) was required.

The L1Topo trigger was commissioned in 2016 to reduce background trigger rates and improve trigger efficiency for select triggers by combining information from both the L1Calo and L1Muon trigger systems [112]. The L1Topo trigger can employ up to 128 topological trigger algorithms that can make kinematic selections (invariant mass, transverse mass, event H_{T}, etc.) and angular selections ($\Delta\eta$, $\Delta\phi$, ΔR, energy within a cone, etc.) using any of the trigger objects from both the L1Calo and L1Muon triggers [113]. Being able to use all of these objects together lends a substantial improvement in background rejection compared to the Run 1 L1 trigger system. This improvement compensates for expected higher trigger

thresholds coming from an increased instantaneous luminosity between Run 1 and Run 2. The L1Topo trigger also allows for a more diverse set of L1 triggers, such as those relying on lower p_{T} objects. It also allows for L1 trigger that would require combined calorimeter and muon system information or would look for more exotic signatures triggering on objects from other bunch crossings such as some long-lived particle signatures [113].

After an Accept has been sent, all Front-End (FE) detector electronics data are read out. This process begins with the ReadOut Drivers (RODs), which perform the initial processing and formatting, before the information is sent to the ReadOut System (ROS) to buffer the data. The ROS data is then sent to the HLT if the HLT requests it [108].

5.2 The High Level Trigger

The HLT is a software-based trigger system integrated with the `Athena` [114, 99] framework, which, itself, is based on `Gaudi` [100], a framework developed for data processing in HEP experiments. HLT algorithms typically employ fast trigger algorithms for early rejection, followed by more precise but CPU-intensive reconstruction algorithms similar to those used in offline reconstruction. Which reconstruction steps are executed and in what order they are executed is defined for each HLT algorithm by a trigger sequence in the trigger chain. Each step in a trigger sequence typically executes one (or more) feature-extraction algorithm(s), which request event-data fragments from within an RoI provided by the L1 trigger, and ends with a hypothesis algorithm that uses these extracted features to decide whether the specific trigger conditions for that step are satisfied. It is also possible for trigger algorithms to request information from the entire detector. This can be done for algorithms that reconstruct more complicated physics objects or calculate global properties of the event, such as the total transverse momentum, E_{T}, and missing transverse momentum, $E_{\mathrm{T}}^{\mathrm{miss}}$ [108].

The HLT output rate during an average ATLAS data-taking run in Run 2 is $\sim 1.2\,\mathrm{kHz}$, which translates to a physics throughput rate of approximately $1.2\,\mathrm{GB/s}$ into permanent storage. Once the HLT accepts an event, the Sub-Farm Output (SFO) system exports the data to a Tier-0 Facility and saves the data to permanent storage [108].

5.3 The Muon RoI Cluster Trigger

The primary trigger used in this analysis (`HLT_j30_muvtx_noiso`) is a signature-driven trigger designed to efficiently identify highly displaced hadronic jets present in the muon spectrometer. This trigger is based on a Run 1 trigger with some criteria changed for Run 2 [115]. This HLT algorithm is seeded by events passing the `L1_2MU10` level-1 trigger. The `2MU10` threshold requires that an event contains at least two muons with a p_{T} greater than 10 GeV. This L1 trigger seed was chosen since it requires two muons and is the lowest p_{T} di-muon L1 trigger with no prescale, meaning all L1-accepted events are recorded [116]. This HLT algorithm is composed of two trigger chain steps: a `j30` step and a `muvtx` step. The `j30` step is a standard ATLAS jet threshold that requires the presence of at least one jet with an E_{T} greater than 30 GeV. The inclusion of the `j30` step sufficiently reduces the HLT trigger rate such that no prescale factor is required. The `muvtx` step is the signature-driven trigger step that looks for evidence of displaced LLP decays and will be described in more detail below. The last portion of the trigger name, `noiso`, does not correspond to a trigger algorithm, but is included to indicate that the isolation criteria originally present in the Run 1 trigger has been removed. A second, supplemental trigger without the `noiso` indicator was also active during Run 2 and did have isolation criteria included, but was not used for this analysis.

The HLT trigger is designed to select events with jet-like objects present in the MS. It is most efficient for LLP decays that occur between the outer edge of the hadronic calorimeter and the MS middle MDT station. Since the L1Muon trigger creates RoIs around charged tracks in the MS, the `msvtx` portion of the trigger looks for tightly grouped clusters of muon RoIs. These muon RoI clusters would be centered around the LLP line-of-flight.

5.3.1 Muon RoI Clustering

The `muvtx` trigger step is the portion of the algorithm that looks at clusters of muon RoIs in the MS. As mentioned above, the L1Muon constructs RoIs that are approximately 0.1×0.1 in $\Delta\eta \times \Delta\phi$ in the RPCs and 0.3×0.3 in the TGCs. In the event of an L1 accept, the collection of all RoIs are passed to the HLT algorithm. The `muvtx` algorithm begins by

treating each muon RoI as a cluster seed. For each seed, the distance with all other muon RoIs is checked. If any other clusters are within a ΔR cone of 0.4, then that RoI is added to the seed cluster and the position of the cluster is updated to be the average position of the RoIs. This process is repeated, per cluster seed, until no new RoIs are added to the cluster.

If any of the final muon RoI clusters are in the barrel and contain at least three (3) muon RoIs or are in the endcap and contain at least four (4) RoIs, the event passes the `muvtx` trigger step criteria and is accepted by the corresponding hypothesis (hypo) algorithm. If there are multiple clusters, the one with the highest number of RoIs is considered the triggering cluster and its location and number of associated RoIs are saved along with the trigger decision. It is also possible that none of the muon RoI seeds have sufficient neighboring muon RoIs in order to produce a passing cluster. If this occurs, the event does not pass the trigger.

The L1 muon RoIs are formed based on hit pattern deviations from a muon track with infinite momentum. This means the RoI does not include any directional information. For this reason, any muon RoIs created by the L1 trigger are assumed to point back toward the IP. The muon RoIs created during a signal-like event are created from hits originating in a displaced hadronic shower. This would generate many hits within a small region of the MS making it more likely for some combination of these hits to resemble a single muon originating from the IP, even though it had been generated by multiple particles. Thus, for signal-like events, it's not possible to assume that individual muon RoIs correspond to individual particles. For this reason, thresholds for the number of RoIs needed in a cluster to accept the event were based on those used for the Run 1 trigger [115].

5.3.2 Muon RoI Cluster Trigger RoI Mismodeling

To estimate possible mismodeling of trigger RoIs in the signal MC samples, a study was conducted to compare the probability of producing RoIs in both data and MC for the same process. The only SM process that can reliably generate signal-like signatures in the MS is high-p_{T} jets that punch-through the calorimeter and continue to shower in the MS. In both data and MC, a jet is considered to be a punch-through jet if it produces at least 50 muon segments within a cone of $\Delta R = 0.4$ centered on the jet axis. This threshold was selected because 50 muon segments was the average number of segments found within a $\Delta R = 0.4$

cone, centered on the LLP line-of-flight, for an LLP that produced a vertex. The details of the vertex reconstruction are further explained in Section 6.6.2.

The comparison between data and MC is expressed as a scale factor, re-scaling the MC RoI-production efficiency to match the efficiency found in data. All events were required to pass the `HLT_j400` and `HLT_j420` triggers as well as pass a set of minimal di-jet selection criteria given in Table 5.1.

The punch-through jet had to have a $p_{\mathrm{T}} > 30\,\mathrm{GeV}$, a log-ratio of $\log_{10}(E_{\mathrm{Had}}/E_{\mathrm{EM}}) < 0.5$, and a jet-vertex tagger (JVT) score of JVT > 0.59 if the punch-through jet had a $p_{\mathrm{T}} < 60\,\mathrm{GeV}$. The *log-ratio* is the log-base-10 of the ratio of jet energy deposited in the HCal divided by the energy deposited in the ECal. The minimum p_{T} threshold assures we select jets with sufficient energy to punch through the calorimeters and leave some activity in the MS. The JVT selection is a standard selection used to remove pileup jets.

Punch-Through Jet Selection Criteria	
Baseline Selection	Passes `HLT_j400` and `HLT_j420` triggers Minimum Associated Muon Segments, $N_{\mathrm{MSeg}} \geq 50$
Punch-Through Jet Quality Criteria	$p_{\mathrm{T}} > 30\,\mathrm{GeV}$ $\log_{10}(E_{\mathrm{Had}}/E_{\mathrm{EM}}) < 0.5$ JVT Score > 0.59 if $p_{\mathrm{T}} < 60\,\mathrm{GeV}$

Table 5.1: "Good" punch-through jet selection criteria used in data-MC comparison of L1Muon RoI production for signal-like signatures in the MS.

Both the leading and sub-leading jets, in terms of jet p_{T}, are considered as potential punch-through (PT) jets. If either jet passes the selection for a "good" PT jet, it is added to the sample of jets with MS activity. The normalized number of PT jets is then compared between di-jet MC and data in bins of number of muon RoIs, which can be seen in Figure 5.3. The trigger scale factor is taken as the ratio of the integrals of the number of jets across all bins above the trigger selection multiplicity (i.e. ≥ 3 RoIs for barrel clusters and ≥ 4 RoIs for endcap clusters) for data and di-jet MC. This trigger scale factor reflects how many RoI clusters are generated in PT jets from data compared to di-jet MC.

The trigger mismodeling scale factors are 1.24 ± 0.01 in the barrel region and 1.20 ± 0.01 in the endcap regions. The difference between the rates in the barrel and endcap regions

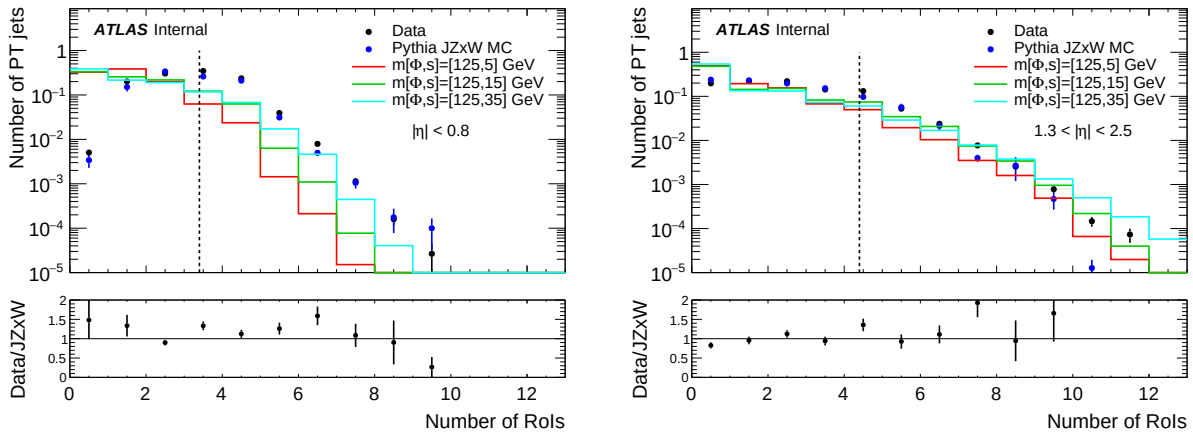

(a) **(b)**

Figure 5.3: Distributions of the number of L1 muon RoIs within a $\Delta R = 0.4$ cone for punch-through jets in the (a) barrel and (b) endcap. The data are shown as black dots while the di-jet MC simulation is shown in blue. Several benchmark SM $H \to ss$ signal MC samples are also shown. The vertical lines show the value of the N_{RoI} cut applied on muon RoI clusters at the trigger level.

is expected due to the different trigger technologies employed in each region (RPCs in the barrel and TGCs in the endcap). Both scale factors are above one, indicting that the data contained more muon RoIs than di-jet MC. Applying the scale factor as weights could risk over-counting the number of signal events in data. To keep the analysis conservative, it was decided to use the scale factors as an additive systematic uncertainty of $\pm 24\%$ in the barrel and $\pm 20\%$ in the endcap. These systematic uncertainties are applied on the trigger efficiency during the lifetime extrapolation procedure, which is discussed further in Section 8.4.

5.3.3 Muon RoI Trigger Efficiencies

The trigger efficiencies are calculated for signal MC samples and are defined as the fraction of truth LLP decays that successfully leave a muon RoI cluster that results in firing the trigger. A triggering cluster must be within a $\Delta R = 0.4$ cone of a truth LLP to be considered as originating from the LLP. The position of the muon RoI cluster is taken to be the average of the positions of all RoIs in the cluster. To assure the scale factors are applicable to events produced in the barrel region and endcap regions used in the analysis, the fiducial regions used in this analysis are enforced. This means that only truth LLPs that decay within the regions summarized in Table 5.2 are considered when calculating the trigger scale factors. In

Table 5.2, the values L_{xy} and L_z represent radial and longitudinal distances, from the origin in the ATLAS coordinate system, respectively.

Detector Region	Fiducial Volume Definition
MS barrel	$3\,\text{m} < L_{xy} < 8\,\text{m}$, $\lvert\eta\rvert < 0.7$
MS endcaps	$L_{xy} < 10\,\text{m}$, $5\,\text{m} < \lvert L_z\rvert < 15\,\text{m}$, $1.3 < \lvert\eta\rvert < 2.5$

Table 5.2: Fiducial volume definition for the MS barrel and endcap regions.

The truth-based Muon RoI Cluster trigger efficiencies for both the SM and non-SM $H \to ss$ samples are shown in Figure 5.4 for LLPs produced in the barrel and endcap regions. The trigger efficiencies are highly dependent on the kinematics and the corresponding effects can be seen by comparing the different LLP mass points. The dependence on detector geometry can also be seen, as several detector component boundaries are indicated with dashed lines in the plots.

The barrel trigger efficiency is high when the LLP decay is close to the end of the hadronic calorimeter ($\sim 4\,\text{m}$) and drops considerably beyond the RPC middle station. This is due to the charged portions of the hadronic showers that the LLPs produce not being sufficiently spatially separated by the time they reach the RPC middle stations, resulting in a higher hit concentration and correspondingly lower number of muon RoIs. This same effect can also be seen in the endcap region for some signal MC samples.

The trigger efficiency distributions for the baryogenesis signal samples are shown in Figure 5.5. The trigger efficiencies with respect to the truth LLP p_{T} for the $H \to ss$ samples can be seen in Figure 5.6.

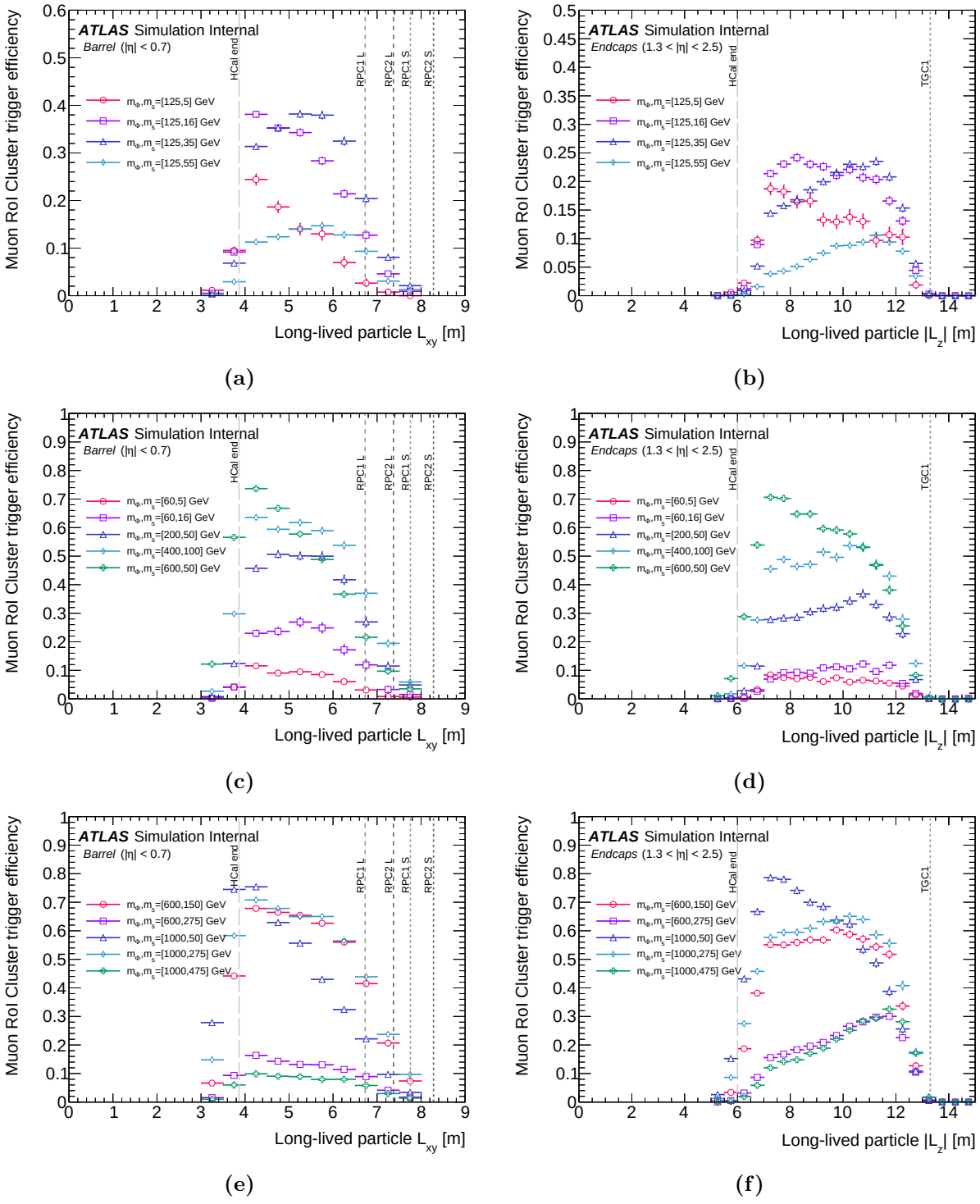

Figure 5.4: Truth-based Muon RoI Cluster trigger efficiencies as functions of LLP decay position for (a-b) SM-like Higgs benchmark samples and (c-f) non-SM Higgs HSS benchmark samples. Figures on the left correspond to barrel LLPs and those on the right correspond to the endcap LLPs. Efficiencies are calculated using only events where a single LLP decays in the MS. This was done to prevent contamination from events where the second LLP may have caused the trigger acceptance.

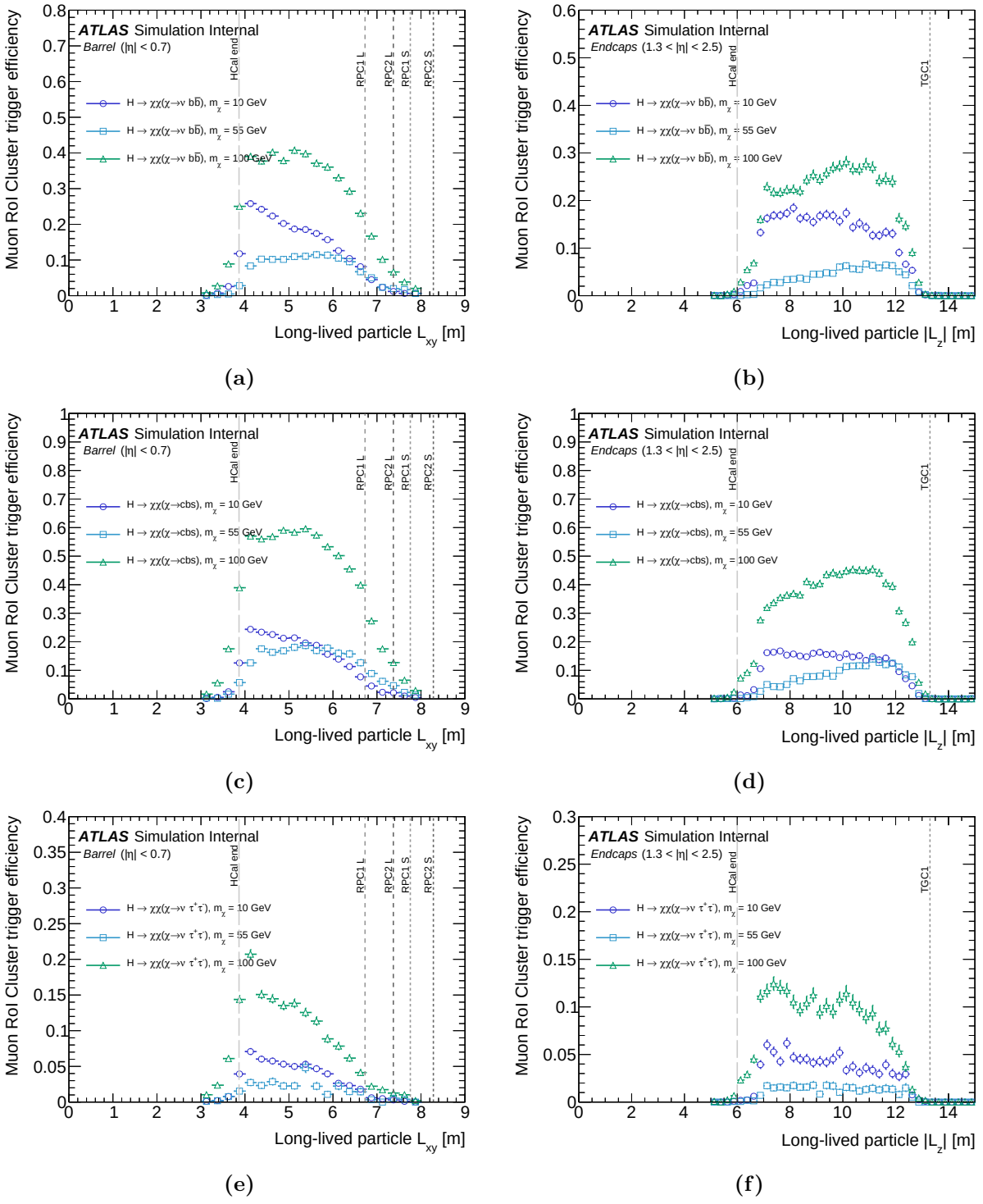

Figure 5.5: Truth-based Muon RoI Cluster trigger efficiencies as functions of LLP decay position for (a-b) $bb\nu$ benchmark samples, (c-d) cbs benchmark samples, and (e-f) $\tau\tau\nu$ baryogenesis benchmark samples. Figures on the left correspond to barrel LLPs and those on the right correspond to the endcap LLPs. Efficiencies are calculated using only events where a single LLP decays in the MS. This was done to prevent contamination from events where the second LLP may have caused the trigger acceptance.

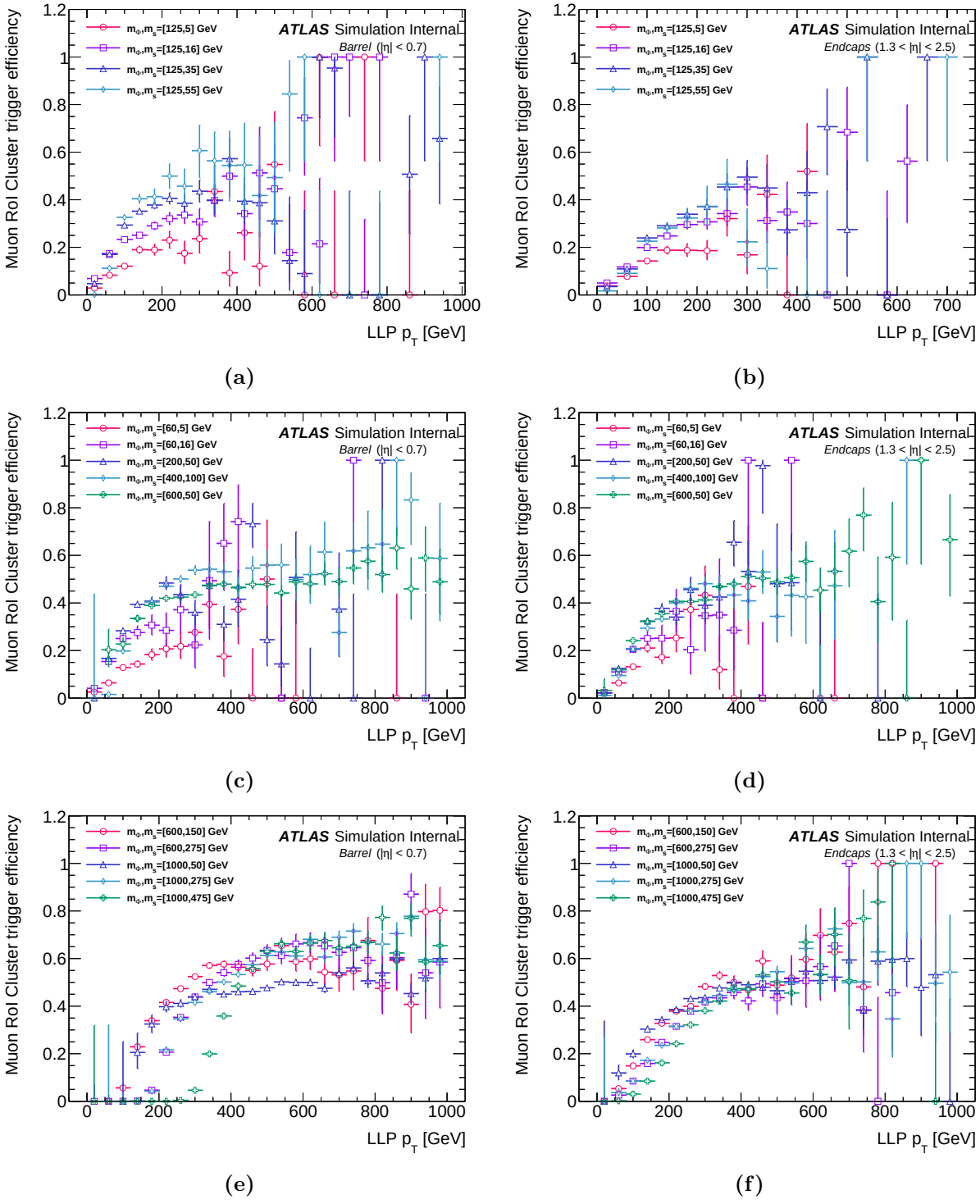

Figure 5.6: Truth-based Muon RoI Cluster trigger efficiencies as functions of LLP p_{T} for (a-b) SM-like Higgs benchmark samples and (c-f) non-SM Higgs $H \to ss$ benchmark samples. Figures on the left correspond to barrel LLPs and those on the right correspond to the endcap LLPs. Efficiencies are calculated using only events where a single LLP decays in the MS. This was done to prevent contamination from events where the second LLP may have caused the trigger acceptance.

Chapter 6

Event Reconstruction

During a pp collision, the ATLAS detector collects information about the energy and location of collision products inside the detector subsystems, often as changes in some voltage with respect to time. This information is digitized, collected, and associated with other digitized detector data in order to identify each underlying particle. This process is called "event reconstruction", as it takes the data from each ATLAS subsystem and attempts to reconstruct the particle decays, trajectories, energies, etc. that created the data. For this analysis, in addition to reconstructing the standard objects, like particle tracks in the ID and MS and calorimeter jets, a decay location for the LLP, a "displaced MS vertex" (MSVtx) is also constructed. This chapter discusses the process used to reconstruct the standard ATLAS physics objects as well as the MS vertices used in this analysis. All events are reconstructed offline using `Athena`[1] release 21.0 for the reconstruction of both data and signal MC samples.

6.1 ID Track and Vertex Reconstruction

Track reconstruction in the inner detector utilizes clusters of hits in the pixel detector and SCT, as well as the drift circles from the TRT. An example of these hits in the ID systems can be seen in Figure 6.1 [117, 118]. The clustering of pixel and SCT hits is done by first employing a connected component analysis to find groups of neighboring pixels. Next, a set of neural networks (NNs) is used to separate large clusters that may correspond to two separate, but spatially close, particles [119]. These clusters are then converted to space-points, which are 3D points with uncertainties along each direction. These space-points are

[1]Subversions of Athena vary between data years and signal MC. For specific versions, see Section 4.2

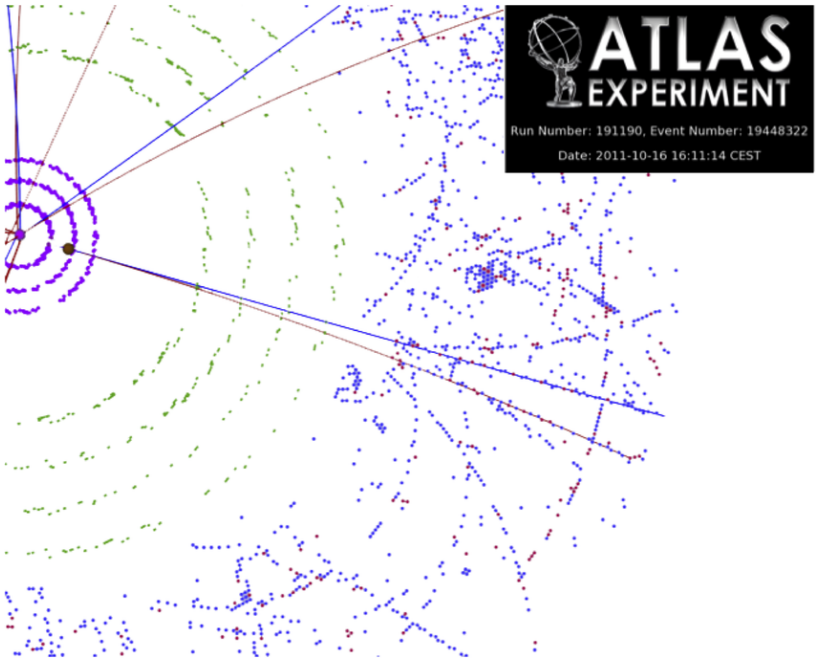

Figure 6.1: An event display showing a close-up view perpendicular to the beam direction with a subset of the total number of hits. Pixel detector hits are shown in magenta, SCT space points are shown in green, and TRT hits above the tracking threshold of 300 eV are in blue while the TRT hits above the transition radiation threshold of 6 keV are in red.

created from single pixel clusters, or *pairs* of SCT clusters occurring on opposite sides of a single sensor module. Pairs of SCT clusters must be used to reconstruct a space-point since a single SCT cluster has poor spacial resolution along its length [120].

Tracks are then reconstructed in a sequence called "inside-out" track finding, which begins from combinatorial groupings of nearby space-points between the pixel layers and the inner SCT layer [119, 120]. These combinatorial groupings are called *track seeds* if they contain three space-points. The initial track seeds can have a fourth space-point added as a *confirmation* space point. This is only done in the case that the new space-point would have produced a track seed with similar curvature if it was used in place of one of the other space-points. This additional space-point is used to help select tracks when overlapped tracks are removed.

The track seeds are then extended toward the outer SCT layers and inner pixel layers, if possible, in "search roads", which reduces the track combinatorics by only considering space-points in the direction of the track seed. The seeds are then extended into tracks through a combinatorial Kalman filter. A Kalman filter is a filtering technique that treats the track

as a state vector of track parameters, such as the track p_{T}. A Kalman filter is the optimal recursive estimator of this track state vector. It aims to optimize the estimates of the track state vector while also smoothing the track, with each additional space-point added [121].

The Kalman filter is fast but not precise, and so does not eliminate duplicate tracks, fake tracks produced by combinatorics, or tracks that share multiple space-points. Fake tracks and duplicate tracks can be removed by applying selections based on the number of associated clusters, the number of shared clusters, and the number of holes per track. A hole is defined as a region where the track crosses a silicon sensor without generating an associated cluster.

A dedicated ambiguity solver is used to help eliminate fake and duplicate tracks by assigning scores to the remaining tracks. If a track is unique and has a good fit across the associated space-points, it will receive a higher score. If a track shares multiple space-points with another track, has a poor fit, or has holes, it will receive a lower score and has a higher chance to be rejected. The remaining selected tracks are then extended into the TRT to associate the drift-circle information within the search road in the direction of the track. Once the track has TRT information, a global fit using all of the pixel and SCT space-points and TRT drift circles is done and these final fits are used to extract the track properties [122].

There is an additional, complementary process of track-finding called "back-tracking" or "outside-in" track-finding, in which a similar process is employed, but the trigger seeds are generated from the TRT drift circles. Only drift circles that remain unassociated with a track after the inside-out tracking has been completed are used in outside-in track finding. This track-finding strategy focuses on finding secondary tracks or tracks associated with decays of long-lived particles [122].

The ID tracks can be used to find the primary vertex, as well as secondary vertices, with a dedicated vertex-finder algorithm. The tracks must have the following properties to be used in the reconstruction of the primary vertex [123]:

- $p_{\mathrm{T}} > 400\,\mathrm{MeV}$
- $|\eta| < 2.5$

- Number of silicon (Pixel or SCT) hits $\geq \begin{cases} 9 & |\eta| \leq 1.65 \\ 11 & |\eta| > 1.65 \end{cases}$
- Insertable B-Layer (IBL) + B-Layer hits ≥ 1
- Maximum of 1 shared module (1 shared pixel hit or 2 shared SCT hits)
- Pixel holes $= 0$
- SCT holes ≤ 1

The primary vertex is determined using a series of steps [124]:

1. The primary vertex is seeded by the beam spot in the transverse plane, where the x- and y-coordinates are taken to be the center of the location of the beam spot in the transverse plane. To find the z-coordinate of the primary vertex, the point of closest approach to the reconstructed center of the beam spot is found for all ID tracks. From this set of points, the mode of all of their z-coordinates is taken to be the z-coordinate of the primary vertex seed. This is done using an iterative algorithm for calculating the mode called the Half-Sample Mode algorithm [125].

2. Once the seed location is determined, an iterative procedure begins to find the actual position of the primary vertex. This algorithm is formulated as an iterative, re-weighted Kalman filter with a simulated annealing process to avoid local minima [126]. This algorithm performs an iterative χ^2 minimization where each track is assigned a weight based on how compatible the track is with the vertex position during that iteration. The vertex position is then recalculated using the track weights and the process repeats. The weights are calculated via the following equation:

$$\omega\left(\hat{\chi}^2\right) = \frac{1}{1 + \exp\left(\frac{\hat{\chi}^2 - \chi^2_{\text{cutoff}}}{2T}\right)} \tag{6.1}$$

Here, $\omega\left(\hat{\chi}^2\right)$ is the track weight, which is a function of $\hat{\chi}^2$. $\hat{\chi}^2$ is the three-dimensional χ^2 value between the last estimated vertex position and the point of closest approach for the track. The χ^2 fitting procedure using these weights to find the primary vertex

location is described in further detail in [126]. The constant χ^2_{cutoff} defines the χ^2 threshold where the weight of the track will be 0.5. For Run 2 vertex-finding, this value was set to nine, which corresponds to three standard deviations. The temperature, T, is a parameter of the fit that controls the smoothness of the fitting function. For very low values of T, the weight, $\omega\left(\hat{\chi}^2\right)$, approaches a step function, and for very high T the weight approaches 0.5 and loses its dependence on $\hat{\chi}^2$. The temperature parameter is decreased from a large initial value down to $T = 1$ over the course of the iterations. The rate at which T decreases is controlled by a predefined sequence of steps. Throughout the fitting process, no tracks are dropped.

3. After the last iteration is complete and the final location of the primary vertex is found, the weights are calculated a final time. This final vertex location is a primary vertex candidate. Any track that has a $\hat{\chi}^2$ incompatibility with the final primary vertex location of more than seven standard deviations, 7σ, is removed from the vertex candidate and returned to the pool of unused tracks. This loose requirement on the minimum $\hat{\chi}^2$ for a candidate track is intended to reduce the number of single pp collisions that get reconstructed as two distinct primary vertices, while maintaining a high reconstruction efficiency.

4. After the vertex candidate is created and all unused tracks are returned to the track pool, steps 1-3 are repeated to calculate additional vertex candidates until there are either no more unassociated tracks or no additional vertices can be created from the remaining tracks.

Of the set of all primary vertex candidates, only those with at least two associated tracks are considered. The primary vertex for the event, the vertex most likely responsible for the hard-scatter, is taken to be the vertex with the highest sum of squared transverse momenta of associated tracks, $\sum p_{\text{T}}^2$.

6.2 Jet Reconstruction

Jets refer to the detector signature left when quarks or gluons fragment into a shower of particles (hadronization). The particles resulting from hadronization interact with both the ID and calorimeter. Charged particles entering the calorimeter produce electromagnetic showers or hadronic showers. The energy deposited in the calorimeter cells by these showers are reconstructed into particle jets. Jets are used as proxies for the hard partons produced in pp collisions.

Jets are reconstructed using topological clusters (topo-clusters) of cells from the calorimeter system as well as tracks from the ID. The clusters are composed of topologically connected cells in the calorimeters, forming "energy blobs" in the calorimeter volume. Individual topo-clusters crudely correspond to individual particles producing electromagnetic or hadronic showers in the calorimeter. The correspondence is not one-to-one since the showers of particles in close proximity can overlap [127].

The clustering begins by calculating the energy significance for each cell at the EM energy scale using the following equation:

$$\varsigma_{\text{cell}}^{\text{EM}} = \frac{E_{\text{cell}}^{\text{EM}}}{\sigma_{\text{noise,cell}}^{\text{EM}}} \tag{6.2}$$

where $\varsigma_{\text{cell}}^{\text{EM}}$ is the cell signal significance, $E_{\text{cell}}^{\text{EM}}$ is the cell signal, and $\sigma_{\text{noise,cell}}^{\text{EM}}$ is the average (expected) cell noise. This noise is estimated for each data year based on the electronic and pileup noise present in minimum bias events [127]. Three different thresholds are set to determine whether a cell should be considered a topo-cluster *seed*, S, a candidate for topo-cluster *growth*, N, or a *filtered* cell that demarcates the edge of a cluster, P, as defined below [127]:

$$\left|E_{\text{cell}}^{\text{EM}}\right| > S\sigma_{\text{noise,cell}}^{\text{EM}} \Rightarrow \left|\varsigma_{\text{cell}}^{\text{EM}}\right| > S \quad \text{(primary seed threshold, default } S = 4) \tag{6.3}$$

$$\left|E_{\text{cell}}^{\text{EM}}\right| > N\sigma_{\text{noise,cell}}^{\text{EM}} \Rightarrow \left|\varsigma_{\text{cell}}^{\text{EM}}\right| > N \quad \text{(threshold for growth control, default } N = 2) \tag{6.4}$$

$$\left|E_{\text{cell}}^{\text{EM}}\right| > P\sigma_{\text{noise,cell}}^{\text{EM}} \Rightarrow \left|\varsigma_{\text{cell}}^{\text{EM}}\right| > P \quad \text{(principal cell filter, default } P = 0) \tag{6.5}$$

Any cells that have an energy signal significance greater than the S threshold of 4 are treated as a *proto-cluster* and the clustering proceeds in an iterative manner. Next, the significance of all neighboring cells within the same calorimeter layer are checked. Additionally, the significance of any cells in adjacent layers that have any partial overlap in (η, ϕ) are also checked. If any of the neighboring cells is also a seed, then these proto-clusters are merged. If any of the neighboring cells pass the growth threshold, $N > 2$, with a significance of two or more, they are merged into the proto-cluster. If a neighboring cell is already a part of a different proto-cluster and passes the threshold $N > 2$, then the proto-clusters are merged. If a neighboring cell passes the threshold $P \geq 0$, it is also added to the proto-cluster. This process proceeds until all cells have either been added to a proto-cluster or are below the P-threshold. As cells are added to a proto-cluster, the location is updated to be the center of all cells in the proto-cluster. All of the proto-clusters at the end of the clustering are taken as the topo-clusters for the event [127].

These topo-clusters are then used in a dedicated jet-finding algorithm. The algorithm used for jet-finding in this analysis is the anti-k_t algorithm. The anti-k_t algorithm combines topo-clusters based on their spatial separation and momentum, and a radius parameter, R, according to the following equations:

$$d_{ij} = \min\left(k_{t,i}^{-2}, k_{t,j}^{-2}\right) \frac{\Delta_{ij}^2}{R^2}, \tag{6.6}$$

$$d_{iB} = k_{t,i}^{-2} \tag{6.7}$$

where $\Delta_{ij}^2 = (y_i - y_j)^2 + (\phi_i - \phi_j)^2$ is the distance between the i^{th} and j^{th} topo-cluster; $k_{t,i}$, y_i, and ϕ_i are the transverse momenta, the rapidity, and the azimuth of the i^{th} topo-cluster, respectively. d_{iB} represents the distance between the i^{th} topo-cluster and the beam (B). The parameter R is the radius parameter and is analogous to the cone-size parameter in cone algorithms [128]. The jets used in this analysis were reconstructed with $R = 0.4$. The name anti-k_t comes from the exponent on the transverse momentum being negative. Using momentum terms with the form $k_{t,i}^2$ in Eqs. 6.6 and 6.7 corresponds to a precursor algorithm called the k_t algorithm [129].

The anti-k_t algorithm combines topo-clusters into pseudo-jets in an iterative manner until the distance between the pseudo-jet and the beam is smaller than the distance to any other topo-cluster or pseudo-jet. At this point, the pseudo-jet is considered a jet. The anti-k_t algorithm begins jet-finding by calculating all d_{ij} and d_{iB} for the i^{th} object (a topo-cluster or a pseudo-jet) and finding the minimum of these distances. If a d_{ij} is the minimum, $d_{ij} < d_{ik}$ for all $k \neq j$ and $d_{ij} < d_{iB}$, then the i^{th} and j^{th} objects are combined. If both the i^{th} and j^{th} objects are topo-clusters, they form a new pseudo-jet. If only one is a topo-cluster, it's combined with the pseudo-jet and the center is recalculated proportionally. If the d_{iB} is the smallest, $d_{iB} < d_{ij}$ for all j, then object i is taken to be a jet and removed from the list of objects (topo-clusters and pseudo-jets). This process is repeated until all topo-clusters are in a jet. The advantage of having the distance being proportional to $1/k_t^2$ is that, for topo-clusters with high k_t, the d_{ij} is dominated by this high k_t (hard) topo-cluster, meaning that any low-k_t topo-clusters close to it are more likely to cluster with it than with each other. This yields roughly conical jets centered on the highest k_t topo-clusters. The resulting jets are robust against infrared (soft) emissions and collinear parton splittings, or are said to be "IRC-Safe" [129, 130].

In the case that two hard topo-clusters are close enough that $R < \Delta_{ij} < 2R$, the two jets have sufficient separation to be individually reconstructed, but at least one of the two resulting jets will only be partly-conical. If $\Delta_{ij} < R$ between two hard topo-clusters, then the topo-clusters are combined and reconstructed as a single jet.

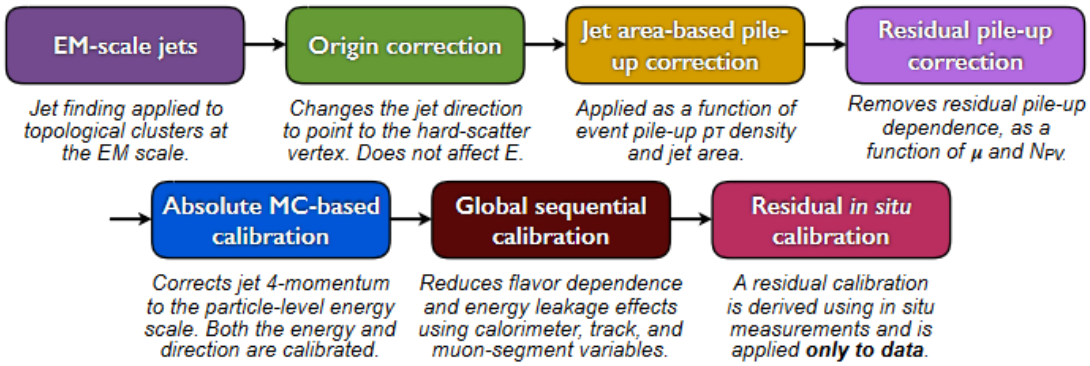

Figure 6.2: Calibration stages for EM-scale jets. Other than the origin correction, each stage of the calibration is applied to the jet four-momentum [131].

The resulting jets are said to be reconstructed at the EM energy scale, since they were

constructed from cells calibrated at the EM scale. Reconstruction at the EM scale is inadequate to correctly measure contributions to jet energy from hadronic sources and must be corrected. There are multiple sources of corrections to the jet energy scale (JES) which must be calculated and applied separately. These corrections are performed using PYTHIA Dijet MC samples and data collected during 2015. A diagram illustrating the different corrections and the order in which they are applied to the jets can be seen in Figure 6.2. Each correction is described in more detail below [131].

- **Origin Correction:** The origin correction recalculates the four-momentum of the jets to point to the hard-scatter primary vertex, instead of the detector center, while preserving the energy.
- **Jet Area-Based Pileup Correction:** Events with higher pileup will have jets with more soft contributions from pileup sources. To mitigate this contribution to total jet p_{T}, an area-based method is utilized that subtracts the pileup p_{T} contributions from each jet according to that jet's area. The pileup p_{T}-density, ρ, is calculated using positive-energy topo-clusters with $|\eta| < 2$ that are clustered using the k_t algorithm with $R = 0.4$. Unlike the anti-k_t algorithm, which is more sensitive to hard topo-clusters for clustering, the k_t algorithm is more sensitive to soft contributions, which makes it useful for clustering pileup. The selection on $|\eta| < 2$ is to eliminate the higher forward calorimeter occupancy from the pileup mitigation calculations.

  The p_{T}-density of each jet is taken to be p_{T}/A, where A is the area of the jet calculated via a ghost association procedure [132]. In this procedure, ghost particles with infinitesimal momentum (i.e. "infinitely soft") are added, uniformly in solid angle, to the event before k_t clustering is performed. The area is then determined by the fraction of the ghost particles that become associated with the jet during clustering. The median p_{T}-density is taken to be ρ for the event. Taking the median p_{T}-density reduces bias from the hard-scatter jets. The pileup contribution to the p_{T} of each jet, i, is taken to be ρA_i. The jet four-momentum is then corrected using the ratio of the pileup-corrected jet p_{T} versus the uncorrected jet p_{T}, $(p_{\mathrm{T}} - \rho A)/p_{\mathrm{T}}$.
- **Residual Pileup Correction:** The area-based correction is based on the low-η region,

and so a residual pileup correction to the anti-k_t jet p_{T} is performed to account for any remaining pileup contributions. This residual correction is based on both N_{PV}, which is sensitive to in-time pileup, and μ, which is sensitive to out-of-time pileup. The residual p_{T} dependence is measured to be the difference between the reconstructed jet p_{T} and the truth-level jet p_{T}, in Dijet MC [131]. The p_{T} dependence on N_{PV} and μ are both fairly linear and independent from each other. Therefore, linear fits are performed on this p_{T} dependence and the fitted values are used to subtract a proportional p_{T} from the anti-k_t jet p_{T} [131].

- **Absolute MC-based Calibration:** Comparisons in PYTHIA Dijet MC events are made in energy and η between reconstructed jets and truth jets, composed of the underlying truth-level particles, in order to calibrate the absolute energy scale and η. This is done to correct the particle-level energy scale due to changes in calorimeter technologies and granularity [131]. Not all calorimeter regions and technologies will have the same response to the same truth-level particle. Gaps and transitions between subdetectors could also cause energy to be lost by absorbed or undetected particles. Both effects are dependent on the η at which the jet is reconstructed in the detector, and so this calibration corrects the reconstructed jet energy, E^{reco}, from the truth energy, E^{truth} as well as the reconstructed η^{reco} from η^{truth} [131].

- **Global Sequential Calibration:** A set of independent corrections to the jet four-momentum based on a set of variables correlated with the detector response are derived by inverting the reconstructed jet response in MC events. These corrections primarily target residual dependencies of the JES on the longitudinal and transverse features of the jets [133, 131].

- **Residual *in situ* Calibration:** The *in situ* calibration corrects for differences between the jet reconstruction in MC and data by balancing the p_{T} of a jet against the detector response of well-measured reference objects [131]. An η-intercalibration procedure corrects the forward ($0.8 < |\eta| < 4.5$) jet energy scale to that of central ($|\eta| < 0.8$) jets using dijet events. The p_{T} of central jets can be balanced using Z/γ+jet events with a well-calibrated Z/γ for a recoiling jet p_{T} up to $\sim 950\,\mathrm{GeV}$. Higher p_{T} central jets

($300 < p_{\mathrm{T}} < 2000\,\mathrm{GeV}$) are calibrated using multijet events. Calibration corrections derived using central jets can be used with forward jets due to the JES corrections provided by the η-intercalibration. These p_{T} corrections are only applied to jets in *data*.

Not all of the calorimeter response will come from real particles originating from the hard-scatter vertex, meaning not all of the reconstructed, calibrated jets will either. Several sources of background can lead to the reconstruction of "fake jets". Beam-Induced Background (BIB) caused by proton-loss upstream of the detector can create fake jets with energies as high as the beam energy. Cosmic rays can generate muon showers that overlap with collision events, generating fake jets. Large-scale coherent noise and small-scale sporadic noise in the calorimeter can also lead to the production of fake jets. To eliminate any jets reconstructed from background sources a set of jet cleaning criteria for $R = 0.4$ anti-k_t jets is defined (Good Jets) [134].

- $\mathbf{Q}_{\mathrm{cell}}^{\mathrm{LAr}}$ reflects the quality of an individual calorimeter cell signal in the LAr calorimeter. It is defined as the quadratic difference in the electronic pulse shape between the measured pulse shape in data and the expected pulse shape from simulations of the electronic response. Several quality criteria can be derived from this value.
  - $\langle \mathbf{Q} \rangle$ is the energy-weighted average of the pulse quality for each calorimeter cell in the jet. This property is normalized such that $0 < \langle Q \rangle < 1$.
  - $\mathbf{f}_{\mathrm{Q}}^{\mathrm{LAr}}$ is the fraction of the energy in a jet coming from cells in the LAr with a poor signal shape quality ($Q_{\mathrm{cell}}^{\mathrm{LAr}} > 4000$).
  - $\mathbf{f}_{\mathrm{Q}}^{\mathrm{HEC}}$ is the fraction of the energy in a jet coming from cells in the hadronic endcap calorimeter (HEC) with a poor signal shape quality ($Q_{\mathrm{cell}}^{\mathrm{LAr}} > 4000$).
- $\mathbf{E}_{\mathrm{neg}}$ is the sum of energy in all cells in a jet with negative energy. Large negative energy deposits are frequently generated by fake jets, giving this variable some discrimination power against jets coming from sporadic and coherent noise.
- $\mathbf{f}_{\mathrm{EM}}$, the *electromagnetic fraction*, is the fraction of jet energy coming from the electromagnetic calorimeter. It is defined as the ratio of energy deposited in the EM

Calorimeter over the total jet energy.

- $\mathbf{f_{HEC}}$, the *HEC energy fraction*, is the fraction of jet energy coming from the hadronic endcap calorimeter. It is defined as the ratio of energy deposited in the HEC over the total jet energy.
- $\mathbf{f_{max}}$, the *maximum energy fraction*, is the maximum fraction of jet energy coming from a single calorimeter layer. Fake jets tend to have higher values of f_{max} than good jets.
- $\mathbf{f_{ch}}$, the *jet charge fraction*, is defined as the ratio of the scalar sum of p_{T} of jet-associated tracks coming from the PV divided by the jet p_{T}. Most real jets will have charged hadrons that leave tracks in the ID.

Figures 6.3 and 6.4 show the distributions of the jet quality criteria for both good-jet-enriched data (black data points) and fake-jet-enriched data (red data points). Some distributions for the jet quality criteria in PYTHIA Dijet MC are also shown (cyan-blue histograms). In this analysis, fake jets are identified using the `BadLoose` jet quality threshold. Any jet that meets at least one of the `BadLoose` selection criteria is considered to be a fake jet:

- $f_{\text{HEC}} > 0.5$ and $\left|f_{\text{Q}}^{\text{HEC}}\right| > 0.5$ and $\langle Q \rangle > 0.8$
- $|E_{\text{neg}}| > 60\,\text{GeV}$
- $f_{\text{EM}} > 0.95$ and $f_{\text{Q}}^{\text{LAr}} > 0.8$ and $\langle Q \rangle > 0.8$ and $|\eta| < 2.8$
- $f_{\text{max}} > 0.99$ and $|\eta| < 2$
- $f_{\text{EM}} < 0.05$ and $f_{\text{ch}} < 0.05$ and $|\eta| < 2$
- $f_{\text{EM}} < 0.05$ and $|\eta| \geq 2$

In addition to selection on these jet quality criteria a jet-vertex-tagger (JVT) is used to remove additional fake jets caused by pileup. The JVT is constructed as a 2D likelihood, based on a k-nearest neighbors algorithm [135], on a plane defined by two new variables: $R_{p_{\text{T}}}$ and corrJVF. $R_{p_{\text{T}}}$ is defined as the ratio of the scalar p_{T} sum of the tracks that originate from the hard-scatter vertex and are associated with a jet divided by the fully calibrated jet p_{T} [136, 137],

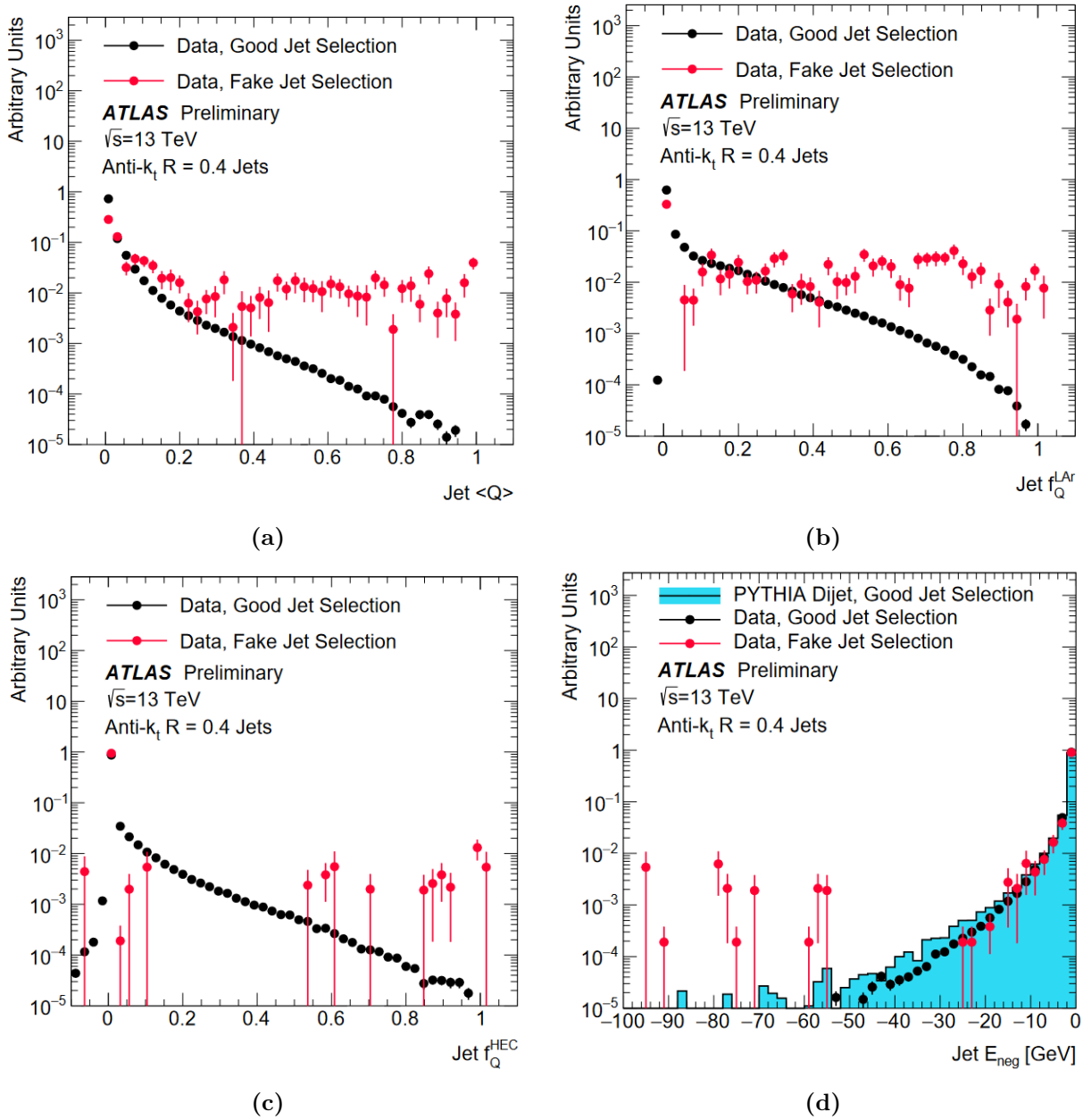

Figure 6.3: Distributions of jet quality parameters (a) $\langle Q \rangle$, (b) $f_{\mathrm{Q}}^{\mathrm{LAr}}$, (c) $f_{\mathrm{Q}}^{\mathrm{HEC}}$, and (d) E_{neg}. Data enriched in good jets are shown in black points while data enriched in fake jets are shown in red. The cyan-blue histogram [shown in (d) only] is the distribution of good jets from PYTHIA Dijet MC events.

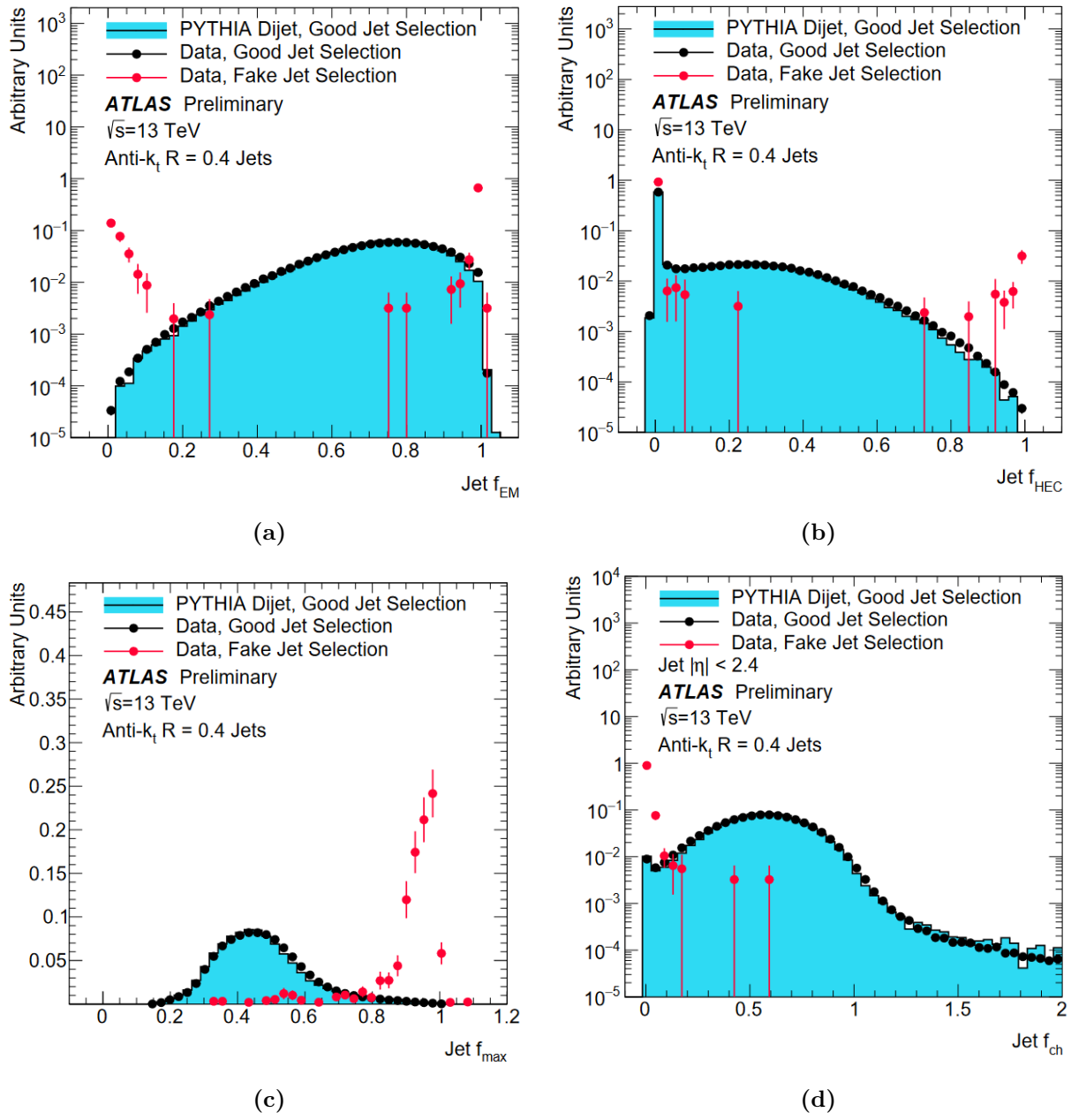

Figure 6.4: Distributions of jet quality parameters (a) f_{EM}, (b) f_{HEC}, (c) f_{max}, and (d) f_{ch}. Data enriched in good jets are shown in black points while data enriched in fake jets are shown in red. The cyan-blue histogram is the distribution of good jets from PYTHIA Dijet MC events.

$$R_{p_{\mathrm{T}}} = \frac{\sum_k p_{\mathrm{T}}^{\mathrm{trk}_k}(\mathrm{PV}_0)}{p_{\mathrm{T}}^{jet}} \tag{6.8}$$

where $p_{\mathrm{T}}^{\mathrm{trk}_k}$ is the p_{T} of the k^{th} track originating from the n^{th} primary vertex, PV_n. Here PV_0 corresponds to the hard-scatter PV. p_{T}^{jet} is the calibrated p_{T} of the jet for which $R_{p_{\mathrm{T}}}$ is being calculated.

The other value, corrJVF, is related to the jet-vertex-fraction (JVF). The JVF is defined as the scalar p_{T} sum of jet-associated tracks originating from the hard-scatter PV divided by the scalar p_{T} sum of all tracks associated with a vertex, as can be seen in Eq. 6.9.

$$\mathrm{JVF} = \frac{\sum_k p_{\mathrm{T}}^{\mathrm{trk}_k}(\mathrm{PV}_0)}{\sum_l p_{\mathrm{T}}^{\mathrm{trk}_l}(\mathrm{PV}_0) + \sum_{n\geq 1}\sum_l p_{\mathrm{T}}^{\mathrm{trk}_l}(\mathrm{PV}_n)} \tag{6.9}$$

Here the numerator contains the same scalar p_{T} sum over all jet-associated tracks that originate from the hard-scatter PV, PV_0, as is present in the definition of $R_{p_{\mathrm{T}}}$ in Eq. 6.8. The denominator is defined as the sum of p_{T} of jet-associated tracks coming from PV_0, plus the scalar sum of p_{T} from all remaining tracks associated to pileup PVs, PV_n with $n \geq 1$. corrJVF takes this definition of JVF and adds an N_{PV}-dependent correction to the scalar p_{T} sum to account for the p_{T} from pileup tracks associated with a jet. Since this is a correction related to the pileup tracks, it is only applied to the second term in the denominator of Eq. 6.9. The resulting equation becomes

$$\mathrm{corrJVF} = \frac{\sum_k p_{\mathrm{T}}^{\mathrm{trk}_k}(\mathrm{PV}_0)}{\sum_l p_{\mathrm{T}}^{\mathrm{trk}_l}(\mathrm{PV}_0) + \frac{\sum_{n\geq 1}\sum_l p_{\mathrm{T}}^{\mathrm{trk}_l}(\mathrm{PV}_n)}{\left(k \cdot n_{\mathrm{trk}}^{\mathrm{PU}}\right)}} \tag{6.10}$$

where all terms in this definition of corrJVF, Eq. 6.10, are the same as in Eq. 6.9, save for the term $k \cdot n_{\mathrm{trk}}^{\mathrm{PU}}$, where $n_{\mathrm{trk}}^{\mathrm{PU}}$ is the number of pileup tracks per event and k is a scaling factor roughly taken as the slope of the average p_{T} contribution coming from pileup PVs. The default value for k is 0.01, though the discrimination power between jets originating from hard-scatter and jets originating from pileup (pileup jets) has been shown to be insensitive to choice of k [136].

Using the 2D likelihood, at each point in the corrJVF$-R_{p_{\mathrm{T}}}$ plane the relative probability that a jet, at that point, would be of a signal-type (associated to the hard-scatter PV) is

computed as the ratio of the number of hard-scatter jets divided by the number of hard-scatter plus pileup jets within a neighborhood around that point. The likelihood model is trained with a sample of signal and pileup jets with $20 < p_{\mathrm{T}} < 50\,\mathrm{GeV}$ in the $|\eta| < 2.4$ region. The resulting probability is bound in the range $[0, 1]$, unless no tracks are associated with the jet, in which case it is assigned a JVT score of -1. Generally, lower JVT scores are associated with pileup.

6.3 Missing Transverse Energy $E_{\mathrm{T}}^{\mathrm{miss}}$ Reconstruction

An ideal particle collision would occur such that the particles involved in the collision are perfectly collinear with the beamline making the initial transverse momentum of the collision is zero. In practice, this is never true [138]. In addition to the intrinsic non-zero p_{T} of the parton-parton interaction in the pp collision, weakly interacting particles, such as neutrinos, are invisible to the detector and any energy they carry with them goes unmeasured. So, too, would the energy carried by a weakly interacting long-lived particle that decays outside of the detector be lost. Energy losses can also come from particles interacting with the dead material in the detector, from interacting with the active material but failing to be properly reconstructed, or from having an $|\eta|$ too large to hit the detector.

To measure the missing transverse energy, the vector sum of all p_{T} sources in an event are calculated. This sum represents the net p_{T} (or transverse energy, E_{T}) in the event. Since the initial net p_{T} in ATLAS collisions ideally comes from the parton momentum scale ($< 938\,\mathrm{MeV}$), any final net p_{T} much greater than this scale indicates some amount of transverse momentum is missing [138]. This *missing* transverse energy, $E_{\mathrm{T}}^{\mathrm{miss}}$, is taken to be the p_{T} of a particle recoiling from the E_{T}. This is equivalent to calculating the negative vector sum of p_{T} for an event [139],

$$E_{\mathrm{T}}^{\mathrm{miss}} = \left\| \underbrace{-\sum_{\substack{\text{selected}\\\text{electrons}}} \mathbf{p}_{\mathrm{T}}{}^{e} - \sum_{\substack{\text{accepted}\\\text{photons}}} \mathbf{p}_{\mathrm{T}}{}^{\gamma} - \sum_{\substack{\text{accepted}\\\tau\text{-leptons}}} \mathbf{p}_{\mathrm{T}}{}^{\tau_{\mathrm{had}}} - \sum_{\substack{\text{selected}\\\text{muons}}} \mathbf{p}_{\mathrm{T}}{}^{\mu} - \sum_{\substack{\text{accepted}\\\text{jets}}} \mathbf{p}_{\mathrm{T}}{}^{\mathrm{jet}}}_{\text{hard term}} \underbrace{- \sum_{\substack{\text{unused}\\\text{tracks}}} \mathbf{p}_{\mathrm{T}}{}^{\mathrm{track}}}_{\text{soft term}} \right\| \tag{6.11}$$

The first five terms in Eq. 6.11, called the *hard* terms, come from fully calibrated reconstructed physics objects, meaning the $E_{\mathrm{T}}^{\mathrm{miss}}$ has little dependence on pileup, since all pileup mitigation and calibration have already been applied. Typically the soft term uses only tracks associated with the hard-scatter PV, but alternative calculations exist which include topo-clusters coming from neutral particles. A more complete description of these alternative formulations is available in [139].

The $E_{\mathrm{T}}^{\mathrm{miss}}$ must be reconstructed from mutually exclusive detector signals and so a standard priority-ordered reconstruction sequence was developed. For the hard objects, the contributions from electrons are added first (e), followed by photons (γ), then hadronically-decaying τ-leptons (τ_{had}), then jets. Muons (μ) typically have little overlap with other signal sources, since they are reconstructed from ID and MS tracks. If a lower-priority (later in the sequence) object shares a calorimeter signal with a higher-priority object, then the lower-priority object is fully rejected from contributing to the $E_{\mathrm{T}}^{\mathrm{miss}}$. Though muons have little overlap with other signal sources, they do lose energy in the calorimeter. If they overlap with a jet or jet-like signature in the calorimeter (i.e. it's non-isolated), then it's not possible to separate the muon contribution to the jet energy, and a jet-muon overlap mitigation procedure determines if the muon (or jet) is rejected.

The soft term in Eq. 6.11 is reconstructed from high-quality ID tracks associated to the hard-scatter vertex, but not associated to any other hard reconstructed objects. There exists a more inclusive soft term reconstruction that also uses signals from soft neutral particles left in the calorimeter topo-clusters. This calorimeter-based soft term is more sensitive to pileup and generally has inferior performance when compared to the track-based soft term, (TST). This analysis uses $E_{\mathrm{T}}^{\mathrm{miss}}$ reconstructed with a track-based soft term.

6.4 Missing Transverse Jet Momentum $H_{\mathrm{T}}^{\mathrm{miss}}$ Reconstruction

The missing transverse jet momentum ($H_{\mathrm{T}}^{\mathrm{miss}}$) in an event is a similar term to the $E_{\mathrm{T}}^{\mathrm{miss}}$, except $H_{\mathrm{T}}^{\mathrm{miss}}$ is reconstructed using only the momentum of accepted, calibrated jets. For this analysis, only jets with a $p_{\mathrm{T}} > 30\,\mathrm{GeV}$ with $|\eta| < 3.2$ were used to calculate $H_{\mathrm{T}}^{\mathrm{miss}}$. The calculation is shown in Eq. 6.12.

$$H_{\mathrm{T}}^{\mathrm{miss}} = \left\| - \sum_{\substack{\text{accepted} \\ \text{jets}}} \mathbf{p}_{\mathrm{T}}{}^{\mathrm{jet}} \right\| \tag{6.12}$$

6.5 Muon Segment Reconstruction

Muon segments in ATLAS are three-dimensional paths through the MS that are used to reconstruct standard muon tracks. These standard muon tracks, as well as the muon segments used to find them, reflect the activity of an event in the MS, and so are of interest to this analysis. Fully reconstructed muons are not used in this analysis, thus this section will focus on the methods used to reconstruct the MS segments and tracks.

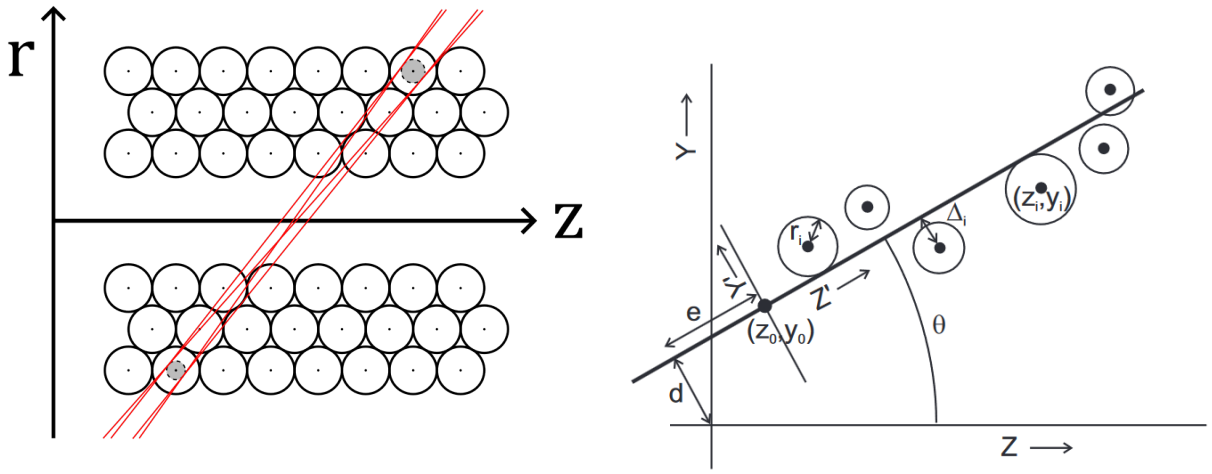

(a) **(b)**

Figure 6.5: (a) Diagram of the four possible segments that can be drawn between two drift circles in the MDT, as is done in the first step of track reconstruction. Segment candidates are drawn in red. The MDT drift circles are gray circles with dashed borders. (b) Illustration of the variables used in the track-centered coordinate system (Y', Z'), in which the χ^2 minimization is performed, versus the ATLAS global coordinate system (Y, Z).

In ATLAS, there are three primary reconstruction categories for muon tracks: standalone reconstruction, combined reconstruction, and tagged muons [140]. Standalone reconstruction only uses hits in the MS to build muon tracks. Combined reconstruction looks at tracks reconstructed in both the MS and the ID and attempts to combine them into single tracks. The tagged muon method looks at ID tracks and attempts to extrapolate them into the MS

to construct full muon tracks. Because this analysis doesn't rely on standard ATLAS muons and performs an analysis specific reconstruction using only MS hits, this section focuses only on the standalone reconstruction of standard ATLAS muons.

Muon segment reconstruction begins with pairs of hits within the same MDT station, with one hit in each MDT multilayer. Because the MDT hits are drift circles, a pair of hits can be connected with a set of four lines, here referred to as "segment ambiguities", as shown in Figure 6.5(a) [141]. Each ambiguity serves as a seed for segment candidates. All additional hits within a distance of 5 mm of the trajectory are added to the list of hits for each ambiguity. If the resulting list contains at least four hits, and each multilayer contains at least two hits, the segment ambiguity is accepted as a segment candidate. Segment candidates are generated this way until all possible pairs of hits have been checked. Duplicates and subsets are then removed, though segments that share hits are not [141].

Muon tracks use these accepted segment candidates as seeds for track-finding. Each segment is modeled as a straight line composed of the hits associated to the seed segment. The segment is then fit by minimizing the following χ^2

$$\chi^2 = \sum_{i=1}^{n} \frac{(\Delta_i - r_i)^2}{\sigma_i^2} \tag{6.13}$$

where Δ_i is the perpendicular distance from the segment to the wire at the center of the MDT that produced the drift circle for hit i and σ_i is the Gaussian error associated with the measured drift circle radius, r_i. These calculations are done in a coordinate system centered on a point collinear with the seeding segment and with the z-axis pointing outward along the segment and the y-coordinate pointing perpendicular to z but still within the bending plane.

Transforming into the ATLAS global coordinates, Eq. 6.13 takes the following form:

$$\chi^2 = \sum_{i=1}^{n} \frac{(|-z_i \sin(\theta) + y_i \cos(\theta) - d| - r_i)^2}{\sigma_i^2} \tag{6.14}$$

The coordinates, (z_i, y_i), correspond to the MDT wire coordinates for the MDT associated with hit i in the global coordinate system, d is the perpendicular distance between the segment and the beamline at the point of closest approach, and θ is the angle between the

beamline and the segment. An illustration of these variables as they relate to the segment location can be seen in Figure 6.5(b). Additionally, the origin of the segment coordinate system is labeled (z_0, y_0) and the distance between the origin and the point of closest approach to the global coordinate system origin, along the segment (Z' axis), is e. This value e is a free parameter of the segment fit and is chosen to make the correlation between θ and d zero [141, 142][2]:

$$e = \cos\theta z_c + \sin\theta y_c \tag{6.15}$$

where the coordinates (z_c, y_c) correspond to the weighted average hit position. This choice of e simplifies the calculation of the minimum chi-squared [141].

Muon tracks are then formed by extrapolating the path of the best segments, called "strict" segments, through the magnetic field in the direction of the next station[3]. This extrapolation is done by scanning a distribution of possible muon p_{T} values and attempting the extrapolation with each segment. If this extrapolated track aligns with the location and direction of a segment in the next MDT chamber, then the two segments are combined into a candidate track. If more than one segment matches the extrapolated track, then the best-matching segment is added. This process is repeated for all strict segments.

A second, finer "momentum scan" fit is then performed on the pairs of segments, refining the fit further around the estimated momentum that can be calculated from the segment pair. The segment pair is then extrapolated to all other potentially crossed MDT stations. Any segments in these other stations that match the extrapolated track are added.

If the collection of matched segments contains at least two segments, then it is considered a track candidate and a new fit is performed to refine the candidate muon position, momentum, and direction. Once this is done, a final global fit is performed on all the hits associated with the segments. If the χ^2 fit of all the hits with the final track is too large, then the track is discarded [81].

The muon segment reconstruction algorithm for the endcaps is nearly identical, save that the track coordinates are mapped differently onto the ATLAS global coordinates. For endcap

[2] According to [142] and [141], the value e is a free parameter of the chi-squared formulation.
[3] See Section 3.3.3 for a brief description of the MS geometry.

segments, the track-centered coordinates (Y', Z') are mapped to the global longitudinal coordinate, Z, and the global radial coordinate, Y, respectively [143]. Further details of the parameterization can be found in [143].

6.6 Analysis-Specific Reconstruction

It is not the case, however, that standard muon segments are used in the reconstruction of the MS displaced vertices. The reconstruction algorithm for standard muon segments assumes a relatively clean environment. The typical number of MDT hits left by a traversing muon is between 20 and 25 hits, while the number of hits generated by the charged particles associated with displaced vertices easily exceeds 100. This presents a problem for the combinatoric reconstruction algorithms used in muon segment reconstruction, which would struggle to combine segments into tracks. A dedicated algorithm was necessary for reconstructing MS displaced vertices, which was developed based on the track-finding techniques used in [144].

6.6.1 Tracklet Reconstruction

A tracklet is a track that spans only the width of a single MDT station and is composed of a pair of segments, each of which is a straight-line segment within a single MDT multilayer. Tracklets can be reconstructed in any of the three layers of MDT chambers in either the barrel or endcap region. In order to reconstruct tracklets between the MDT multilayers within a station, first segments must be reconstructed within each multilayer. The segment reconstruction looks only at the first (ML1) and second (ML2) MDT multilayers. Segments are constructed by performing a minimum χ^2 fit on groups of at least three MDT hits. If a segment has a χ^2 probability greater than 0.05, it is considered a good segment and kept [144].

Tracklets are then created from pairs of segments, one from each MDT multilayer. This matching is done using two parameters, Δb and $\Delta\alpha$. The parameter Δb is the minimum distance between the point where one segment passes the middle plane between ML1 and ML2 and the line defined by the other. Since there are two segments, there are two such

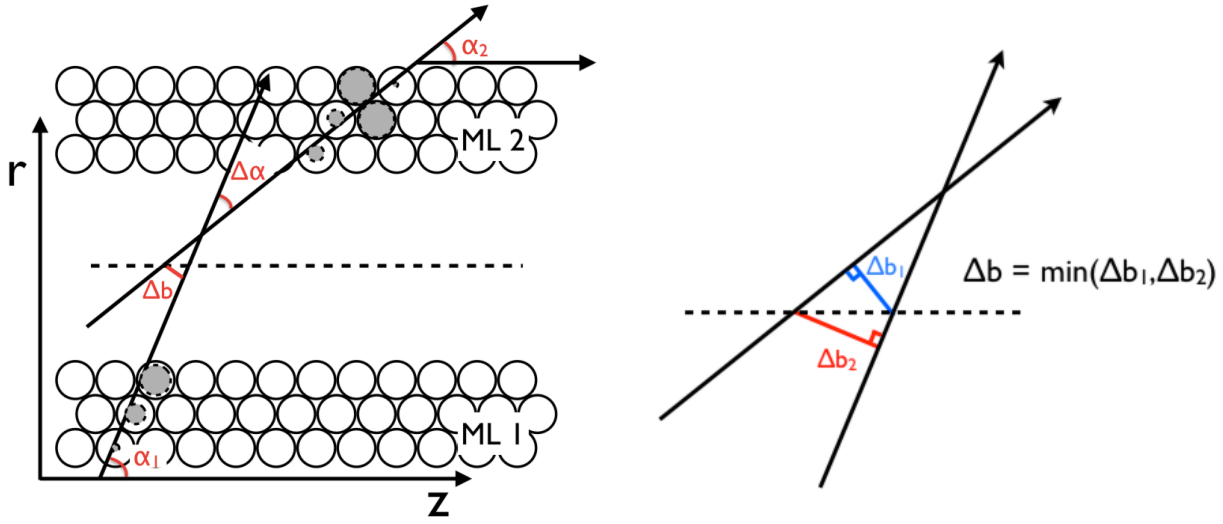

(a) **(b)**

Figure 6.6: (a) Diagram of a segment from each MDT multilayer, ML1 and ML2, and the parameters Δb and $\Delta\alpha$. (b) Diagram of the two possible values for Δb, of which the smaller is taken.

lengths as shown in Figure 6.6(b) [144], of which the smaller is taken as the value of Δb. For chambers in the magnetic field, a $\Delta b \sim 0$ selects segments tangent to the same circle, which must belong to the same charged particle. For all tracklets, a $\Delta b_{\text{max}} \leq 3\,\text{mm}$ is required. The parameter $\Delta\alpha$ corresponds to the angle between the two segments, defined as $\Delta\alpha \equiv \alpha_1 - \alpha_2$. For segments in regions of the MS outside of the magnetic field, a minimum $\Delta\alpha$ of 12 mrad is used to match segments. Inside the magnetic field, it is used to measure the tracklet p_{T} for low-p_{T} particles. A diagram showing the tracklet parameters as related to the two constituent segments can be seen in Figure 6.6(a) [144].

Because signal events produce far more RPC(TGC) hits in the barrel (endcap) region than typical muons, it is not possible for an accurate RPC-ϕ measurement to be associated with the MDT hits. For this reason, they are excluded, limiting the ϕ coordinate precision to what is provided by the MDT stations [145]. For this reason, reconstructed tracklets are assigned the ϕ coordinate of the MDT center and are assumed to be traveling radially outward [144].

The angular resolution of the single-multilayer MDT segments was found using a simulated MC sample of single muons with a momentum of 1 TeV, distributed evenly between $-\pi < \phi < \pi$ and $|\eta| < 1$ generated using the full ATLAS simulation chain. The RMS for $\Delta\alpha$ and

Δb was found to be 4.3 mrad and 1.0 mm, respectively, for segments containing three MDT hits [144].

The Muon Spectrometer has a different MDT geometry between different regions of the detector, so different tracklet selection criteria are defined for each MDT chamber. A summary of these selection criteria is shown in Table 6.1 [144]. The variable $\Delta\alpha_{\text{max}}$ refers to the maximum amount of bending between the two segments between the multilayers to be considered matched. This maximum angle corresponds to a tracklet momentum of 0.8 GeV. Tracklets with a $|\Delta\alpha| < 12$ mrad are refit as a straight-line spanning both multilayers and utilizing all of the MDT hits associated with each constituent segment.

Chamber Type	Number of Layers	ML Spacing (mm)	$\lvert\Delta\alpha_{\text{max}}\rvert$ (mrad)	$\lvert\Delta b_{\text{max}}\rvert$ (mm)	Refit
BIS	4	6.5	12	3	Always
BIL	4	170	36	3	if $\Delta\alpha < 12$ mrad
BMS	3	170	67	3	if $\Delta\alpha < 12$ mrad
BML	3	317	79	3	if $\Delta\alpha < 12$ mrad
BOS	3	317	12	3	Always
BOL	3	317	36	3	if $\Delta\alpha < 12$ mrad
Endcap	3	170	12	3	Always

Table 6.1: Summary of tracklet selection criteria in each MS MDT chamber. "Number of Layers" indicates the number of layers in the MDT multilayer. "ML Spacing" indicates the separation between multilayers in the MDT station. The tracklets are refit as a single straight-line if the criteria in the "Refit" column are met.

The Barrel Inner Small (BIS) chamber, Barrel Outer Small (BOS) chamber, and all layers in the endcap regions are outside of the magnetic field and so always have their tracklets refit as straight-line segments.

For all barrel chambers within the magnetic field, the tracklet momentum can be calculated using an equation of the form $p = k/|\Delta\alpha|$. The factor k is found using MC simulations of v-hadrons, π_ν, which are LLPs from a model similar to the $H \to ss$ model used in this analysis [145, 146]. It is calculated separately for each MDT chamber type by taking a linear fit of the $\Delta\alpha$ distribution versus $1/p_{\text{T}}$ [145]. By propagating the uncertainty in $\Delta\alpha$, the uncertainty in tracklet momentum is found to be $\sigma_p/p \approx 0.06 \cdot p/\text{GeV}$ in the BML chambers, $\sigma_p/p \approx 0.08 \cdot p/\text{GeV}$ in the BMS chambers, and $\sigma_p/p \approx 0.13 \cdot p/\text{GeV}$ in the BOL and BIL

chambers.

6.6.2 MS Vertex Reconstruction

Most barrel chambers are immersed in a magnetic field ($|\eta| < 1$) while the endcap chambers ($1 < |\eta| < 2.7$) are not. This means most tracklets reconstructed in the barrel chambers will have an associated p_{T}, while tracklets in the endcap will not. Because of this, different vertex reconstruction algorithms are used in the barrel and the endcap, however both algorithms are tuned to maximize the vertex reconstruction efficiency in exchange for vertex position resolution.

The vertex reconstruction for both the barrel and endcap regions follow a few general steps [144]:

1. Tracklets are reconstructed in the MDT chambers, as outlined in Section 6.6.1.
2. A clustering algorithm groups the tracklets and selects the group to be used.
3. The RPC(TGC) hits are used along with the tracklets in the barrel (endcap) to calculate the lines-of-flight in η and ϕ for the LLPs.
4. The ϕ line-of-flight is used to map the clustered tracklets onto a single $r - z$ plane.
5. The vertex position is calculated by back-extrapolating the tracklets, taking into account the bending caused by the magnetic field for the barrel tracklets.

Each algorithm uses tracklets exclusively reconstructed within the respective detector region. For displaced vertices decaying near $|\eta| = 1$, it is possible for two vertices to be reconstructed. If sufficient tracklets are reconstructed in each detector region, one vertex can be reconstructed by the barrel algorithm and a second can be reconstructed by the endcap algorithm. If this occurs, the reconstruction algorithm keeps both and leaves the decision between the two for subsequent analysis steps. For this analysis, the overlap region was explicitly excluded so these duplicates were not considered. Beyond what is described below, more details can be found in [147].

MS Vertex Barrel Algorithm

The first step of the barrel vertex reconstruction is to identify the cluster of tracklets to be used. This is done by a clustering algorithm similar to the muon RoI cluster algorithm described in Section 5.3.

Each tracklet is treated as a seed and is checked against all other tracklets. If another tracklet is found within $\Delta\eta = 0.7$ and $\Delta\phi = \pi/3$ of the seed, it is added to that seed's cluster. Every time a tracklet is added to a cluster, the cluster center in (x, y, z) is recalculated as the average position of all associated tracklets. The position of a tracklet is taken to be its centroid [145]. This process repeats until all tracklets have been checked. This cluster location is then used as a seed in the next clustering iteration. If no additional tracklets were added to the cluster and it contains at least three tracklets, then the location of this cluster is returned as a final cluster position. If new tracklets were added, then the clustering process repeats one more time, using the updated cluster location as the starting seed location. This clustering process can be performed up to five times. Any clusters that undergo five clustering iterations and include at least three tracklets are considered good clusters [147].

If there are tracklets remaining in the event that were not included in the first cluster, the same clustering procedure is rerun on those remaining tracklets. This is done until either there are fewer than three unclustered tracklets remaining or those that do remain cannot form a cluster with at least three tracklets. Of the clusters produced in this way, the one with the highest tracklet multiplicity is used to reconstruct the vertex location.

The line-of-flight of the LLP in the θ direction is then reconstructed by drawing a line between the IP and the averaged location of all tracklets contained within the selected cluster. Using π_v signal MC samples [145], it has been demonstrated that this process reconstructs the true θ line-of-flight with an RMS of 21 mrad [145].

The line-of-flight in ϕ is reconstructed using the average ϕ location of all of the tracklets as a seed, recalling that the tracklet ϕ location is taken to be the center of its respective MDT chamber. This ϕ value is then used along with the θ line-of-flight to draw a cone of radius $R = 0.6$ toward the tracklet cluster center, with its apex at the IP. The ϕ coordinate of all RPC hits within this cone are then averaged to determine the ϕ line-of-flight of the

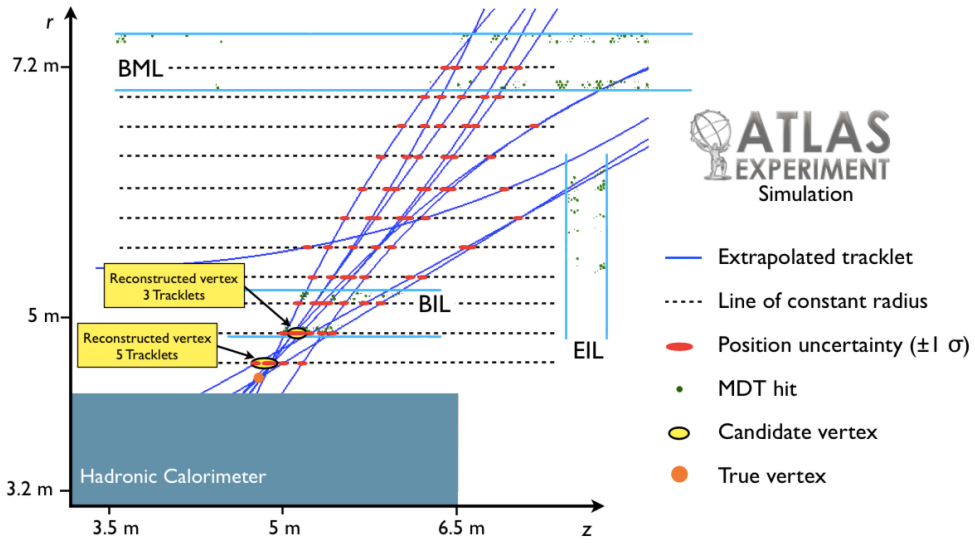

Figure 6.7: Simulated reconstruction of a vertex in the MS barrel region, illustrating the reconstruction technique in this region.

LLP with an RMS of 50 mrad.

This uncertainty in the ϕ-direction corresponds to $\sim 1/8$ of a large MDT chamber, making the vertex resolution in the ϕ-direction quite poor. Because of this, along with the inhomogeneous magnetic field in the barrel, all of the tracklets are rotated into a single $r-z$ plane, centered on the ϕ line of flight, in order to perform the vertex reconstruction [144].

The tracklets are then back-propagated in the direction of the IP within this $r-z$ plane through a series of lines parallel with the z-axis. These lines are spaced evenly at 25 cm intervals along the line-of-flight between the radii of $r = 3.5$ m and $r = 7.0$ m. This would result in 15 lines at $\eta = 0$ and 22 lines at $|\eta| = 1$. A representation of these lines can be seen in Figure 6.7 [144]. By fixing the length between each of these lines, it assures that all of the tracklets, regardless of η, are extrapolated the same way. Each tracklet is extrapolated from one such line to the next until the tracklet intersects all lines.

Because there is low ϕ resolution, the extrapolation path has high uncertainty in ϕ. Since the magnetic field strength is dependent on the path location, this ϕ uncertainty causes a low magnetic field strength accuracy. To estimate the uncertainty caused by this poor magnetic field accuracy, the extrapolation is redone for the same tracklets, but with the $r-z$ plane rotated 200 mrad around the z-axis. This rotation causes the backpropagation of the tracklets to pass through a different portion of the magnetic field, which changes where

the tracklets will intersect the lines of constant radius. The difference in the z-position of the extrapolated tracklet intersection at each line is taken as its uncertainty due to magnetic field resolution. This uncertainty is added in quadrature to the position uncertainty due to the uncertainty in the tracklet momentum. Any tracklets with an uncertainty $\sigma_z > 20\,\text{cm}$ are removed from the vertex-finding algorithm.

At each line of constant radius, the average tracklet z-position is calculated, with each tracklet weighted by the inverse of its z-position uncertainty, $w = 1/\sigma_z$. A χ^2 minimization is performed and the χ^2 probability is calculated for the average z-position of each line of constant radius and treated as a candidate vertex. For all such candidate vertices, if the χ^2 probability is less than 0.05, then the tracklet with the largest χ^2 value is dropped and the χ^2 probability is recalculated. This continues until either the χ^2 probability becomes greater than 0.05, or until the number of tracklets used drops below three. The location of the reconstructed vertex is taken as the radius and z-position of the line of constant radius that had the highest number of tracklets. If there are multiple vertices that have the same number of tracklets, the one with the highest χ^2 probability is taken as the location of the reconstructed vertex.

Any MDT hits from a chamber with a center within a cone of $\Delta R = 0.6$ of the vertex are considered to be associated to the vertex. The number of associated RPC hits is similarly calculated. The number of associated MDT stations is taken to be any of the stations with a center within the same cone with at least a 25% occupancy [145].

MS Vertex Endcap Algorithm

In the endcap, all tracklets are straight-line segments independent of tracklet charge or momentum. The toroid magnet sits between the inner and middle MDT stations, so the trajectory of some charged particles from decays that occur closer to the IP may be bent. The MDT stations, themselves, are not immersed in the magnetic field. For this reason, only straight-line segments are reconstructed and all endcap tracklets must be back-extrapolated into the toroid as straight lines.

The first step to reconstructing an endcap vertex is the same as in the barrel region: a clustering algorithm is run to produce clusters of tracklets within regions of $\Delta\eta = 0.7$ and

$\Delta\phi = \pi/3$. Any clusters with three or more tracklets are saved. The average position of the cluster is calculated and the average ϕ-position further refined using hits from the TGC chambers within a cone of $\Delta R = 0.6$ centered on the line-of-flight. All of the tracklets are then rotated into the $r - z$ plane described above and the resolution of the line-of-flight is comparable to that in the barrel.

The next step is to extrapolate the tracklets within each cluster back toward the IP. Unlike in the barrel, where lines-of-constant-radius were used for a discretized back-extrapolation, all of the endcap tracklets are straight-lines, so a least squares regression fit to a line of the form $\beta_i = -r\tan(\theta_i) + z$ is used. For the i^{th} cluster, β_i is the z-intercept and θ_i is the tracklet angle from the z-axis. The following formulae are used in the weighted least squares regression [148],

$$r_{\text{vertex}} = \frac{\left(\sum \frac{\tan\theta_i}{\sigma_i^2}\right)\left(\sum \frac{\beta_i}{\sigma_i^2}\right) - \left(\sum \frac{\tan\theta_i}{\sigma_i^2}\right)\left(\sum \frac{\beta_i \tan\theta_i}{\sigma_i^2}\right)}{\left(\sum \frac{1}{\sigma_i^2}\right)\left(\sum \frac{\tan^2\theta_i}{\sigma_i}\right) - \left(\sum \frac{\tan\theta_i}{\sigma_i^2}\right)^2} \tag{6.16}$$

$$z_{\text{vertex}} = \frac{\left(\sum \frac{\tan\theta_i}{\sigma_i^2}\right)\left(\sum \frac{\beta_i}{\sigma_i^2}\right) - \left(\sum \frac{1}{\sigma_i^2}\right)\left(\sum \frac{\beta_i \tan\theta_i}{\sigma_i^2}\right)}{\left(\sum \frac{1}{\sigma_i^2}\right)\left(\sum \frac{\tan^2\theta_i}{\sigma_i}\right) - \left(\sum \frac{\tan\theta_i}{\sigma_i^2}\right)^2} \tag{6.17}$$

where each term has σ_i, the uncertainty on β_i, in the denominator. This weight makes it so the tracklets with a higher uncertainty contribute less to the vertex position.

The most probable location of the vertex returned by the regression is then iteratively improved. The distance between the vertex and the closest point of each tracklet is calculated. The tracklet with the largest distance is dropped and the vertex location recalculated. This is repeated until the farthest tracklet from the vertex is 300 mm, or there are fewer than three tracklets associated with the vertex. The number of associated MDT hits is taken to be the number of hits within MDT stations that have a center inside of a cone of $\Delta R = 0.6$ centered on the vertex location. The number of TGC hits are calculated the same way.

The number of associated MDT chambers is taken to be any of the chambers within the cone of $\Delta R = 0.6$ that have at least 25% occupancy. An example of the vertex reconstruction procedure in the endcap is shown in Figure 6.8 [144].

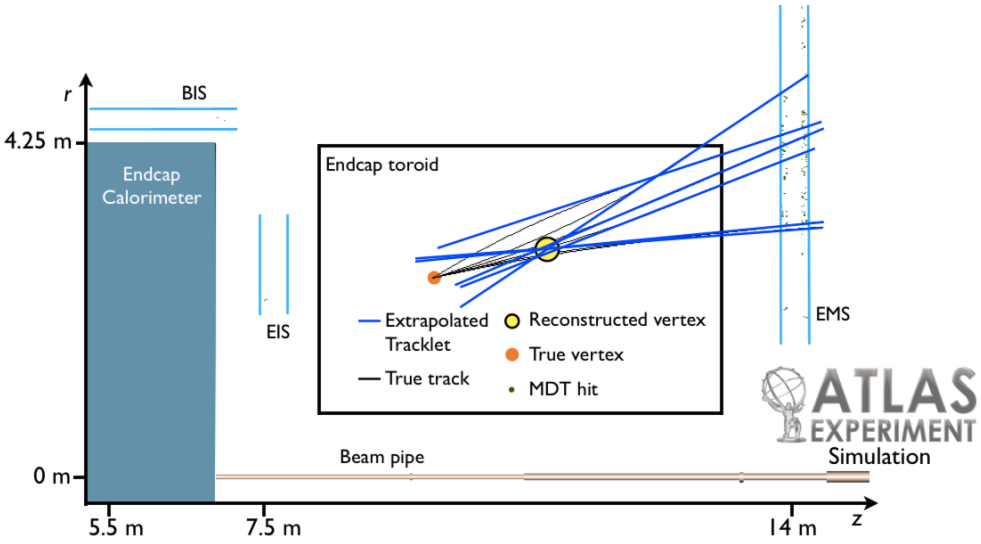

Figure 6.8: Simulated reconstruction of a vertex in the MS endcap region, illustrating the reconstruction technique in this region.

Chapter 7

MS Vertex Identification and Quality Criteria

The goal of this analysis is to identify the presence of a displaced decay of an LLP, making the reconstructed MS vertices discussed in Section 6.6.2 rather important physics objects. For this reason, it is necessary to guarantee that only the most well-modeled vertices are used. This includes separating the vertices reconstructed from signal events from those reconstructed from background processes. While this sort of event selection is typically handled at the event level, placing preselection criteria on the MS vertices is also employed to assure they match the expected signature. This chapter will discuss these selections, called the "Good Vertex Criteria" (GVC), along with other criteria applied to the MSVtx objects. Reconstruction efficiencies and other performance metrics are discussed.

7.1 MS Vertices in the Overlap Region ($0.7 < |\eta| < 1.3$)

As mentioned in Section 6.6.2, there are complications reconstructing an MS vertex near the MS overlap region owing to the use of separate algorithms in the barrel and endcap. For any LLP that decays in the overlap region, two issues arise. First, any MDT hits produced by the resulting shower would be split between the barrel and endcap MDT stations, meaning each reconstruction algorithm would see fewer hits. This decreases the chance that a vertex could even be reconstructed, making reconstruction in the overlap region less efficient than in the barrel or endcap regions. Second, if there are sufficient hits to produce enough tracklets to reconstruct a vertex, there is a chance that *both* algorithms could produce a vertex. Given that the reconstruction algorithms are optimized for reconstruction efficiency and not position accuracy, even though they both originated from the same true vertex it is unlikely

they'd be reconstructed in the same location. This position ambiguity makes duplicate removal, with the aim of using these events in an analysis, a rather complicated procedure to develop.

Figure 7.1(a) shows the normalized $|\eta|$ distribution of pairs of vertices that were matched using a cone of $\Delta R = 0.4$ to the same truth LLP. For some samples, this "double matching" occurs in as many as a quarter of all reconstructed vertices in the overlap region. However, the efficiency, shown in Figure 7.1(b), is low in this η region of $0.7 < |\eta| < 1.3$ compared to the barrel ($|\eta| < 0.7$) and endcap ($1.3 < |\eta| < 2.5$) regions. Of the small number of vertices that are reconstructed in the overlap region, out of all the vertices in the event, a significant fraction of them are duplicate vertices. This makes the overall vertex quality in this region rather low. To eliminate uncertainties introduced by attempting to select between duplicate vertices, any events with vertices reconstructed within this overlap region are removed.

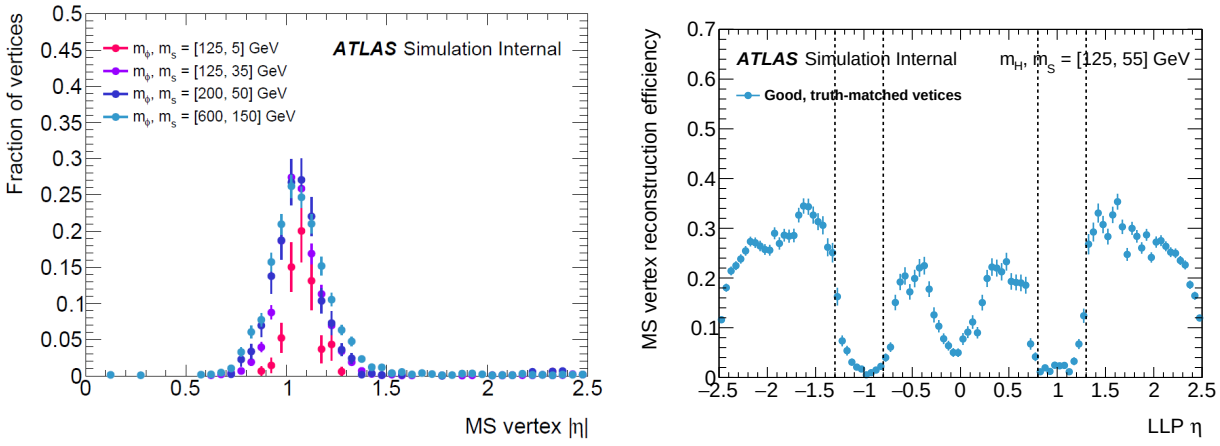

(a) **(b)**

Figure 7.1: (a) Fraction of MS vertices matched to an LLP that matches *two* good MS vertices, such as those produced by LLPs decaying close to the MS overlap region, for $H \to ss$ benchmark models with Higgs decays (H) to lighter LLPs (s). (b) The efficiency for reconstructing good MS vertices as a function of LLP η, for the SM $H \to ss$ sample with $m_H = 125\,\text{GeV}$ and $m_s = 55\,\text{GeV}$.

Additionally, studies using punch-through jets occurring in the crack region between the barrel and endcap portions of the hadronic calorimeter found that the probability of reconstructing a "bad" punch-through jet is higher than in the other regions. A "bad" punch-through jet is one that fails any of the following jet selection criteria: jet $p_{\text{T}} > 20\,\text{GeV}$, a "log-ratio" of $\log_{10}\left(E_{\text{Had}/E_{\text{EM}}}\right) < 0.5$, and a jet-vertex tagger (JVT) score > 0.59 if the

$p_{\mathrm{T}} < 60\,\mathrm{GeV}$. Jets failing this criteria are more likely to punch through the calorimeter and leave a signature in the MS. Since the HCal crack region ($0.7 < |\eta| < 1.2$) overlaps with the MS overlap region, and the vertex reconstruction efficiency is low within this region, events with vertices in the η range, $0.7 < |\eta| < 1.3$, are rejected.

7.2 Good Vertex Criteria

The vertex reconstruction algorithm will reconstruct a signature consistent with that of a displaced hadronic decay, regardless of whether it originated from a true signal event or was generated by a background process. In order to increase the acceptance for signal-produced vertices over background-produced vertices, a set of "Good Vertex Criteria" (GVC) were developed.

These selections were developed by comparing the acceptance of signal MC events against the acceptance of background events, with the selection being a compromise between maximizing signal acceptance versus maximizing background rejection. Additionally, to reduce the punch-through jet background entering the ABCD plane to very low levels, as discussed in Section 8.3.1, it was necessary to tighten some selection beyond what would have otherwise been optimal. Any vertices that pass all of the GVC are referred to as "good MS vertices" or an "MSVtx".

7.2.1 Number of Associated Hits

The number of MDT and RPC (TGC) hits associated with a barrel (endcap) MSVtx is an effective selection variable to reduce background contributions from both noise bursts and punch-through jets. Noise bursts are random electrical fluctuations that can occur in the MDT and trigger sub-detectors in the MS. Because they are random, they are typically not coherent between sub-detectors. By comparing the associated number of hits in the MDT with the associated number of hits in the trigger sub-detector (the RPC or TGC), it can be determined if a vertex was likely reconstructed from noise. This is done, in practice, by enforcing a minimum number of associated hits from both the MDTs and the trigger system for each vertex. The minimum thresholds applied to MS vertices are $N_{\mathrm{MDT}} > 300$

and $N_{\mathrm{RPC}}\,(N_{\mathrm{TGC}}) > 250$ for barrel (endcap) vertices. If a vertex fails to meet these minimum hit requirements, it is rejected.

An additional selection that can further reduce contamination from noise bursts is an upper threshold on the number of MDT hits. Typically, noise bursts will generate many hits within one MDT station that can be reconstructed as an MS vertex through combinatorics. If the number of trigger detector hits associated with one of these combinatorial vertices happened to pass the hit threshold, then the vertex would be accepted. To prevent this kind of background from being accepted, an upper threshold on the number of associated MDT hits is also applied: $N_{\mathrm{MDT}} < 3000$. This threshold is not determined by comparing signal and background acceptance, but was instead set high enough that all signal vertices were below the threshold. Distributions of signal acceptance and signal-to-background ratio for different thresholds of MDT and trigger detector hits are shown in Figures 7.2 and 7.3.

7.2.2 Vertex Isolation Criteria

The primary process that can generate fake vertices occurs when high-energy jets punch through the calorimeter and continue their shower into the MS. These jets will often leave enough of a signature in the calorimeter to be reconstructed as a jet. Additionally, if any of the showering particles are charged, they will also leave tracks in the inner detector. Displaced hadronic jets originating from decaying LLPs will will generate no track in the inner detector and deposit very little energy in the outer calorimeter because the LLP is uncharged. This means that none of the signal vertices should have aligned tracks or jets. A selection on the angular distance between the vertex and the nearest jet or track is effective in removing these background contributions.

Jet Isolation

A collection of anti-k_t EM topo jets, as described in Section 6.2, are the calibrated jets used to isolate the MS vertices. Applying selection criteria to the jet collection reduces the number of jets considered when performing the isolation, which has the effect of making the MS vertex isolation requirement "looser", or less restrictive. The inverse is also true. In considering the background contributions entering the ABCD plane, described in detail in

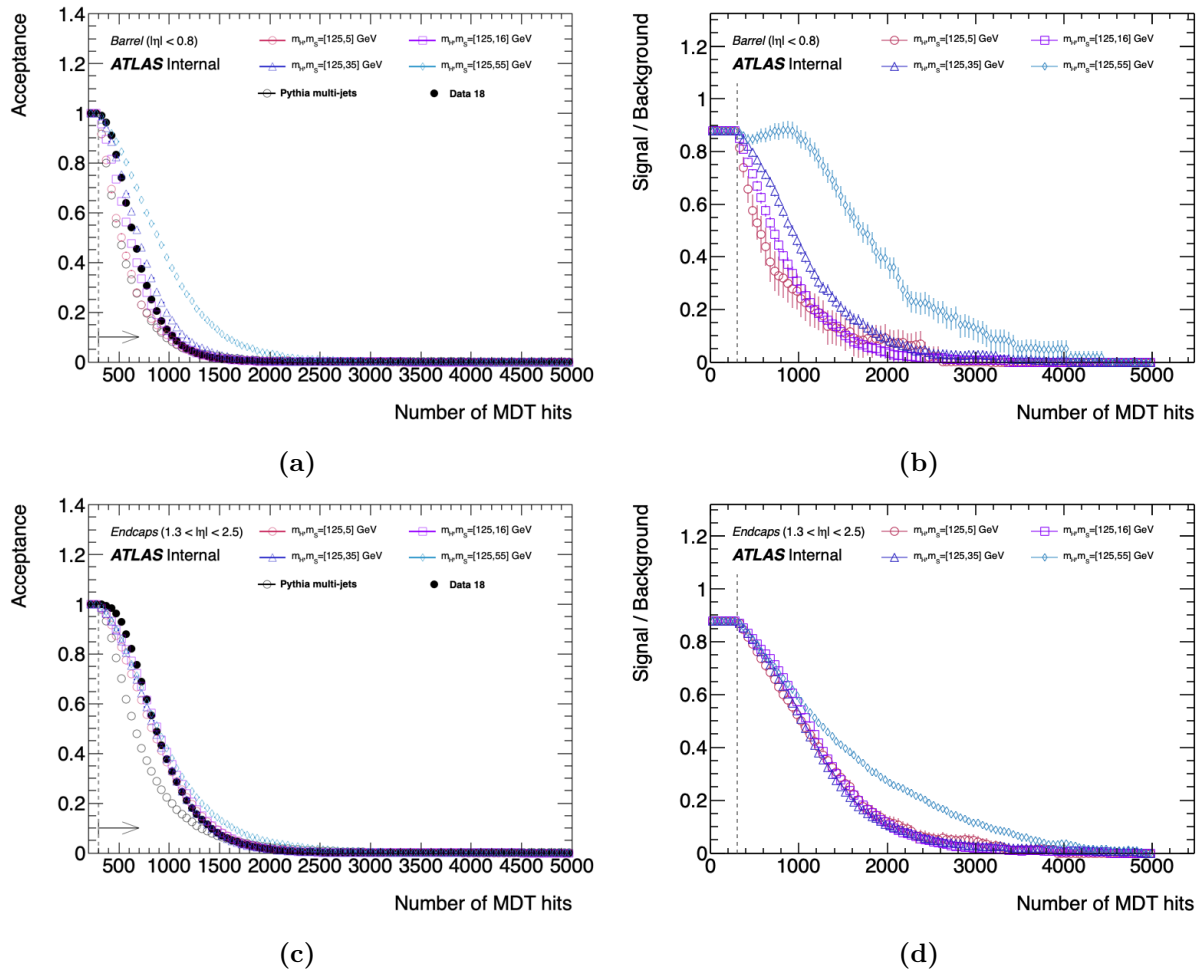

Figure 7.2: Acceptance and signal-to-background ratio for hit-based vertex selection criteria. The distributions with respect to the number of MDT hits are shown, separately, for both barrel and endcap vertices. Signal distributions from SM Higgs mass ($m_H = 125\,\text{GeV}$) $H \to ss$ MC samples are compared to simulated QCD multijet events and Run2 2018 data events. The threshold used in this analysis is indicated with a vertical line. An arrow indicates which region is accepted.

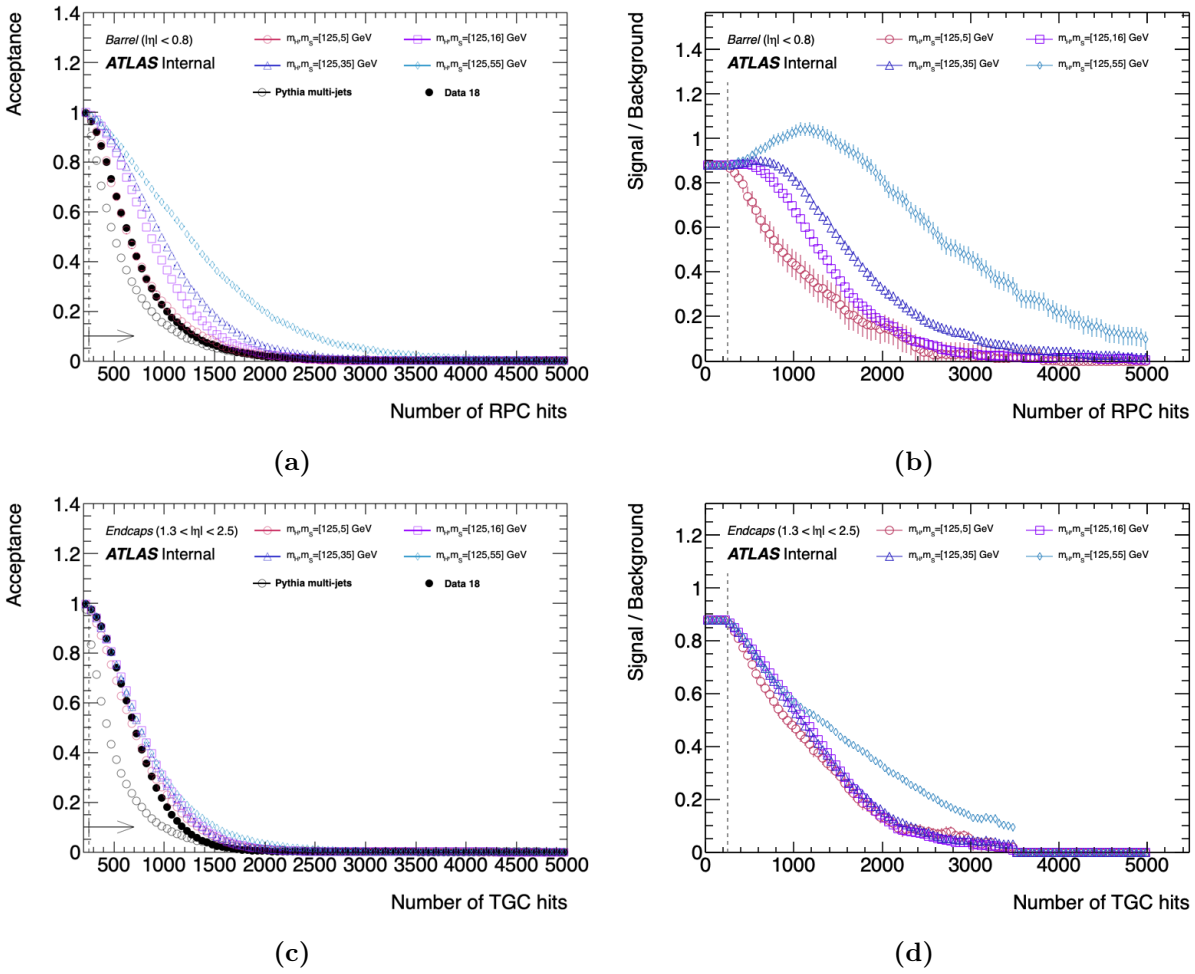

Figure 7.3: Acceptance and signal-to-background ratio for hit-based vertex selection criteria. The distributions with respect to the number of RPC and TGC hits are shown for barrel and endcap vertices, respectively. Signal distributions from SM Higgs mass ($m_H = 125\,\text{GeV}$) $H \to ss$ MC samples are compared to simulated QCD multijet events and Run2 2018 data events. The threshold used in this analysis is indicated with a vertical line. An arrow indicates which region is accepted.

Section 8.3.1, it was found that there were contributions from at least two distinct sources, one being punch-through jets. To reduce this contribution, the only jet selection criteria that was applied was jet $p_{\mathrm{T}} > 20\,\mathrm{GeV}$. If a jet passed this requirement, it was considered a "good" jet.

For each MS vertex, an *isolation cone* of 0.8 centered on the MS vertex is defined. If any good jet, as defined above, fell within this cone, the vertex was rejected. Figure 7.4 shows how the signal and background acceptance rates change, both with ΔR and with jet p_{T}. The selection threshold of both is indicated with a vertical line and an arrow that points toward the region of acceptance.

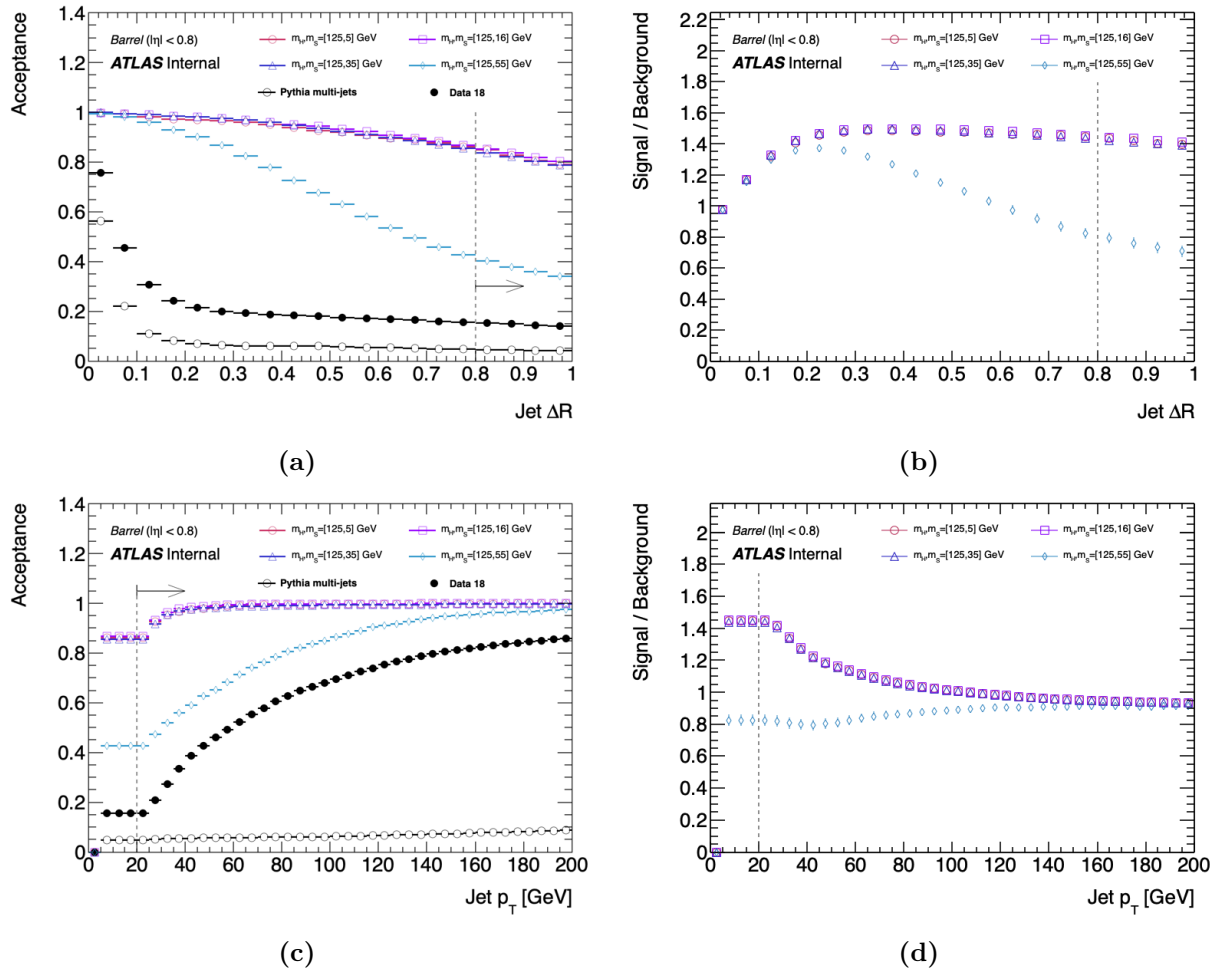

Figure 7.4: Acceptance and signal-to-background ratio shown for selecting vertices passing jet isolation criteria. The distributions with respect to the isolation cone ΔR and jet p_{T} threshold are shown. Signal distributions from SM Higgs mass ($m_H = 125\,\mathrm{GeV}$) $H \to ss$ MC samples are compared to simulated QCD multijet events and Run2 2018 data events. The threshold used in this analysis is indicated with a vertical line. An arrow indicates which region is accepted.

7.2.3 Track Isolation

Isolation criteria are also applied using inner detector tracks. In the event that a jet is poorly reconstructed or not reconstructed, which can occur, especially near the calorimeter crack region, there may be no jet to use in jet isolation. These poor quality jets may have associated inner detector tracks that point toward the vertex and can be used for MS vertex isolation.

High-energy tracks are defined as tracks with $p_{\mathrm{T}} > 5\,\mathrm{GeV}$. Isolation with respect to high-energy tracks is treated in a similar way to jets. An isolation cone of $\Delta R = 0.8$ and centered on the vertex is used for MS vertex isolation. If any track with a p_{T} greater than 5 GeV is found within this isolation cone, the MS vertex is rejected. Figure 7.5 shows the acceptance and signal-to-background ratio for different p_{T} thresholds of high-p_{T} tracks along with isolation cone sizes.

Regarding the algorithmic implementation of the jet and high-p_{T} track isolation criteria, since the MS vertex is rejected if *either* object is found within an isolation cone of $\Delta R = 0.8$, it is simpler to check for the closest jet *or* high-p_{T} track. For this reason, a single loop over all jets with $p_{\mathrm{T}} > 20\,\mathrm{GeV}$ and tracks with $p_{\mathrm{T}} > 5\,\mathrm{GeV}$ is used to find the closest *object*, and the MS vertex is rejected if that object is within the $\Delta R = 0.8$ cone. If either selection used a different ΔR cone, this simplification would not be possible.

If a jet were to form sufficiently promptly and hadronize to many constituent particles, there is a chance that a single high-p_{T} track is not reconstructed, but instead several low-p_{T} tracks are reconstructed. For this reason isolation is also performed with respect to high track *activity* within a small region around the MS vertex. Applying such a secondary isolation criteria assures that the Good Vertex Criteria are collinear safe.

This low-p_{T} track isolation looks at the magnitude of the vector sum of the track p_{T} within a cone of $\Delta R = 0.2$, centered on the MS vertex. If this sum of p_{T} is greater than 5 GeV, then the vertex is considered not to be isolated with respect to ID track activity and is rejected. Acceptance and signal-to-background ratios for different cone sizes and p_{T} thresholds can be seen in Figure 7.6. Vertical lines indicate the thresholds used in this analysis while arrows designate the region that is accepted.

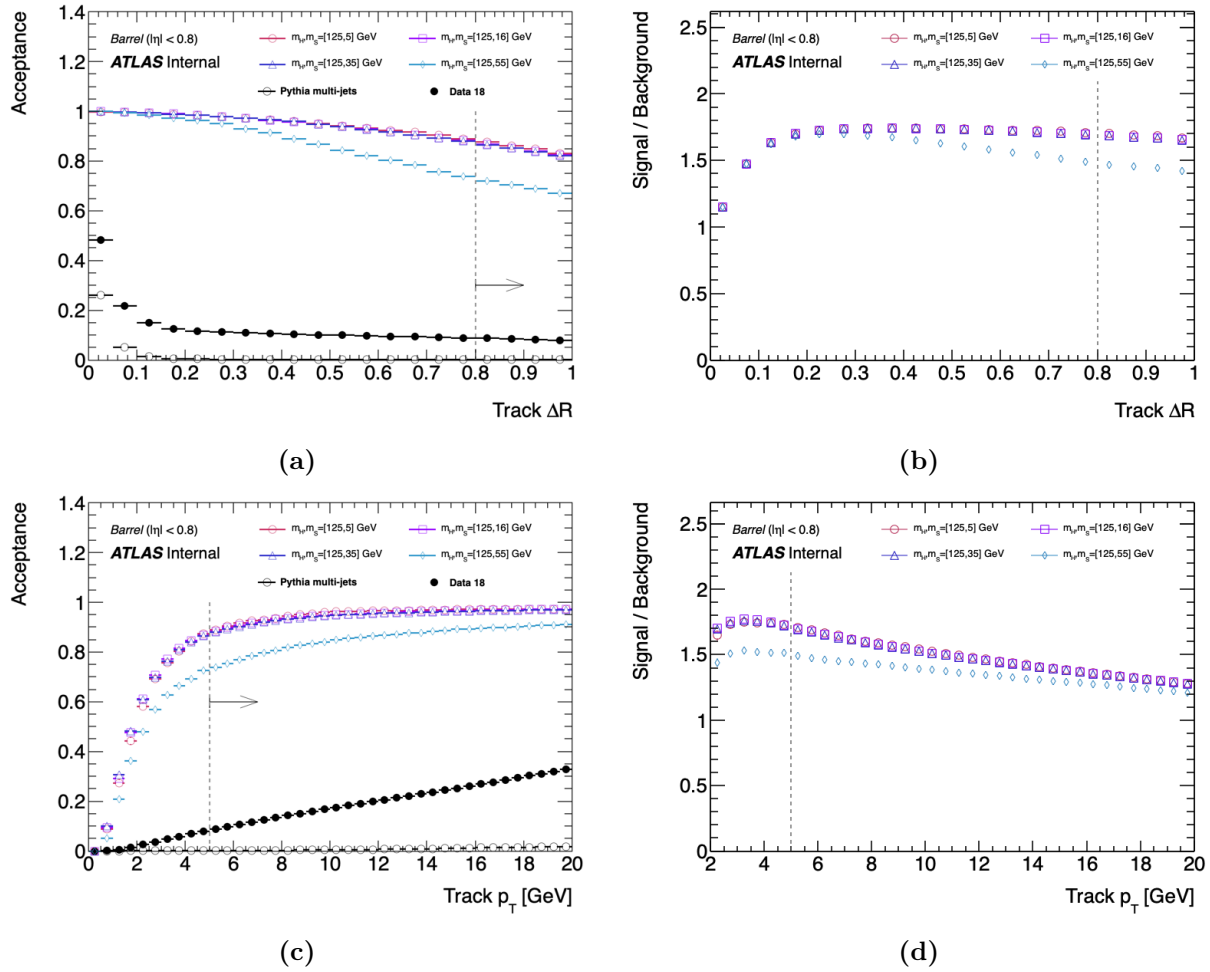

Figure 7.5: Acceptance and signal-to-background ratio shown for selecting vertices passing high-p_{T} track isolation criteria. The distributions with respect to the isolation cone ΔR and track p_{T} are shown. Signal distributions from SM Higgs mass ($m_H = 125\,\mathrm{GeV}$) $H \to ss$ MC samples are compared to simulated QCD multijet events and Run2 2018 data events. The threshold used in this analysis is indicated with a vertical line. An arrow indicates which region is accepted.

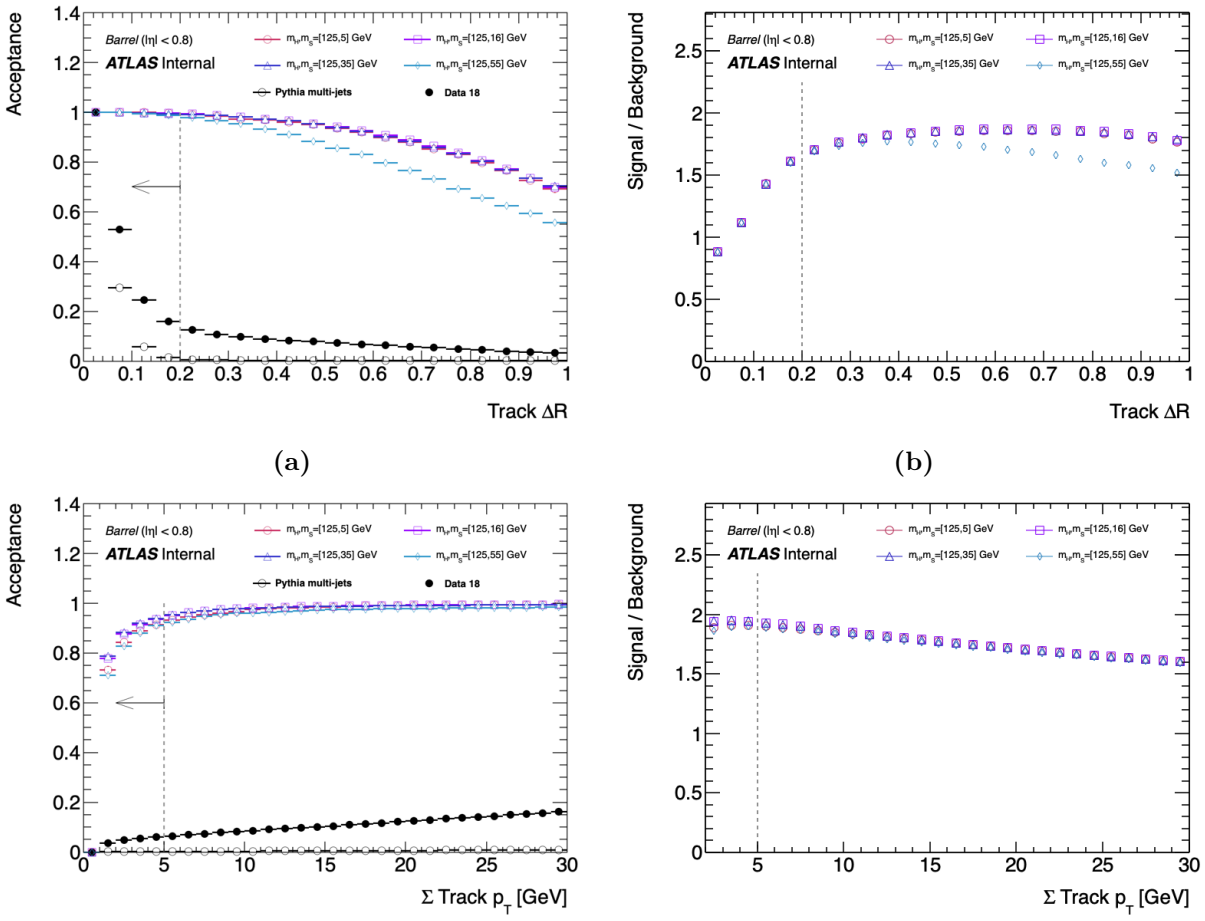

Figure 7.6: Acceptance and signal-to-background ratio shown for selecting vertices passing low-p_{T} track isolation criteria. The distributions with respect to the cone ΔR and sum of track p_{T} are shown. Signal distributions from SM Higgs mass ($m_H = 125\,\mathrm{GeV}$) $H \to ss$ MC samples are compared to simulated QCD multijet events and Run2 2018 data events. The values used in this analysis are indicated with a vertical line. In subfigure (a), the arrow indicates the region included in the p_{T} sum. In subfigure (c), the arrow indicates which region is accepted.

A summary of the GVC is shown in Table 7.1. Figure 7.7 shows the effect of the GVC on the MS vertex reconstruction efficiency at different locations L_{xy} (L_z) for barrel (endcap) vertices. A detailed description of the MS vertex reconstruction efficiency is provided in Section 7.3.1. Additional selection applied on the MS vertices is described in Section 8.2.

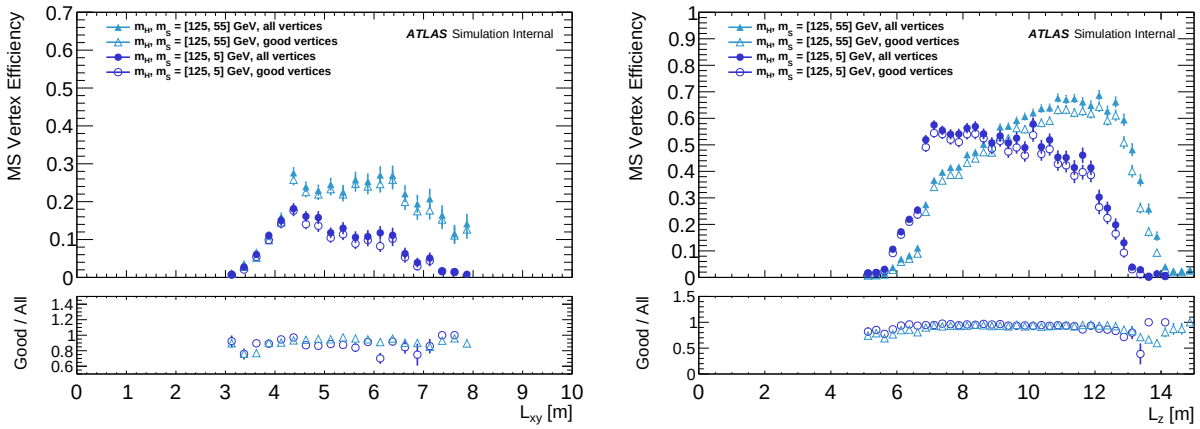

(a) **(b)**

Figure 7.7: The MS vertex reconstruction efficiency of vertices in the (a) barrel and (b) endcap, with and without the GVC applied. Distributions shown are for the lowest-mass scalar (m_S = 5 GeV) and highest mass scalar (m_S = 55 GeV) for signal MC samples with a SM Higgs mass (m_H = 125 GeV).

Requirement	Barrel	Endcap
RPC/TGC hits	$N_{\text{RPC}} \geq 250$	$N_{\text{TGC}} \geq 250$
MDT hits	$300 \leq Nn_{\text{MDT}} < 3000$	
Jet isolation $\left(p_T^{jet} > 20\,\text{GeV}\right)$	$\Delta R\,(\text{vtx}, \text{jet}) > 0.8$	
High-p_{T} track isolation $\left(p_T^{jet} > 5\,\text{GeV}\right)$	$\Delta R\,(\text{vtx}, \text{trk}) > 0.8$	
Low-p_{T} track isolation $(\Delta R\,(\text{vtx}, \text{trk}) > 0.2)$	$\left\lvert\sum_i^{\text{tracks}} \mathbf{p}_{\text{T}}^i\right\rvert < 5\,\text{GeV}$	

Table 7.1: Summary of the criteria used to identify "good" MS vertices, (Good Vertex Criteria). This represents the minimum quality criteria required for vertices used in this analysis.

7.3 Vertex Reconstruction Performance

To quantify the performance of the vertex reconstruction algorithm and the GVC, both the reconstruction efficiency and the reconstruction accuracy are considered. The reconstruction efficiency provides an understanding of how reliably the reconstruction procedure is able to

produce an MS vertex when one exists within the event. The reconstruction accuracy is a measure of how close the location of each reconstructed MS vertex is to the truth-level LLP decay location.

7.3.1 Vertex Reconstruction Efficiency

The MS vertex reconstruction efficiency is defined as the fraction of LLP decays that produce a good reconstructed MS vertex within the detector fiducial region.

$$\epsilon_{\text{vtx}} = \frac{N_{\text{passReco}}}{N_{\text{passTrig}}} \tag{7.1}$$

where ϵ_{vtx} is the reconstruction efficiency, N_{passTrig} is the number of events that fired the trigger, described in Section 5.3, and N_{passReco} is the number of events with a vertex that passed the GVC, the event selection described in Section 8.2, and fired the trigger. This efficiency is dependent on the decay location, and so is calculated as a function of L_{xy} (L_z) for barrel (endcap) vertices. These distributions are shown in Figure 7.8 below.

In Figure 7.8(a), most SM-like Higgs samples with LLP decays in the barrel region reach their peak efficiency ($\sim 10-20\%$) around the first MDT station ($\sim 4.5\,\text{m}$). The only exception is the sample with a scalar LLP mass of 55 GeV, which was generated with a longer LLP proper lifetime. The efficiency begins decreasing as the decay location approaches the second (middle) MDT station ($\sim 7-8\,\text{m}$), and drops to zero beyond the second station. The reason for this decrease in efficiency is due to any charged hadrons or photons (and the corresponding EM showers) not being sufficiently spatially separated to be reconstructed as separate tracklets in the vertex reconstruction algorithm. This leads to fewer reconstructed tracklets, which reduces the chance of reconstructing a good vertex. Any LLPs that decay at or before the edge of the HCal have a lower efficiency because some of the shower products are absorbed by the HCal and do not leave signatures in the MS.

For the SM-like Higgs mass samples with LLP decays in the endcap region, shown in Figure 7.8(b), the peak efficiency is much higher ($\sim 50-70\%$), though the peak occurs between the first and second MDT stations. The increased overall efficiency is due to the endcap tracklets being reconstructed as straight-line segments, which leads to a higher num-

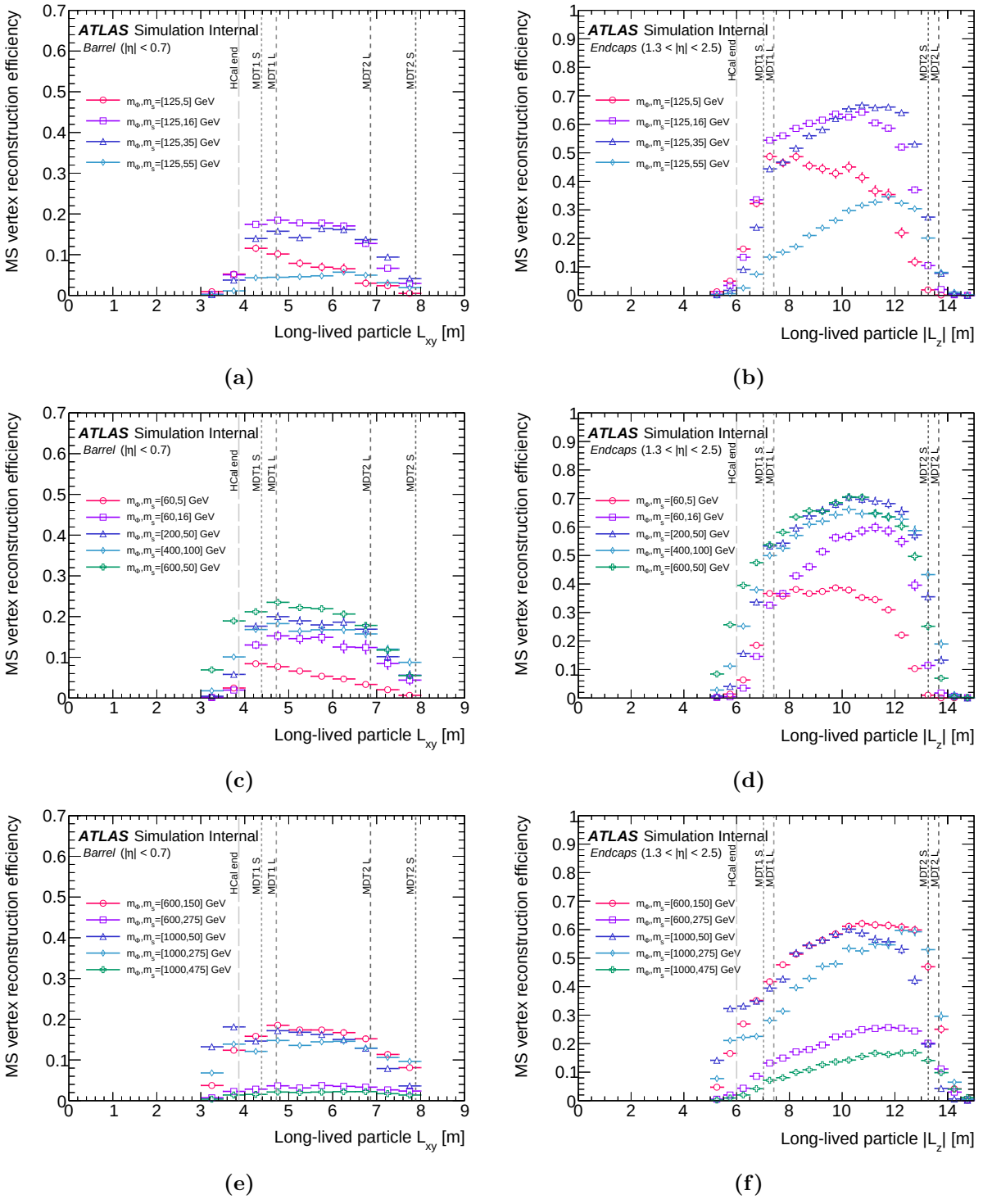

Figure 7.8: MS vertex reconstruction efficiencies calculated using truth signal MC $H \to ss$ samples for (a-b) SM-like Higgs mass benchmark samples, (c-f) non-SM Higgs mass benchmark samples. Plots on the left side are for MS vertices in the barrel region, while plots on the right are for endcap vertices. The dashed lines represent various detector boundaries and are labeled as such.

ber of reconstructed tracklets and, as a consequence, a higher likelihood of reconstructing a good vertex.

7.3.2 Vertex Reconstruction Residuals

As mentioned in Section 6.6.2, the vertex reconstruction algorithm was designed to maximize the reconstruction efficiency of vertices in the fiducial region over the reconstruction position accuracy. The vertex position uncertainty associated with this algorithm is given by the residual between the truth-level LLP decay location and the reconstructed MS vertex location. The residuals are calculated as a function of η, ϕ, R, and z. The residual distributions for each of the signal MC samples are shown in Figures 7.9–7.12.

The residuals from barrel and endcap vertices are shown separately and exhibit different behavior. This difference in the reconstruction accuracy is expected since different algorithms are employed in each region, as detailed in Section 6.6.2. One major difference is the presence of a double-peak in the z-residuals for the endcap vertices in a few of the samples (both SM and non-SM Higgs). This feature isn't present in any of the barrel residuals because it comes from a property of the endcap reconstruction. After the LLP decays, the magnetic field in the endcap toroid bends the trajectories of the charged decay particles while preserving the line-of-flight of the LLP. This leads to trajectories with a larger angle with respect to the beamline. When the MDT hits that the particle generates are reconstructed into tracklets, their trajectories are back-extrapolated through the magnetic field as straight lines. This will have the effect of systematically shifting reconstructed endcap vertices to higher $|z_{\text{reco}}|$ as compared to $|z_{\text{truth}}|$. This will only affect LLPs that decay early enough for charged decay products to be affected by the endcap magnetic field.

The resolution in η, ϕ, R, and z is taken to be the RMS of the normalized distributions for each sample. The normalized residual is defined as the residual divided by the truth value:

$$\begin{aligned} (\text{norm residual})_x = \bar{r}_x &= \frac{x_{\text{reco}} - x_{\text{truth}}}{x_{\text{truth}}} \\ \text{resolution}_x &= \sqrt{\frac{1}{n}\sum_i (r_x)_i^2} \end{aligned} \tag{7.2}$$

for each of the variables $x = \{\eta, \phi, R, z\}$. Tables summarizing these resolutions for each

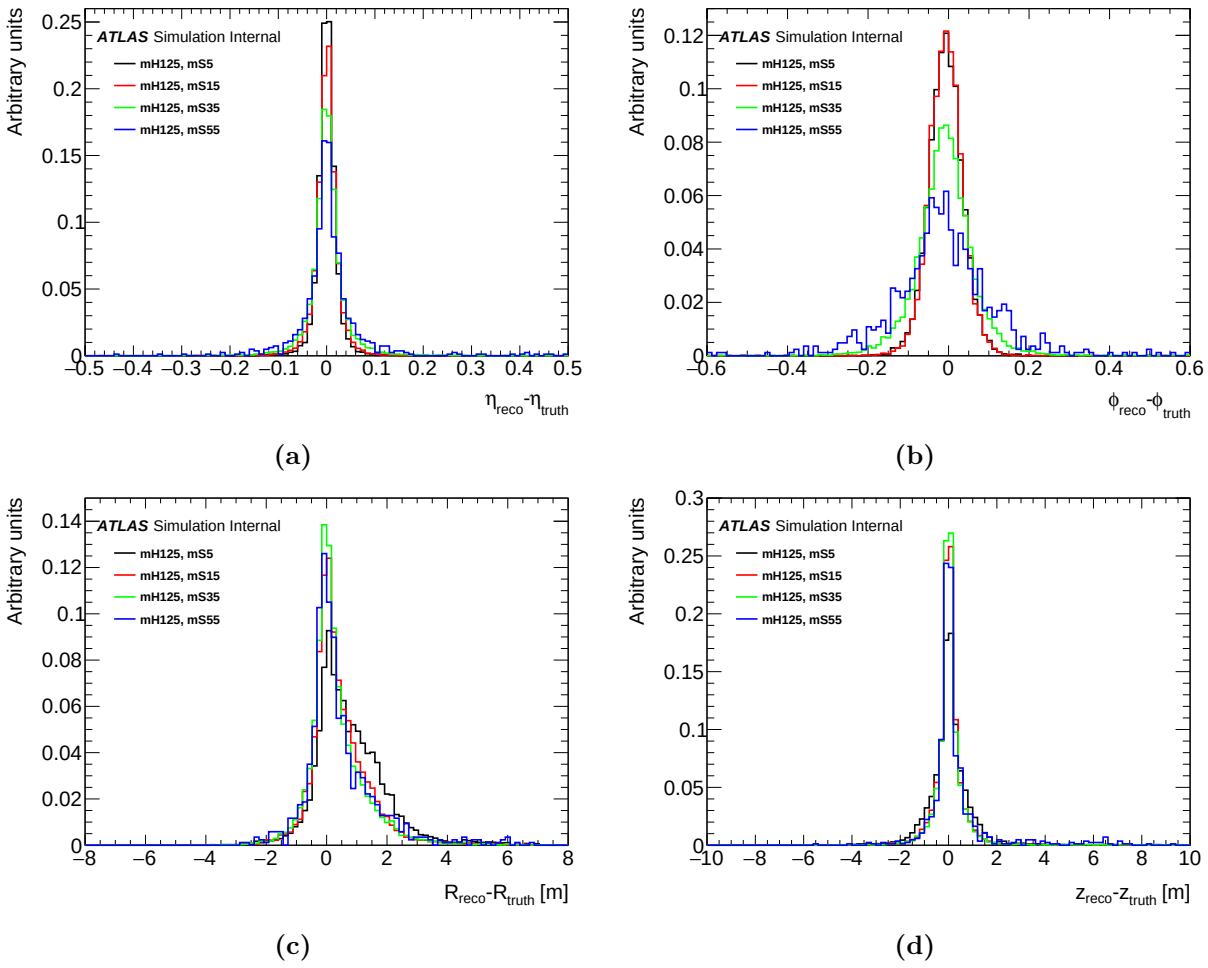

Figure 7.9: Residuals for barrel MS vertices in (a) η, (b) ϕ, (c) R, and (d) z coordinates for SM Higgs mass ($m_H = 125\,\text{GeV}$) samples.

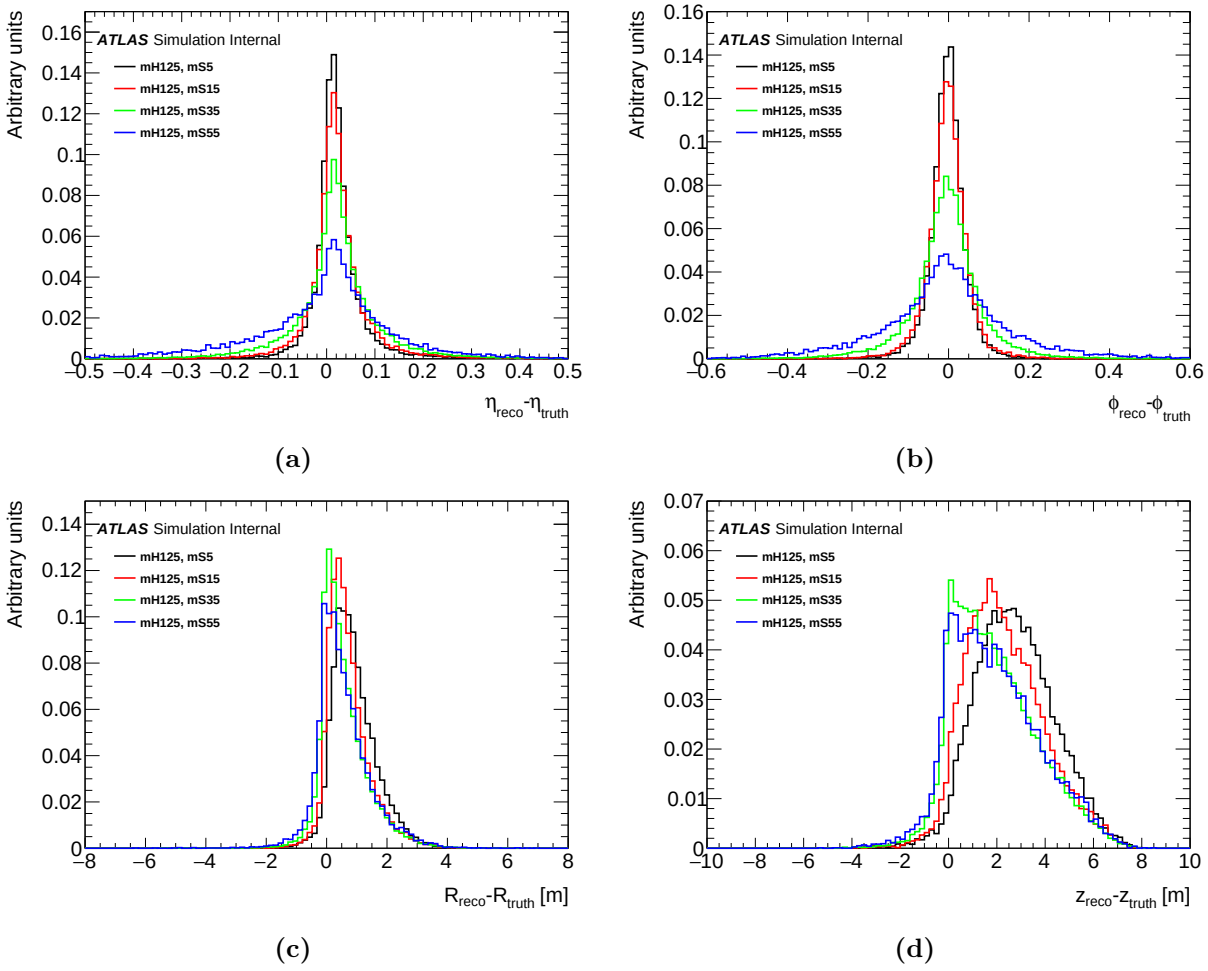

Figure 7.10: Residuals for endcap MS vertices in (a) η, (b) ϕ, (c) R, and (d) z coordinates for SM Higgs mass ($m_H = 125\,\text{GeV}$) samples.

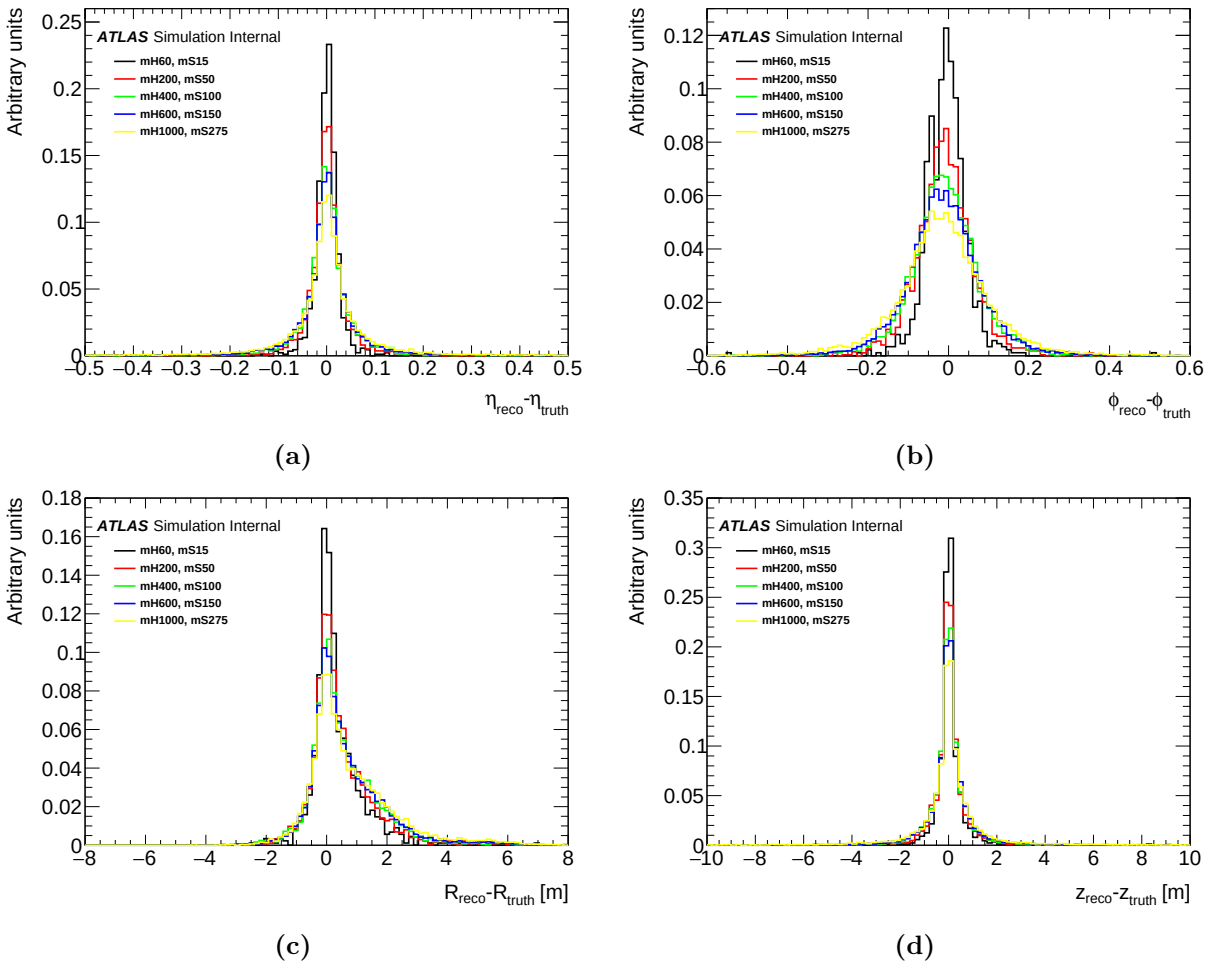

Figure 7.11: Residuals for barrel MS vertices in (a) η, (b) ϕ, (c) R, and (d) z coordinates for non-SM Higgs mass ($m_H \neq 125\,\text{GeV}$) samples.

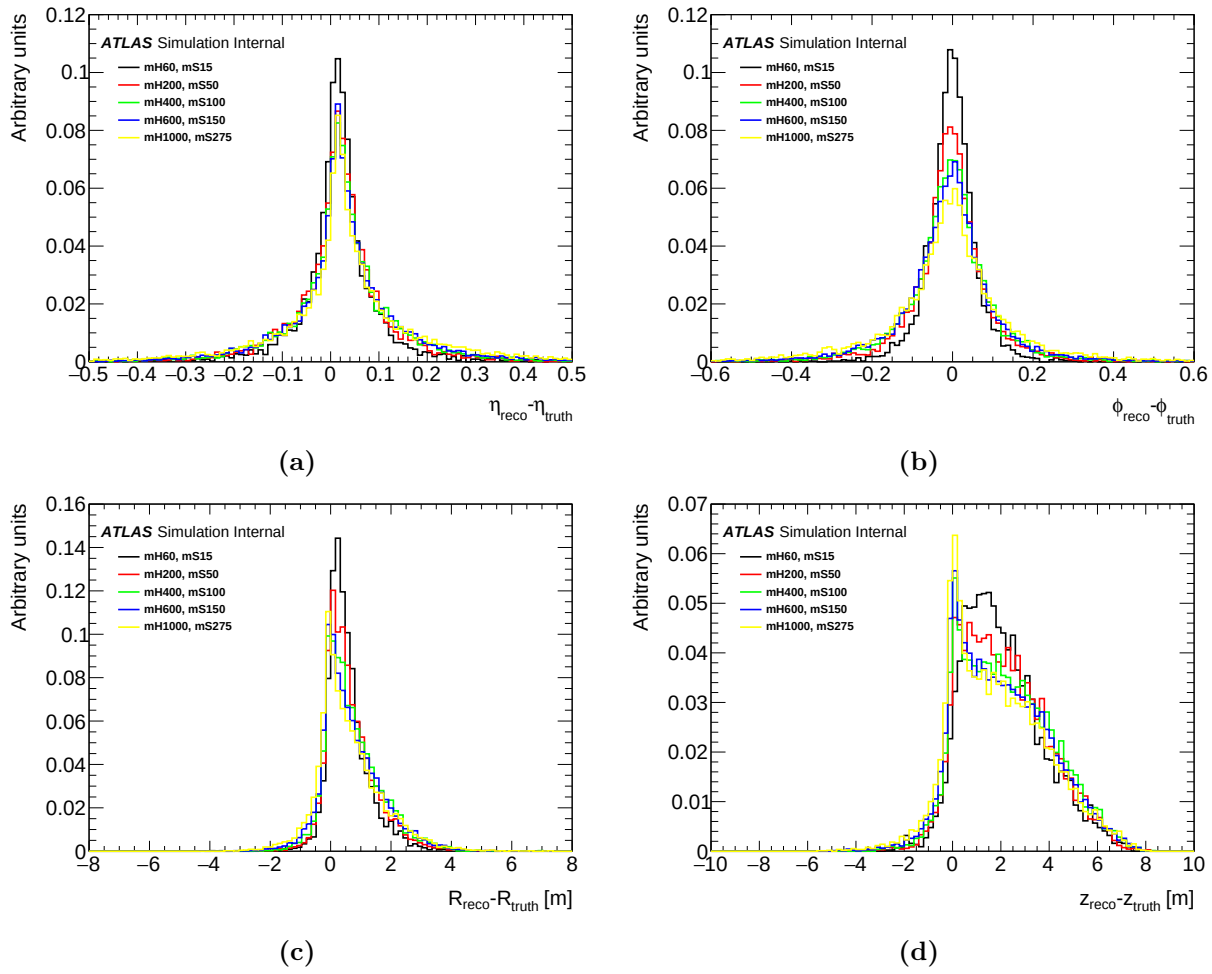

Figure 7.12: Residuals for endcap MS vertices in (a) η, (b) ϕ, (c) R, and (d) z coordinates for non-SM Higgs mass ($m_H \neq 125\,\text{GeV}$) samples.

$H \to ss$ signal sample can be seen in Tables 7.2–7.5.

Sample	η	ϕ	R	z
$m_H = 125\,\text{GeV}$, $m_s = 5\,\text{GeV}$	0.058	0.084	0.25	0.34
$m_H = 125\,\text{GeV}$, $m_s = 15\,\text{GeV}$	0.072	0.081	0.20	0.34
$m_H = 125\,\text{GeV}$, $m_s = 35\,\text{GeV}$	0.094	0.096	0.19	0.46
$m_H = 125\,\text{GeV}$, $m_s = 55\,\text{GeV}$	0.11	0.12	0.22	0.68

Table 7.2: Summary of coordinate resolutions for barrel region MS vertex reconstruction in SM Higgs samples.

Sample	η	ϕ	R	z
$m_H = 125\,\text{GeV}$, $m_s = 5\,\text{GeV}$	0.033	0.072	0.28	0.25
$m_H = 125\,\text{GeV}$, $m_s = 15\,\text{GeV}$	0.037	0.076	0.27	0.24
$m_H = 125\,\text{GeV}$, $m_s = 35\,\text{GeV}$	0.050	0.10	0.31	0.24
$m_H = 125\,\text{GeV}$, $m_s = 55\,\text{GeV}$	0.072	0.14	0.41	0.24

Table 7.3: Summary of coordinate resolutions for endcap region MS vertex reconstruction in SM Higgs samples.

Sample	η	ϕ	R	z
$m_H = 60\,\text{GeV}$, $m_s = 15\,\text{GeV}$	0.071	0.081	0.18	0.30
$m_H = 200\,\text{GeV}$, $m_s = 50\,\text{GeV}$	0.10	0.099	0.23	0.57
$m_H = 400\,\text{GeV}$, $m_s = 100\,\text{GeV}$	0.12	0.10	0.25	0.70
$m_H = 600\,\text{GeV}$, $m_s = 150\,\text{GeV}$	0.13	0.11	0.28	0.80
$m_H = 1000\,\text{GeV}$, $m_s = 275\,\text{GeV}$	0.14	0.12	0.32	1.03

Table 7.4: Summary of coordinate resolutions for barrel region MS vertex reconstruction in non-SM Higgs samples.

Sample	η	ϕ	R	z
$m_H = 60\,\text{GeV}$, $m_s = 15\,\text{GeV}$	0.043	0.083	0.30	0.23
$m_H = 200\,\text{GeV}$, $m_s = 50\,\text{GeV}$	0.055	0.10	0.33	0.26
$m_H = 400\,\text{GeV}$, $m_s = 100\,\text{GeV}$	0.066	0.11	0.37	0.29
$m_H = 600\,\text{GeV}$, $m_s = 150\,\text{GeV}$	0.073	0.12	0.39	0.30
$m_H = 1000\,\text{GeV}$, $m_s = 275\,\text{GeV}$	0.093	0.13	0.45	0.33

Table 7.5: Summary of coordinate resolutions for endcap region MS vertex reconstruction in non-SM Higgs samples.

7.4 Vertex Mismodeling Scale Factor

It is possible for the vertex reconstruction to behave differently in signal MC than in data due to the MC simulation mismodeling of certain physics processes, such as punch-through jets. To quantify the significance of this potential mismodeling, a comparison was made between the number of MS tracklets reconstructed from punch-through jets in data versus QCD multijet MC samples.

Events used in this study were required to pass both the `HLT_j400` and `HLT_j420` jet triggers. Additionally, only the leading and subleading jets, in terms of jet p_{T}, were considered. The jets had to have a $p_{\mathrm{T}} > 30\,\mathrm{GeV}$, a "log-ratio" of $\log_{10}(E_{\mathrm{Had}}/E_{\mathrm{EM}}) < 0.5$, and a jet-vertex tagger (JVT) score > 0.59 if the jet $p_{\mathrm{T}} < 60\,\mathrm{GeV}$. The "log-ratio" represents the relative energy deposited in the HCal versus the ECal, with a smaller value representing a larger fraction of energy being deposited in the ECal. In order for the passing jet to be considered a punch-through jet, it was also required to have more than 50 muon segments within a cone of $\Delta R = 0.4$.

Figure 7.13 shows the distribution of punch-through jets with a given number of tracklets with a ΔR cone of 0.4 of the punch-through jet. The ratio of the number of punch-through jets in data divided by the number in QCD multijet events is used as a scale factor on the number of tracklets. This ratio is calculated by taking the integral of the normalized distributions of punch-through jets above the cut on the minimum number of tracklets ($N_{\mathrm{tracklets}} \geq 3\,(4)$ for barrel (endcap) MS vertices) in data and QCD multijet MC. This scale factor on the number of tracklets in a punch-through jet cone is 0.80 ± 0.01 in the barrel region and 0.75 ± 0.01 in the endcap regions. This ratio provides a measure of how many more tracklets are reconstructed in the MC samples than in the data.

In order to correct the vertex reconstruction in MC events, these tracklet scale factors were used to randomly drop a proportional fraction of the tracklets used during the clustering step of the vertex reconstruction. The result is that, average over all barrel vertices, 20% of reconstructed tracklets were dropped during the vertex reconstruction and, when averaged over endcap vertices, 25% of tracklets were dropped. This reduction in tracklet multiplicity leads to a reduced vertex reconstruction efficiency. A comparison of this reduced efficiency

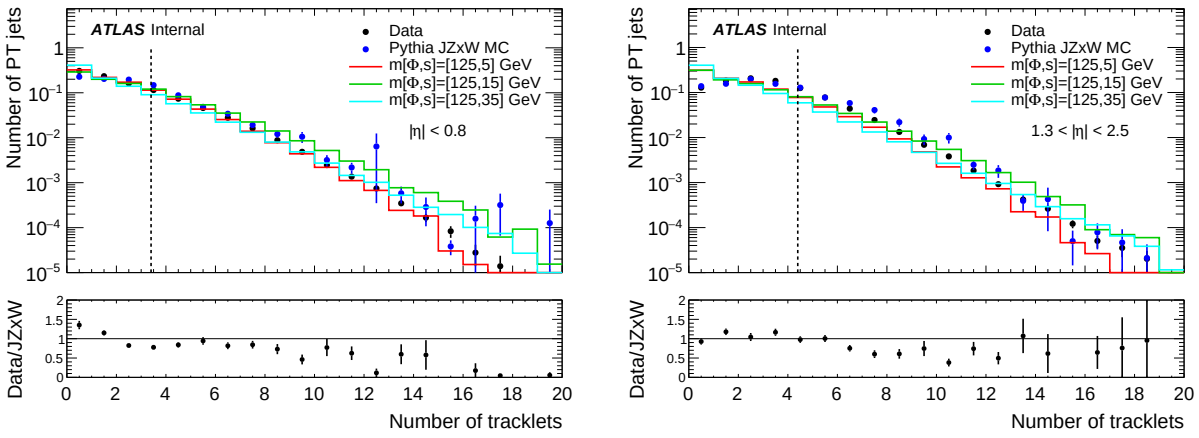

(a) (b)

Figure 7.13: Distribution of the number of tracklets within a $\Delta R = 0.4$ cone of the punch-through jet axis for the (a) barrel and (b) endcap regions. The black dots correspond to the full Run2 (2015-2018) data, the blue dots correspond to the multijet MC simulations, and the solid lines show benchmark $H \to ss$ signal MC samples. The vertical dotted lines indicate the $N_{\text{tracklets}}$ selection applied during vertex reconstruction.

compared with the nominal efficiency is shown separately for barrel and endcap vertices in Figures 7.14 and 7.15 for the $H \to ss$ benchmark samples. The ratio of the reduced efficiency to the nominal efficiency is taken as the reconstruction efficiency scale factor for that sample. Summary tables of the reduced reconstruction efficiency, and the associated scale factor, are shown in Tables 7.6–7.9. For simplicity, the final scale factor applied to the reconstruction efficiency of all signal MC samples is the average scale factor across all samples. The average scale factor is 0.73 for barrel vertices and 0.91 for endcap vertices.

A separate method of applying the tracklet mismodeling is to reweight the MC distribution to match the data distribution, bin-by-bin. This weight is then applied to each tracklet and then applied to each vertex according to the number of associated tracklets. The final reconstruction scale factor can then be derived by comparing the reconstruction efficiency calculated using the weighted vertices versus that calculated using the unweighted vertices.

The difference in the scale factor between the two methods is taken as the uncertainty in the scale factor, which is 8% in the barrel and 12% in the endcaps.

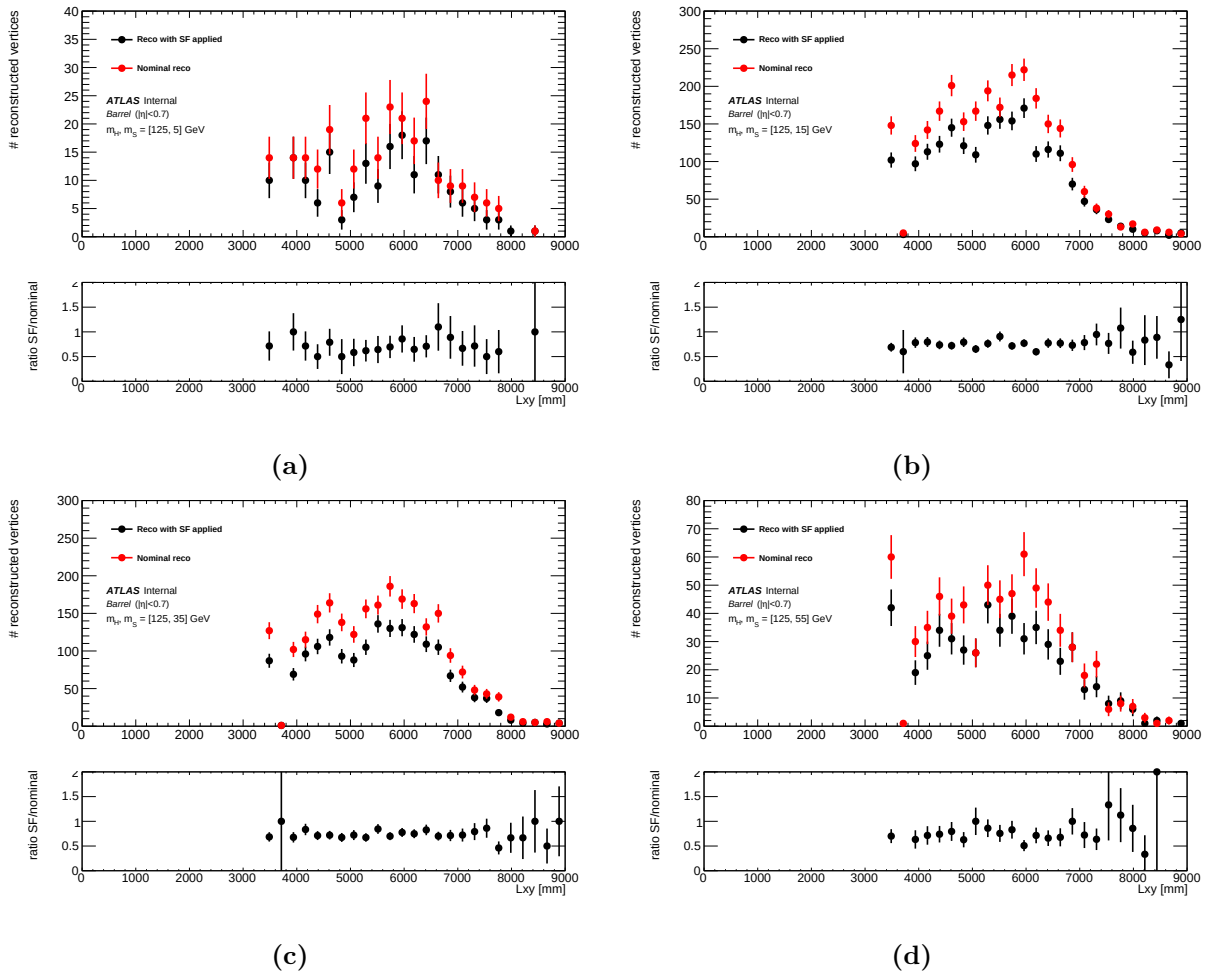

Figure 7.14: Vertex reconstruction efficiency for barrel MS vertices before (red) and after (black) the vertex scale factor is applied for SM $H \to ss$ benchmark samples.

Sample $m_H = 125\,\text{GeV}$	Nominal Reconstruction $[N_{\text{vtx}}]$	Reconstruction with Dropped Tracklets $[N_{\text{vtx}}]$	Efficiency Loss
$m_s = 5\,\text{GeV}$	266	193	27.4%
$m_s = 15\,\text{GeV}$	2723	2047	24.8%
$m_s = 35\,\text{GeV}$	2414	1765	26.9%
$m_s = 55\,\text{GeV}$	720	531	26.3%

Table 7.6: Summary of change in barrel MS vertex reconstruction efficiency between nominal reconstruction and reconstruction with the vertex scale factor applied for SM $H \to ss$ MC samples.

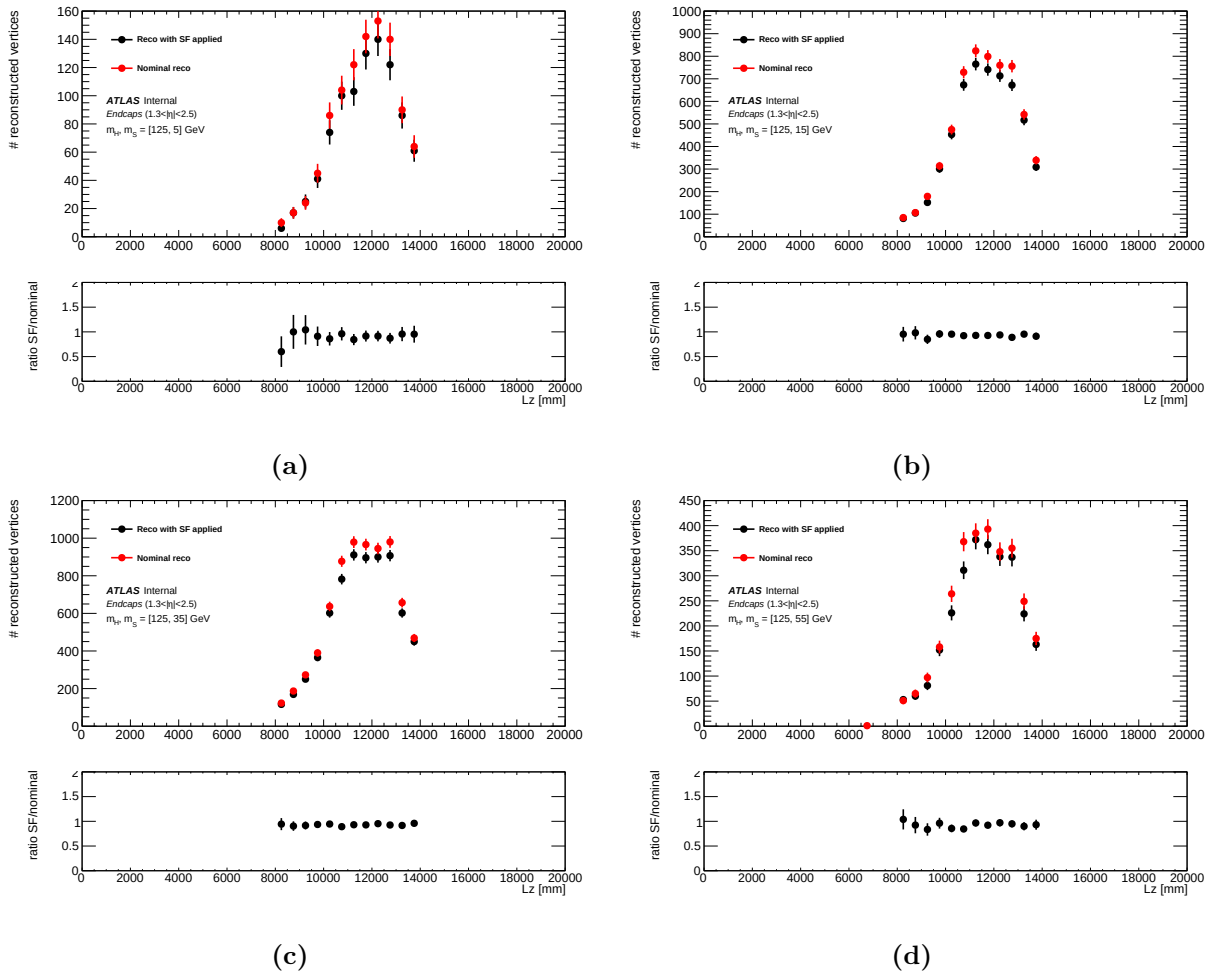

Figure 7.15: Vertex reconstruction efficiency for endcap MS vertices before (red) and after (black) the vertex scale factor is applied for SM $H \to ss$ benchmark samples.

Sample $m_H = 125\,\text{GeV}$	Nominal Reconstruction $[N_{\text{vtx}}]$	Reconstruction with Dropped Tracklets $[N_{\text{vtx}}]$	Efficiency Loss
$m_s = 5\,\text{GeV}$	2072	1864	10.0%
$m_s = 15\,\text{GeV}$	11887	11031	7.2%
$m_s = 35\,\text{GeV}$	15224	14118	7.3%
$m_s = 55\,\text{GeV}$	5982	5525	7.6%

Table 7.7: Summary of change in endcap MS vertex reconstruction efficiency between nominal reconstruction and reconstruction with the vertex scale factor applied for SM $H \to ss$ MC samples.

m_H [GeV]	m_s[GeV]	Nominal Reconstruction [N_{vtx}]	Reconstruction with Dropped Tracklets [N_{vtx}]	Efficiency Loss
60	5	1921	1403	27.0%
	15	1417	1085	23.4%
200	50	3481	2617	24.8%
400	100	6536	4463	31.7%
600	50	17060	12943	24.1%
	150	11254	7736	31.3%
1000	50	10414	7144	28.7%
	275	15598	11546	26.0%
	475	3077	2071	32.7%

Table 7.8: Summary of change in barrel MS vertex reconstruction efficiency between nominal reconstruction and reconstruction with the vertex scale factor applied for non-SM $H \to ss$ MC samples.

m_H [GeV]	m_s[GeV]	Nominal Reconstruction [N_{vtx}]	Reconstruction with Dropped Tracklets [N_{vtx}]	Efficiency Loss
60	5	20440	18162	11.1%
	15	12104	11085	8.4%
200	50	17408	16218	6.8%
400	100	20690	18002	13.0%
600	50	29403	27765	5.6%
	150	25759	22333	13.3%
1000	50	12996	12001	7.7%
	275	26006	24194	7.0%
	475	28078	23805	15.2%

Table 7.9: Summary of change in endcap MS vertex reconstruction efficiency between nominal reconstruction and reconstruction with the vertex scale factor applied for non-SM $H \to ss$ MC samples.

Chapter 8

Single Vertex Search

8.1 Overview

The goal of this analysis is to discover long-lived particles of the type predicted by the BSM models discussed in Sections 2.2.1 and 2.2.2. If no evidence is found, then limits are set on the maximum possible cross section for this process that would be consistent with a non-observation given the amount of data collected. The signature of the BSM models considered is the production of two long-lived particles (LLPs), one or more of which decay into hadronic jets that are detected in the Muon Spectrometer (MS). Though an $H \to ss$ Hidden Sector model and an $H \to \chi\chi$ Baryogenesis model are used at benchmark models in this analysis, this common signature of displaced hadronic jets in the MS is shared with other LLP models, meaning the search would also be sensitive to these other BSM processes.

SM particles, save for neutrinos, will produce some kind of detector response that can be measured since all SM particles should either decay within the detector fiducial volume or otherwise interact with the active detector regions. A SM decay resulting in a hadronic jet with an origin close to the inner edge of the MS would not occur without some other activity in the calorimeter or inner detector (ID). The MS is not equipped to measure jet activity in the same way as the calorimetry system. To compensate for this, a dedicated reconstruction algorithm for MS tracks, designed to operate in a high-multiplicity detector environment, was developed. This reconstruction algorithm is described in Chapter 6. This algorithm attempts to reconstruct the vertex at which the LLP decay occurred by using the MS tracks generated by the hadronic jet. These displaced MS vertices (MSVtx) are the primary reconstructed objects this analysis uses.

A previous search investigated the case where both LLPs produced displaced hadronic jets [83]. This search specifically targets a signature where one LLP produces a displaced jet in the MS while the other decays before or after the MS. A requirement is made that each event considered must contain a single, good MSVtx that passes the MSVtx quality criteria described in Chapter 7. Even with this criteria, this signature can still be faked by several sources of background:

- **Punch-Through (PT) Jets** - The primary source of background comes from high-p_{T} jets that fail reconstruction in the calorimeter that leave a shower of tracks in the MS and whose showers are not contained by the calorimeters. Jets can also punch-through the overlap region of the calorimeter and induce showers on the edge of the barrel and endcap regions that could be reconstructed as displaced vertices.

- **Beam Halo** - Muons and other particles generated by proton collisions between beam halo protons and portions of the detector can be reconstructed as high-η displaced vertices in the endcap regions [149].

- **Cosmic Ray Muons** - Muons from cosmic rays can enter from the top of the detector, leaving MDT hits in the MS which may contribute to the reconstruction of an isolated fake vertex [149].

- **MS Noise Bursts** - Since the vertex reconstruction relies on combinations of tracks in the MS, if there are sufficient noise bursts in the MDTs and trigger systems, fake vertices can be created purely through combinatorics.

Because jets that punch through the calorimeter are not well-modeled in MC, a data-driven background strategy is used to estimate contributions from QCD. Non-collision Background (NCB), like cosmics and beam halo, are estimated using the Late Stream data. Noise burst contributions to background are mitigated using an upper limit on the number of MDT hits. Details of these techniques are explained in Section 8.3

8.2 Cutflow

In addition to requiring a single MSVtx to be reconstructed in the event, additional selection criteria are applied to maximize the number of signal events versus background events. All selection criteria are given in Table 8.2. These selection criteria define the signal region (SR) for this analysis. The selection on $H_{\mathrm{T}}^{\mathrm{miss}}$, which is defined in Section 6.4, is reversed to define a validation region (VR) in which the selection criteria were tested and validated. An example of the fraction of events passing each selection is given in Figure 8.7 for one of the $m_H = 125\,\mathrm{GeV}$ samples.

ATLAS Standard Cleaning Selection	
Selection	Description
isCompleteEvent	Flag indicating that the event was a complete event
isGoodLAr	Flag is true if LAr system was working properly
isGoodSCT	Flag is true if SCT system was working properly
isGoodTile	Flag is true if Tile Calo system was working properly
hasGoodPV	Flag is true if a well-reconstructed primary vertex exists

Table 8.1: All standard ATLAS event cleaning criteria.

The ATLAS event cleaning selections are applied to remove events that were recorded when a part of the detector was not operating normally. If the LAr system, SCT system in the inner detector, or the tile calorimeter were experiencing problems, then the event would be missing information and shouldn't be included in any analysis. For this reason, the ATLAS cleaning selection requires each flag in Table 8.1 to be true in order to accept the event.

All of the events considered in this analysis also must pass the `HLT_j30_muvtx_noiso` trigger. The details of this trigger are discussed in Section 5.3.

Selection thresholds were chosen to maximize the signal selection efficiency while minimizing the background selection efficiency. Figures 8.1–8.6 show properties of the MSVtx compared to data. The only selection applied in these figures is the requirement that each event have only one MSVtx.

The selection on the number of RPC and TGC hits for MS vertices in the barrel and

Region		Selection Criteria
All		Event passes `HLT_j30_muvtx_noiso` trigger Event passes event cleaning criteria [Table 8.1] Event has exactly one MSVtx MSVtx has $300 <$ nMDT hits < 3000 MSVtx is matched to the triggering muon RoI cluster (ΔR(MSVtx,cluster)< 0.4) MSVtx jet isolation (ΔR_{min} (MSVtx, jet with $p_{\text{T}} > 20\,\text{GeV}$) > 0.8) MSVtx track isolation (ΔR_{min} (MSVtx, track with $p_{\text{T}} > 5\,\text{GeV}$) > 0.8) Low p_{T} track isolation ($\lvert\sum_{\Delta R^{\text{cone}}}\rvert < 5\,\text{GeV}$ in 0.2 cone centered on MSVtx) Event has $E_{\text{T}}^{\text{miss}} > 20\,\text{GeV}$
	SR	Event has $H_{\text{T}}^{\text{miss}} > 40\,\text{GeV}$
	VR	Event has $H_{\text{T}}^{\text{miss}} < 40\,\text{GeV}$
Barrel		$\lvert\eta_{\text{MSVtx}}\rvert < 0.7$ $3000 < L_{xy}^{\text{MSVtx}} < 8000\,\text{mm}$ nRPC hits > 800 Number of muon segments in the outer MDT station (nBOL) > 15 NN1(barrel) > 0.5, NN2(barrel) > 0.5
Endcap		$1.3 < \lvert\eta_{\text{MSVtx}}\rvert < 2.5$ $L_{xy}^{\text{MSVtx}} < 10\,000\,\text{mm}$ and $5000 < \lvert L_{xy}^{\text{MSVtx}}\rvert < 15\,000\,\text{mm}$ nTGC hits > 900 Number of muon segments in the outer MDT station (nEOL) > 30 NN1(endcap) > 0.8, NN2(endcap) > 0.8

Table 8.2: All selection applied on events used in this analysis. Good Vertex Criteria (GVC) have been included explicitly. ATLAS standard cleaning selection are included by reference. The $H_{\text{T}}^{\text{miss}}$ selection used to define the signal region and validation region are indicated.

endcap regions, respectively, were informed by comparisons with late stream data, which is described in Section 4.1.1. Comparisons between the number of hits associated with the MSVtx between some of the $H \to ss$ signal MC samples and the late stream data are shown in Figures 8.1(a) and 8.1(b).

Figures 8.1(c) and 8.1(d) show comparisons between the $H \to ss$ signal MC samples and late stream data for the number of events in bins of the number of muon segments (MSeg) in the barrel outer (BO) MDT stations and the endcaps outer (EO) MDT stations, respectively. In order to suppress the non-collision background (NCB) represented in the late stream samples from entering the ABCD plane, tight selection was applied on these variables. The thresholds of nMSegBO > 15 and nMSegEO > 30 provide a considerable

amount of NCB removal, though at the cost of removing a fair amount of signal.

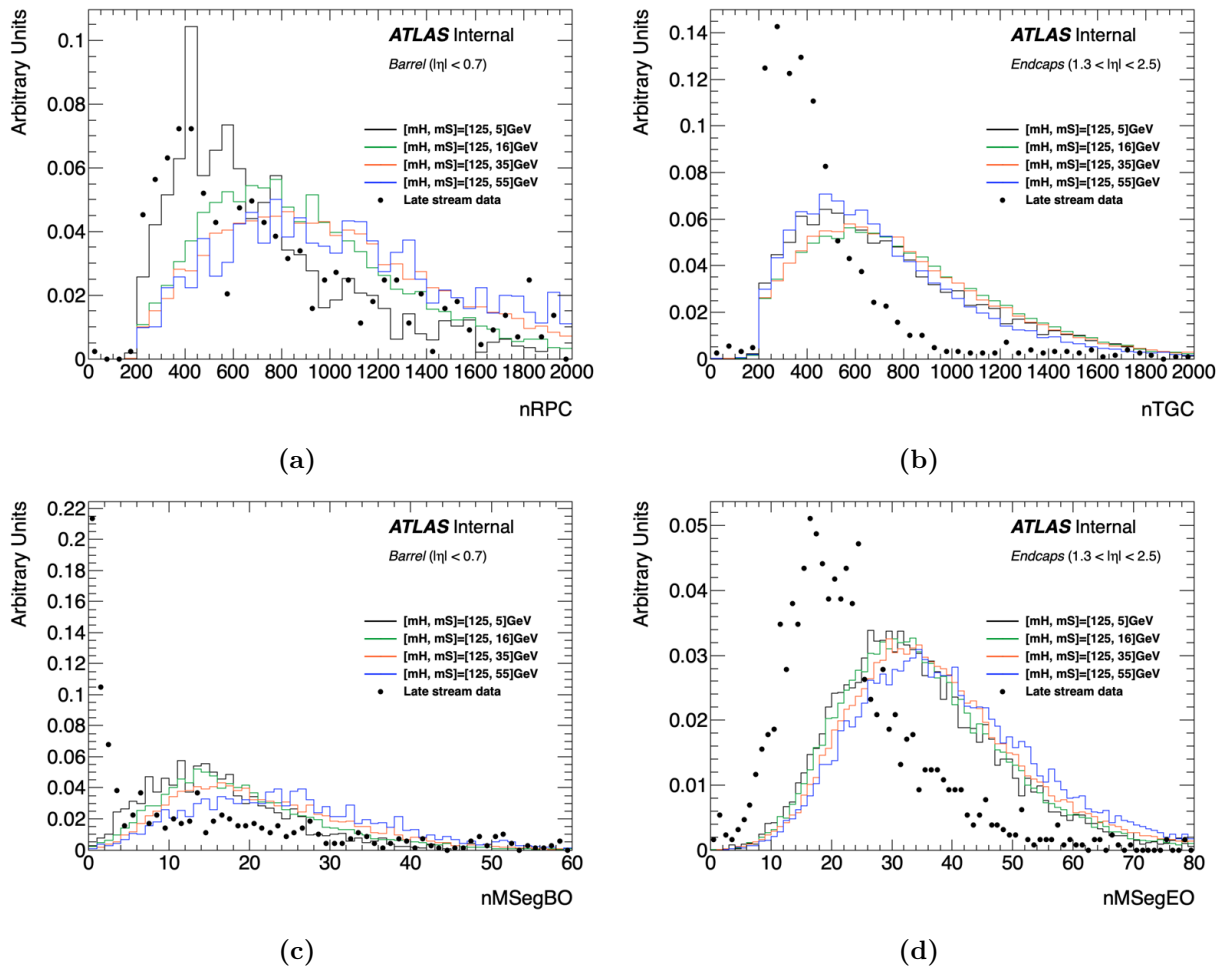

Figure 8.1: Figures (a) and (b) show the fraction of one-MSVtx events in the SM-Higgs signal MC samples versus the number of RPC hits for barrel events and the number of TGC hits for endcap events, as compared with Late stream data, respectively. Figures (c) and (d) show the distributions in terms of the number of muon segments (MSeg) in the barrel-outer- (BO) and endcap-outer- (EO) MDT stations, respectively.

Figures 8.2(a) and 8.2(b) show the number of events in bins of $H_{\mathrm{T}}^{\mathrm{miss}}$ between several signal MC samples and the Run 2 data. The only selection applied is the requirement that each event only have one MSVtx, making the Run 2 data overwhelmingly background-dominated. A threshold of 40 GeV eliminates much of the background while retaining most signal events, which is why it is used to define the validation and signal regions. Figures 8.2(c) and 8.2(d) show the same information, but in terms of the selection efficiency for minimum $H_{\mathrm{T}}^{\mathrm{miss}}$ thresholds. From this second set of figures, it can be seen that, at an $H_{\mathrm{T}}^{\mathrm{miss}}$ threshold

of 40 GeV, about $55-60\%$ of background events enter the validation region whereas only $5-15\%$ of signal events enter, making the region background-enriched.

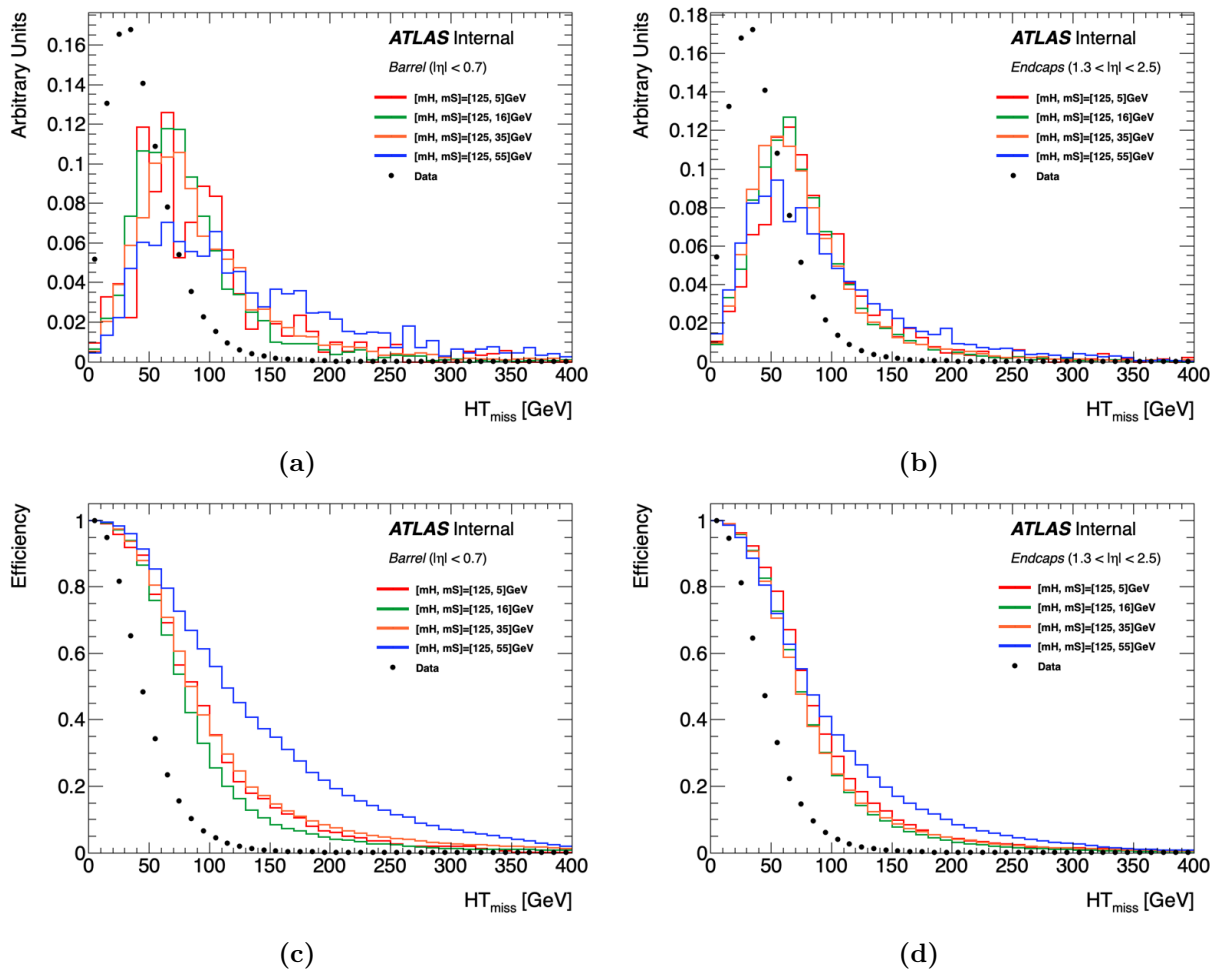

Figure 8.2: Figure (a) shows the fraction of barrel MSVtx in bins of $H_{\mathrm{T}}^{\mathrm{miss}}$, while Figure (b) shows the same distributions but for endcap events. Figures (c) and (d) show the selection efficiency for different $H_{\mathrm{T}}^{\mathrm{miss}}$ thresholds for the barrel and endcap MSVtx, respectively. The black points are Run 2 data while the colored lines are the SM Higgs $H \to ss$ samples.

Figures 8.3(a) and 8.3(b) show the number of events in bins of $E_{\mathrm{T}}^{\mathrm{miss}}$ between several signal MC samples and the Run 2 data. An $E_{\mathrm{T}}^{\mathrm{miss}}$ threshold of 20 GeV was found to remove more background than signal. Figures 8.3(c) and 8.3(d) show the same comparison, but in terms of a selection efficiency for a given minimum $E_{\mathrm{T}}^{\mathrm{miss}}$ threshold.

Figures 8.4(a) and 8.4(b) show a comparison in the number of RPC and TGC hits between some $H \to ss$ signal MC samples and the Run 2 data for events with one MSVtx in the barrel or endcap, respectively. The peak location in the Run 2 data justifies higher selection

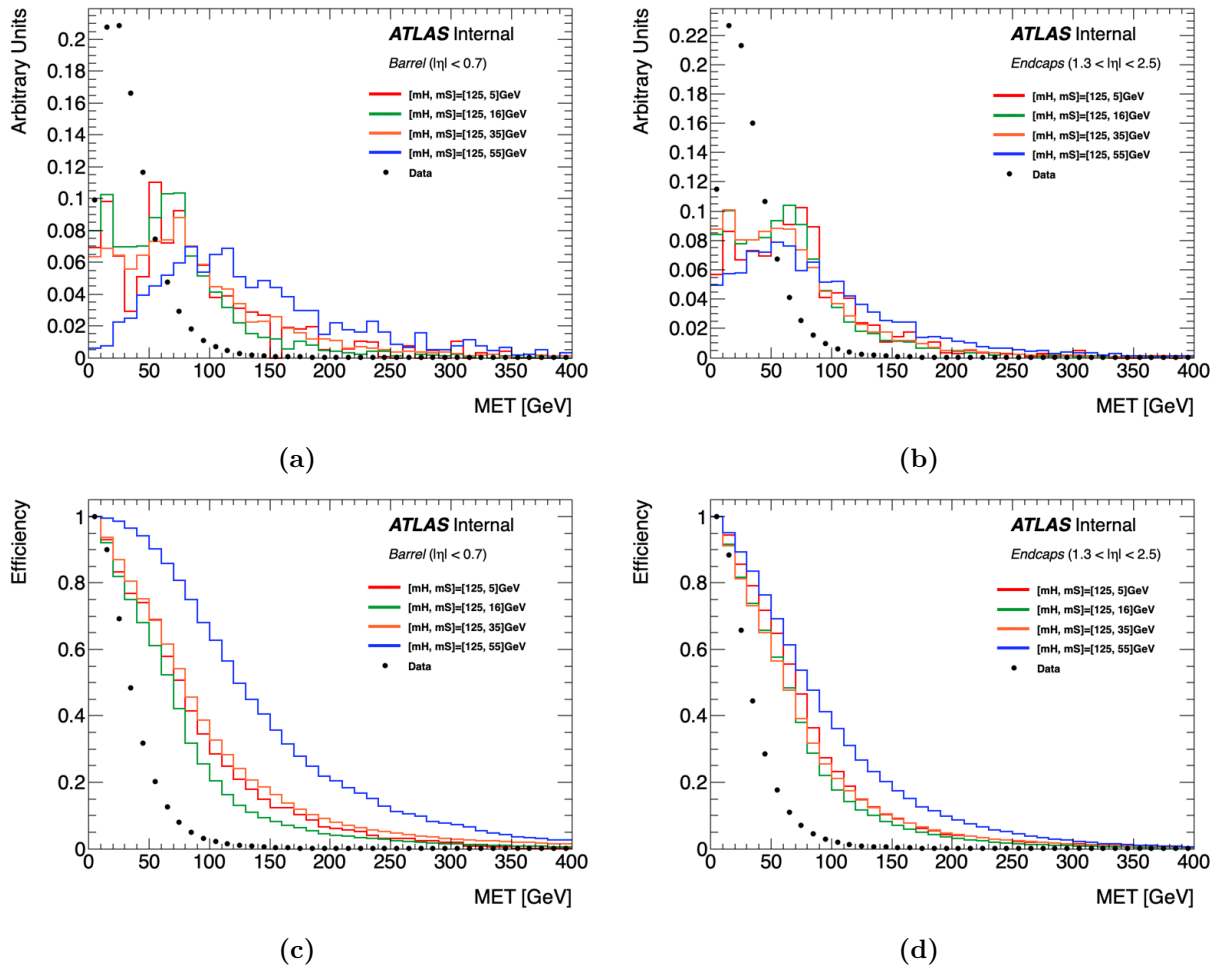

Figure 8.3: Figure (a) shows the fraction of barrel MSVtx in bins of $E_{\mathrm{T}}^{\mathrm{miss}}$, while Figure (b) shows the same distributions but for endcap events. Figures (c) and (d) show the selection efficiency for different $E_{\mathrm{T}}^{\mathrm{miss}}$ thresholds for the barrel and endcap MSVtx, respectively. The black points are Run 2 data while the colored lines are the SM Higgs $H \to ss$ samples.

thresholds for both the number of RPC and TGC hits than what was introduced in the GVC in Table 7.1. In addition to removing NCB contributions, the increased hit thresholds reduce contributions from other background sources present in data. Figures 8.4(c) and 8.4(d) show the same information as Figures 8.4(a) and 8.4(b), but as a selection efficiency for a minimum hit threshold.

Figures 8.5(a) and 8.5(b) show the number of events in bins of the number of MS segments in the barrel outer MDT stations and endcap outer MDT stations, respectively, for several $H \to ss$ signal MC samples and the Run 2 data. Figures 8.5(c) and 8.5(d) show the same information, but expressed as a selection efficiency with a minimum threshold on the MSeg

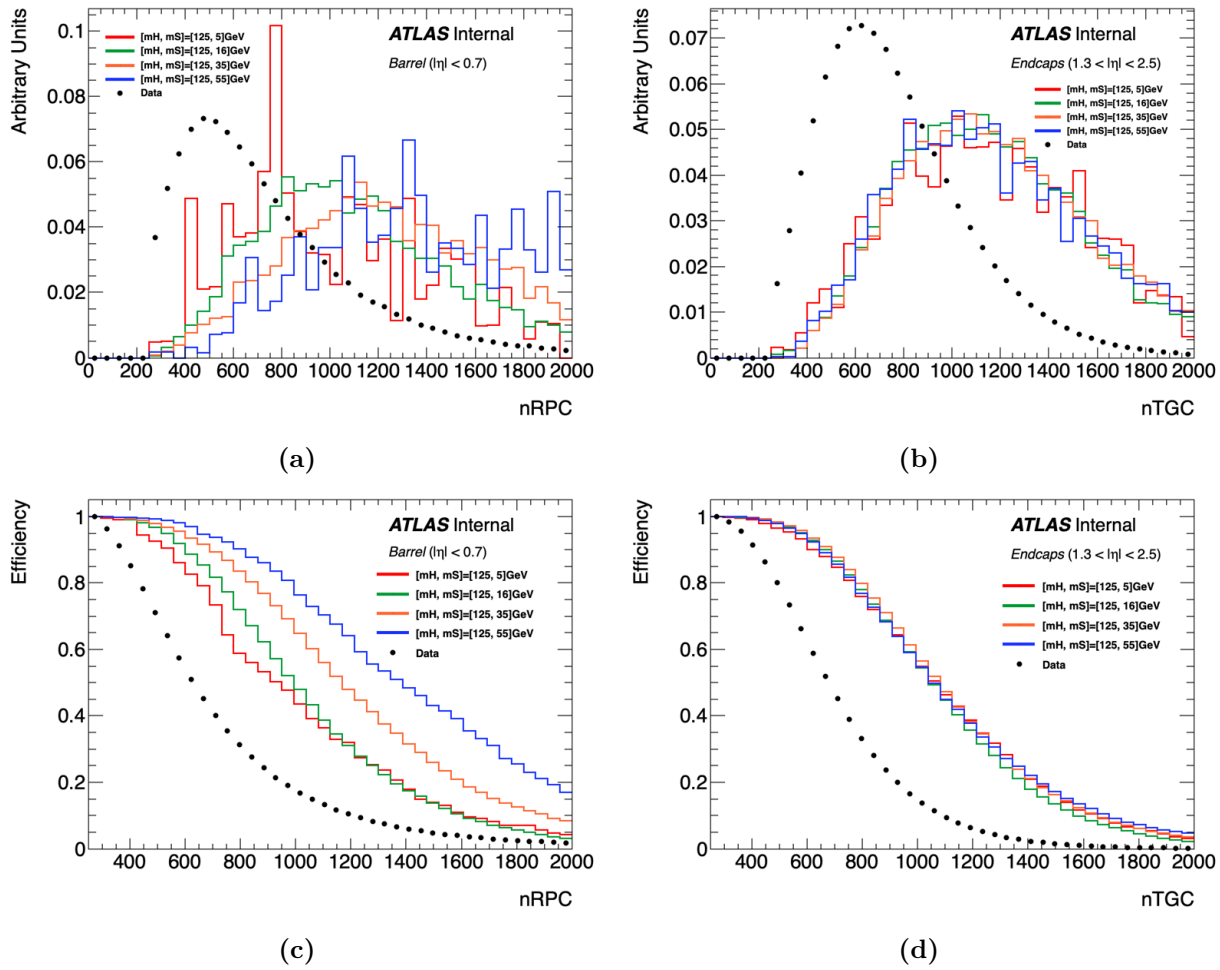

Figure 8.4: Figure (a) shows the distribution of nRPC hits for barrel MSVtx, while Figure (b) shows the nTGC distributions for endcap events. Figures (c) and (d) show the selection efficiency for different nRPC hit thresholds and nTGC hit thresholds for the barrel and endcap MSVtx, respectively. The black points are Run 2 data while the colored lines are the SM Higgs $H \to ss$ samples.

multiplicity. The thresholds of nMSegBO > 15 and nMSegEO > 30 still provide a bit of background removal in data.

Unlike the NCB shown in Figures 8.1(c) and 8.1(d), the dominant background sources present in data have a shape more consistent with signal events. These selection are meant to primarily suppress NCB events from entering the ABCD plane.

Figures 8.6(a) and 8.6(b) show the number of events in bins of minimum ΔR between the MSVtx and the closest jet (with a $p_{\mathrm{T}} > 20\,\mathrm{GeV}$) or track (with a $p_{\mathrm{T}} > 5\,\mathrm{GeV}$) for some $H \to ss$ signal samples and Run 2 data. Figures 8.6(a) and 8.6(b) show these distributions for

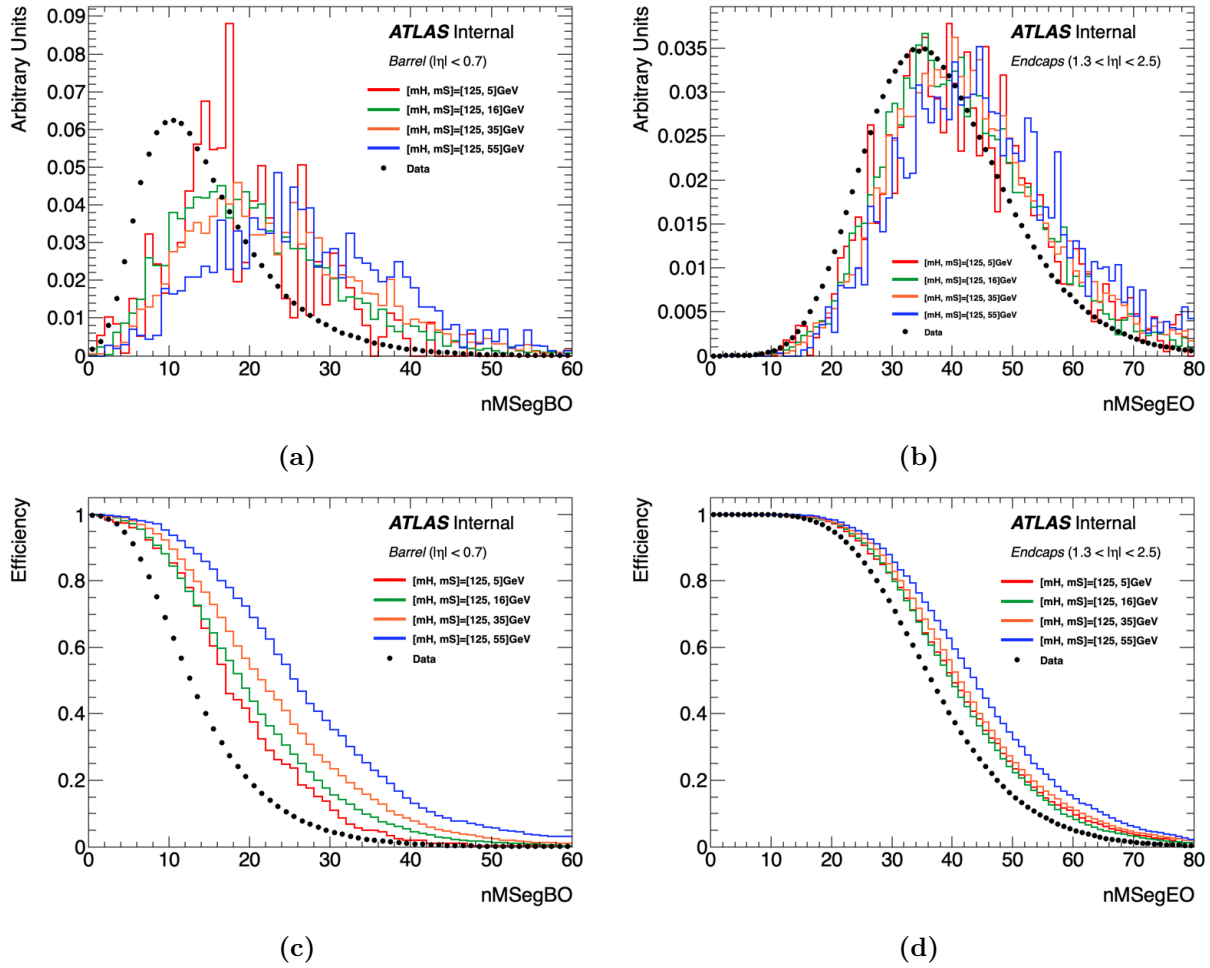

Figure 8.5: Figure (a) shows the distribution of the number of MS segments in the barrel outer MDT station for barrel MSVtx events, while Figure (b) shows the distributions of the number of MS segments in the endcap outer MDT stations for endcap events. Figures (c) and (d) show the selection efficiency for different thresholds of BO MS segments and EO MS segments for barrel and endcap MSVtx events, respectively. The black points are Run 2 data while the colored lines are the SM Higgs $H \to ss$ samples.

MS vertices in the barrel and endcap, respectively. The dominant background contribution in data are punch-through jets, described in more detail in Section 5.3.2. One of the most effective selection to remove contributions from jets that punch through the calorimeter are isolation criteria on jets and high-p_{T} tracks. Figures 8.6(c) and 8.6(d) show the same information expressed as an efficiency with a minimum ΔR threshold. From these plots, it can be shown that, with a minimum ΔR threshold of 0.8, around 95% of Run 2 data events can be removed, while only around 20% of the $H \to ss$ signal MC events are removed.

Not mentioned above were the selection on the neural network scores, NN1 and NN2,

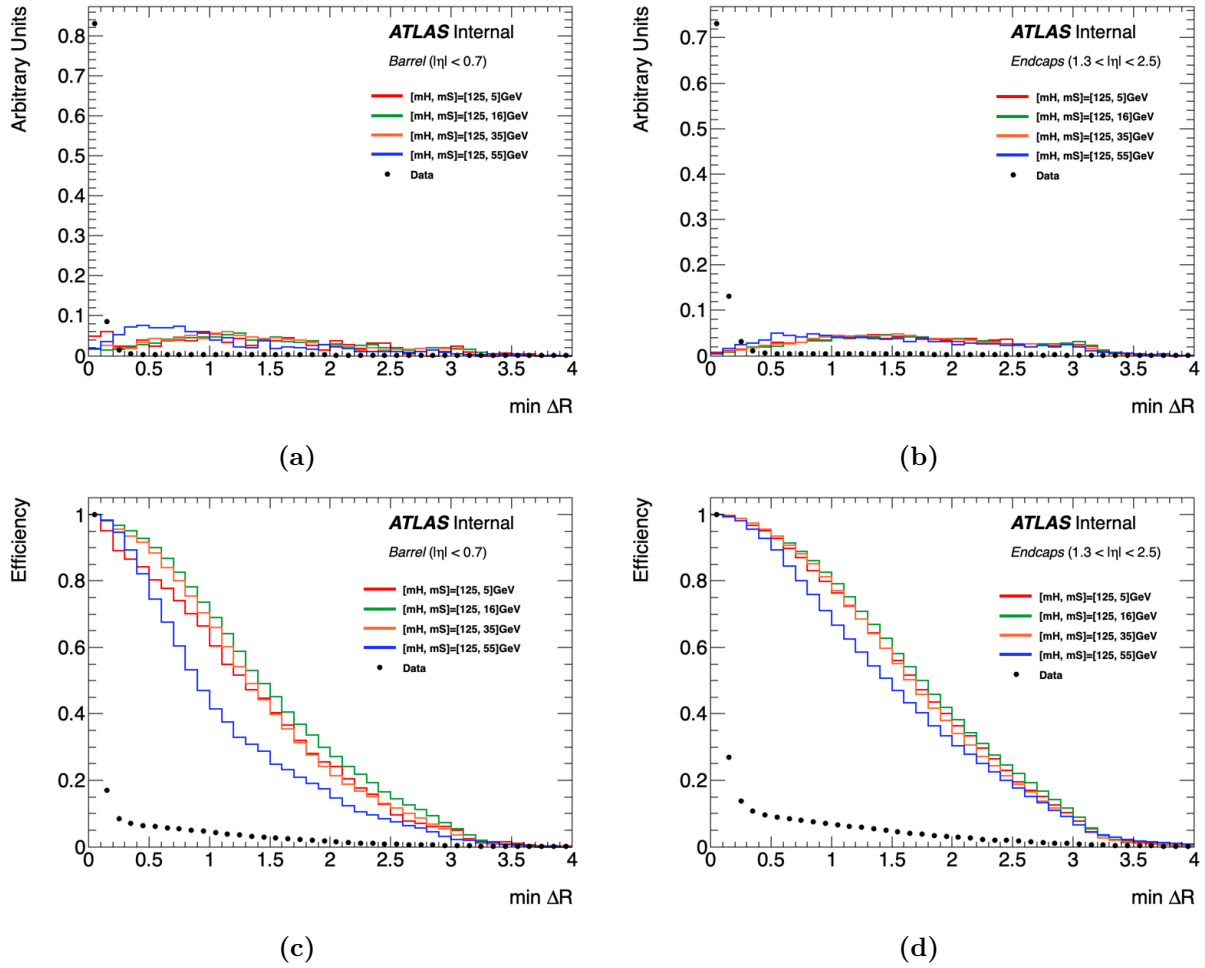

Figure 8.6: Figures (a) and (b) show the distribution of the minimum ΔR between the MSVtx with the closest jet with $p_{\mathrm{T}} > 20\,\mathrm{GeV}$ or track with $p_{\mathrm{T}} > 5\,\mathrm{GeV}$ in barrel MSVtx and endcap MSVtx events, respectively. Figures (c) and (d) show the selection efficiency for different thresholds of this minimum ΔR. The black points are Run 2 data while the colored lines are the SM Higgs $H \to ss$ samples.

which are described in detail in Section 8.3.2.

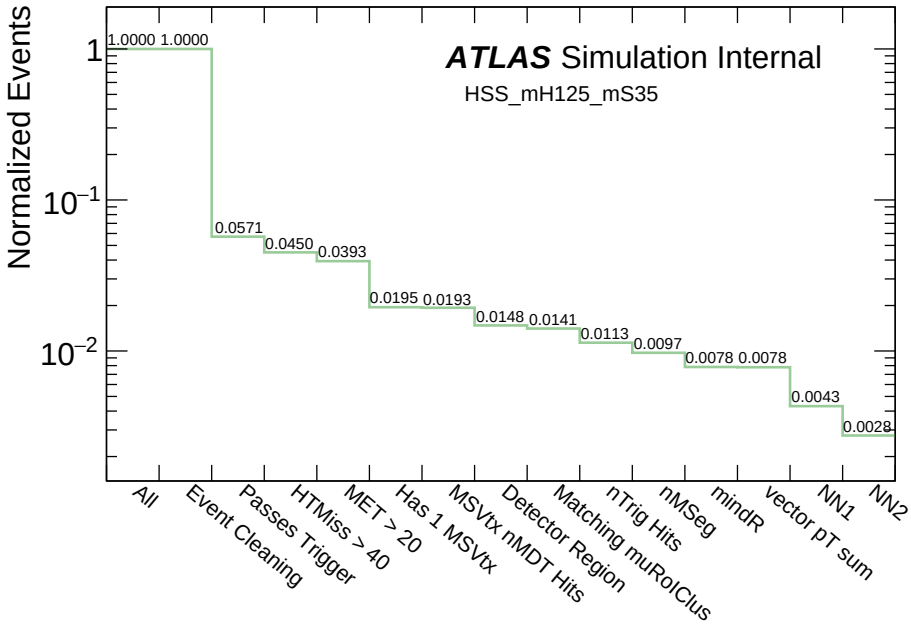

Figure 8.7: Normalized cutflow for the signal MC samples with $m_H = 125\,\text{GeV}, m_s = 35\,\text{GeV}$.

Selection	Event Yields for $m_\Phi,\ m_s$			
$m_\Phi,\ m_s\ =$	125, 5	125, 16	125, 35	125, 55
All Events	1070000	510000	1229000	3608000
Event passes event cleaning criteria	1069988	509996	1228975	3607973
Event passes HLT_j30_muvtx_noiso trigger	36879	30761	70237	63066
Event has $H_{\text{T}}^{\text{miss}} > 40\,\text{GeV}$	29791	25294	55260	53846
Event has $E_{\text{T}}^{\text{miss}} > 20\,\text{GeV}$	26630	21816	48355	52826
Event has exactly one MS vertex	11412	11154	23956	28999
MS Vertex passes nMDT hits	11275	11068	23758	28276
MS Vertex is in Fiducial Region	8690	8616	18146	22369
MS Vertex matched to triggering muon RoI cluster	8375	8342	17306	21270
MS Vertex passes nRPC(nTGC) Hits	6024	6505	13943	18137
MS Vertex passes nBOL(nEOL) Selection	5059	5348	11955	16173
MS Vertex passes jet and track isolation	4139	4418	9630	7204
MS Vertex passes low p_{T} track isolation	4127	4410	9588	7181
NN1 (barrel > 0.5 OR endcap > 0.8)	2062	2269	5300	3821
NN2 (barrel > 0.5 OR endcap > 0.8)	984	1291	3388	2497

Table 8.3: Cutflow signal yields for SM Higgs mass $H \to ss$ MC samples. The yields reflect the number of events passing each selection and all prior selection.

Selection	Event Yields for m_Φ, m_s				
$m_\Phi,\ m_s\ =$	60, 5	60, 16	200, 50	400, 100	600, 50
All Events	1190000	899000	200000	200000	300000
Event passes event cleaning criteria	1189991	898987	199999	199999	299998
Event passes HLT_j30_muvtx_noiso trigger	13545	13471	16962	33408	67730
Event has $H_{\mathrm{T}}^{\mathrm{miss}} > 40\,\mathrm{GeV}$	9139	9596	15349	31692	64377
Event has $E_{\mathrm{T}}^{\mathrm{miss}} > 20\,\mathrm{GeV}$	8241	9102	14405	31329	63897
Event has exactly one MS vertex	3776	4776	7657	15796	31100
MS Vertex passes nMDT hits	3730	4742	7551	15154	27886
MS Vertex is in Fiducial Region	2976	3650	5812	11194	19596
MS Vertex matched to triggering muon RoI cluster	2859	3509	5583	10344	18460
MS Vertex passes nRPC(nTGC) Hits	1877	2638	4934	9839	17396
MS Vertex passes nBOL(nEOL) Selection	1605	2158	4430	9039	15261
MS Vertex passes jet and track isolation	1211	1489	3561	7098	11161
MS Vertex passes low p_{T} track isolation	1207	1486	3543	7079	11118
NN1 (barrel > 0.5 OR endcap > 0.8)	611	786	1941	3847	5789
NN2 (barrel > 0.5 OR endcap > 0.8)	296	449	1428	3334	5087
$m_\Phi,\ m_s\ =$	600, 150	600, 275	1000, 50	1000, 275	1000, 475
All Events	450000	1000000	300000	450000	1600000
Event passes event cleaning criteria	449998	999996	299999	449995	1599968
Event passes HLT_j30_muvtx_noiso trigger	102165	75943	83733	129143	112587
Event has $H_{\mathrm{T}}^{\mathrm{miss}} > 40\,\mathrm{GeV}$	96402	71755	80101	122977	107198
Event has $E_{\mathrm{T}}^{\mathrm{miss}} > 20\,\mathrm{GeV}$	95584	71053	79684	122208	106319
Event has exactly one MS vertex	44919	30034	34548	51355	43045
MS Vertex passes nMDT hits	40680	27791	27715	40158	36476
MS Vertex is in Fiducial Region	28937	23331	18648	27613	30719
MS Vertex matched to triggering muon RoI cluster	26002	19272	17020	23318	22341
MS Vertex passes nRPC(nTGC) Hits	25085	18005	15982	22594	21270
MS Vertex passes nBOL(nEOL) Selection	23331	17371	13898	21248	21037
MS Vertex passes jet and track isolation	17457	12472	8596	14461	14435
MS Vertex passes low p_{T} track isolation	17396	12416	8549	14402	14371
NN1 (barrel > 0.5 OR endcap > 0.8)	9737	6010	4496	8367	7621
NN2 (barrel > 0.5 OR endcap > 0.8)	8710	4077	4004	7456	5656

Table 8.4: Cutflow signal yields for non-SM Higgs mass $H \to ss$ MC samples. The yields reflect the number of events passing each selection and all prior selection.

Selection	Event Yields for m_Φ, m_χ, $c\tau_{gen}$		
$m_\Phi,\ m_\chi,\ c\tau_{gen}\ =$	125, 10, 0.920	125, 55, 5.550	125, 100, 3.500
All Events	398000	400000	399000
Event passes event cleaning criteria	398000	399993	398989
Event passes HLT_j30_muvtx_noiso trigger	23148	7118	45212
Event has Event has $H_{\mathrm{T}}^{\mathrm{miss}} > 40\,\mathrm{GeV}$	17996	5929	39881
Event has Event has $E_{\mathrm{T}}^{\mathrm{miss}} > 20\,\mathrm{GeV}$	15944	5784	38629
Event has exactly one MS vertex	7238	2591	17125
MS Vertex passes nMDT hits	7179	2584	16811
MS Vertex is in Fiducial Region	5330	1957	11951
MS Vertex matched to triggering muon RoI cluster	5072	1879	11111
MS Vertex passes nRPC(nTGC) Hits	3664	1394	10072
MS Vertex passes nBOL(nEOL) Selection	2999	1182	8873
MS Vertex passes jet and track isolation	2415	835	6899
MS Vertex passes Low p_{T} track isolation	2412	832	6863
NN1(barrel > 0.5 OR endcap > 0.8)	1241	471	3851
NN2(barrel > 0.5 OR endcap > 0.8)	656	268	2858

Table 8.5: Cutflow signal yields for $bb\nu$ $H \to \chi\chi$ MC samples. The yields reflect the number of events passing each selection and all prior selection. Mediator and Scalar masses are in GeV. Proper decay lengths are in m.

Selection	Event Yields for $m_\Phi,\ m_\chi, c\tau_{gen}$		
$m_\Phi,\ m_\chi,\ c\tau_{gen}\ =$	125, 10, 0.920	125, 55, 5.550	125, 100, 3.500
All Events	400000	399000	400000
Event passes event cleaning criteria	399988	398989	399989
Event passes HLT_j30_muvtx_noiso trigger	22946	12237	70545
Event has $H_{\mathrm{T}}^{\mathrm{miss}} > 40\,\mathrm{GeV}$	17860	9859	63922
Event has $E_{\mathrm{T}}^{\mathrm{miss}} > 20\,\mathrm{GeV}$	15638	9555	62549
Event has exactly one MS vertex	7429	4617	30983
MS Vertex passes nMDT hits	7347	4573	29686
MS Vertex is in Fiducial Region	5392	3489	21314
MS Vertex matched to triggering muon RoI cluster	5128	3276	19770
MS Vertex passes nRPC(nTGC) Hits	3739	2773	18822
MS Vertex passes nBOL(nEOL) Selection	3065	2503	17462
MS Vertex passes jet and track isolation	2519	1729	13504
MS Vertex passes Low p_{T} track isolation	2509	1725	13450
NN1(barrel > 0.5 OR endcap > 0.8)	1270	986	7743
NN2(barrel > 0.5 OR endcap > 0.8)	756	647	6572

Table 8.6: Cutflow signal yields for cbs $H \to \chi\chi$ MC samples. The yields reflect the number of events passing each selection and all prior selection. Mediator and Scalar masses are in GeV. Proper decay lengths are in m.

Selection	Event Yields for $m_\Phi,\ m_\chi, c\tau_{gen}$		
$m_\Phi,\ m_\chi,\ c\tau_{gen}\ =$	125, 10, 0.920	125, 55, 5.550	125, 100, 3.500
All Events	400000	400000	400000
Event passes event cleaning criteria	399996	399990	399993
Event passes HLT_j30_muvtx_noiso trigger	6329	2187	18313
Event has $H_{\mathrm{T}}^{\mathrm{miss}} > 40\,\mathrm{GeV}$	4396	1857	15942
Event has $E_{\mathrm{T}}^{\mathrm{miss}} > 20\,\mathrm{GeV}$	3870	1817	15327
Event has exactly one MS vertex	1216	527	4735
MS Vertex passes nMDT hits	1200	523	4643
MS Vertex is in Fiducial Region	949	434	3516
MS Vertex matched to triggering muon RoI cluster	910	405	3259
MS Vertex passes nRPC(nTGC) Hits	525	262	2718
MS Vertex passes nBOL(nEOL) Selection	431	212	2367
MS Vertex passes jet and track isolation	336	147	1783
MS Vertex passes Low p_{T} track isolation	335	147	1777
NN1(barrel > 0.5 OR endcap > 0.8)	177	79	934
NN2(barrel > 0.5 OR endcap > 0.8)	51	33	513

Table 8.7: Cutflow signal yields for $\tau\tau\nu\ H \rightarrow \chi\chi$ MC samples. The yields reflect the number of events passing each selection and all prior selection. Mediator and Scalar masses are in GeV. Proper decay lengths are in m.

8.3 Background Estimation

The last two selection criteria in Table 8.2 use scores from two pairs of multilayer perceptron (MLP) neural networks (NNs) trained on a subset of the signal MC and a background-enriched subset of the Run 2 data. The two neural nets are used to create a 2D plane, which is used to estimate the background via the so-called "ABCD Method" [150, 151]. This data-driven method is used to estimate the number of background events in the Signal Region (SR). A data-driven method is necessary since there are no MC samples sufficiently well-modeled from which to draw an accurate background estimate. By looking at regions of the ABCD plane near, but outside of, the SR, it is possible to investigate data as if it were a background sample without the risk of unblinding the region where the analysis would be most sensitive to the signal.

8.3.1 The ABCD Method

The ABCD method relies on a plane constructed from two, uncorrelated variables, X and Y, with some signal-background separation power. Region A is typically defined to be the SR, the region with the highest signal sensitivity. The background should primarily occupy the B, C, and D regions, with minimal contamination into region A. An example sketch of this plane is shown in Figure 8.8 [151].

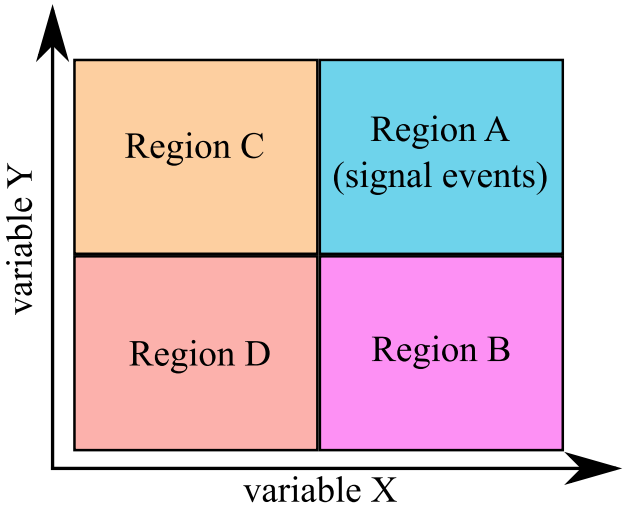

Figure 8.8: Sketch of the ABCD method used for background estimation.

Since X and Y are uncorrelated, any distribution of events along the X axis should be independent of the value of Y, and vice-versa. This implies that, for a given value of $X = X_0$,

$$\frac{N_{X>X_0}}{N_{X<X_0}} \tag{8.1}$$

should be constant as a function of Y. A similar ratio would also be constant as a function of X for given value of $Y = Y_0$.

Using the expression in Eq. 8.1, the ratio of two adjacent regions of the ABCD plane must be equal to the equivalent ratio of the other two. For the ABCD plane shown in Figure 8.8, the following equation can be written:

$$\frac{N_A}{N_B} = \frac{N_C}{N_D} \tag{8.2}$$

where the N_i for $i \in \{A, B, C, D\}$ corresponds to the number of events in the region i. Rearranging this equation gives us a way to estimate the number of expected background events in region A:

$$N_A^{\text{expected}} = N_B \times \frac{N_C}{N_D} \tag{8.3}$$

where N_A^{expected} is the expected number of background events entering the SR.

In order to verify that the ABCD method works for this analysis, a validation region (VR) was developed in which the number of events entering region A could be counted without unblinding. The VR is defined to pass all event selection criteria except for the $H_{\text{T}}^{\text{miss}}$ selection, which is inverted ($H_{\text{T}}^{\text{miss}} < 40\,\text{GeV}$).

To validate that the ABCD plane works as expected, a closure test is performed. In the VR, the expected number of events in region A is compared to the actual number of events in region A. If it is found that $N_{A,\text{VR}}^{\text{expected}} = N_{A,\text{VR}}^{\text{observed}}$, within the statistical uncertainty of $N_{A,\text{VR}}^{\text{expected}}$, then confidence is gained that the ABCD method can be used given the background for this analysis. For this analysis, the scores from a pair of NNs are used to define the ABCD plane. Before the NNs can return scores for each event, they needed to be constructed and trained.

8.3.2 Neural Networks and Background Estimation

In order to construct the ABCD plane used in this analysis, two multilayer perceptrons (MLPs) were developed. A multilayer perceptron is a fully-connected, feed-forward neural network with an input layer, multiple hidden layers, and an output layer. Every neuron in a given layer is connected to all neurons from the previous and following layers, making them fully-connected. The networks are called feed-forward because information feeds from one layer to the next without sending any information to a previous layer. The input layer takes the value of each input feature and passes them, multiplied by some weight, to the next layer. A neuron receiving these values takes their sum, adds a bias term, and then passes it through an activation function. This can be expressed as the following equation [152].

$$f_j(\mathbf{x}) = g(b_j + \sum_{i=1}^{n} w_{ij} x_i) \tag{8.4}$$

where $f_j(\mathbf{x})$ is the output of j^{th} neuron in any layer but the first, as a function of the output of all neurons in the previous layer, $\mathbf{x}$. Each x_i is and element of $\mathbf{x}$ and corresponds to the output of the i^{th} neuron from the preceding layer. The weight, w_{ij}, is applied to x_i when being used to calculate the value of the j^{th} neuron. The bias, b_j, is added to the value of the j^{th} neuron, which is not dependent on any input. The activation function, $g()$, acts on the weighted sum of inputs. The output of this activation function then becomes that neuron's output. This proceeds until the value of the output layer neurons are calculated.

For a classifier-style network, all of the weights, w_{ij}, and the bias, b_j, terms are modified during training by taking the classification target (label), which is provided as part of the training sample, and comparing it to the calculated (inferred) classification produced by the network. A process called *backpropagation* is performed where the difference between the expected classification and the inferred classification is used to determine the size of the changes that are applied to all of the weights and bias terms. This is done for every event in the training set, often many times, until the accuracy of the network stops improving. A sketch of one of the NNs used in this analysis is shown as a directional graph in Figure 8.9.

The two NNs were implemented in `keras-2.12.0` with the `tenserflow-2.12.1` backend [153, 154]. Figure 8.9 is an accurate depiction of both NN architectures. There are two

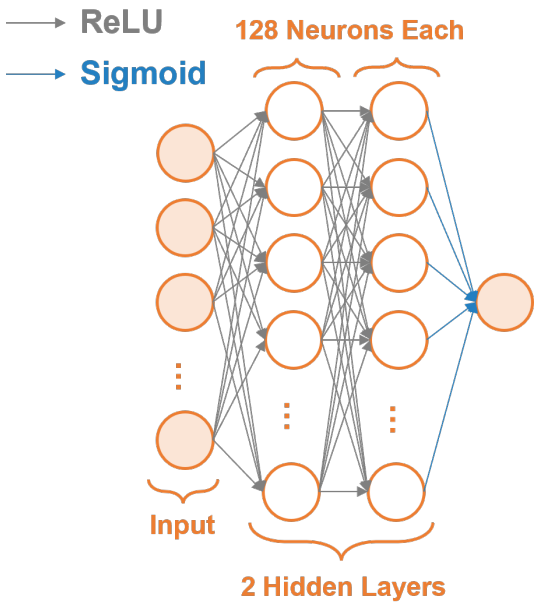

Figure 8.9: Sketch of the directional graph representation of one of the NNs used in this analysis. Two hidden layers of 128 neurons, each, were connected to each other and input features using ReLU activation functions. The last hidden layer was then connected to the output node using sigmoid activation functions.

hidden layers containing 128 neurons each. All input and hidden layers are connected using the Rectified Linear Unit (ReLU) activation function, and the output layer uses a sigmoid activation function. The output layer contains a single node which returns a value between 0 and 1, which corresponds to the data type: background or signal. The NNs were trained for ten epochs with a batch size of 32 (default). The loss function used was binary crossentropy. The optimizer used was `Adam`. The Receiver Operating Characteristic (ROC) curves for NN1 in the barrel and endcap are shown in Figure 8.10. The area under the curve (AUC) values are also shown.

In order to assure the pair of NNs could be used to define the ABCD plane, each NN used uncorrelated sets of features. The first neural network, NN1, uses features related to how isolated the vertex is, how much activity occurs close to it, and general activity within the event. The second neural network, NN2, uses features that relate to how objects are distributed within the detector. For NN1, the following features are used:

– Ratio of the number of muon segments in the inner MDT versus the middle MDT station

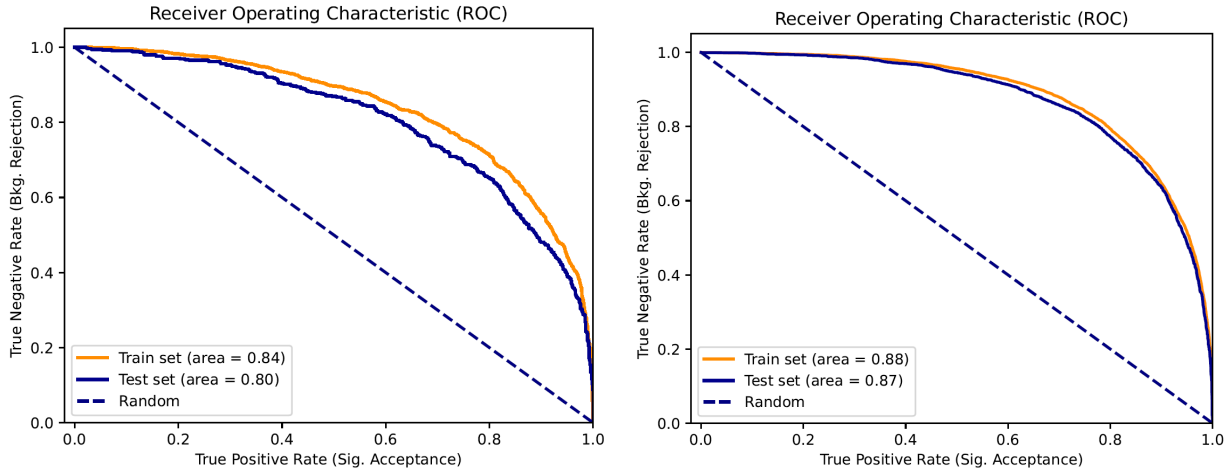

Figure 8.10: Receiver Operating Characteristic (ROC) curves for NN1 in the (a) barrel region and (b) endcap region. The similar AUC between test and train sets indicates a low likelihood significant overtraining occurred.

- Scalar sum of ID track p_{T} for tracks with $p_{\mathrm{T}} > 5\,\mathrm{GeV}$ in a ΔR cone of 0.4
- Total, average, RMS, and maximum value of the energy of calorimeter topo clusters inside a cone of $\Delta R = 0.4$ centered on the MSVtx
- Calorimeter cluster energy inside a cone of $\Delta R = 0.4$ centered on the MSVtx at all four sampling layers of the EM calorimeter and all four layers of the hadronic calorimeters
- MSVtx high-p_{T} track and jet isolation variable [(ΔR_{min} (MSVtx, track with $p_{\mathrm{T}} > 5\,\mathrm{GeV}$ and jet with $p_{\mathrm{T}} > 20\,\mathrm{GeV}$)] [1]
- MSVtx low p_{T} track isolation variable ($|\sum_{\Delta R^{\mathrm{cone}}} \vec{p_{\mathrm{T}}}|$ in a cone of $\Delta R = 0.2$ centered on the MSVtx for tracks with $p_{\mathrm{T}} < 5\,\mathrm{GeV}$)

For NN2, the following features are used:

- Average and RMS values of ΔR(MSVtx, tracklets)
- Average and RMS values of ΔR(MSVtx, muon segments)
- Total number of MDT and trigger hits associated with the MSVtx[2]

[1] Only events passing the isolation selection described in Table 8.2 are considered, so this variable is a distribution of ΔR_{min} with a minimum of 0.8.

[2] For details, see Section 6.6.2

- $\Delta\phi$ between the MSVtx and $E_{\mathrm{T}}^{\mathrm{miss}}$
- Average, RMS, and maximum value of the time of the calorimeter topo clusters inside a cone of $\Delta R = 0.4$ centered on the MSVtx
- Number of tracklets inside a cone of $\Delta R = 0.4$ centered on the MSVtx

To train the NNs a background-enriched sample of the full Run 2 data is used, with $H_{\mathrm{T}}^{\mathrm{miss}} < 40\,\mathrm{GeV}$, as the background sample. For the signal, a combination of the signal samples with Higgs and Scalar masses of $m_H = 60\,\mathrm{GeV}$, $m_H = 125\,\mathrm{GeV}$, and m_H, $m_S = 1000\,\mathrm{GeV}$, $475\,\mathrm{GeV}$ samples were used as signal input. Training on all signal samples yielded worse separation than training on a representative subset by inspection of the NN score distributions for each data type. The signal and background populations were reweighted so the sum of weights of each population were equal. The train/test separation used 75% of the sample statistics to train and 25% to test.

Signal MC statistics in the $H_{\mathrm{T}}^{\mathrm{miss}} < 40\,\mathrm{GeV}$ region were prohibitively low, meaning the full statistics had to be used. In order to justify this, the same type of background had to occur in the both $H_{\mathrm{T}}^{\mathrm{miss}} < 40\,\mathrm{GeV}$ and $H_{\mathrm{T}}^{\mathrm{miss}} > 40\,\mathrm{GeV}$ regions. Using the already unblinded 2015-2016 data, distributions of the NN input features were compared between the two regions and demonstrated good agreement.

Distributions of the NN scores for all four NNs is shown in Figure 8.11. Based on the score distributions and the signal-to-background ratio (S/B) in each region, the A region for the barrel is defined as NN1 > 0.5 and NN2 > 0.5, while the endcap region A is defined as NN1 > 0.8 and NN2 > 0.8. The close agreement between the train and test distributions for all four NNs indicates that the models were not overtrained.

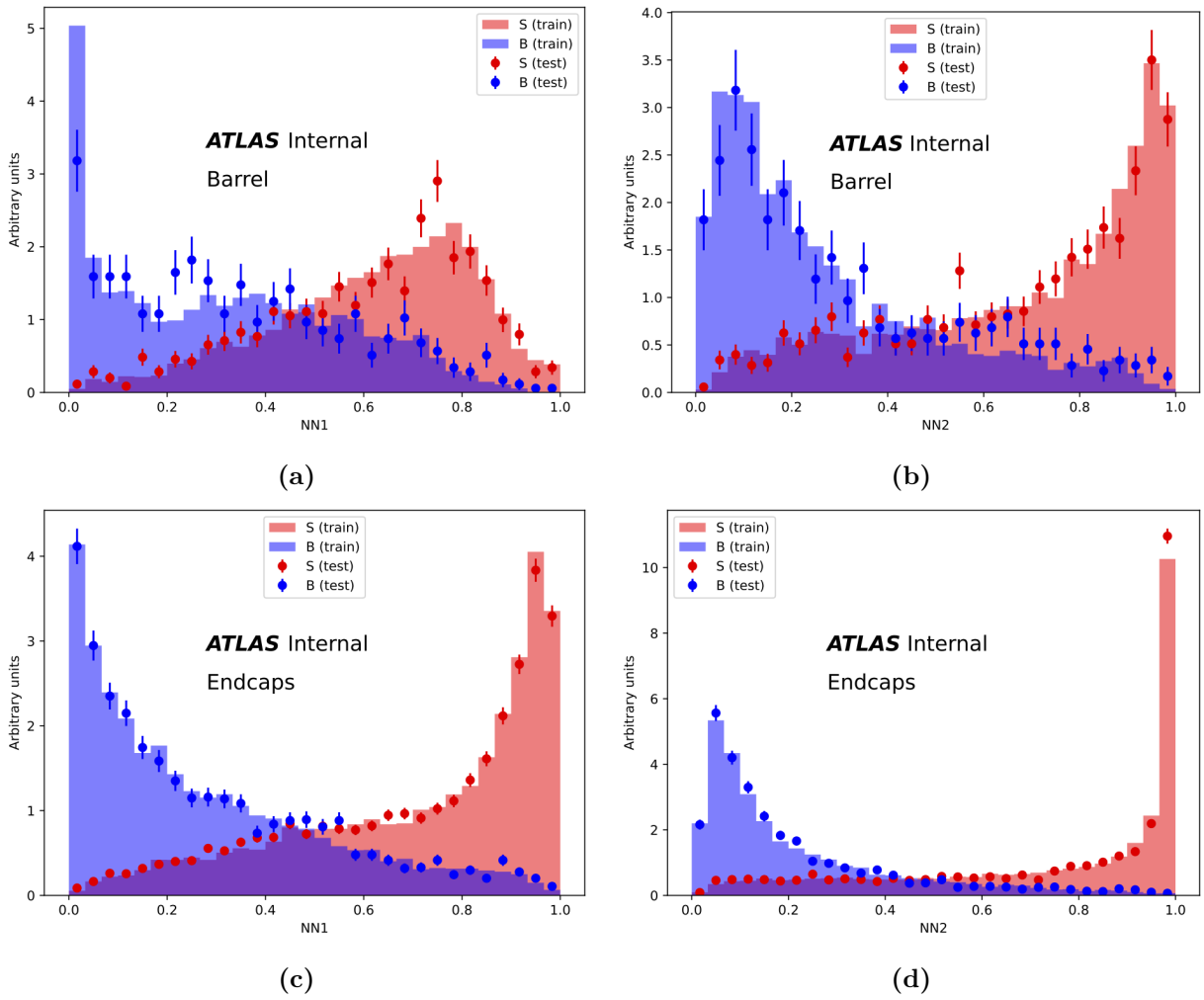

Figure 8.11: Score distributions for the train and test samples. Figures (a) and (b) show the distributions for NN1 and NN2 in the barrel. Figures (c) and (d) show the distributions for NN1 and NN2 in the endcap.

8.3.3 ABCD Validation

The ABCD method is validated using events with $H_{\mathrm{T}}^{\mathrm{miss}} < 40\,\mathrm{GeV}$. Figure 8.12 shows 2D histograms that correspond to the ABCD planes for data with a single MSVtx in either the barrel or endcap regions. The Pearson correlation of these planes was found to be less than 2%. The barrel region ABCD plane had a correlation of 1% and the endcap region ABCD plane had a correlation of 2%.

Table 8.8 shows the number of events in each region of these ABCD planes, along with the expected number of events in region A, as calculated using Eq. 8.3. If the number of observed events in region A matches the expected number of events, within the uncertainty, the ABCD plane is reliable. There were 60 events observed in the barrel region with 65 ± 6 expected. In the endcap region, 162 events were observed with 150 ± 7 expected. This corresponds to a significance of $\sim 1.7\sigma$, which is fairly good agreement of the ABCD plane in the validation region.

The ABCD planes were validated using NN threshold of 0.5 for both the barrel and the endcap to increase available statistics in regions A and C.

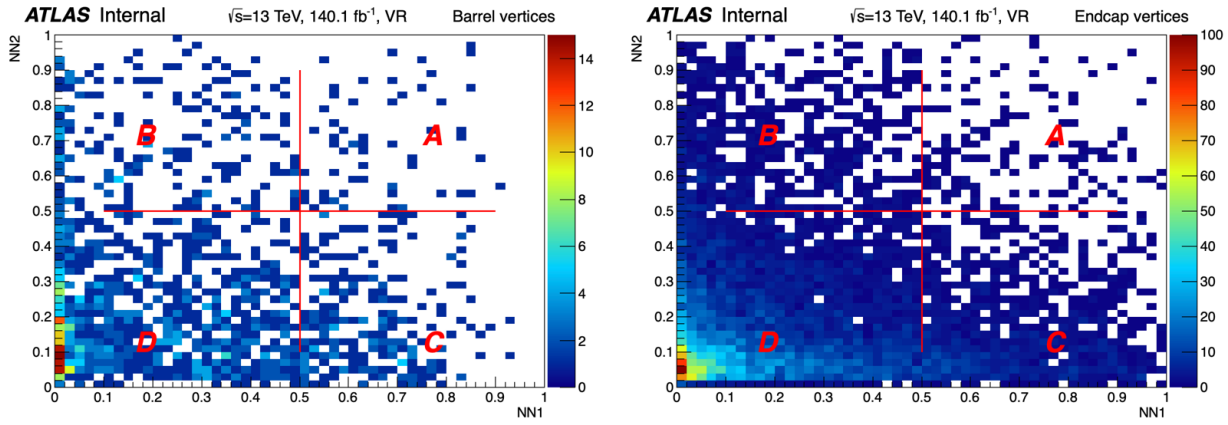

(a) **(b)**

Figure 8.12: ABCD planes in the VR subset of the Run 2 data for the (a) barrel and (b) endcaps.

Additional validation can be done using sub-regions of the full ABCD plane. These sub-regions can be defined by subdividing regions B and D (likewise, C and D), and using the event counts from these sub-regions in Eq. 8.3. This additional validation was done for this analysis to further establish that the NN scores used to construct the planes are not cor-

	Region	A_{obs}	B×C/D	B	C	D	p-value
Barrel	VR	60	65 ± 6	219	255	859	0.405
Endcaps	VR	162	150 ± 7	690	1189	5455	0.086

Table 8.8: Events counts for all four regions of the ABCD plane for the VR subset of Run 2 data, as well as the expected number of events predicted by the ABCD method. The background prediction in the barrel and endcaps validation regions is statistically consistent with the observation.

related. The B and D regions, jointly called the BD plane, were divided into five regions of equal size and numbered VR1 through VR5. VR1 spans NN1 values from 0 to 0.1, VR2 spans NN1 values from 0.1 to 0.2, and so on. An example of how these subregions are defined can be seen in Figure 8.13.

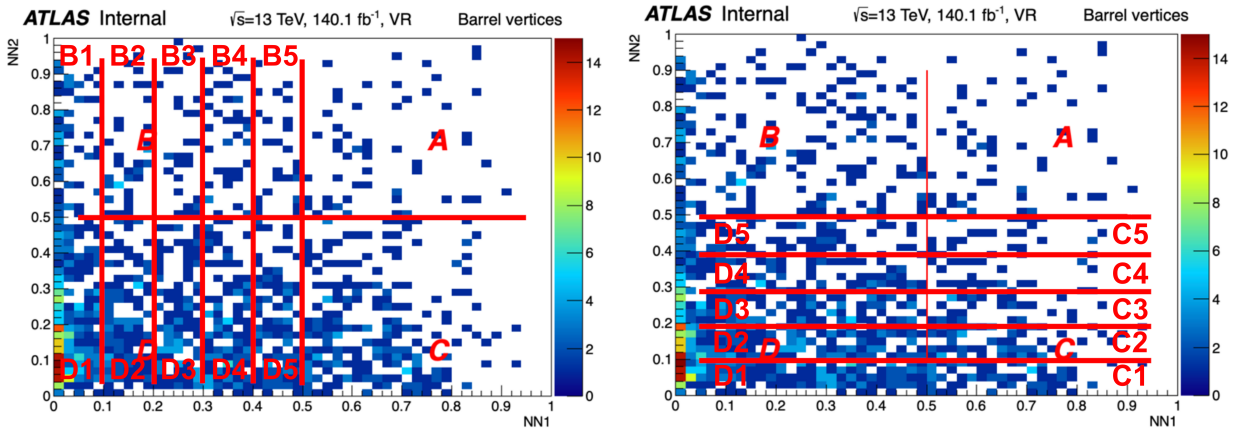

(a) **(b)**

Figure 8.13: Example of ABCD validation subregions, for Run 2 events with an MS vertex in the barrel, with subregions in (a) the BD plane and (b) the CD plane.

The results of this study can be seen in Figure 8.14. This same procedure is done for the CD plane, the results of which can be seen in Figure 8.15.

The overall agreement is generally good, though some validation subregions in both the BD and CD planes have expected values that fall outside of their 1σ errors. A systematic uncertainty on the background estimation is introduced to accommodate these points. The difference between the average expected number of events across all VR subregions and the number of observed events was taken as a global uncertainty on the number of estimated background events in the SR. In the barrel region, it was measured to be an 8% difference, while in the endcap region it was measured to be 5%.

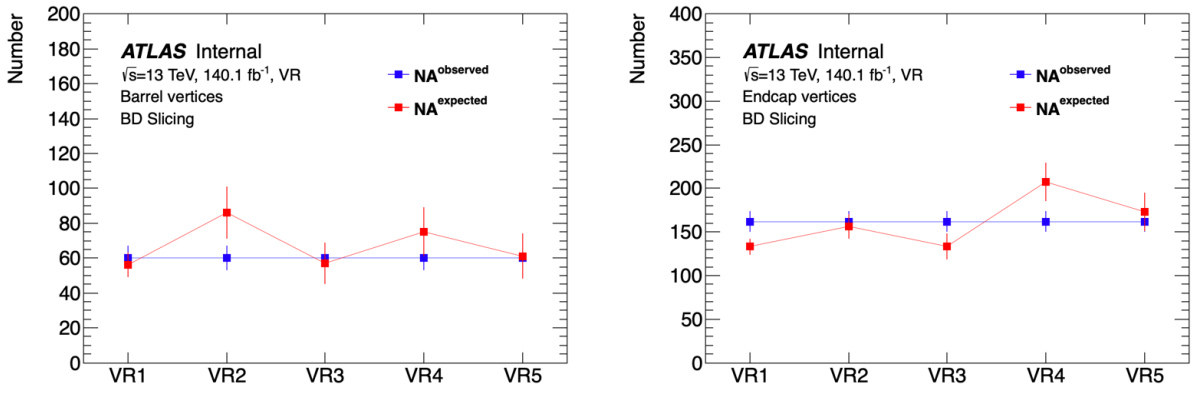

(a) **(b)**

Figure 8.14: Plot of expected (red) versus observed (blue) background events in the A region using VR1 - VR5 of the BD plane for (a) barrel and (b) endcap MS vertices. The expected number of vertices is consistent with the observed number for all sub-planes.

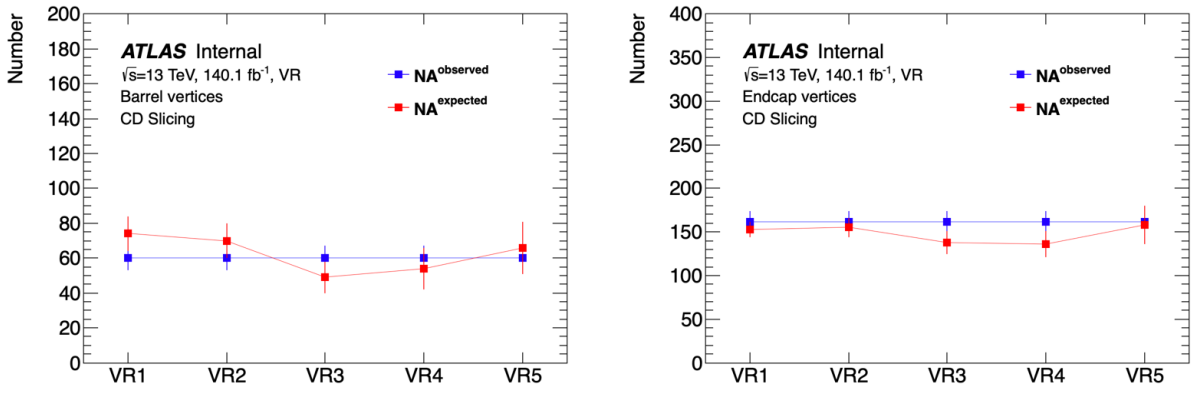

(a) **(b)**

Figure 8.15: Plot of expected (red) versus observed (blue) background events in the A region using VR1 - VR5 of the CD plane for (a) barrel and (b) endcap MS vertices. The expected number of vertices remains around the observed number for all sub-planes.

Validation was performed on the ABCD plane in the $H_{\mathrm{T}}^{\mathrm{miss}} > 40\,\mathrm{GeV}$ region as well. To remain blinded to the SR, only the B, C, and D regions were used. Since the ABCD plane is composed of two uncorrelated variables, the BD and CD regions could be split into four quadrants and an ABCD strategy could be performed on them by treating the upper-right quadrant as if it were the A-region. An example of this is shown in Figures 8.16 and 8.17 for the barrel and endcap regions, respectively.

By changing the value of the subplane division along one of the ABCD plane axes, it is

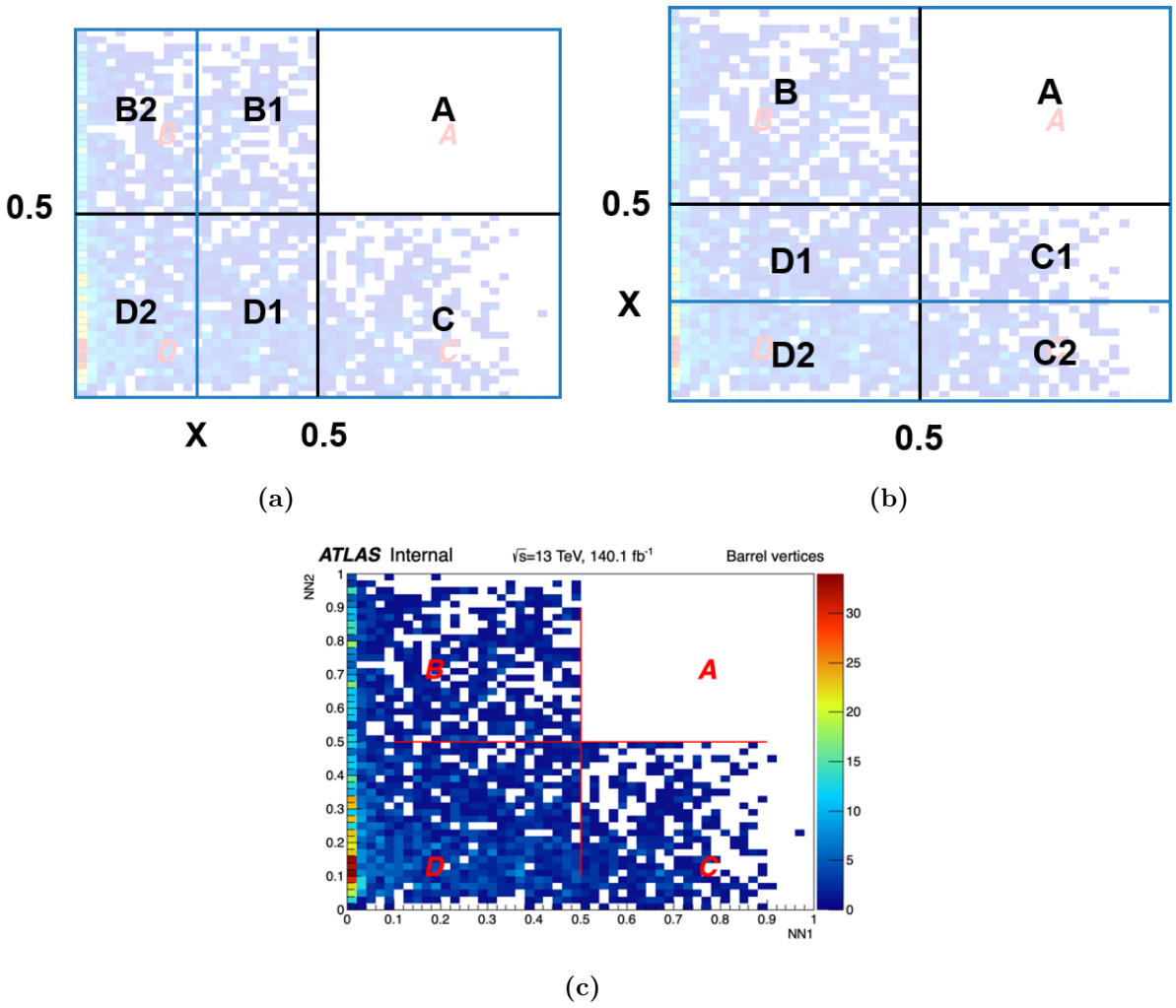

Figure 8.16: Overlay diagrams demonstrating subplane validation method for barrel region. The X division is variable and was set to seven different values between 0.1 and 0.4. (a) Overlay of the BD subplane used as ABCD validation. (b) Overlay of CD subplane used for ABCD validation. (c) Blinded ABCD plane for Run 2 data in the barrel region.

possible to evaluate the ABCD plane closure for a region close to the SR. For each region, the BD plane was split at seven different values of X along the NN1 axis and the CD plane was split along seven different values of X along the NN2 axis. The number of expected events is plotted against the number of observed events in Figure 8.18. These trends demonstrate either no change, or an improvement in the agreement between expected and observed numbers of events entering the subplane test region (B1 in the BD plane and C1 in the CD plane). This indicates stability in the ABCD method for this plane as the test threshold, X, approaches the actual ABCD region threshold.

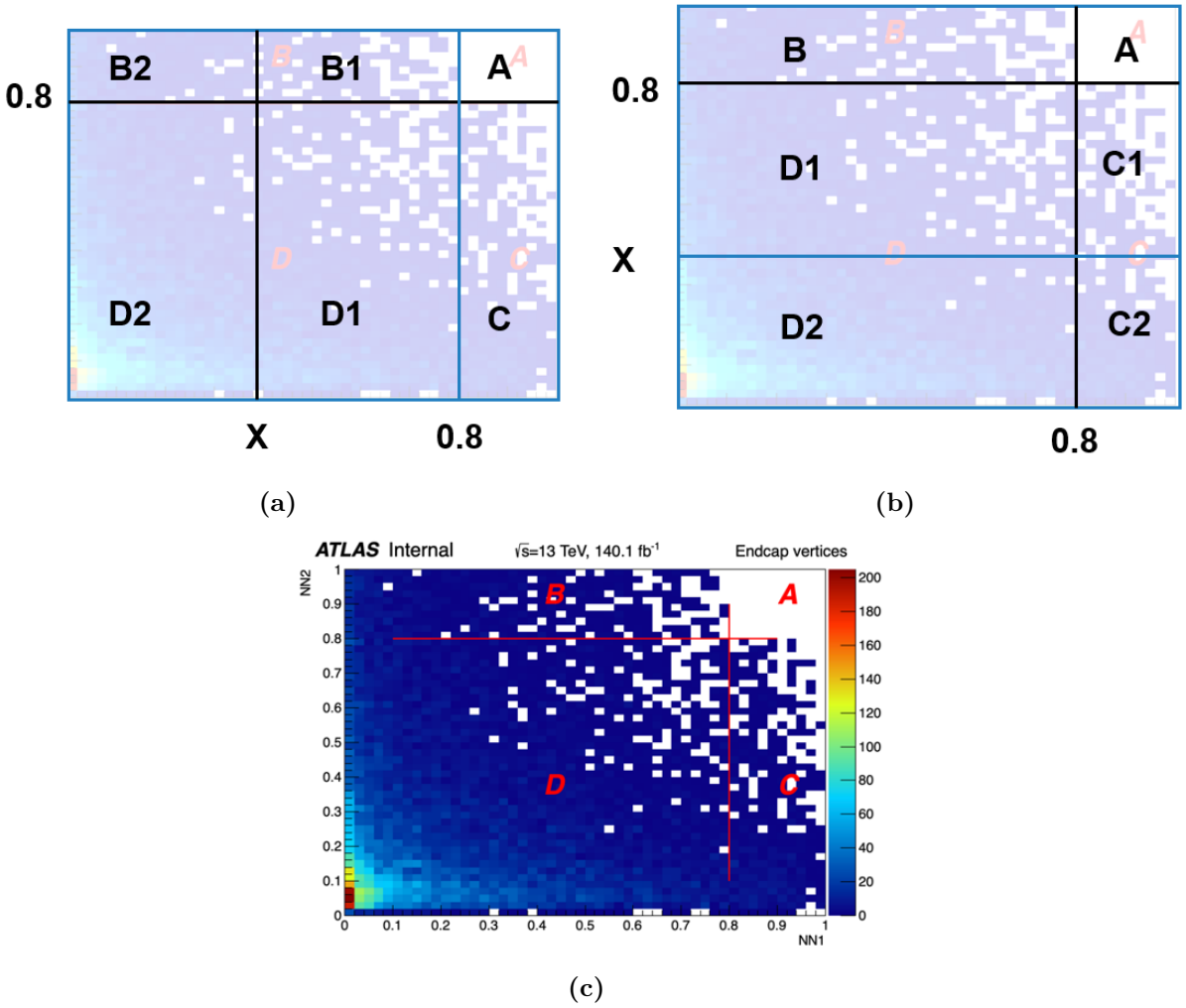

Figure 8.17: Overlay diagrams demonstrating subplane validation method for endcap region. The X division is variable and was set to seven different values between 0.1 and 0.7. (a) Overlay of the BD subplane used as ABCD validation. (b) Overlay of CD subplane used for ABCD validation. (c) Blinded ABCD plane for Run 2 data in the endcap region.

Figures 8.19–8.22 show the ABCD planes for the SM Higgs $H \to ss$ samples under the SR selection criteria, ($H_{\mathrm{T}}^{\mathrm{miss}} > 40\,\mathrm{GeV}$). As can be seen, a considerable number of signal events enter into the B, C, and D regions for most samples. Signal contamination outside of the SR could impact the expected number of events in the A-region, which risks masking the presence of true signal. The signal MC samples were used to estimate the number of signal events expected to fall outside of the SR compared to the expected background in those regions. The expected number of signal events observed outside of the A region for these SM Higgs samples is given in Tables 8.9 and 8.10.

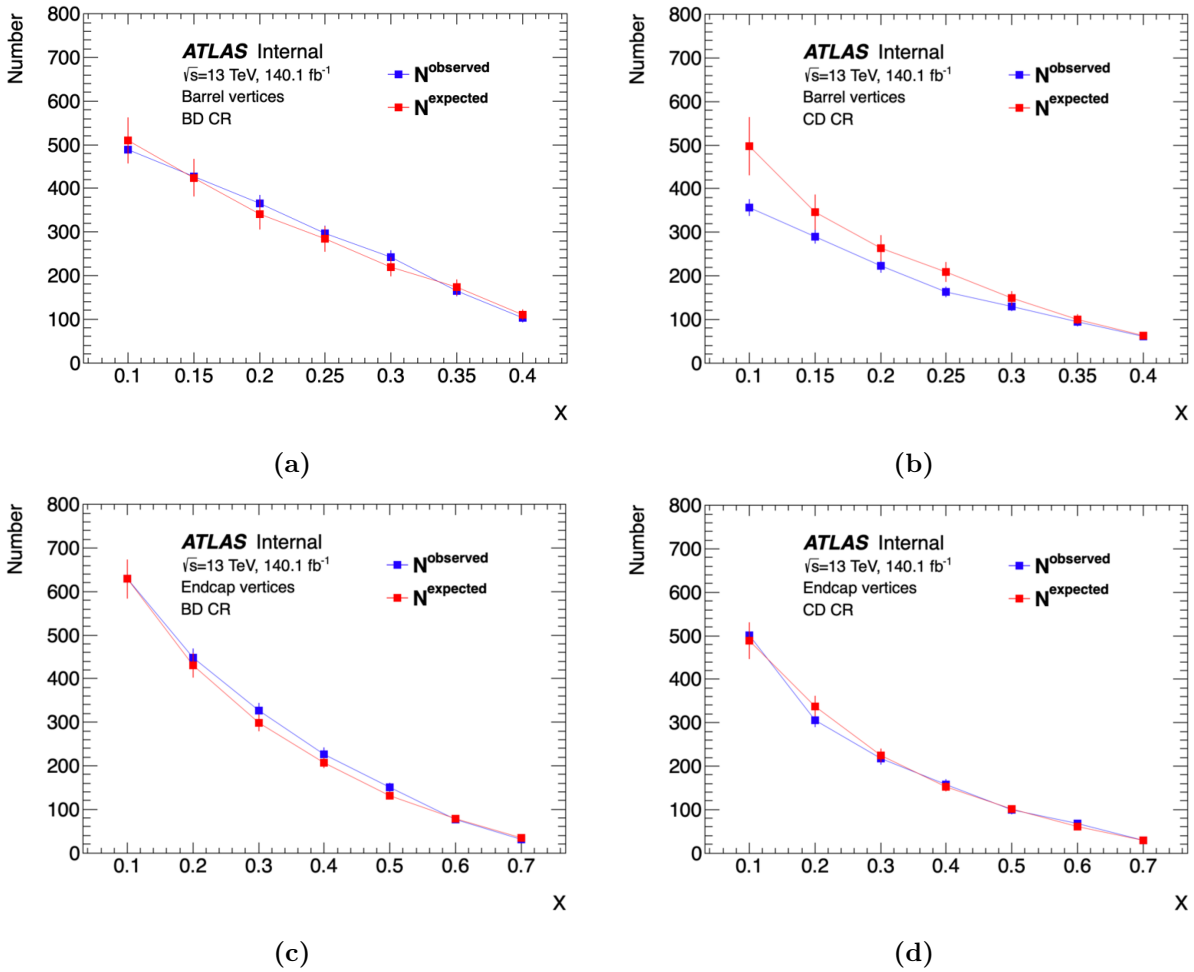

Figure 8.18: Number of observed events, N^{observed} (blue), compared to number of expected events N^{expected} (red) in Run 2 data for (a) the BD subplane of the barrel ABCD plane, (b) the CD subplance of the barrel ABCD plane, (c) the BD subplane of the endcap ABCD plane, and (d) the CD subplane of the endcap ABCD plane.

This signal contamination must also be accounted for when estimating the significance of events present in the signal region, or the upper limits on the LLP production process in the case that no signal events are observed. This contamination is taken into account by using a simultaneous ABCD likelihood fit in all four ABCD regions, across all ABCD planes. This method is described in more detail in Section 9.1.

		Barrel VR			Endcaps VR		
	m_S	MC	Data	S/B	MC	Data	S/B
$H \to ss$	5	0	1287	0	23	6822	0.003
	16	12		0.01	56		0.008
	35	11		0.009	61		0.009
	55	3		0.002	24		0.004

Table 8.9: The signal contamination across B, C, and D in the VR for the $H \to ss$ samples with SM Higgs mass, assuming the SM Higgs production cross section and a 1% branching ratio to LLPs, separated by barrel and endcap. The total number of background events (Data), as well as the signal-to-background (S/B) ratio are also shown. The S/B shows very little signal contamination outside of the A region for the VR selection.

		Barrel VR			Endcaps VR		
	m_χ	MC	Data	S/B	MC	Data	S/B
$\chi \to cbs$	10	3	1287	0.002	9	6822	0.001
$\chi \to bb\nu$	10	2		0.002	9		0.001
$\chi \to \tau\tau\nu$	10	31		0.02	208		0.03

Table 8.10: The signal contamination across B, C, and D in the VR for the $H \to \chi\chi$ samples with SM Higgs mass, assuming the SM Higgs production cross section and a 1% branching ratio to LLPs, separated by barrel and endcap. The total number of background events (Data), as well as the signal-to-background (S/B) ratio are also shown. The S/B shows very little signal contamination outside of the A region for the VR selection.

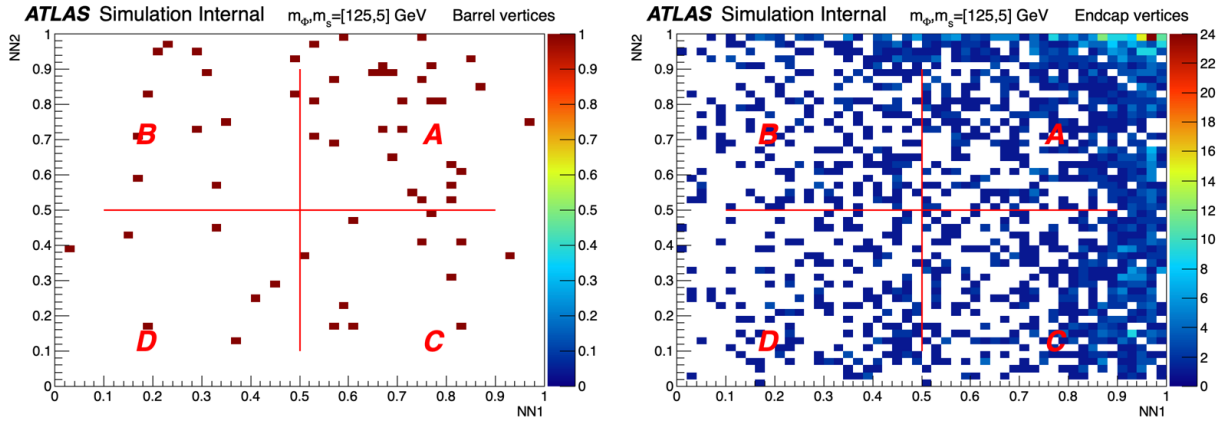

(a) (b)

Figure 8.19: ABCD planes for $H \to ss$ signal with $m_H = 125\,\text{GeV}, m_s = 5\,\text{GeV}$ in the barrel and endcap regions in the signal region.

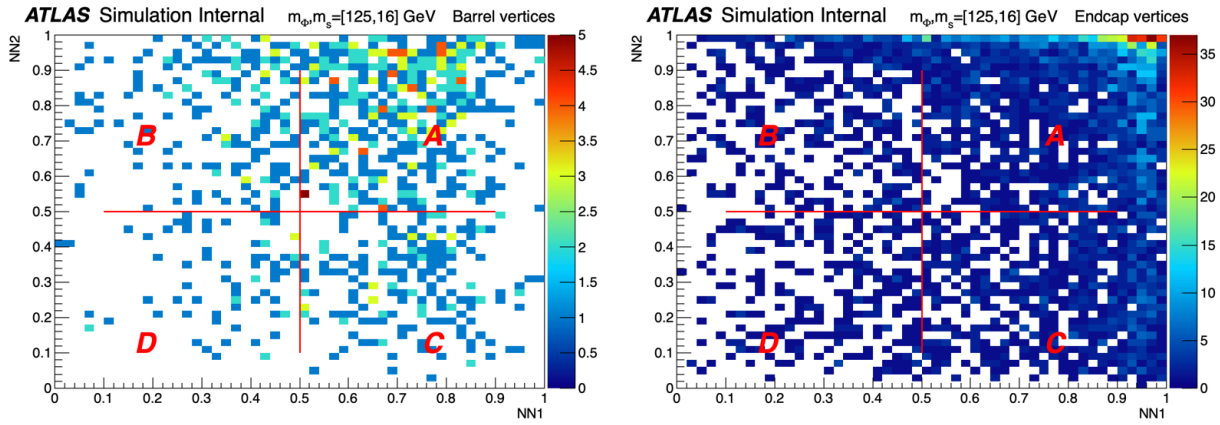

(a) (b)

Figure 8.20: ABCD planes for $H \to ss$ signal with $m_H = 125\,\text{GeV}, m_s = 16\,\text{GeV}$ in the barrel and endcap regions in the signal region.

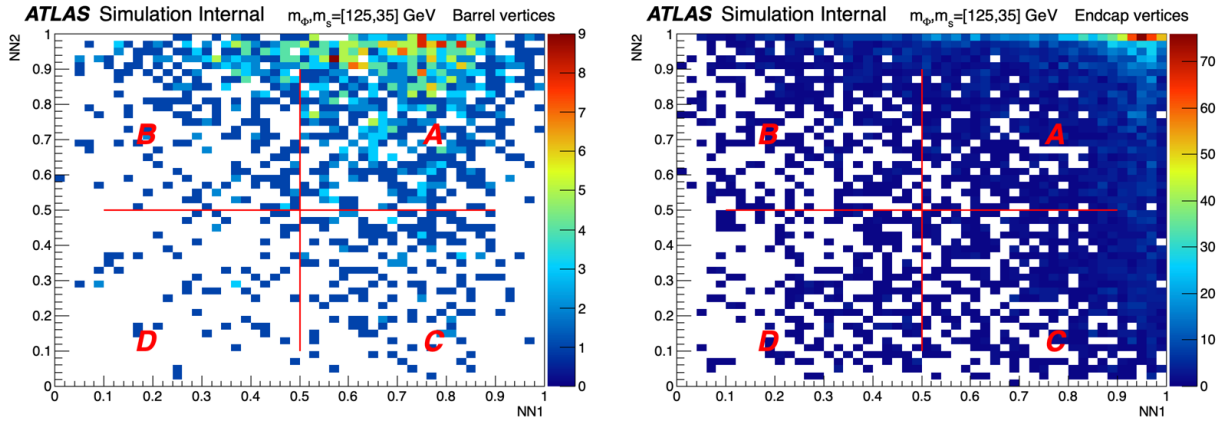

(a) (b)

Figure 8.21: ABCD planes for $H \to ss$ signal with $m_H = 125\,\text{GeV}, m_s = 35\,\text{GeV}$ in the barrel and endcap regions in the signal region.

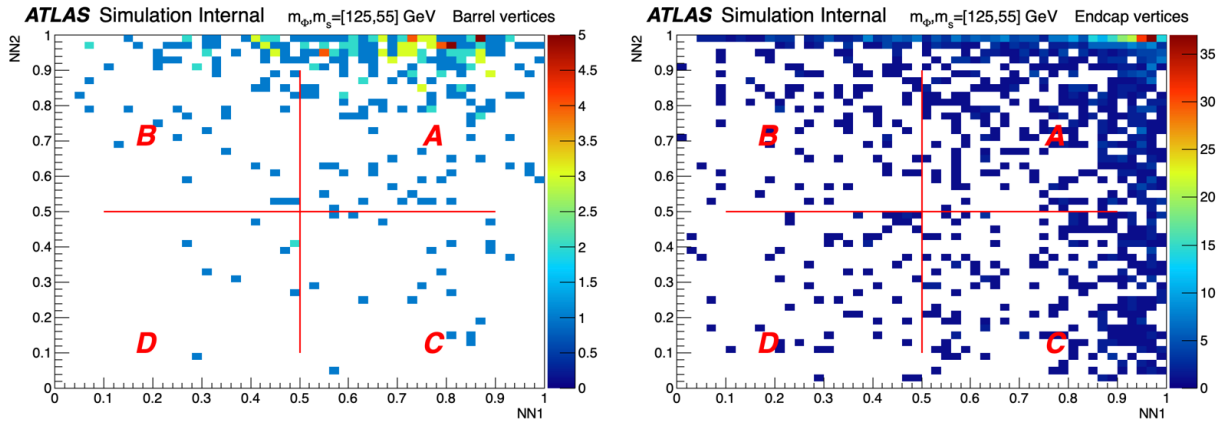

(a) (b)

Figure 8.22: ABCD planes for $H \to ss$ signal with $m_H = 125\,\text{GeV}, m_s = 55\,\text{GeV}$ in the barrel and endcap regions in the signal region.

8.3.4 Non-Collision Background Estimation

Non-collision background (NCB) primarily arises from beam induced sources and cosmic ray muons, both of which were briefly described in Section 8.1. Beam induced backgrounds (BIB) arise from interactions of beam protons with residual gas molecules in the beam pipe or with components of the detector [155]. Cosmic ray muons can enter through the top of ATLAS, mainly through the two access shafts, and leave signatures in the detector [156]. Since both sources of background have the potential to produce fake MS vertices, it is necessary to estimate the NCB contribution to signal events.

The late stream data, described in Section 4.1.1 was used to estimate the NCB contribution to our signal events. All selection described in Table 8.2 were applied except the ATLAS cleaning criteria. The ATLAS cleaning criteria were excluded because late stream data, being composed of empty and half-filled bunch crossings (BCs), cannot have a good primary vertex (PV). The number of events passing all other selection were then multiplied by two factors, R_{live} and R_{clean}, making the full expression

$$N_i^{\text{Main data}} = N_i^{\text{NCB data}} \cdot R_{\text{live}} \cdot R_{\text{clean}} \tag{8.5}$$

where the subscript $i = \{\text{cosmics},\ \text{BIB}\}$, since the background contributions are calculated separately for each NCB source.

The factors R_{live} and R_{clean} are ratios. The ratios are shown in Eqs. 8.6 and 8.7.

$$R_{\text{live}}^{\text{cosmics}} = \frac{N_{(\text{Paired BC})}}{N_{(\text{Empty BC})}} \quad ; \quad R_{\text{live}}^{\text{BIB}} = \frac{N_{(\text{Paired BC})}}{N_{(\text{Unpaired BC})}} \tag{8.6}$$

$$R_{\text{clean}} = \frac{N_{(track\ sel)}}{N_{(track-free\ sel)}} \tag{8.7}$$

The R_{live} factor is a ratio of the number of paired bunch crossings, $N_{(\text{Paired BC})}$, divided by either the number of empty bunch crossings, $N_{(\text{Empty BC})}$, for cosmic NCB, or the number of unpaired bunch crossings, $N_{(\text{Unpaired BC})}$, for BIB NCB. This produces a reweighting factor used to scale the number of events in the NBC data sample to match the number of events in the main stream data. The R_{clean} factor is the ratio of the number of main stream data

events that pass all event selection criteria, $N_{(\text{track sel})}$, divided by the number that pass a set of "track-free" selection, $N_{(\text{track-free sel})}$. This set of track-free selection criteria includes all event selection except those involving ID tracks: the minimum ΔR isolation selection on high-p_{T} tracks, and sum of track p_{T} isolation for low-p_{T} tracks. This ratio gives a reweighting factor that scales the selection efficiency in the NCB data, which will have no tracks from hard scatter, to the selection efficiency in main stream data.

Each data-taking year was treated separately. After applying all event selection, only 6 events were found to enter the ABCD plane across all of the late stream data collected in Run 2, and all events came from empty bunch crossings. For this reason, only the cosmic live time, $R_{\text{live}}^{\text{cosmics}}$, was calculated. The number of late stream events passing all selection with empty bunch crossings (N_{cosmics}) and with unpaired bunch crossings (N_{BIB}), the values for R_{live} and R_{clean}, and the final estimates for NCB contributions in the ABCD plane are shown in Table 8.11.

Year	N_{cosmics}	N_{BIB}	$R_{\text{live}}^{\text{cosmics}}$	$R_{\text{live}}^{\text{BIB}}$	R_{clean}	Cosmic NCB	BIB NCB
2016	4	0	$2.12 \pm (3 \times 10^{-7})$	–	0.309 ± 0.007	$2.62^{+4.69}_{-1.37}$	$0^{+1.21}_{-0.00}$
2017	2	0	$2.36 \pm (4 \times 10^{-7})$	–	0.282 ± 0.005	$1.33^{+3.08}_{-0.47}$	$0^{+1.22}_{-0.00}$
2018	0	0	$3.56 \pm (6 \times 10^{-7})$	–	0.279 ± 0.005	$0.00^{+1.83}_{-0.00}$	$0^{+1.83}_{-0.00}$

Table 8.11: Summary of non-collision backgrounds estimates for Run 2 data using empty and unpaired bunch crossings. The raw number of passing events from cosmic ray muon (cosmics) and beam induced backgrounds (BIB) sources are shown along with NCB estimates from each source, separated by data-taking year. Reweighting factors $R_{\text{live}}^{\text{cosmics}}$ and R_{clean} are also shown for each data-taking year. $R_{\text{live}}^{\text{BIB}}$ was not calculated since no events with unpaired bunch crossings passed the selection applied.

Because the total contribution from NCB entering the ABCD plane in each data-taking year is only a few events, and the amount of data events entering the ABCD plane is $\sim O\,(1000)$ in both the barrel and endcaps, contributions from NCB are negligible and no additional corrections are necessary.

8.4 Lifetime Extrapolation

The goal of the lifetime extrapolation procedure is to estimate the number of expected signal events that pass the selection criteria at lifetimes other than those at which the full simulation (full-sim) MC samples were generated.

Each full-sim MC sample is generated with a fixed LLP lifetime, the generated lifetime or $c\tau_{\text{gen}}$, assigned to the truth-level LLPs. This lifetime was chosen by members of the UEH subgroup to maximize the signal yields of all analyses that would make use of these samples. Since this search places no strong constraints on the possible lifetimes of the truth-level LLPs, it is desirable to be able to make some statement about the sensitivity to LLP production at higher and lower lifetimes.

Unfortunately, generating new full-sim samples at each possible lifetime with sufficient statistics is prohibitively expensive in terms of sample production time, disk-space, and other computing resource usage. Instead, a procedure to extrapolate the expected signal yields from full-sim generated lifetimes was developed. With an adequately robust extrapolation procedure, it is possible to set reasonable sensitivity limits across a wide range of LLP lifetimes without the need to produce excessive numbers of fully simulated MC samples.

To do this, fully simulated "full-sim" signal MC are used in order to calculate efficiencies associated with the truth-level LLPs used to generate reconstruction-level MS vertices. Sections 8.4.1–8.4.3 explain the different parts of the lifetime extrapolation procedure. For simplicity, the term "LLP" will be used exclusively when referring to the truth-level particles and "MSVtx" will be used exclusively to refer to the reconstructed displaced vertex for the remainder of this section.

8.4.1 Overview

In general, the expected number of signal events, N_{evt}, is given by

$$N_{\text{evt}} = \sigma \cdot \epsilon \cdot \int L dt \tag{8.8}$$

where L is the instantaneous luminosity, σ is the cross section of the process of interest,

and ϵ is some selection efficiency. The cross section here could represent the full process of Higgs production from gluon-gluon fusion, then LLP production from that Higgs decay. Multiplied by the integrated luminosity, it could represent the number of true LLP events delivered by the LHC.

In a similar way, the number of events that pass the event selection can be thought of as a product of the total number of signal events and the selection efficiency. It would be expected that the selection efficiency decreases when the proper decay length, $c\tau$, falls outside of the detector fiducial region where this analysis is sensitive. For this reason, the selection efficiency can be modeled as being a function of the LLP lifetime, making the signal yield a function of $c\tau$:

$$N_{\text{yield}}(c\tau) = N_{\text{total}} \cdot \epsilon_{\text{selection}}(c\tau) \tag{8.9}$$

where N_{total} represents the total number of LLPs in a given MC sample and $\epsilon_{\text{selection}}(c\tau)$ represents the $c\tau$-dependent efficiency.

Because the selection criteria from Table 8.2 are sensitive to the kinematics and decay location of the LLP, both the number of events and efficiency are expected to be a function of the LLP decay location as well as the LLP Lorentz boost, β. To account for this, the number of LLPs and the selection efficiency are parameterized by the LLP decay location and boost:

$$N_{\text{yield}}(c\tau, L_{\text{xyz}}, \beta_{\text{LLP}}) = N_{\text{total}}(L_{\text{xyz}}, \beta_{\text{LLP}}) \cdot \epsilon_{\text{selection}}(c\tau, L_{\text{xyz}}, \beta_{\text{LLP}}) \tag{8.10}$$

where L_{xyz} is the LLP decay location and β_{LLP} is the LLP boost.

With finite statistics, continuous functions for N_{total} and $\epsilon_{\text{selection}}$ cannot be produced with any reasonable statistical uncertainty, so the parameter ranges are separated into discrete bins. In this way, $\epsilon_{\text{selection}}$ becomes a discrete value defined in bins of L_{xyz} and β_{LLP}, and so can be visualized as 2D histograms. An example of the efficiency 2D histograms can be seen in Figure 8.23. The number of events, N_{total}, are MC generated events and so become grouped into bins of L_{xyz} and β_{LLP}. For this reason, N_{total} can also be treated as a binned quantity, and the ij^{th} bin, N^{ij}_{total}, can be used.

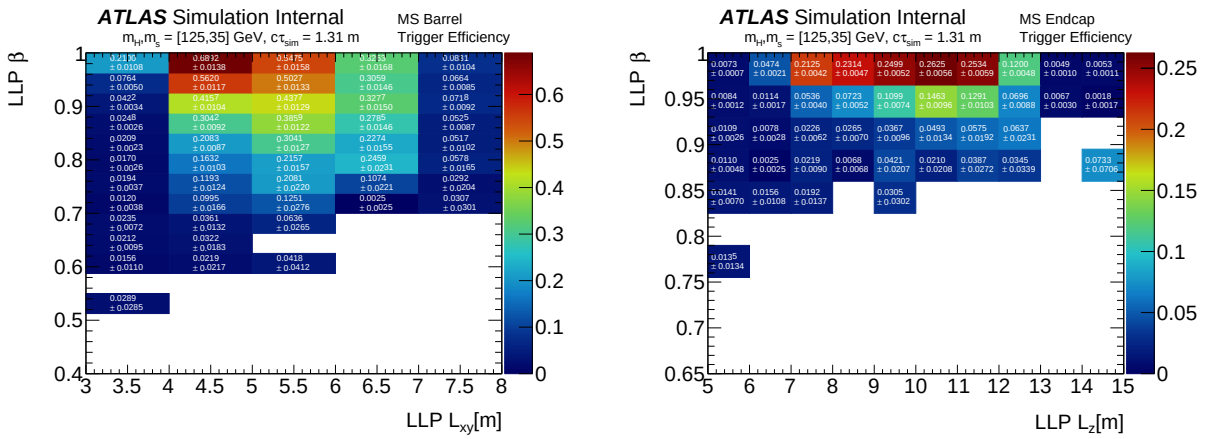

(a) Trigger Efficiency in the Barrel

(b) Trigger Efficiency in the Endcap

Figure 8.23: Example of the discrete binning in LLP β and LLP decay location L_{xy} (L_z) of the selection efficiency for $m_H = 125\,\text{GeV}$ and $m_s = 35\,\text{GeV}$ in the (a) barrel region and (b) endcap regions.

Because N^{ij}_{total} is the total number of truth-level LLPs, it is not necessary to run the time-intensive full-sim reconstruction on LLP signal MC to produce this distribution. Instead, truth-only "toy" signal MC events can be used to sample this distribution. This is an additional advantage of the toy MC lifetime extrapolation procedure: by factoring out the selection as an efficiency, the need for large full-sim samples in order to accurately estimate signal yields is eliminated. Instead, full-sim statistics only enters the procedure as a statistical uncertainty associated with the selection efficiency. In fact, information from the full-sim samples and selection criteria only enter the lifetime extrapolation procedure through the trigger and reconstruction efficiencies, making the procedure quite versatile.

Because of the vertex reconstruction mismodeling between the data and signal MC, as discussed in Section 7.4, it is useful to separate the selection efficiency into a trigger efficiency and a vertex reconstruction efficiency. The trigger efficiency reflects the fraction of signal MC events accepted by the trigger. The vertex reconstruction efficiency (or "vertex efficiency") reflects the fraction of signal MC events, which already pass the trigger, that also have a good vertex, which passes the selection criteria described in Table 8.2. Equation 8.10 can be modified to express this as shown in 8.11:

$$N_{\text{yield}}(c\tau) = \sum_{i \text{ bins}}^{L_{xyz}} \sum_{j \text{ bins}}^{\beta_{\text{LLP}}} N^{ij}_{\text{total}} \cdot \epsilon^{ij}_{\text{trig}}(c\tau) \cdot S_{\text{vtx}}\ \epsilon^{ij}_{\text{vtx}}(c\tau)$$
$$\text{with}\quad \epsilon^{ij}_{\text{selection}}(c\tau) = \epsilon^{ij}_{\text{trig}}(c\tau) \cdot \epsilon^{ij}_{\text{vtx}}(c\tau) \tag{8.11}$$

where i indexes the L_{xyz} bins and j indexes the β_{LLP} bins. N^{ij}_{total}, $\epsilon^{ij}_{\text{trig}}(c\tau)$, and $\epsilon^{ij}_{\text{vtx}}(c\tau)$ represent the number of LLPs, the $c\tau$-dependent trigger efficiency, and the $c\tau$-dependent vertex efficiency, respectively, in the i^{th} bin in L_{xyz}, and the j^{th} bin in β_{LLP}. Since Eq. 8.11 is expressed as a sum over all considered bins, $N_{\text{yield}}(c\tau)$ is the number of expected passing signal MC events as a function of $c\tau$. The vertex efficiency is also multiplied by the global vertex reconstruction mismodeling scale factor, S_{vtx}, discussed in Section 7.4. In actuality, Eq. 8.11 is used twice: once with the term L_{xyz} replaced with the transverse radial distance, L_{xy} for LLPs produced in the barrel region, then separately with L_{xyz} replaced with the longitudinal displacement, $|L_{\text{z}}|$, for LLPs produced in the endcap region.

Each efficiency is then estimated by taking the ratio of events passing the corresponding selection divided by the total number of events considered. For the trigger efficiency, all events that have exactly one LLP decay located in the detector fiducial region are considered. For the reconstruction efficiency, all events passing the trigger are considered. The efficiencies are defined in Eq. 8.12:

$$\epsilon^{ij}_{\text{trig}}(c\tau) = \frac{\hat{N}^{ij}_{\text{passTrig}}}{\hat{N}^{ij}_{\text{total}}}$$
$$\epsilon^{ij}_{\text{vtx}}(c\tau) = \frac{\hat{N}^{ij}_{\text{passReco}}}{\hat{N}^{ij}_{\text{passTrig}}} \tag{8.12}$$

where $\hat{N}$ is used to indicate the number of events from full-sim signal MC (as opposed to toy MC). $\hat{N}^{ij}_{\text{total}}$ is the total number of full-sim signal MC events in the ij^{th} bin with exactly one LLP decay in the detector fiducial region. $\hat{N}^{ij}_{\text{passTrig}}$ is the number of single LLP full-sim events that pass the LLP trigger in the ij^{th} bin. $\hat{N}^{ij}_{\text{passReco}}$ is the number of single LLP full-sim events that pass all of the vertex reconstruction and signal selection criteria, summarized in Table 8.2. Since each event should have only one LLP associated with it in the single vertex channel, the number of events and number of LLPs are equivalent. An

example of the trigger efficiency has been shown in Figure 8.23.

For the vertex efficiency, only those events that passed the LLP trigger are considered. The denominator in each of those bins is then the same as the numerator in the trigger efficiency. The numerator of the vertex efficiency is a little more complicated, as the vertex selection criteria described in 8.2 are defined in terms of an *MSVtx*, not the LLP. To get a passing number of LLPs, ΔR-matching between the LLP and the MSVtx is used. An MSVtx is considered matched to an LLP if the ΔR between them is less than 0.4. If a matched MSVtx fails one of the vertex selection criteria and would be rejected, the matched LLP is rejected and is not counted in the vertex efficiency numerator. If an LLP cannot be matched to an MSVtx, then the MSVtx would fail the selection criteria and wouldn't be passed anyway. If an event has two LLPs in the detector fiducial region, the event is skipped. This is done so only the events that are able to produce a single MSVtx are considered. The vertex efficiency then takes the form of

$$\epsilon_{vtx}^{ij} = \frac{N_{\text{pass}}^{ij}}{N_{\text{pass trig}}^{ij}} \tag{8.13}$$

where ϵ_{vtx}^{ij} is the vertex efficiency, in the $(i,j)^{th}$ bin, N_{pass}^{ij} is the number of events passing all cutflow criteria and have an LLP matched to an MSVtx, and $N_{\text{pass trig}}^{ij}$ is all events in the $(i,j)^{th}$ bin passing the trigger and event cleaning criteria. An example of the vertex efficiency can be seen in Figure 8.24.

8.4.2 Extrapolation Procedure

To get an expected signal yield as a function of $c\tau$, 100 points are sampled between 0.01 m and 200 m, covering the region where the greatest sensitivity is expected. The points are distributed exponentially as in Eq. 8.14, so more samples are taken at lower $c\tau$ and the points are evenly distributed when plotted on a log scale,

$$c\tau_n = c\tau_{\text{min}} \cdot \left(\frac{c\tau_{\text{max}}}{c\tau_{\text{min}}}\right)^{\frac{n}{(N-1)}} \tag{8.14}$$

where $c\tau_n$ is the n^{th} sampled value of $c\tau$, starting at $n = 0$. $c\tau_{\text{min}}$ and $c\tau_{\text{max}}$ are the minimum and maximum sampled value of $c\tau$, respectively, and N is the total number of

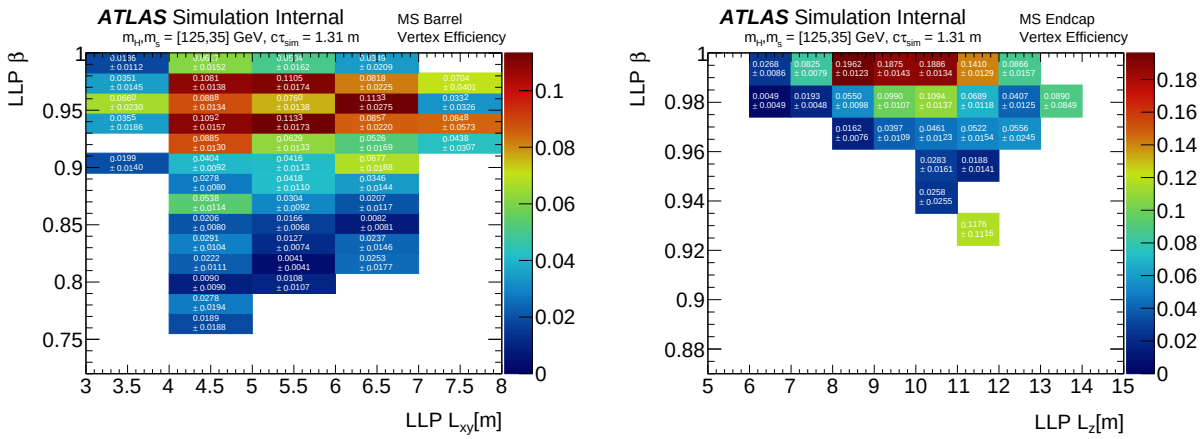

(a) Vertex Efficiency in the Barrel

(b) Vertex Efficiency in the Endcap

Figure 8.24: Example of the discrete binning in LLP β and LLP decay location L_{xy} (L_z) of the vertex reconstruction efficiency for $m_H = 125\,\text{GeV}$ and $m_s = 35\,\text{GeV}$ in the (a) barrel and (b) endcaps.

points sampled.

For each sampled value of $c\tau$, all toy signal MC events are analyzed. For each of the two LLPs in each toy event, the LLP boost and Lorentz factor are used along with the sampled value of $c\tau$ to resample the lab frame decay length. The probability distribution, from which the new lab-frame decay length is sampled, is given by

$$L_{\text{xyz},n}\left(t|\tau_n,\beta,\gamma\right) = \exp\left(\frac{-t}{\beta\gamma c\tau_n}\right) \tag{8.15}$$

where β is the Lorentz boost, γ is the Lorentz factor, $c\tau_n$ is the sampled $c\tau$ given by Eq. 8.14, and $L_{\text{xyz},n}$ is the lab frame decay length probability distribution at $c\tau_n$, and t is the survival time in the lab-frame. The two LLP decay locations are then checked to make sure that only one of them is inside the detector fiducial region. If the event doesn't have exactly one LLP in the fiducial region, the event is rejected.

In order to determine whether the LLP would have passed the LLP trigger, the trigger efficiency, calculated using the full-sim signal MC, is used. The toy LLP boost, along with the new decay location, is used to sample the trigger efficiency from the appropriate (i,j) bin in the trigger efficiency histogram. A random number in the range [0,1) is sampled from a uniform probability distribution. If the random number is less than the value of ϵ_{trig} for this LLP, the event is said to have passed the trigger. The same process is used to check if

the event passes the vertex efficiency times the reconstruction scale factor, $S_{\text{vtx}} \cdot \epsilon_{\text{vtx}}$. Since all instances of the vertex efficiency will have this scale factor applied, going forward the vertex efficiency refers to this product. This process is repeated for every toy MC event.

Once the final number of passing toy MC events have been counted, this number can be rescaled by the following equation to give an estimate to the number of events expected in $140.1\,\text{fb}^{-1}$ of data:

$$\begin{aligned} N_{\text{SM yield}}^{\text{Run2}} &= N_{\text{yield}} \cdot \left(\sigma_{\text{Higgs}}^{\text{SM}} \times \frac{\mathcal{L}^{\text{Run2}}}{N_{\text{total}}^{\text{toyMC}}} \right) \\ &= \frac{N_{\text{yield}}}{N_{\text{total}}^{\text{toyMC}}} \cdot \left(48.61\,\text{pb} \cdot 140.1\,\text{fb}^{-1}\right) \end{aligned} \tag{8.16}$$

where $N_{\text{yield}}^{\text{Run2}}$ is the expected yield in Run 2 data, $\sigma_{\text{Higgs}}^{\text{SM}}$ is the SM Higgs production cross section, $\mathcal{L}^{\text{Run2}}$ is the integrated luminosity for Run 2 data, and $N_{\text{total}}^{\text{toyMC}}$ is the total number of toy MC samples used to generate N_{yield}, itself the raw count of toy MC events that passed the extrapolation procedure. For samples with a non-SM Higgs mass, the production cross section is set to 1 pb.

$$N_{\text{non-SM yield}}^{\text{Run2}} = \frac{N_{\text{yield}}}{N_{\text{total}}^{\text{toyMC}}} \cdot \left(1\,\text{pb} \cdot 140.1\,\text{fb}^{-1}\right) \tag{8.17}$$

The extrapolation steps for the single vertex channel are as follows:

1. Starting with $c\tau = 0.01\,\text{m}$, generate a random decay position for each of the two LLPs, sampled from an exponential distribution, Eq. 8.15.
2. Calculate the physical decay position in the detector for each of the particles, using their 4-momenta, preserving the original η and ϕ directions.
3. Determine if the resulting decay position topology is a detectable one, thus worth keeping. Since only events with one LLP decay within the fiducial region are considered for this analysis, the resulting decay topologies are classified into two categories:
   (a) Barrel MS: Exactly one particle decays with $|\eta| < 0.8,\ 3\,\text{m} < L_{\text{xy}} < 8\,\text{m}$.
   (b) Endcap MS: Exactly one particle decays with $1.3 < |\eta| < 2.5,\ 5\,\text{m} < |L_{\text{z}}| < 15\,\text{m},\ L_{\text{xy}} < 3\,\text{m}$.

4. Each topology has a distinct set of trigger and vertex reconstruction efficiencies and thus a slightly different procedure. They are outlined individually below:

   (a) Barrel MS

      i. Determine if the barrel decay is in time with respect to the Level-1 barrel trigger response in data. The decay is considered "in time" if its randomly generated probability is less than the efficiency for the RPC response at the particle's delay time, Δt. The particle delay time is the difference between its time of flight and that of a particle traveling at c [147]. This is to correct for how the RPC timing response is modeled in MC simulation.

      ii. If the event is in time, determine if it will pass the LLP muon RoI cluster trigger by using the estimated efficiency for the trigger, ϵ_{trig}, where the LLP decays in the barrel.

      iii. If the event passes the trigger, the MS vertex reconstruction efficiency ϵ_{vtx} is tested. If the decay "reconstructs" a vertex, the event is counted as a good event.

   (b) Endcap MS

      i. Determine if the endcap decay is in time ($\Delta t < 25\,\text{ns}$).

      ii. If the event is in time, determine if it will pass the LLP muon RoI cluster trigger by using the estimated efficiency for the trigger ϵ_{trig}.

      iii. If the event passes the trigger, the MS vertex reconstruction efficiency ϵ_{vtx} is tested. If the decay "reconstructs" a vertex, the event is counted as a good event.

5. Steps 2 through 4 are repeated for 100 values of $c\tau$ between 0.05 m and 100 m or 0.1 m and 200 m with an exponential spacing. The step size is changed because the change in efficiency between $c\tau$ values decreases with higher $c\tau$, so a linear spacing would be excessive at higher $c\tau$. The reason some samples have different $c\tau$ ranges is based on where the $c\tau$ peak of each sample is expected to be. For those samples generated at a higher $c\tau$, or which are expected to have a wider sensitivity range, a larger $c\tau$ range is required.

6. The final result is the expected number of signal events as a function of proper lifetime for each detector region. The total selection efficiency is found by dividing the yield by the total number of toy MC events. For each detector region, this efficiency is rescaled by the Higgs production cross section multiplied by the Run 2 integrated luminosity, as shown in Eq. 8.16. This rescaling is done to obtain the number of expected signal events in $140.1\,\text{fb}^{-1}$ of data.

The results of the lifetime extrapolation process can be seen for several of the signal MC samples in Figures 8.26–8.30. Tables comparing the trigger and total (trigger × reco) selection efficiencies between the full-sim sample and its lifetime extrapolation result, at the generated $c\tau$ used for full-sim ($c\tau_{\text{gen}}$), can be seen in Tables 8.12–8.15.

m_Φ	m_s	Lifetime [m]	$f_{trig}^{toy\ estimation}$	$f_{trig}^{fullsim}$	% difference
125	5	0.127	$0.0952^{+0.0062}_{-0.0061}$	0.0950 ± 0.0010	0.21%
125	5	0.411	$0.0710^{+0.0047}_{-0.0047}$	0.0713 ± 0.0006	0.38%
125	16	0.580	$0.1532^{+0.0061}_{-0.0063}$	0.1515 ± 0.0011	1.12%
125	35	1.310	$0.1414^{+0.0055}_{-0.0054}$	0.1391 ± 0.0009	1.62%
125	35	2.630	$0.1231^{+0.0056}_{-0.0056}$	0.1219 ± 0.0009	1.01%
125	55	1.050	$0.1212^{+0.0045}_{-0.0048}$	0.1109 ± 0.0007	9.29%
125	55	5.320	$0.0604^{+0.0055}_{-0.0054}$	0.0576 ± 0.0007	4.85%
60	5	0.217	$0.0430^{+0.0026}_{-0.0027}$	0.0435 ± 0.0005	1.28%
60	16	0.661	$0.0662^{+0.0046}_{-0.0046}$	0.0658 ± 0.0007	0.62%
200	50	1.255	$0.2190^{+0.0127}_{-0.0124}$	0.2168 ± 0.0020	1.01%
400	100	1.608	$0.3628^{+0.0149}_{-0.0147}$	0.3625 ± 0.0022	0.10%
600	50	0.590	$0.4467^{+0.0097}_{-0.0097}$	0.4474 ± 0.0018	0.17%
600	150	1.840	$0.4471^{+0.0114}_{-0.0115}$	0.4462 ± 0.0018	0.19%
600	150	3.309	$0.4098^{+0.0155}_{-0.0154}$	0.4101 ± 0.0024	0.08%
600	275	4.288	$0.1847^{+0.0062}_{-0.0060}$	0.1815 ± 0.0008	1.73%
1000	50	0.406	$0.5116^{+0.0103}_{-0.0104}$	0.5108 ± 0.0018	0.16%
1000	275	2.399	$0.5329^{+0.0121}_{-0.0120}$	0.5363 ± 0.0018	0.64%
1000	275	4.328	$0.4855^{+0.0164}_{-0.0162}$	0.4894 ± 0.0024	0.80%
1000	475	6.039	$0.1611^{+0.0051}_{-0.0051}$	0.1599 ± 0.0008	0.81%

Table 8.12: Fraction of $H \to ss$ toy MC events passing trigger selection criteria in the lifetime extrapolation at the sample $c\tau_{\text{gen}}$, compared with the trigger efficiency calculated in the full-sim MC.

Channel	m_χ	Lifetime [m]	$f_{trig}^{toy\ estimation}$	$f_{trig}^{fullsim}$	% difference
$bb\nu$	10	0.920	$0.1085^{+0.0055}_{-0.0056}$	0.1089 ± 0.0010	0.29%
$bb\nu$	55	5.550	$0.0383^{+0.0048}_{-0.0047}$	0.0362 ± 0.0006	5.72%
$bb\nu$	100	3.500	$0.2043^{+0.0090}_{-0.0090}$	0.2114 ± 0.0013	3.37%
cbs	10	0.920	$0.1084^{+0.0052}_{-0.0052}$	0.1077 ± 0.0010	0.59%
cbs	55	5.550	$0.0682^{+0.0072}_{-0.0071}$	0.0660 ± 0.0010	3.34%
cbs	100	3.500	$0.3200^{+0.0098}_{-0.0098}$	0.3325 ± 0.0015	3.75%
$\tau\tau\nu$	10	0.920	$0.0289^{+0.0028}_{-0.0029}$	0.0286 ± 0.0005	1.27%
$\tau\tau\nu$	55	5.550	$0.0113^{+0.0027}_{-0.0027}$	0.0110 ± 0.0003	2.53%
$\tau\tau\nu$	100	3.500	$0.0807^{+0.0061}_{-0.0061}$	0.0844 ± 0.0009	4.36%

Table 8.13: Fraction of $H \to \chi\chi$ toy MC events passing trigger selection criteria in the lifetime extrapolation at the sample $c\tau_{\text{gen}}$, compared with the trigger efficiency calculated in the full-sim MC. The mediator mass for all samples is 125 GeV.

m_Φ	m_s	Lifetime [m]	$\epsilon_{global}^{toy\ estimation}$	$\epsilon_{global}^{fullsim}$	% diff.	$\frac{\lvert\epsilon_{toy}-\epsilon_{fullsim}\rvert}{\sqrt{\sigma_{toy}^2+\sigma_{fullsim}^2}}$
125	5	0.127	$0.800^{+0.292}_{-0.294} \cdot 10^{-3}$	$0.797 \pm 0.044 \cdot 10^{-3}$	0.45%	0.009
125	5	0.411	$0.535^{+0.219}_{-0.206} \cdot 10^{-3}$	$0.592 \pm 0.032 \cdot 10^{-3}$	9.62%	0.188
125	16	0.580	$1.819^{+0.551}_{-0.533} \cdot 10^{-3}$	$1.847 \pm 0.058 \cdot 10^{-3}$	1.48%	0.036
125	35	1.310	$2.033^{+0.600}_{-0.614} \cdot 10^{-3}$	$2.125 \pm 0.054 \cdot 10^{-3}$	4.33%	0.107
125	35	2.630	$1.644^{+0.523}_{-0.529} \cdot 10^{-3}$	$1.851 \pm 0.060 \cdot 10^{-3}$	11.19%	0.278
125	55	1.050	$0.361^{+0.117}_{-0.108} \cdot 10^{-3}$	$0.347 \pm 0.010 \cdot 10^{-3}$	4.08%	0.089
125	55	5.320	$0.652^{+0.309}_{-0.314} \cdot 10^{-3}$	$0.661 \pm 0.037 \cdot 10^{-3}$	1.22%	0.018
60	5	0.217	$0.179^{+0.058}_{-0.062} \cdot 10^{-3}$	$0.187 \pm 0.013 \cdot 10^{-3}$	4.11%	0.089
60	16	0.661	$0.300^{+0.116}_{-0.118} \cdot 10^{-3}$	$0.329 \pm 0.019 \cdot 10^{-3}$	8.71%	0.172
200	50	1.255	$5.598^{+1.686}_{-1.712} \cdot 10^{-3}$	$5.589 \pm 0.171 \cdot 10^{-3}$	0.16%	0.004
400	100	1.608	$12.826^{+3.576}_{-3.564} \cdot 10^{-3}$	$12.990 \pm 0.263 \cdot 10^{-3}$	1.26%	0.032
600	50	0.590	$13.045^{+3.409}_{-3.413} \cdot 10^{-3}$	$13.060 \pm 0.212 \cdot 10^{-3}$	0.12%	0.003
600	150	1.840	$14.915^{+3.829}_{-3.906} \cdot 10^{-3}$	$14.878 \pm 0.225 \cdot 10^{-3}$	0.25%	0.007
600	150	3.309	$13.408^{+3.772}_{-3.816} \cdot 10^{-3}$	$13.336 \pm 0.302 \cdot 10^{-3}$	0.54%	0.013
600	275	4.288	$2.725^{+0.781}_{-0.768} \cdot 10^{-3}$	$2.680 \pm 0.054 \cdot 10^{-3}$	1.69%	0.041
1000	50	0.406	$9.905^{+2.618}_{-2.685} \cdot 10^{-3}$	$9.939 \pm 0.183 \cdot 10^{-3}$	0.34%	0.009
1000	275	2.399	$11.954^{+3.283}_{-3.291} \cdot 10^{-3}$	$12.051 \pm 0.206 \cdot 10^{-3}$	0.80%	0.021
1000	275	4.328	$10.934^{+3.303}_{-3.403} \cdot 10^{-3}$	$11.074 \pm 0.278 \cdot 10^{-3}$	1.26%	0.029
1000	475	6.039	$2.295^{+0.669}_{-0.667} \cdot 10^{-3}$	$2.356 \pm 0.053 \cdot 10^{-3}$	2.60%	0.065

Table 8.14: Estimated global signal MC selection efficiency from lifetime extrapolation method, at the sample $c\tau_{\text{gen}}$, and global signal efficiency from full-sim $H \to ss$ signal sample. The percent difference is used as systematic uncertainty on the signal.

Channel	m_χ	Lifetime [m]	$\epsilon_{global}^{toy\ estimation}$	$\epsilon_{global}^{fullsim}$	% diff.	$\frac{\lvert\epsilon_{toy}-\epsilon_{fullsim}\rvert}{\sqrt{\sigma_{toy}^2+\sigma_{fullsim}^2}}$
$bb\nu$	10	0.920	$1.045^{+0.357}_{-0.332} \cdot 10^{-3}$	$1.146 \pm 0.052 \cdot 10^{-3}$	8.85%	0.207
$bb\nu$	55	5.550	$0.347^{+0.211}_{-0.204} \cdot 10^{-3}$	$0.344 \pm 0.028 \cdot 10^{-3}$	0.90%	0.011
$bb\nu$	100	3.500	$4.453^{+1.346}_{-1.323} \cdot 10^{-3}$	$5.140 \pm 0.116 \cdot 10^{-3}$	13.36%	0.363
cbs	10	0.920	$1.298^{+0.411}_{-0.414} \cdot 10^{-3}$	$1.410 \pm 0.060 \cdot 10^{-3}$	7.89%	0.190
cbs	55	5.550	$0.952^{+0.393}_{-0.418} \cdot 10^{-3}$	$0.957 \pm 0.055 \cdot 10^{-3}$	0.59%	0.010
cbs	100	3.500	$10.738^{+2.862}_{-2.887} \cdot 10^{-3}$	$12.322 \pm 0.179 \cdot 10^{-3}$	12.86%	0.389
$\tau\tau\nu$	10	0.920	$0.051^{+0.033}_{-0.033} \cdot 10^{-3}$	$0.065 \pm 0.012 \cdot 10^{-3}$	20.17%	0.268
$\tau\tau\nu^\dagger$	55	5.550	$0.009^{+0.008}_{-0.008} \cdot 10^{-3}$	$0.037 \pm 0.009 \cdot 10^{-3}$	75.88%	1.962
$\tau\tau\nu$	100	3.500	$0.787^{+0.337}_{-0.340} \cdot 10^{-3}$	$0.913 \pm 0.049 \cdot 10^{-3}$	13.82%	0.262

Table 8.15: Estimated global signal MC selection efficiency from lifetime extrapolation method, at the sample $c\tau_{\text{gen}}$, and global signal efficiency from full-sim $H \to \chi\chi$ signal sample. The percent difference is used as systematic uncertainty on the signal. The mediator mass for all samples is 125GeV. †The $m_\chi = 55\,\text{GeV}$ $\tau\tau\nu$ sample had very low signal MC statistics, so the vertex reconstruction efficiency used a coarser binning strategy than what was used for the other samples.

8.4.3 Extrapolation Fitting

The results from the lifetime extrapolation procedure are 100 bin histograms, with the value in each bin corresponding to the expected efficiency at that lifetime. In order to produce smooth limits, it would be useful to have a smooth distribution from which sampling could be done. Fitting the yield distribution would also permit limits to be set for values of $c\tau$ at which the extrapolation procedure was never performed. The histograms are fit with a Novosibirsk function, which is defined as [157]:

$$f(x; x_0, \sigma, \tau) = \exp\left[-\frac{1}{2}\left\{\frac{\ln^2\left(1 + \Lambda\tau\left(x - x_0\right)\right)}{2\tau^2} + \tau^2\right\}\right], \tag{8.18}$$

$$\text{where} \quad \Lambda = \frac{\sinh\left(\tau\sqrt{\ln 4}\right)}{\sigma\tau\sqrt{\ln 4}} \tag{8.19}$$

where τ, σ, and x_0 are parameters that are fit to the yield distribution, along with an overall normalization factor. An example of the Novosibirsk fit for the lifetime extrapolation yield of the $m_H = 125\,\text{GeV}, m_s = 35\,\text{GeV}$ sample is shown in Figure 8.25.

The fit is performed by the `ROOT TF1::Fit` functional fit method with the options `LMRQE` set. This performs a log likelihood fit on the histogram within the range provided. Fit results

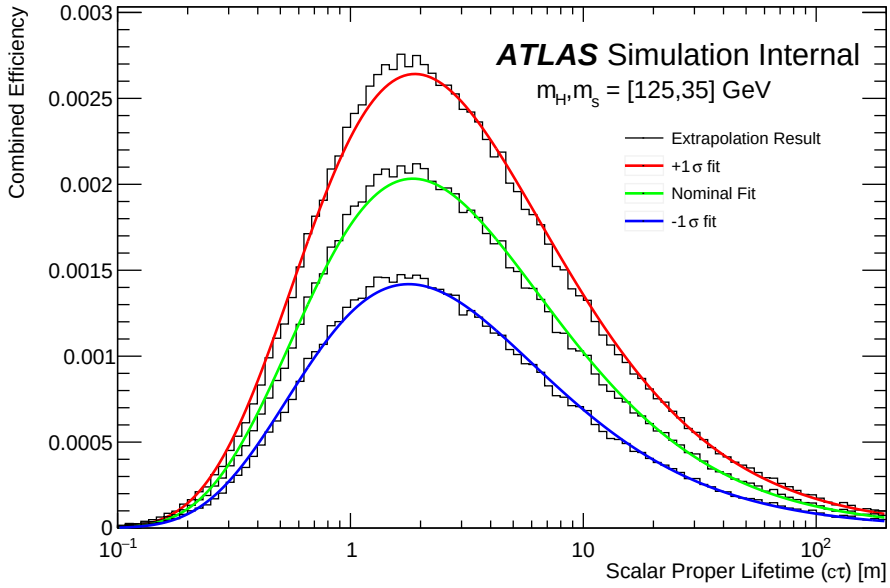

Figure 8.25: Example of the Novosibirsk fit applied to the extrapolated efficiency curve for the $m_H = 125\,\text{GeV}, m_s = 35\,\text{GeV}$ $H \to ss$ sample.

are improved by using the `IMProve` function implemented in `MINUIT` via the `ROOT TMinuit` interface [158, 159]. Better error estimation is achieved using the MINOS technique [159].

8.4.4 Novosibirsk Fits for Signal MC

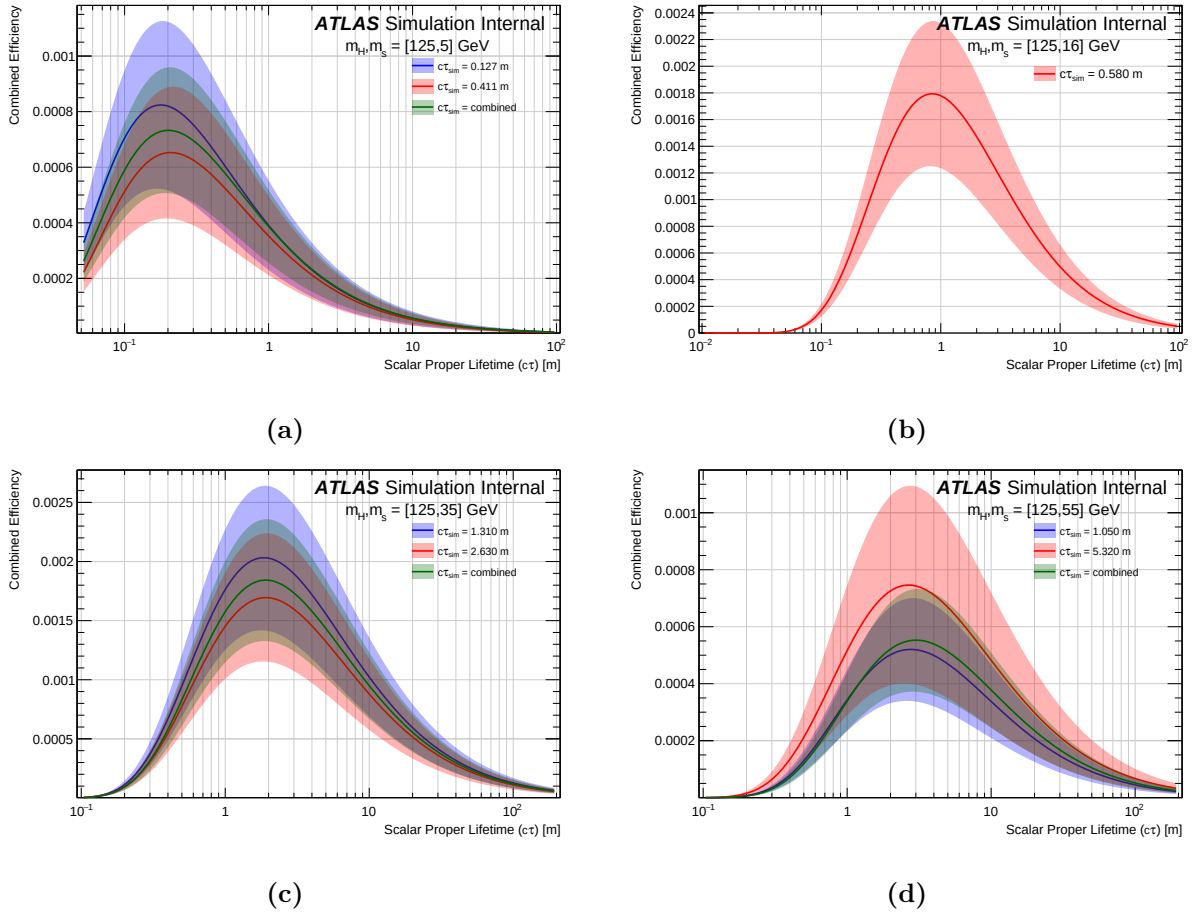

Figure 8.26: Extrapolated global signal efficiencies for different samples. The plots show agreement between extrapolations performed with signal MC samples with different lifetimes for $H \to ss$ decays with SM Higgs mass ($m_H = 125\,\text{GeV}$). Uncertainties are the result of statistical uncertainties of the full-sim efficiencies and systematic uncertainties in the trigger and reconstruction efficiencies arising from the data-MC correction scale factors, pileup, and PDF.

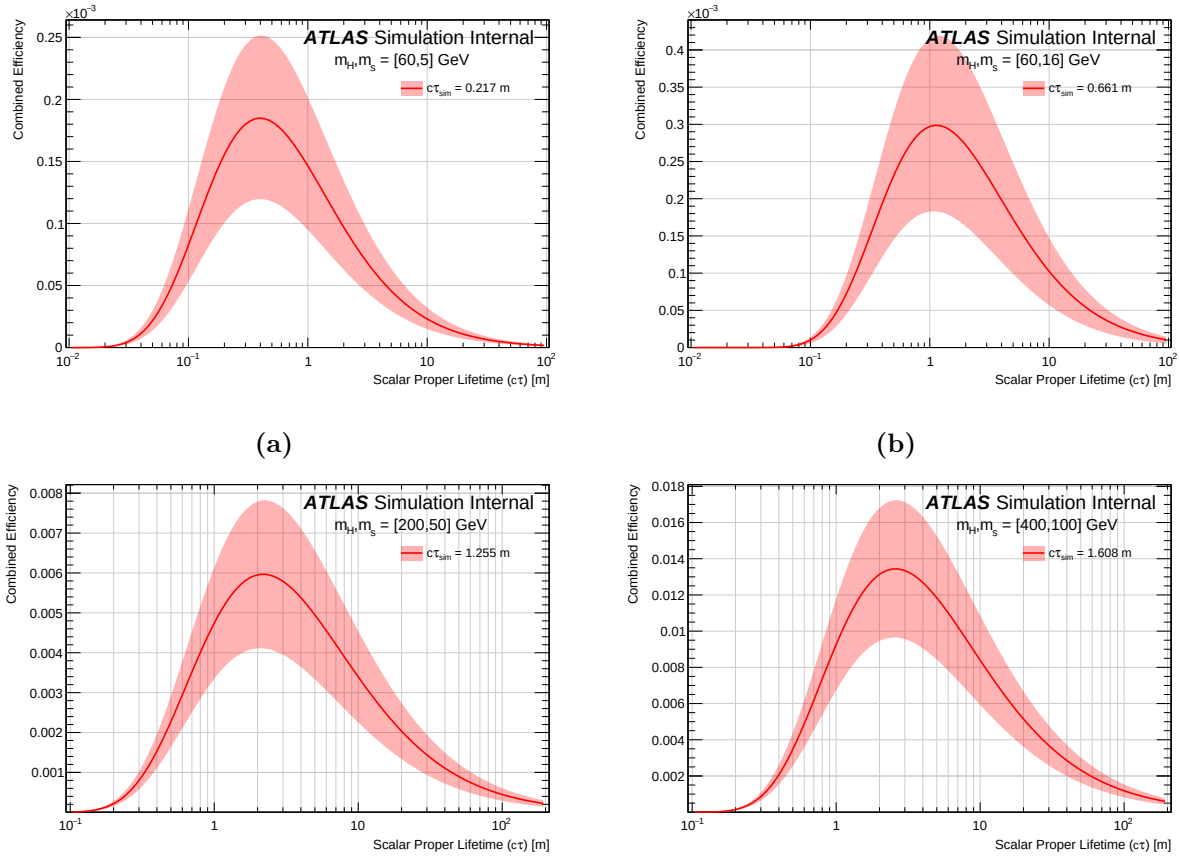

Figure 8.27: Extrapolated global signal efficiencies for different samples. The plots show agreement between extrapolations performed with official MC samples with different lifetimes for $H \to ss$ decays with some of the non-SM Higgs mass ($m_H \neq 125\,\text{GeV}$). Uncertainties are the result of statistical uncertainties of the full-sim efficiencies and systematic uncertainties in the trigger and reconstruction efficiencies arising from the data-MC correction scale factors, pileup, and PDF.

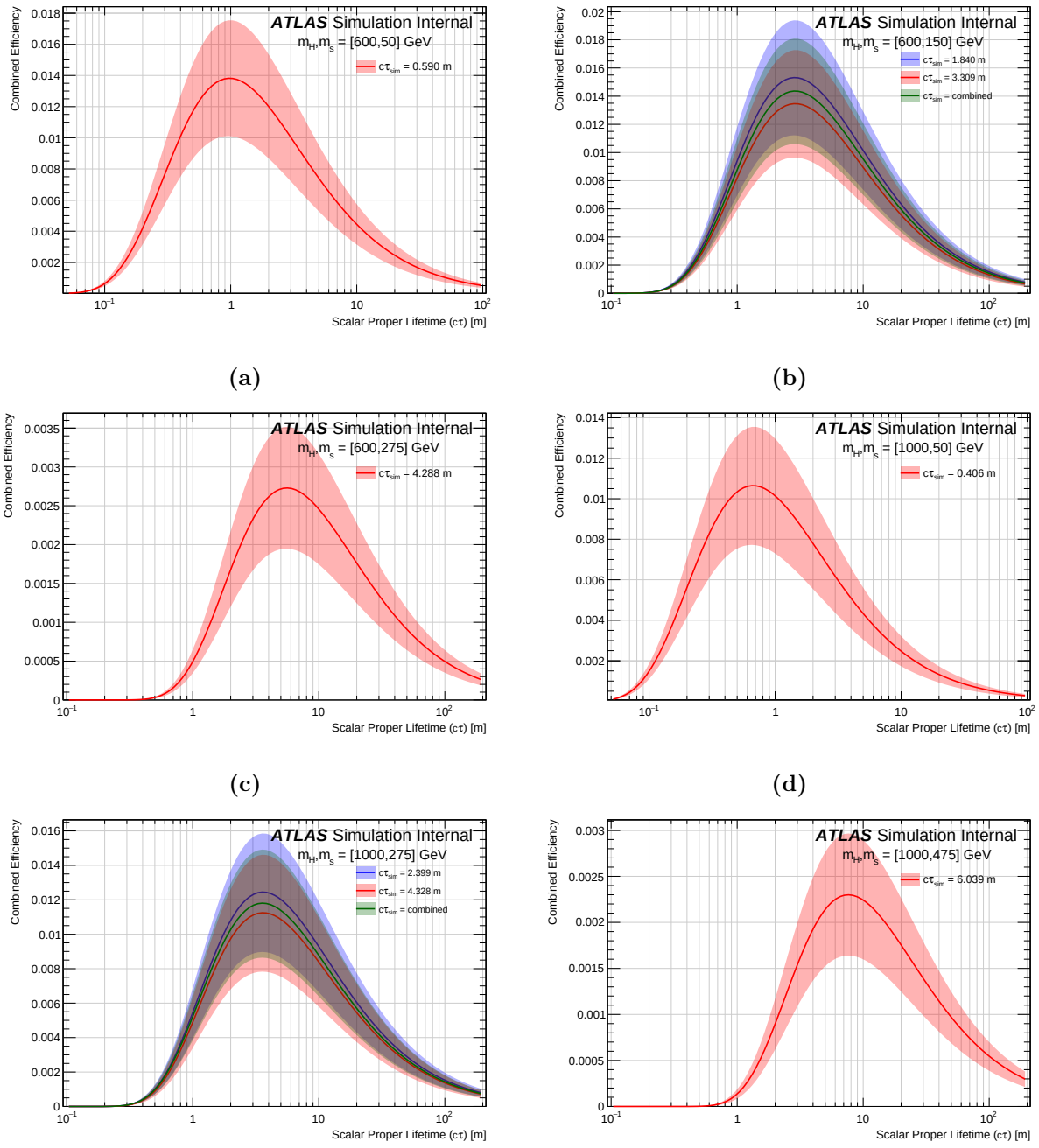

Figure 8.28: Extrapolated global signal efficiencies for different samples. The plots show agreement between extrapolations performed with official MC samples with different lifetimes for $H \to ss$ decays with some of the non-SM Higgs mass ($m_H \neq 125\,\text{GeV}$). Uncertainties are the result of statistical uncertainties of the full-sim efficiencies and systematic uncertainties in the trigger and reconstruction efficiencies arising from the data-MC correction scale factors, pileup, and PDF.

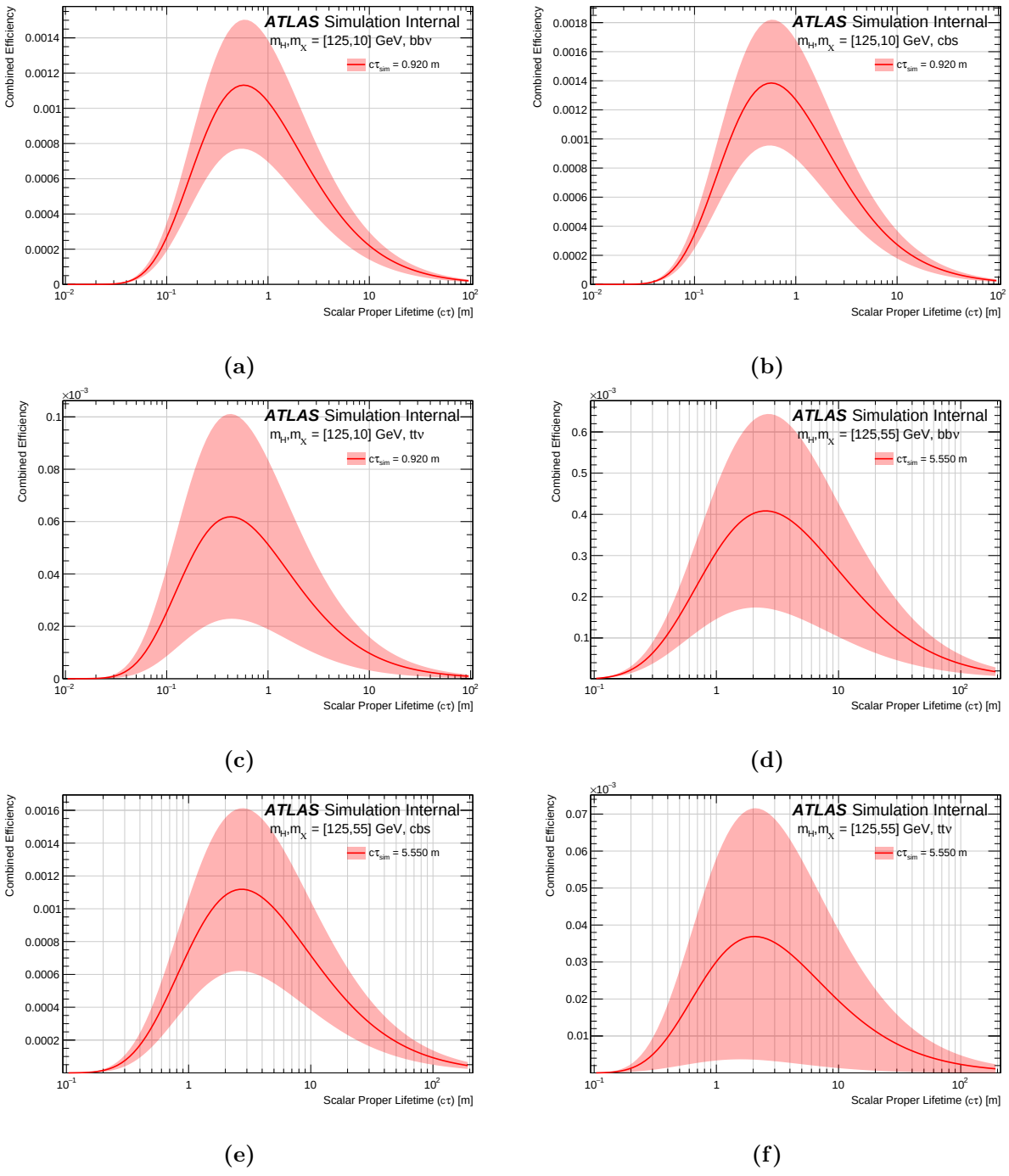

Figure 8.29: Extrapolated global signal efficiencies for different samples. The plots show agreement between extrapolations performed with official MC samples with different lifetimes for $H \to \chi\chi$ decays with $m_\chi = [10, 55]$ GeV. Uncertainties are the result of statistical uncertainties of the full-sim efficiencies and systematic uncertainties in the trigger and reconstruction efficiencies arising from the data-MC correction scale factors, pileup, and PDF.

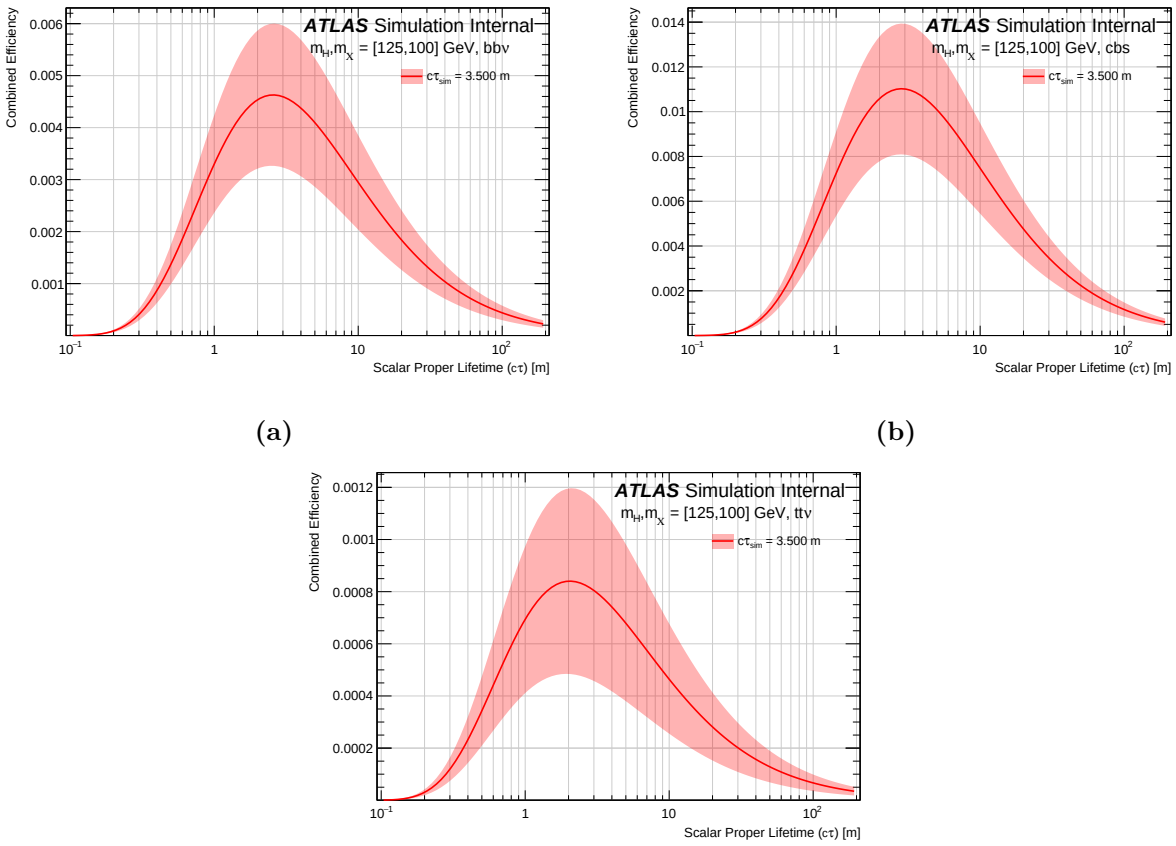

Figure 8.30: Extrapolated global signal efficiencies for different samples. The plots show agreement between extrapolations performed with official MC samples with different lifetimes for $H \to \chi\chi$ decays with $m_\chi = 100\,\text{GeV}$. Uncertainties are the result of statistical uncertainties of the full-sim efficiencies and systematic uncertainties in the trigger and reconstruction efficiencies arising from the data-MC correction scale factors, pileup, and PDF.

8.5 Systematic Uncertainties

There are several systematic uncertainties associated with the physics objects and analysis methodologies in this analysis. This section describes each set of systematic uncertainties. A summary of all systematics is shown in Table 8.18.

8.5.1 Pileup Uncertainty

The distribution of the average number of events per bunch crossing, $\langle\mu\rangle$, versus the number of primary vertices (PVs) in the signal MC simulation doesn't match what is seen in data due to imperfect modeling of the number of PVs in minimum bias simulation. Even after reweighting the simulation such that the $\langle\mu\rangle$ distribution matches what is seen in data, there is still an uncertainty associated with this disagreement.

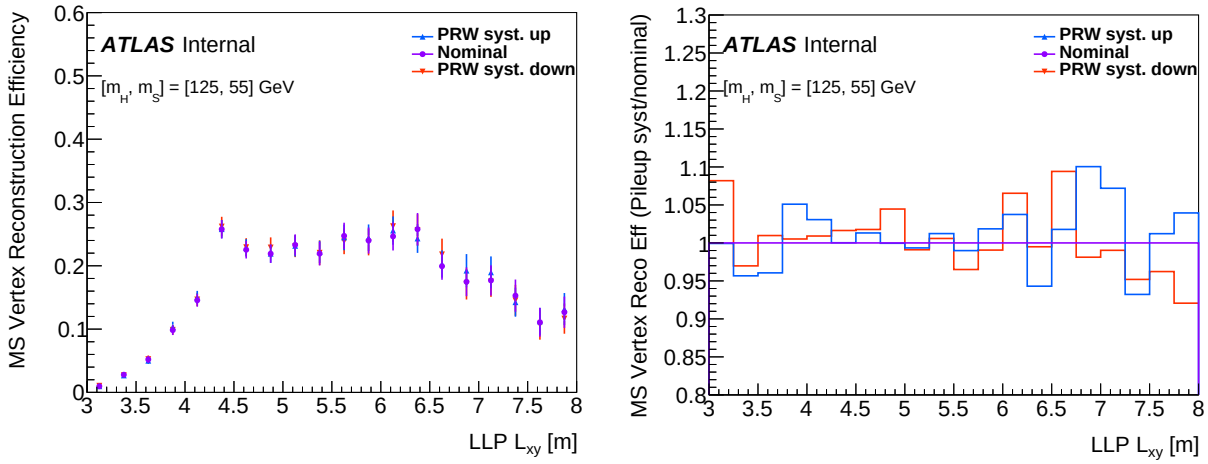

(a) **(b)**

Figure 8.31: Effect of pileup systematic uncertainty on the reconstruction efficiency in the barrel for the $H \to ss$ sample $m_H = 125\,\text{GeV}, m_s = 55\,\text{GeV}$. PRW stands for "pileup reweighting".

Figure 8.31 shows the impact that pileup uncertainty has on the $[m_H, m_s] = [125, 55]\,\text{GeV}$ sample. Figure 8.31(b) shows that the pileup uncertainty isn't dependent on the LLP decay position, meaning that the pileup systematic can be applied to all of the LLPs as a global uncertainty. For this sample, the pileup systematic contributes $+0.8$, -1.6% to the overall reconstruction systematic uncertainty. Using this same process, the impact of the pileup uncertainty on the muon RoI trigger is calculated. This was done for all signal MC samples and

the average uncertainty for each efficiency was calculated. These average uncertainties were applied as systematics to trigger and reconstruction efficiency, respectively, for all samples. The average uncertainty contribution from pileup systematics can be seen in Tables 8.16 and 8.17. Since the effect of the pileup uncertainty is small for all samples, the average across all samples is used. This is done for the impact on both the vertex reconstruction and the trigger efficiency. The average uncertainty for the vertex reconstruction efficiency is ±0.51% in the barrel and ±0.24% in the endcap. The average uncertainty for the muon RoI trigger efficiency is ±0.47% in the barrel and ±0.58% in the endcap.

8.5.2 PDF Uncertainty

Another systematic uncertainty is introduced by the choice of parton distribution function (PDF), which is used to generate the signal MC samples as described in Chapter 4. The samples used for this analysis were generated with the PDF NNPDF3.1 set with QED corrections, `NNPDF31_lo_as_0130`. The PDF set is extracted from data collected by numerous particle experiments and fit to a truncated perturbative expansion of the particle theory that describes the parton distributions [160]. An ensemble of PDF replicas are generated from this PDF set using a MC procedure, the mean of which is used in the production of signal MC samples [160, 161]. The PDF uncertainty contribution to the trigger and reconstruction efficiencies is found by first calculating the efficiency using each PDF replica, separately. The variation from the ensemble mean for each efficiency can then be calculated from this set. The distribution of these variations versus the LLP L_{xy} can be seen in Figure 8.32.

The average variation is determined per bin in L_{xy} and the uncertainty, $\pm 1\sigma$, is taken to be the square root, which is drawn on Figure 8.32(a) in black. Figure 8.32(b) is a plot of only the $\pm 1\sigma$ points and their associated uncertainties. Because the uncertainties are overall small, the same procedure is used here as was used for the pileup efficiency. The average uncertainty across all bins and samples is taken and the result is applied as a global uncertainty on each sample. For the sample in Figure 8.32, the average PDF uncertainty on the MSVtx reconstruction was only ±0.004, or ±0.4%. The average uncertainty across all samples for the vertex reconstruction efficiency is ±0.19% in the barrel and ±0.19% in the endcaps. The average uncertainty on the trigger efficiency is ±0.23% in the barrel and

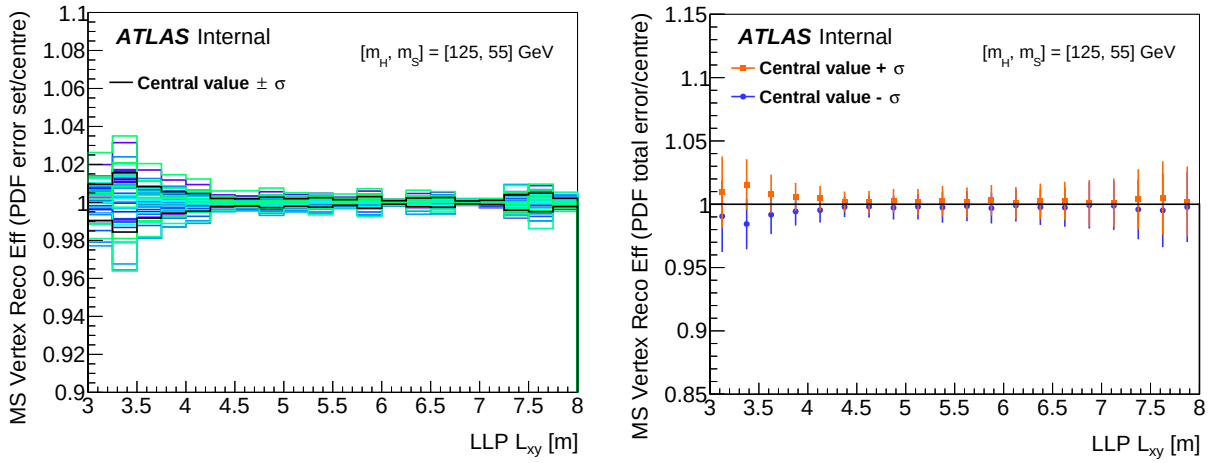

(a) **(b)**

Figure 8.32: Effect of the parton distribution function on the MSVtx reconstruction efficiency (MS Vertex Reco Eff) in the barrel for the $H \to ss$ sample $m_H = 125\,\text{GeV}$, $m_s = 55\,\text{GeV}$. (a) Variations of all 100 PDF replicas with respect to the average MSVtx reco efficiency are shown in bins of L_{xy}, with the average variation (taken as the standard deviation) shown in black. (b) Plot of only $\pm\sigma$, the average variation in the reco efficiency.

$\pm 0.22\%$ in the endcaps.

Total Barrel Uncertainty [%]	Total Endcap Uncertainty [%]
+0.3, -0.8	+0.7, -0.6

Table 8.16: Average systematic uncertainties on the Muon RoI Cluster trigger efficiency for the $H \to ss$ MC samples. Uncertainties are the combined effect of pileup and PDF uncertainties on the trigger efficiency.

Total Barrel Uncertainty [%]	Total Endcap Uncertainty [%]
+0.6, -0.5	+0.2, -0.4

Table 8.17: Average systematic uncertainties on the MSVtx reconstruction efficiency for the $H \to ss$ MC samples. Uncertainties are the combined effect of pileup and PDF uncertainties on the reconstruction efficiency.

8.5.3 Lifetime Extrapolation Uncertainty

The lifetime extrapolation should reproduce exactly the full-sim efficiency when extrapolating to the full-sim generated lifetime, $c\tau_{\text{gen}}$. The difference in the total sample efficiency,

$N_{\text{pass}}/N_{\text{all}}$, between the full-sim efficiency and the extrapolated efficiency is taken to be a systematic uncertainty of the lifetime extrapolation method for that sample and applied during limit setting. The variations are shown in Tables 8.14 and 8.15 and vary from 0.4% to 75.9%, depending on sample.

For the MC samples generated at two different proper lifetimes, a closure test of the extrapolated efficiencies was performed between the two samples and was found to close within the total (combined statistical and systematic) uncertainty at all $c\tau$ within the range tested. For this reason, no systematic uncertainty is needed to accommodate the difference in extrapolated efficiency between the two samples.

8.5.4 Signal MC Mismodeling Uncertainty

As mentioned in Section 5.3, the mismodeling of the muon RoI cluster trigger in the signal MC introduces a global uncertainty. This uncertainty is 24% in the barrel and 20% in the endcaps. There are also systematic uncertainties associated with the tracklet-dropping used to correct the vertex reconstruction efficiency in the signal MC as described in Section 7.4. The magnitude of this vertex reconstruction uncertainty is 2% in the barrel and 5% in the endcap.

The uncertainty on the muon RoI trigger is applied as a systematic uncertainty to the trigger efficiency used in the lifetime extrapolation, as it is sampled from the trigger efficiency histogram. The uncertainty associated with the tracklet-dropping procedure is applied as a global systematic to the vertex reconstruction efficiency in the lifetime extrapolation, as it is sampled from the reconstruction efficiency histogram.

8.5.5 Additional Sources of Uncertainty

The systematic uncertainty on the luminosity for Run 2 is 0.83% [84].

There are additional systematic uncertainties associated with the use of tracks and jets, but their impact is negligible compared to other sources of uncertainty. The impact caused by the uncertainty on the gluon-gluon fusion Higgs production branching fraction was also investigated and was also found to be negligible.

Systematic	Barrel Region	Endcap Region
Lifetime Extrapolation Non-Closure	$\pm 0.12\% - \pm 75.9\%$	
Trigger Mismodeling	$\pm 24\%$	$\pm 20\%$
PDF (Trigger Efficiency)	$\pm 0.23\%$	$\pm 0.22\%$
Pileup (Trigger Efficiency)	$\pm 0.47\%$	$\pm 0.58\%$
Reconstruction Mismodeling	$\pm 11\%$	$\pm 13\%$
PDF (Vertex Mismodeling)	$\pm 0.19\%$	$\pm 0.19\%$
Pileup (Vertex Mismodeling)	$\pm 0.51\%$	$\pm 0.24\%$
Run 2 Luminosity	$\pm 0.83\%$	

Table 8.18: Summary of the systematic uncertainties in this analysis. Uncertainties from pileup and PDF variations were applied to the Trigger and Reconstruction (Vertex) efficiencies, the results of which are shown here. The luminosity uncertainty reflects the systematic on $140\,\text{fb}^{-1}$ of Run 2 data. The Lifetime Extrapolation non-closure uncertainties are the result of a non-closure between the selection efficiency calculated from the fully simulated MC sample and the corresponding selection efficiency returned, at the sample generated lifetime, $c\tau_{\text{gen}}$, from the extrapolation procedure.

8.6 Unblinded Results

Following the validation of the ABCD plane and the lifetime extrapolation procedure, the expected number of background events in the signal region were known and expected limits were set. At this point, major changes to the analysis were frozen and the signal region was unblinded. A total of $226 \pm 14 \pm 18$ background events were expected in the barrel region and $46 \pm 2 \pm 2$ background events were expected in the endcap region, where the first uncertainty corresponds to the statistical uncertainty and the second corresponds to the systematic uncertainty. For the full Run 2 data set, 235 events were observed in the barrel region and 35 events were observed in the endcap region. The observed number of events are statistically consistent with the expected amount of background events, indicating no new physics has been observed.

Table 8.19 shows the number of events from data, with $H_{\text{T}}^{\text{miss}} > 40\,\text{GeV}$, in each of the B, C, and D regions for each subset of the Run 2 data, as well as the expected number of events in the A region, $N_A^{\text{expected}} = N_B \times N_C/N_D$, and the observed number of events in the A region, A_{obs}. Figure 8.33 shows the unblinded ABCD planes for barrel and endcap MSVtx events for the full Run 2 data with $H_{\text{T}}^{\text{miss}} > 40\,\text{GeV}$.

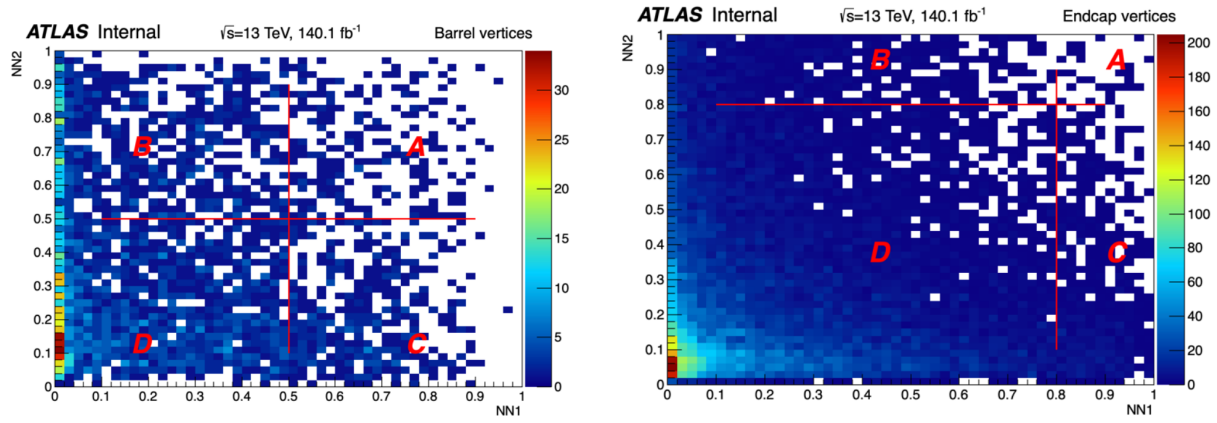

(a) **(b)**

Figure 8.33: Unblinded ABCD planes for all Run 2 data with the full event selection applied. ABCD planes correspond to (a) barrel MS vertices and (b) endcap MS vertices.

	Data Period	A_{obs}	B×C/D $\pm\sigma_{stat} \pm \sigma_{syst}$	B	C	D
Barrel	Data 15&16	49	$58 \pm 7 \pm 5$	237	124	504
	Data17	99	$71 \pm 8 \pm 6$	282	166	655
	Data18	87	$97 \pm 9 \pm 8$	393	184	747
	Run2	235	$226 \pm 14 \pm 18$	912	474	1906
Endcaps	Data15&16	12	$16 \pm 1 \pm 1$	248	261	4170
	Data17	13	$15 \pm 1 \pm 1$	316	255	5419
	Data18	10	$14 \pm 1 \pm 1$	480	209	6989
	Run2	35	$46 \pm 2 \pm 2$	1044	725	16578

Table 8.19: Event counts from the ABCD plane in data with $H_{\mathrm{T}}^{\mathrm{miss}} > 40\,\mathrm{GeV}$. N_A^{expected} is given by B×C/D. A_{obs} is the unblinded result. The cut on the NN1 and NN2 to define the A region is 0.5 in the barrel and 0.8 in the endcap regions.

Chapter 9

Statistical Interpretation of Results

A procedure is needed to quantitatively determine the statistical significance of analysis results. A sufficient level of certainty is required in order to claim that a certain signature has been observed. If no such signature is seen, then these results can be used to set a limit on the physics associated with it. This chapter will explain the pieces necessary to calculate the significance of the results as well as the tools to set these limits.

The results of this analysis are the number of events observed in the signal region (SR) defined by the ABCD plane, compared to the number of expected background events. The expected background contamination in the signal region is calculated to be $226 \pm 14 \pm 18$ events in the barrel region and $46 \pm 2 \pm 2$ events in the endcap regions. The observed numbers of events in the signal region are 235 in the barrel region and 35 in the endcap region. This indicates there is no statistically significant excess. A negative result is still a useful result, as it can be used to place an upper limit on the likelihood that the physical process occurs. In the case of this analysis, this is done by placing a limit on the production cross section times branching ratio of the BSM process.

9.1 Observation of Signal

A frequentist statistical method is used to quantify the likelihood that the data yield contains events matching the signal, given the estimated backgrounds. This can be constructed as a hypothesis test. The null hypothesis, H_0, corresponds to the background-only hypothesis. The hypothesis supposes that the data yield observed in the signal region completely comes from SM processes and none of the events correspond to the LLP BSM physics. The

alternative hypothesis, H_1, corresponds to a signal-plus-background hypothesis. To evaluate how well the observed data agree with a given hypothesis, H, a probability, or p-value, can be computed reflecting the chance of finding data of equal or greater incompatibility with H [162]. The smaller this p-value, the larger the incompatibility with the predictions corresponding to the hypothesis.

The p-value is often converted to its equivalent significance, Z. Z is defined as

$$Z = \Phi^{-1}(1-p) \tag{9.1}$$

where Φ^{-1} is the Gaussian inverse cumulative distribution function (CDF), often called the quantile. The particle physics community has traditionally rejected the background hypothesis of particle searches only when a significance of $Z \geq 5$ is reached. This is the threshold for one to claim discovery. A significance of $Z \geq 3$ is sufficient to claim evidence of a new particle. To reject signal-plus-background hypotheses, a lower threshold of $Z \geq 1.64$, corresponding to a p-value of 0.05 (i.e., a 95% confidence level (CL)), is required [162].

In order to find this probability, a test statistic is used to distinguish between the background-only and signal-plus-background hypotheses. This test statistic is often taken as the log-likelihood ratio between the two hypotheses. A statistical model for the background and signal would include features that are important to the physics process, like the cross section, as well as a set of *nuisance parameters* that allow the model to vary according to systematic uncertainties.

For this analysis, the statistical model is a likelihood function composed of the product of a Poisson probability and constraints. The constraints are modeled as functions of the nuisance parameters. Since this analysis utilizes ABCD planes for background estimation in the signal region, the likelihood function that is used contains a Poisson distribution for each region of the ABCD planes:

$$\mathcal{L}\left(n_{A_k}, n_{B_k}, n_{C_k}, n_{D_k} | \mu, \theta_\mu\right) = \prod_{k=\text{region}} \left\{ \prod_{i=A_k,B_k,C_k,D_k} \frac{e^{-N_i} N_i^{n_i}}{n_i!} \right\} \prod_{\theta_j \in \theta} \pi_j\left(\theta_j\right) \tag{9.2}$$

where the subscript k corresponds to the detector region (barrel or endcap) for the ABCD plane, n_{A_k}, n_{B_k}, n_{C_k}, and n_{D_k} are the four observed number of events from data in each

region of the ABCD plane in the k^{th} detector region, (barrel or endcap). The N_i are defined in the following way:

$$\begin{aligned} N_A &= \mu N^S_{A,\text{expected}} + N^B_A \\ N_B &= \mu\epsilon_B N^S_{A,\text{expected}} + N^B_A \tau_B \\ N_C &= \mu\epsilon_C N^S_{A,\text{expected}} + N^B_A \tau_C \\ N_D &= \mu\epsilon_D N^S_{A,\text{expected}} + N^B_A \tau_B \cdot \tau_C \end{aligned} \tag{9.3}$$

Here, the k index has been dropped since the expressions are the same between the barrel and endcap ABCD planes. The values N^S and N^B correspond to estimated numbers of signal and background events, respectively. The subscript corresponds to the region of the ABCD plane. The parameter of interest (POI), μ, represents the expected signal strength. A value of $\mu = 0$ represents the background-only hypothesis. Any value of $\mu > 0$ would represent the signal-plus-background hypothesis. The definitions of N_i also contain several nuisance parameters, τ_i. These parameters correspond to transfer ratios of background events between the different ABCD regions. The product $N^B_A \tau_C$, for example, corresponds to the number of background events in region C. The ϵ_i are signal scaling factors that relate the number of expected signal events in the B, C, and D regions to the number of events in the A region, $\left(\text{e.g. } N^S_{B,\text{expected}} = \epsilon_B N^S_{A,\text{expected}}\right)$. The value of each N_i is fit to match the corresponding number of observed events, n_i, as closely as possible, while μ, N^B_A, and the τ_i terms are all allowed to float in the simultaneous likelihood fit of the eight ABCD regions. The set of nuisance parameters, $\theta = \{\theta_j\}$, in Eq. 9.2 describe all of the systematic and statistical uncertainties for both signal and background. The functions of these parameters, $\pi_j(\theta_j)$, represent the probability distributions of each of the nuisance parameters. Given that all of the nuisance parameters are uncertainties, these distributions are all taken to be Gaussian distributions.

To actually evaluate the agreement with a given hypothesis, the profile likelihood ratio, as defined in [162], is used:

$$\tilde{\lambda}(\mu) = \begin{cases} \frac{L\left(\mu,\hat{\hat{\theta}}(\mu)\right)}{L\left(\hat{\mu},\hat{\theta}\right)} & \hat{\mu} \geq 0 \\ \frac{L\left(\mu,\hat{\hat{\theta}}(\mu)\right)}{L\left(0,\hat{\hat{\theta}}(0)\right)} & \hat{\mu} < 0 \end{cases} \tag{9.4}$$

where $\hat{\mu}$ and $\hat{\theta}$ are the maximum-likelihood (ML) estimators for the maximized likelihood (or the "unconditional" likelihood). The parameter $\hat{\hat{\theta}}(\mu)$ in the numerator is the conditional ML estimator of the nuisance parameters, θ. The conditional ML estimator is the set of nuisance parameter values that maximizes the likelihood for any given value of μ. For $\hat{\mu} \geq 0$, the profile likelihood ratio $\tilde{\lambda}(\mu)$ takes a form where the denominator is the maximized likelihood, and the numerator is the maximized conditional likelihood for a given value of μ. For $\hat{\mu} < 0$, the denominator changes to the maximized conditional likelihood for $\mu = 0$. This is done because any value of $\hat{\mu} < 0$ would correspond to a signal strength less than 0, and thus be unphysical since it is impossible to have negative signal events. So the best agreement that can be expected between the data and the background-only hypothesis occurs at $\mu = 0$. For this reason, the conditional ML estimator $\hat{\hat{\theta}}(0)$ is used.

A common test statistic, and the statistic that was used in this analysis, is the profile log-likelihood ratio:

$$q_0 = -2\ln\tilde{\lambda}(0) = \begin{cases} -2\ln\frac{L\left(0,\hat{\hat{\theta}}\right)}{L\left(\hat{\mu},\hat{\theta}\right)} & \hat{\mu} \geq 0 \\ 0 & \hat{\mu} < 0 \end{cases} \tag{9.5}$$

This statistic is used for signal-discovery, testing the background-only hypothesis, with $\mu = 0$, against the signal-plus-background hypothesis. It is a convenient choice of test statistic given that $\tilde{\lambda}(\mu)$ is bounded between $[0, 1]$, by construction. Defining the test statistic in this way lets us calculate the p-value using the statistic directly. Since higher values of q_0 correspond to higher discrepancy between the data and the background-only hypothesis, the p-value can be calculated with

$$p_0 = \int_{q_{0,obs}}^{\infty} f(q_0|0)\, dq_0 \tag{9.6}$$

where $f(q_0|0)$ is the probability distribution function (pdf) of q_0 under the assumption

of the background-only hypothesis. The pdf of q_0 is constructed by toy MC experiments, where values of the nuisance parameters fluctuate inside the $\hat{\hat{\theta}}$ terms. For each set of nuisance parameters, q_0 is calculated. The accumulation of different values of q_0 produces the pdf. $f\left(q_0|0\right)$ can be integrated from the value of q_0 obtained by fitting to the observed numbers of events [162].

9.2 Limit Setting Formulation

In the event that the signal-plus-background hypothesis is rejected, the analysis is still able to provide limits on the maximum strength of the process being investigated. This is done by treating the signal-plus-background as the null hypothesis and writing the test statistic in terms of the signal strength, μ:

$$\tilde{q}_\mu = \begin{cases} -2\ln\tilde{\lambda}\left(\mu\right) & \mu \geq \hat{\mu} \\ 0 & \mu < \hat{\mu} \end{cases} = \begin{cases} -2\ln\frac{L\left(\mu,\hat{\hat{\theta}}(\mu)\right)}{L\left(\hat{\mu},\hat{\theta}\right)} & \mu \geq \hat{\mu} \geq 0 \\ -2\ln\frac{L\left(\mu,\hat{\hat{\theta}}(\mu)\right)}{L\left(0,\hat{\hat{\theta}}(0)\right)} & \hat{\mu} < 0 \\ 0 & \mu < \hat{\mu} \end{cases} \tag{9.7}$$

where Eq. 9.5 has been written such that only ranges where the signal strength ML estimator, $\hat{\mu}$, has values less than the uncertainty are considered. The reason for this is because a $\hat{\mu} > \mu$ would indicate the data is more compatible with a larger signal strength, so a test statistic value of 0 is assigned. Recall that higher values of the test statistic represent larger incompatibility between data and the hypothesized value of μ [162, 163].

The additional splitting of the $\mu \geq \hat{\mu}$ range is to account for a negative $\hat{\mu}$ by replacing the likelihood in the denominator with the conditionally maximized likelihood for a value of $\mu = 0$, as was done in Eq. 9.4. With the test statistic, $\tilde{q}_\mu$, defined in this way, the p-value is found in the same way as the signal observation p-value:

$$p_\mu = \int_{\tilde{q}_{\mu,obs}}^{\infty} f\left(\tilde{q}_\mu|\mu\right) d\tilde{q}_\mu \tag{9.8}$$

where, similar to Eq. 9.6, the function $f\left(\tilde{q}_\mu|\mu\right)$ is the pdf of $\tilde{q}_\mu$ under the signal-plus-background hypothesis assuming a signal strength of μ [162, 163].

Like q_0, the pdf of $\tilde{q}_\mu$ is typically constructed using toy MC experiments. With a sufficiently large data sample, an approximation of $\tilde{q}_\mu$ can be made that no longer relies on a toy MC process to find the pdf, but permits a direct calculation to be made. This is the formulation used in this analysis.

As the data sample size increases, the pdf of $\tilde{q}_\mu$ asymptotically approaches the form

$$f\left(\tilde{q}_\mu|\mu\right) = \frac{1}{2}\delta\left(\tilde{q}_\mu\right) + \begin{cases} \frac{1}{2}\frac{1}{\sqrt{2\pi}}\frac{1}{\sqrt{\tilde{q}_\mu}}e^{-\tilde{q}_\mu/2} & 0 < \tilde{q}_\mu \leq \mu^2/\sigma^2 \\ \frac{1}{\sqrt{2\pi}(2\mu/\sigma)}\exp\left[-\frac{1}{2}\frac{\left(\tilde{q}_\mu+\mu^2/\sigma^2\right)^2}{(2\mu/\sigma)^2}\right] & \tilde{q}_\mu > \mu^2/\sigma^2 \end{cases} \tag{9.9}$$

where all variables have the same meaning as defined above save σ, which is the standard deviation of $\hat{\mu}$ under an assumption of signal strength, μ. This standard deviation can be found using the covariance matrix of the nuisance parameters, θ_i, which is defined as $V_{ij} = \mathrm{cov}\left[\theta_i, \theta_j\right]$ [162]. This includes the signal strength as a parameter, typically the nuisance parameter labeled θ_0, so the variance σ^2 corresponds to the V_{00} term. The inverse covariance matrix is related to the likelihood function in the following way.

$$V_{ij}^{-1} = -E\left[\frac{\partial^2 \ln \mathcal{L}}{\partial\theta_i \partial\theta_j}\right] \tag{9.10}$$

Here, $E\left[\ \right]$ represents the expectation value of the function inside the brackets, which is the second-derivative of the log-likelihood function with respect to the i^{th} and j^{th} nuisance parameters [162]. Once the inverse correlation matrix is found, it can be inverted to get the variance on $\hat{\mu}$ and the asymptotic form of the pdf in Eq. 9.9 can be found.

9.3 The CL$_s$ Method

If a p-value is obtained from a test of the signal-plus-background hypothesis below a threshold α, the signal-plus-background hypothesis can be said to be excluded at a confidence of $1-\alpha$. Typically, a signal-plus-background hypothesis is rejected at the 95% confidence level (CL), which corresponds to an α of 0.05. An upper limit on the signal strength, μ_{up}, can be set by constructing the confidence interval (CI) $[0, \mu_{\mathrm{up}}]$ using the 95% CL.

If the p-value is calculated using in Eq. 9.8, the method is referred to as the CL$_{s+b}$ method

since it involves only a test of the signal-plus-background hypothesis. This method is useful in situations where the analysis has good sensitivity to the signal, but fails when the signal sensitivity is small compared to the amount of background, $s \ll b$. In this case, the background-only and signal-plus-background hypotheses are almost identical. The CL_{s+b} method creates confidence intervals that are very sensitive to small fluctuations in the number of observed events. This could lead to over-excluding values of μ which, if the number of observed events had been a single event higher, would not have been excluded [164]. To mitigate this, p_μ can be scaled by the complement of the background-only hypothesis, CL_b. The p-value for CL_b is given by

$$p_b = \int_{\tilde{q}_{\mu,\mathrm{obs}}}^{\infty} f\left(\tilde{q}_\mu | 0, \hat{\hat{\theta}}\left(0, \mathrm{obs}\right)\right) d\tilde{q}_\mu \tag{9.11}$$

where the integral is over the pdf of $\tilde{q}_\mu$, but given a signal strength of $\mu = 0$, and a nuisance parameter conditional optimizer, $\hat{\hat{\theta}}$, locked to the observed values and using a signal strength of 0. Since the p-value is interpreted as the probability of finding data of equal or greater incompatibility with the hypothesis, the compliment can be interpreted as the probability of finding data that is more *compatible* with the hypothesis. In this case, this would be the probability of finding data that agreed *more closely* to the background-only hypothesis. This scaled p-value, p'_μ, is given as

$$p'_\mu = \frac{p_\mu}{1 - p_b} \tag{9.12}$$

A sketch of the pdfs of $\tilde{q}_\mu$ in the background-only and signal-plus-background hypotheses are shown in Figure 9.1 [165].

9.4 Results

The CLs Method is used to derive the upper limits on the signal strength, μ_{up} by finding the value of μ that returns a p-value of 5% using Eq. 9.12. This upper limit on the signal strength can then be used to set an upper limit on the product $(\sigma \times B)$, which can be denoted as $(\sigma \times B)_{\mathrm{up}}$, in the following way:

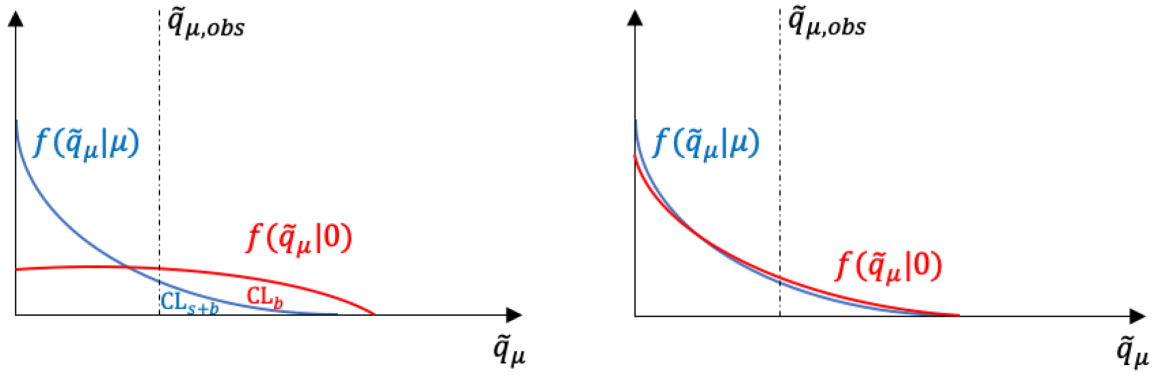

Figure 9.1: Sketch comparison of the pdfs of CL_{s+b} and CL_b in two different analyses. (a) An analysis with high sensitivity to signal. (b) An analysis with low sensitivity to signal. Use of the CL_s method would be necessary in Figure (b) to prevent over-excluding μ.

$$\mu_{\text{up}} = (\sigma \times B)_{\text{up}} \cdot \mathcal{L} \cdot \epsilon_{\text{global}} \tag{9.13}$$

This product, $(\sigma \times B)$, is the product of the production cross section for the Higgs-like mediator, H, and the branching fraction for the $H \to ss$ process, B. A branching fraction of 100% for the $s \to f\overline{f}$ process is assumed. $\mathcal{L}$ is the ATLAS Run 2 integrated luminosity and ϵ_{global} is the global signal efficiency, which includes the trigger and reconstruction efficiencies calculated in Chapter 8. It also takes into account the detector acceptance and event selection efficiency.

For the signal samples that use the SM Higgs mass, $m_H = 125\,\text{GeV}$, it is possible to set the upper limits on the production cross section as a fraction of the SM Higgs production cross section, $\sigma_{\text{SM}} = 48.61^{+5.6\%}_{-7.4\%}\,\text{pb}$ [33]. The branching fraction of a SM Higgs to invisible final states is also used as the SM branching fraction for these samples [166].

The upper limits are calculated using the `pyhf-v0.7.2` package [167]. The expected number of background events entering the signal region, N_A^B, the expected number of signal events, $N_{A,\text{expected}}^S$, and the uncertainties on these values, as nuisance parameters θ_i, are used as input to produce the expected limits. For the observed limits, the number of observed events in each ABCD region, $\{n_{A_k}, n_{B_k}, n_{C_k}, n_{D_k}\}$, are also included. The CLs confidence interval $[0,\mu_{\text{up}}]$ is calculated, at the 95% level, for 50 points along the $c\tau$ range that this search is sensitive to. These points can then be connected with a curve along $c\tau$. The

uncertainty on these limits are typically reported at $\pm 1\sigma$ and $\pm 2\sigma$, which are found using the pdf defined by $p'_{\mu_{\text{up}}}$ [163].

The limits for this analysis can be seen in Figures 9.2–9.6. Figure 9.2 contains both the expected and observed limits for Hidden Scalar benchmark samples with a SM Higgs mass, $m_H = 125\,\text{GeV}$. Figures 9.3 and 9.4 both show the expected and observed limits for Hidden Scalar benchmark samples with a non-SM Higgs mass, $m_H \neq 125\,\text{GeV}$. Figures 9.5 and 9.6 contain both the expected and observed limits for Baryogenesis benchmark samples.

For all benchmark samples, observed limits are consistent with expected limits within the uncertainty. For the $m_H = 125\,\text{GeV}$ Hidden Sector samples, stronger limits could be set on the branching ratio for intermediate Scalar masses, m_s. This is due to very low and very high mass LLPs being kinematically less likely to leave a well-reconstructed vertex within the detector fiducial region. This is reflected in the trigger and reconstruction efficiencies for these samples and can be seen in the expected signal efficiencies shown in Figure 8.26.

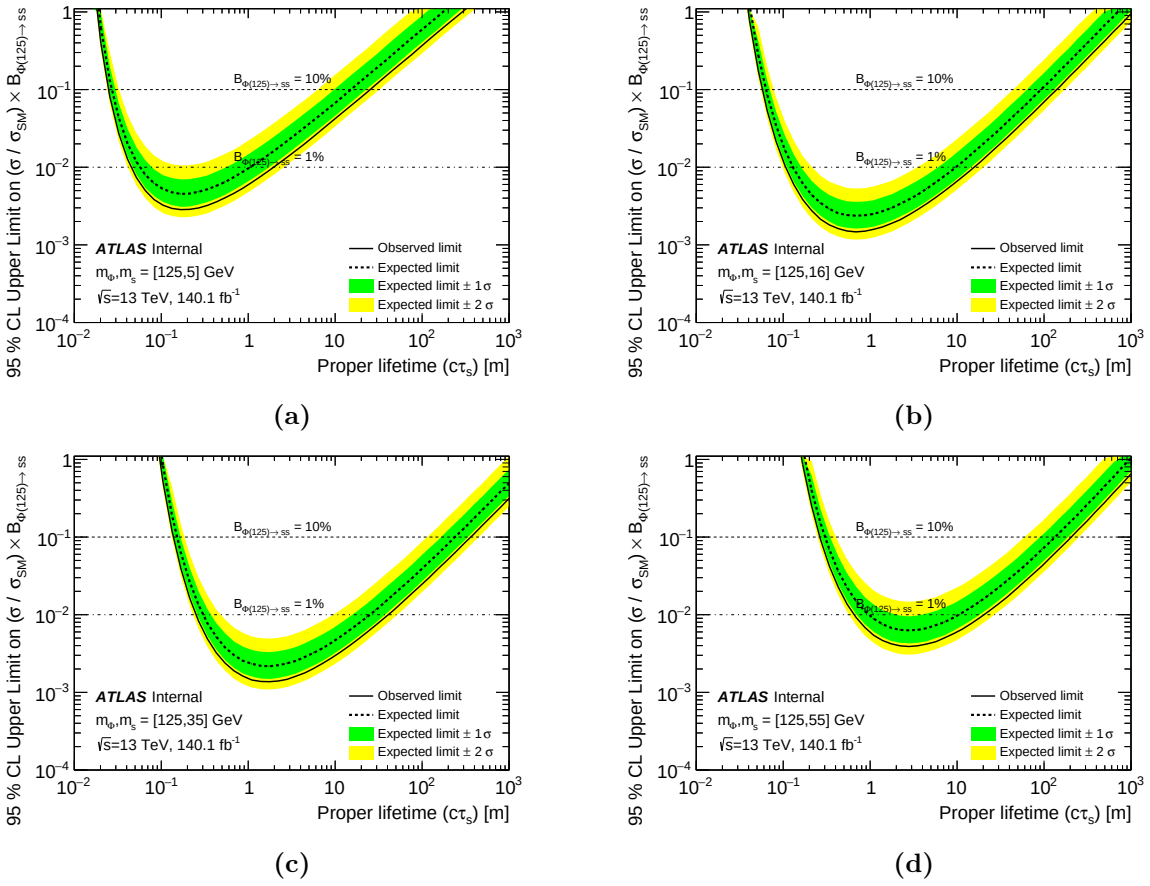

Figure 9.2: Branching ratio sensitivity upper limits over $c\tau$ range for $m_H = 125\,\text{GeV}$ Hidden Sector benchmark samples. Limits are set at 95% CL.

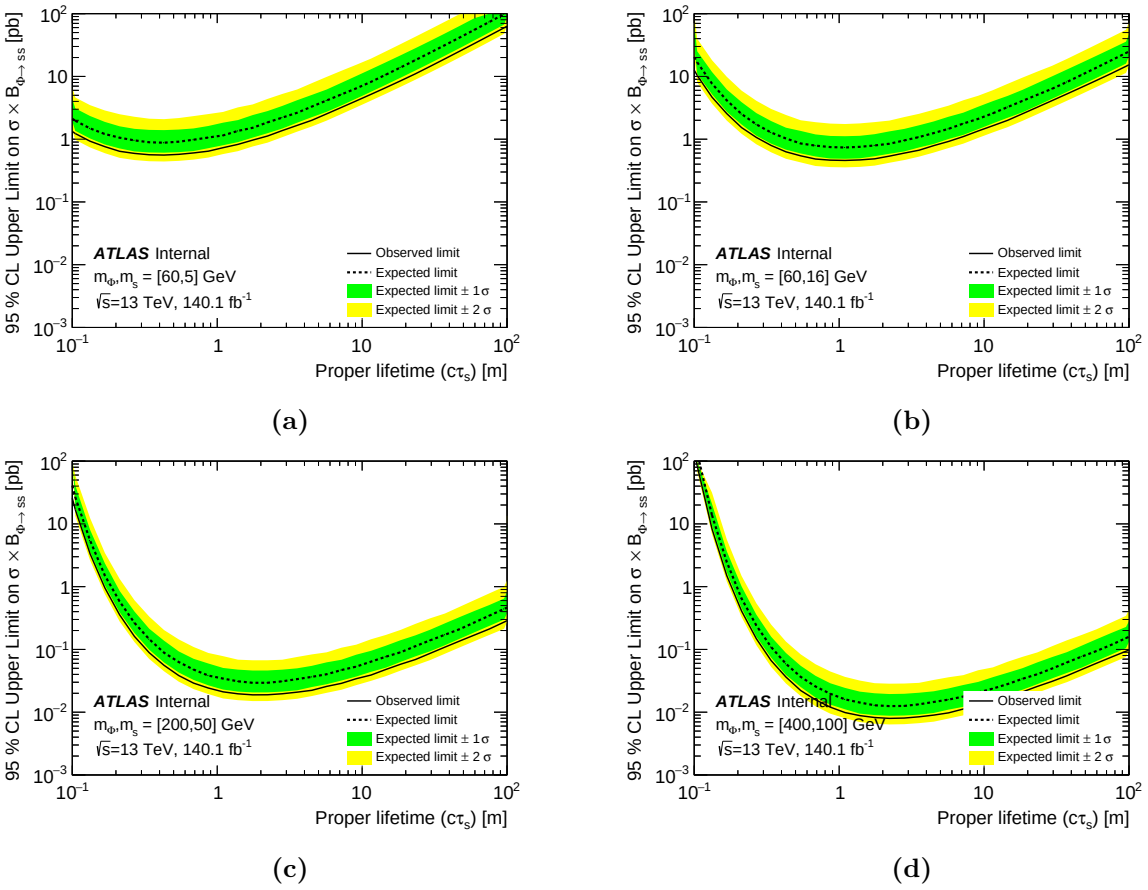

Figure 9.3: Cross section times branching ratio sensitivity upper limits over $c\tau$ range for $m_H \neq 125\,\text{GeV}$ Hidden Sector benchmark samples with m_H of 60 GeV, 200 GeV, and 400 GeV. Limits are set at 95% CL.

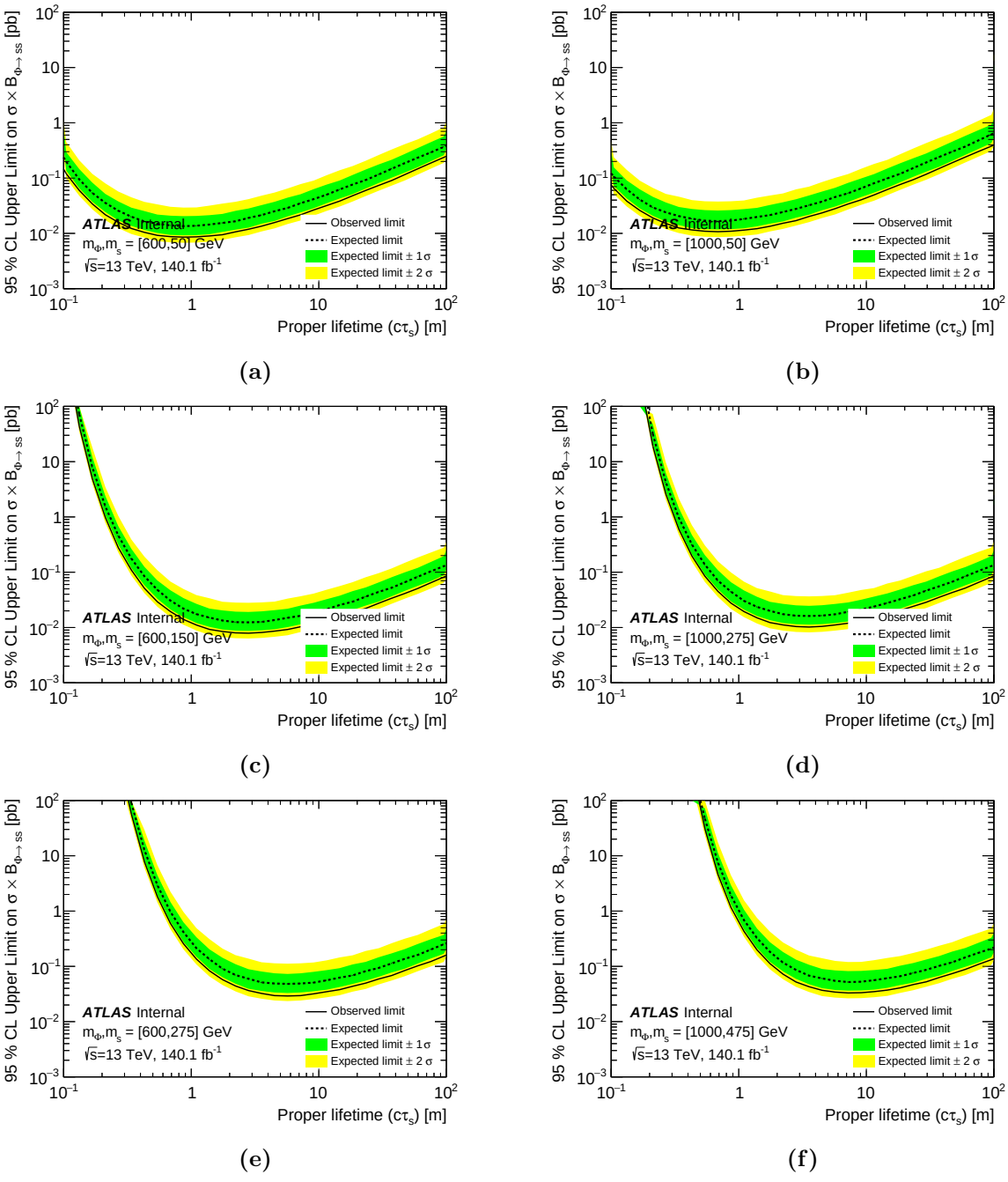

Figure 9.4: Cross section times branching ratio sensitivity upper limits over $c\tau$ range for $m_H \neq 125\,\text{GeV}$ Hidden Sector benchmark samples with m_H of 600 GeV and 1000 GeV. Limits are set at 95% CL.

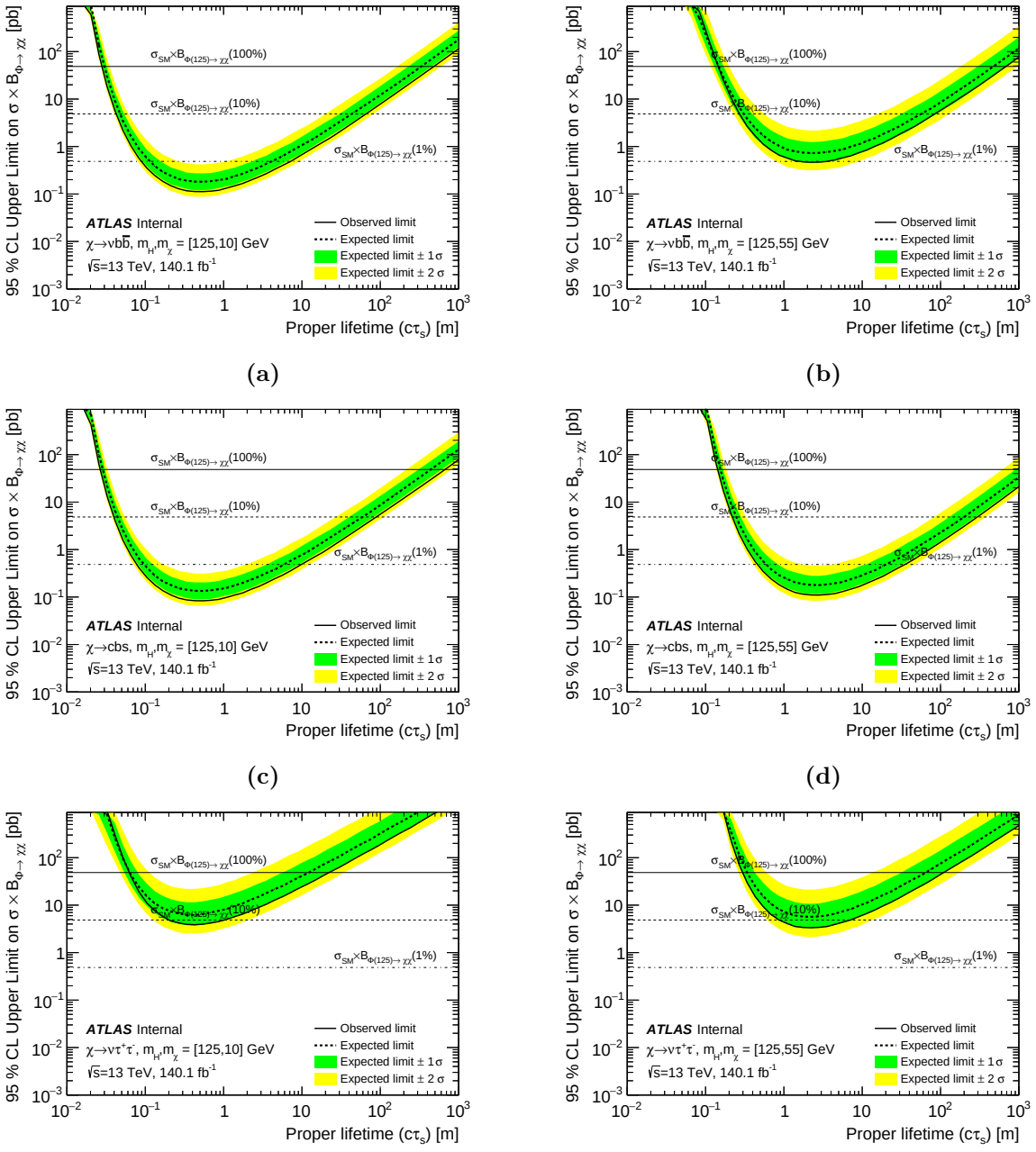

Figure 9.5: Cross section times branching ratio sensitivity upper limits over $c\tau$ range for $m_\chi = 10\,\text{GeV}$ and $m_\chi = 55\,\text{GeV}$ baryogenesis benchmark samples. Limits are set at 95% CL.

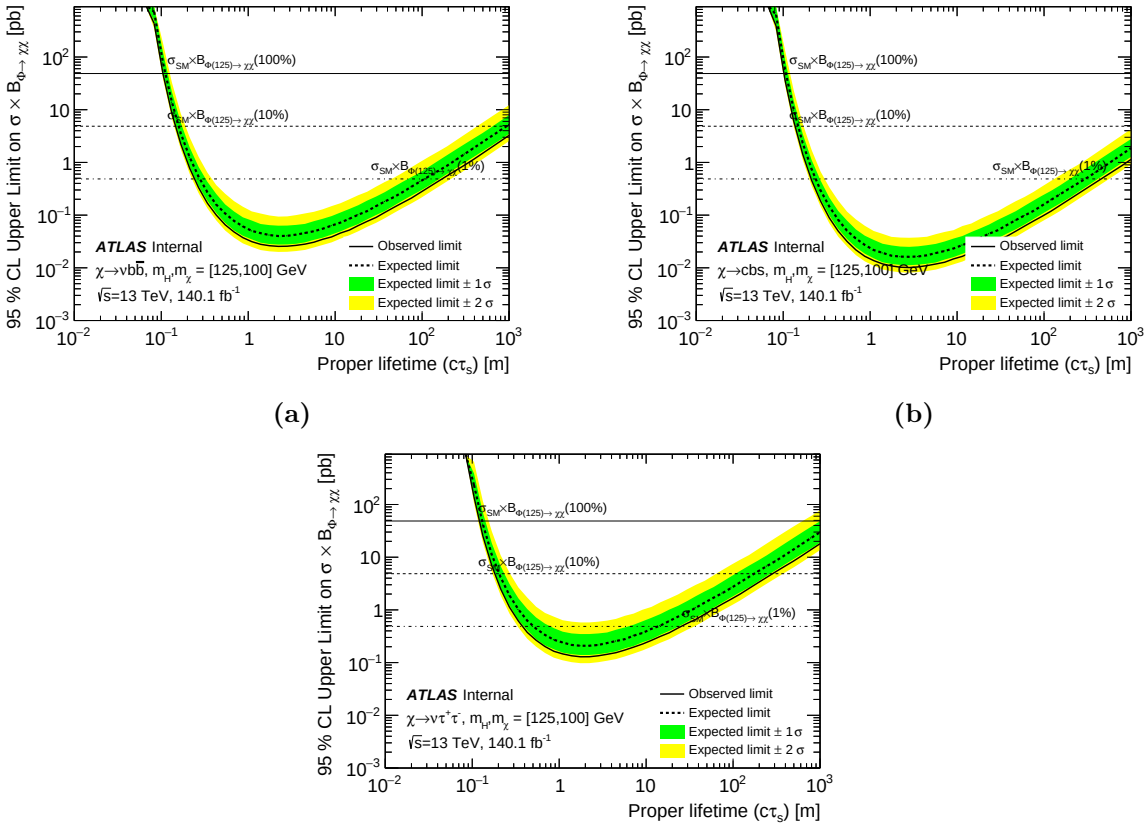

Figure 9.6: Cross section times branching ratio sensitivity upper limits over $c\tau$ range for $m_\chi = 100\,\text{GeV}$ baryogenesis benchmark samples. Limits are set at 95% CL.

9.4.1 Combined Limits

A previous study [83] investigated the two-vertex signature using Run 2 data. This search focused on the pair of LLPs both decaying within the detector and leaving two displaced vertices in the MS. The limits in the two-vertex analysis were found for the same $H \to ss$ benchmark models as this analysis, and so the limits can be combined to give a tighter upper limit on the $H \to ss$ process.

For all combined limits, it is evident that the one-MSVtx signature is much more sensitive to longer and shorter lifetimes compared to the two-MSVtx signature. Because the two-MSVtx signature requires both LLPs to decay and leave good vertices in the MS, the likelihood of this occurring drops rapidly as the proper lifetime increases or decreases. In exchange for a higher background contamination, the one-MSVtx signature can have candidate events occur where one of the LLPs doesn't decay within the analysis fiducial volume, increasing the sensitivity to lower and higher LLP lifetimes.

The combined limits place constraints on the LLP production process. The combined upper limits on the branching ratio, B, for benchmark samples with a SM Higgs mediator are shown in Figure 9.7. The combined limits for benchmark samples with a non-SM Higgs are shown in Figures 9.8 and 9.9. Limits were not set on the Baryogenesis samples ($H \to \chi\chi$) in the two-vertex analysis. The exclusion ranges for the $H \to ss$ process using the SM Higgs mass at $B = 10\%$ and $B = 1\%$ can be seen in Table 9.1.

$H \to ss$	Excluded $c\tau_s$ range for s [m]		
m_s [GeV]	$B = 0.1\%$	$B = 1\%$	$B = 10\%$
5	N/A	0.05–3.1	0.03–26.2
16	0.34–3.6	0.11–20.8	0.06–141.0
35	0.82–7.5	0.26–50.5	0.14–366.9
55	N/A	0.66–28.1	0.27–211.0

Table 9.1: Exclusion ranges for mean proper lifetime at 95% CL for the Hidden Sector models with $m_H = 125\,\text{GeV}$, assuming production cross section for $H \to ss$ process times branching fraction equal to 10%, 1%, and 0.1% of the SM Higgs boson production cross section [33].

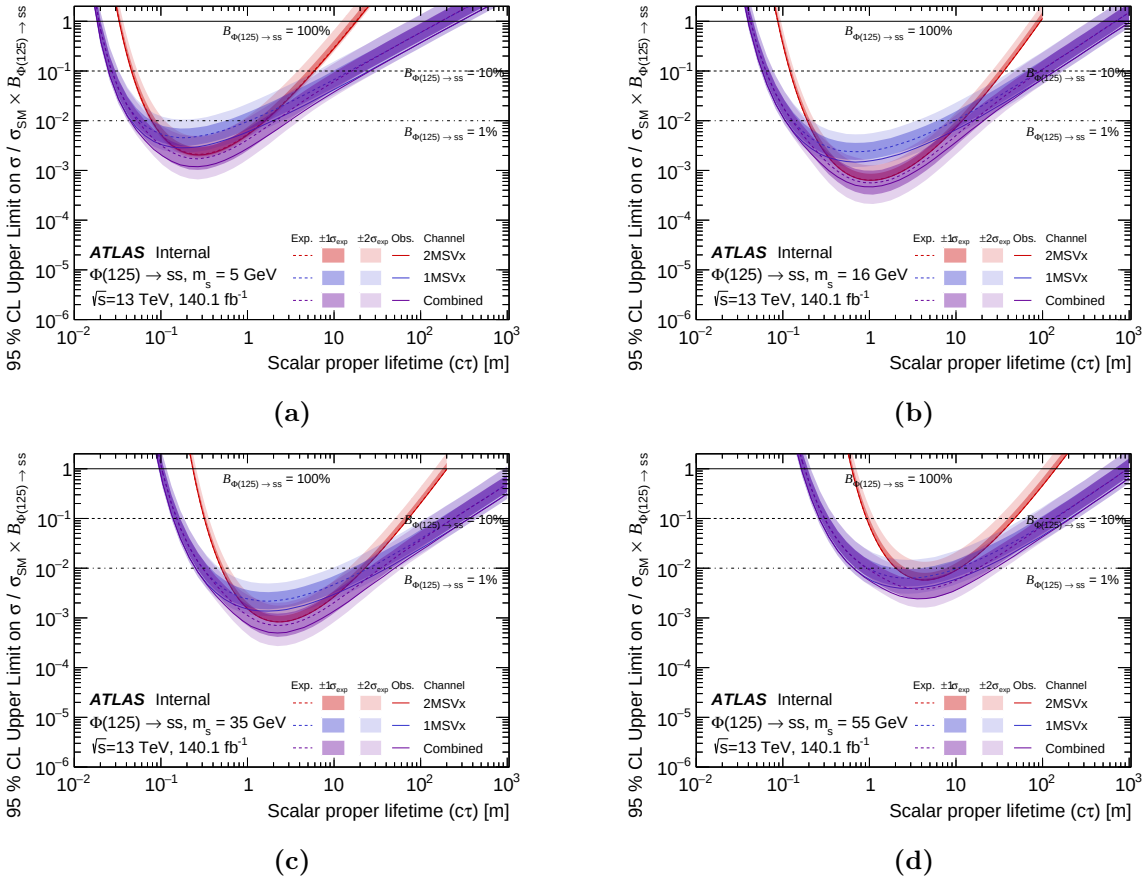

Figure 9.7: Branching ratio sensitivity upper limits over $c\tau$ range for $m_H = 125\,\text{GeV}$ Hidden Sector benchmark samples for the one-vertex channel, the two-vertex channel, and combined. Limits are set at 95% CL.

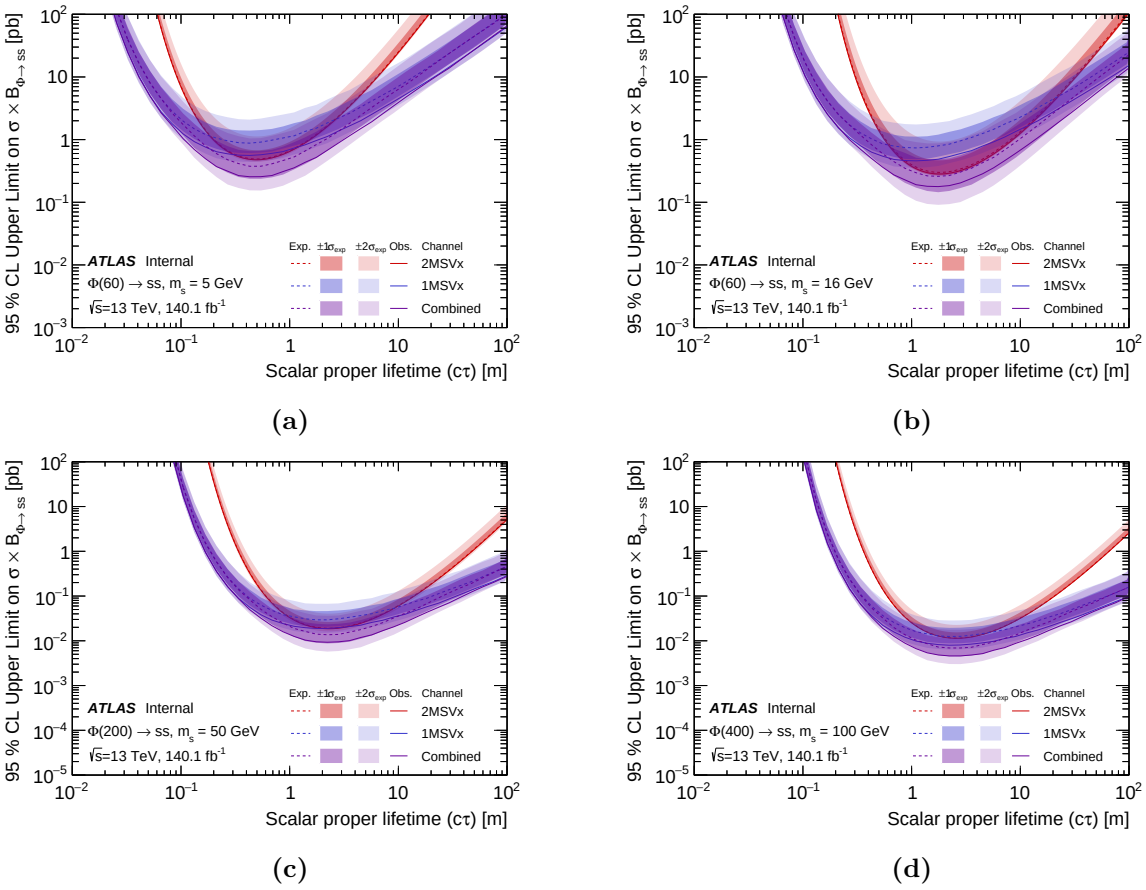

Figure 9.8: Branching ratio sensitivity upper limits over $c\tau$ range for $m_H \neq 125\,\text{GeV}$ Hidden Sector benchmark samples with m_H of 60 GeV, 200 GeV, and 400 GeV. Limits shown for the one-vertex channel, the two-vertex channel, and combined. Limits are set at 95% CL.

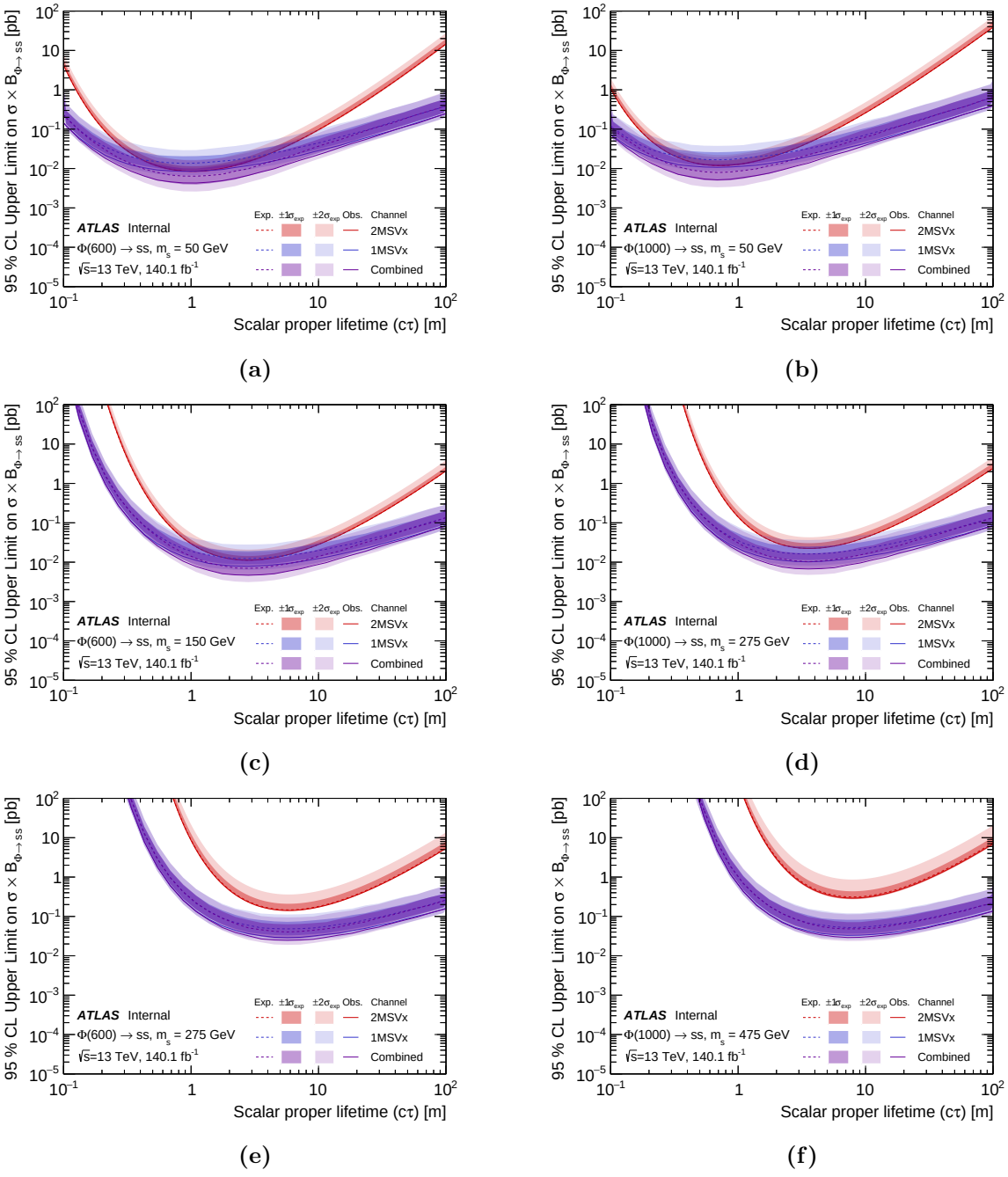

Figure 9.9: Branching ratio sensitivity upper limits over $c\tau$ range for $m_H \neq 125\,\text{GeV}$ Hidden Sector benchmark samples with m_H of 600 GeV and 1000 GeV. Limits shown for the one-vertex channel, the two-vertex channel, and combined. Limits are set at 95% CL.

9.4.2 Stat-Only Limits

The limits shown in Figures 9.2–9.6 account for all sources of uncertainty. It is often useful to show limits using only statistical sources of uncertainty as a comparison. If the limits using all sources of uncertainty are very close to the limits produced by using only statistical uncertainties, then it indicates that the sensitivity of the analysis is more constrained by statistics than it is by systematics. For LHC particle searches, this is considered ideal given additional statistics are produced with each run of the LHC. The statistical-only limits are given in Figures 9.10–9.14. Figure 9.10 contains the stat-only limits for Hidden Scalar benchmark samples with a SM Higgs mass, $m_H = 125\,\text{GeV}$. Figures 9.11 and 9.12 contain the stat-only limits for Hidden Scalar benchmark samples with a non-SM Higgs mass, $m_H \neq 125\,\text{GeV}$. Figures 9.13 and 9.14 contain the stat-only limits for Baryogenesis benchmark samples.

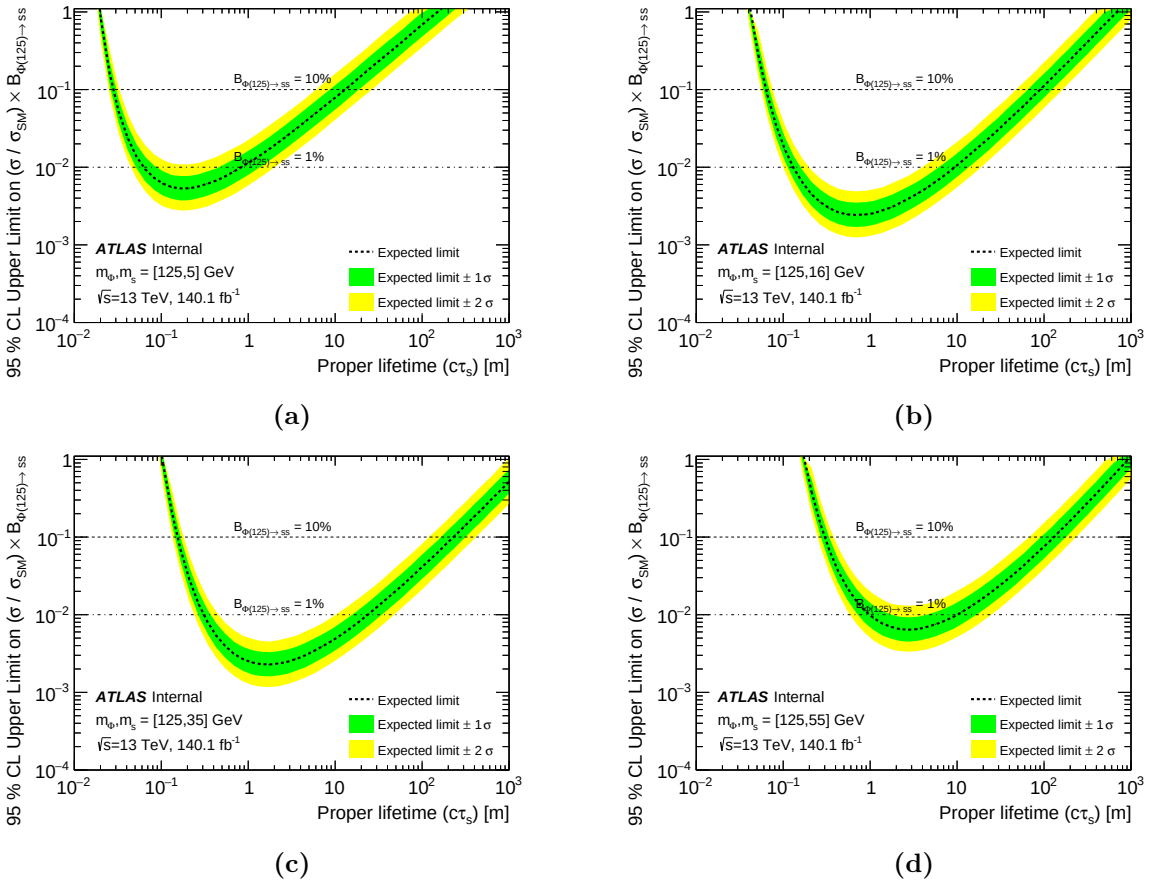

Figure 9.10: Branching ratio sensitivity upper limits over $c\tau$ range for $m_H = 125\,\text{GeV}$ Hidden Sector benchmark samples. Limits are set at 95% CL and only consider statistical uncertainties.

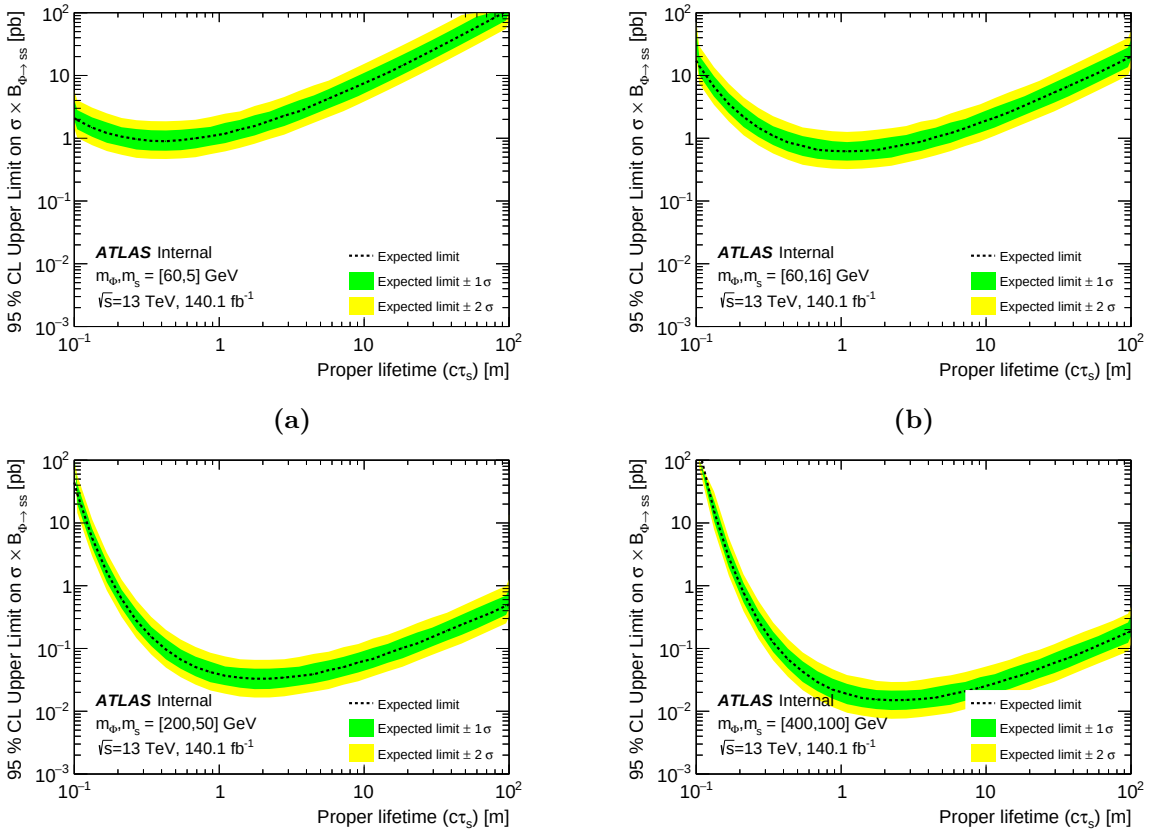

Figure 9.11: Branching ratio sensitivity upper limits over $c\tau$ range for $m_H \neq 125\,\text{GeV}$ Hidden Sector benchmark samples. Limits are set at 95% CL and only consider statistical uncertainties.

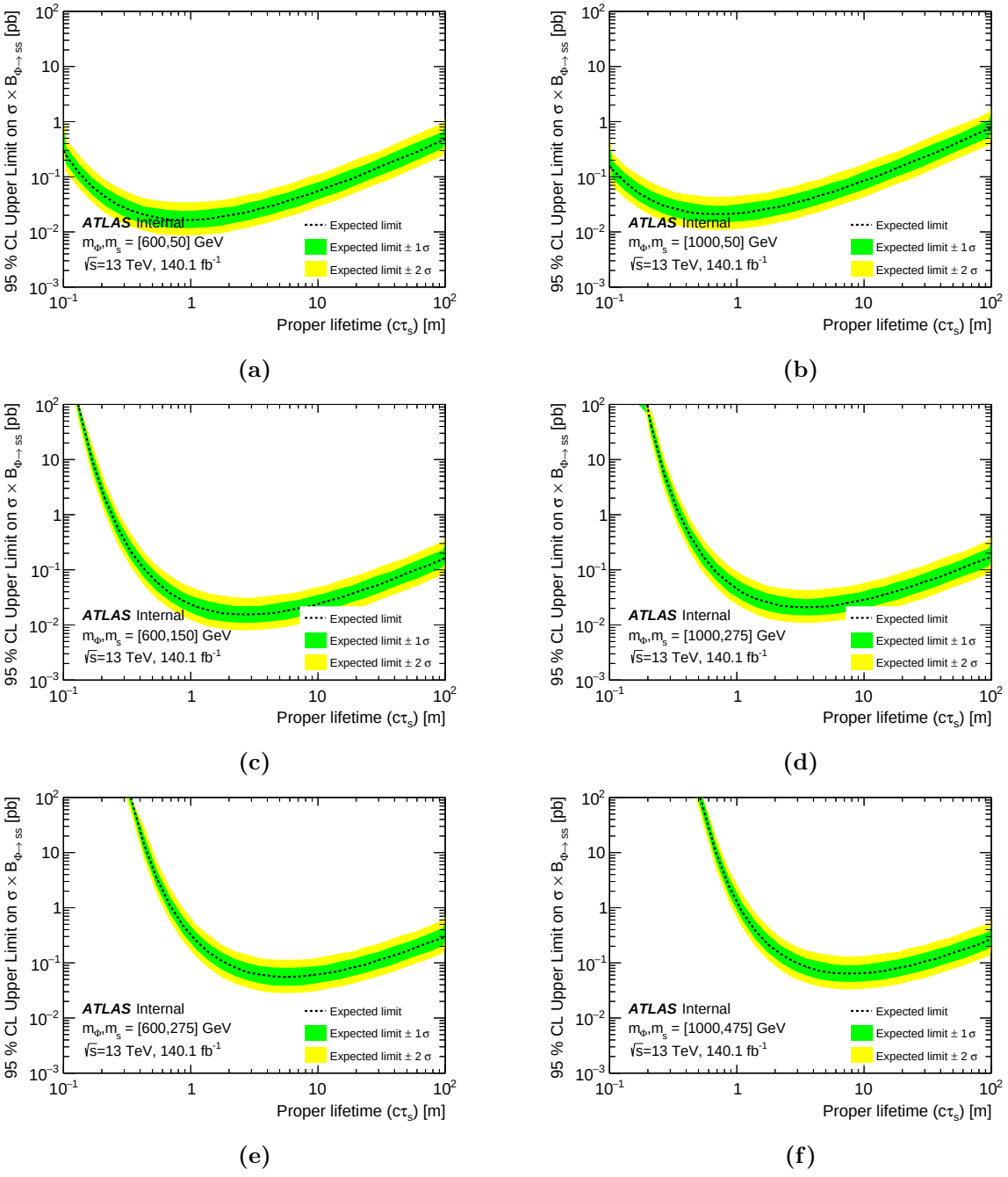

Figure 9.12: Branching ratio sensitivity upper limits over $c\tau$ range for $m_H \neq 125\,\text{GeV}$ Hidden Sector benchmark samples. Limits are set at 95% CL and only consider statistical uncertainties.

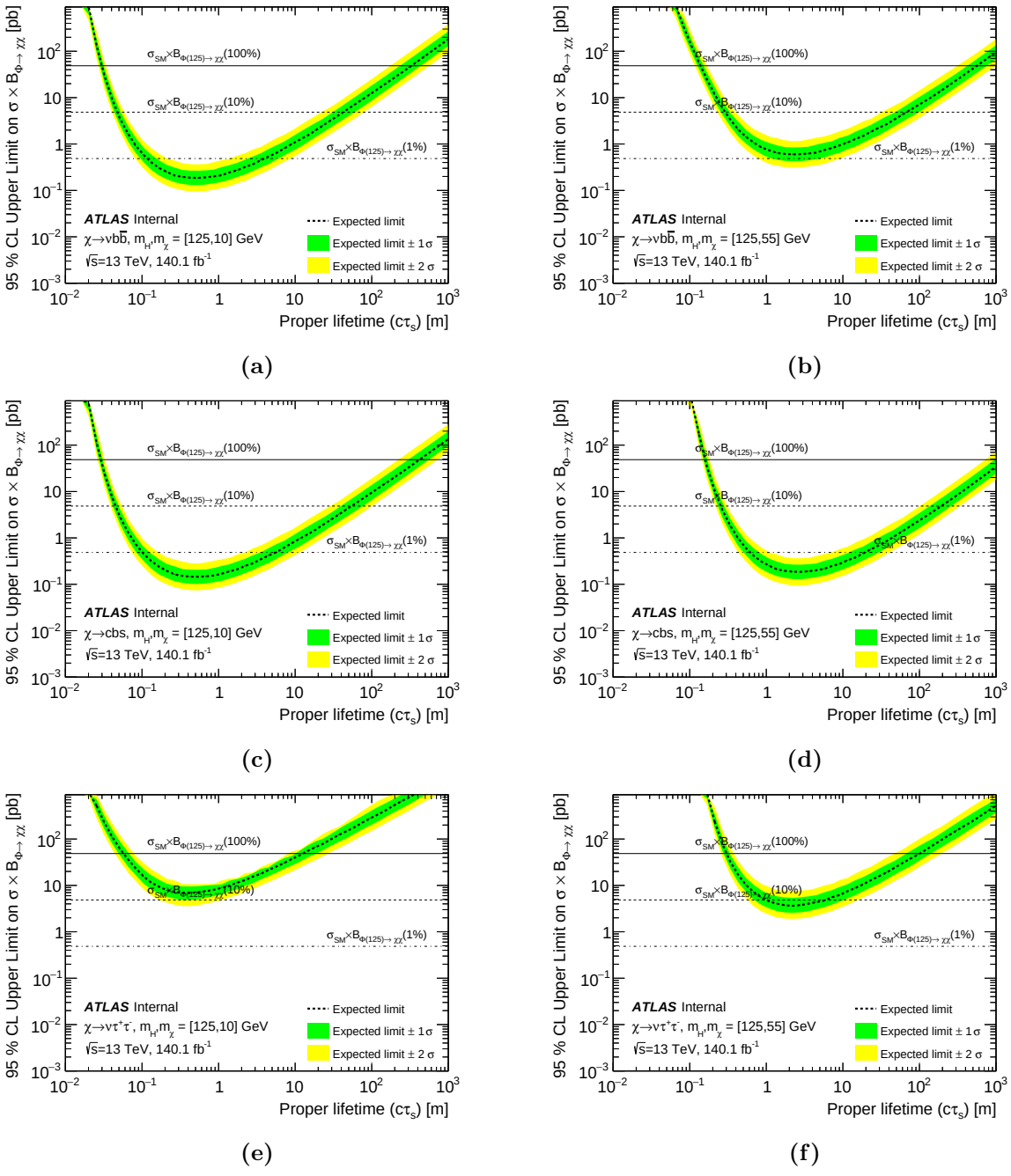

Figure 9.13: Branching ratio sensitivity upper limits over $c\tau$ range for $m_\chi = 10\,\text{GeV}$ and $m_\chi = 55\,\text{GeV}$ baryogenesis benchmark samples. Limits are set at 95% CL and only consider statistical uncertainties.

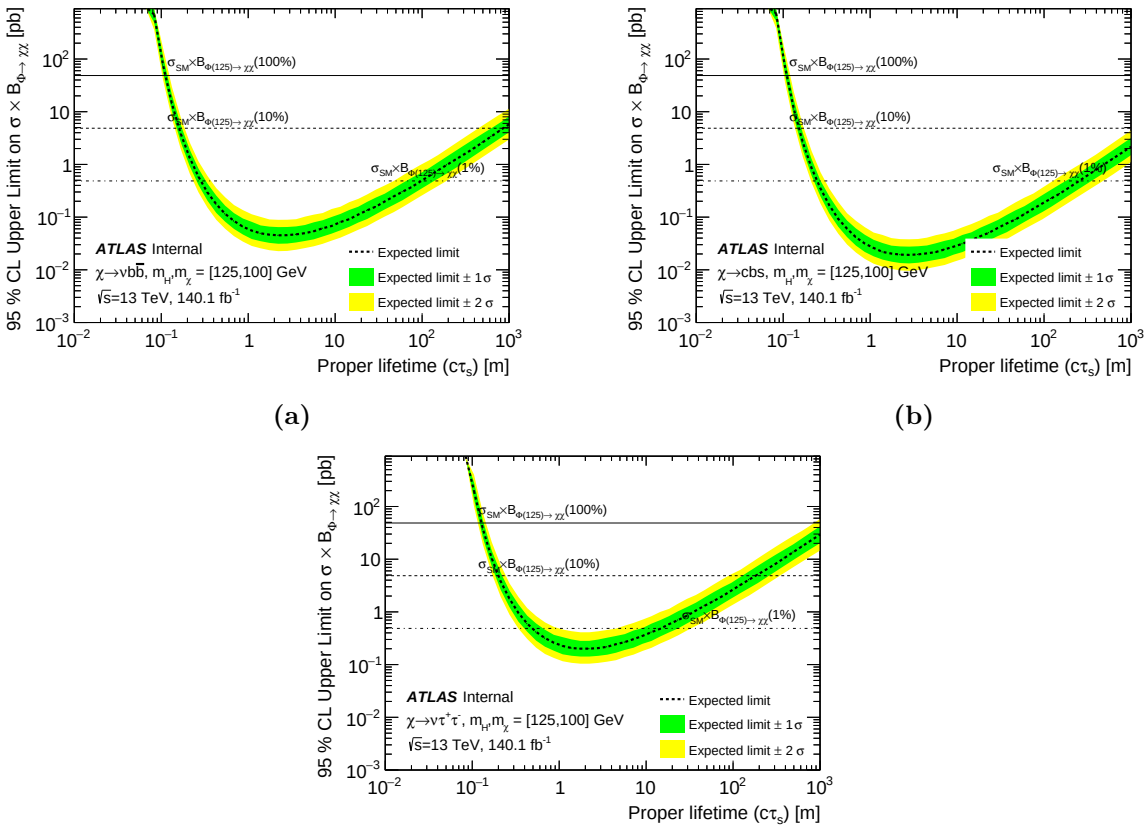

Figure 9.14: Branching ratio sensitivity upper limits over $c\tau$ range for $m_\chi = 100\,\text{GeV}$ baryogenesis benchmark samples. Limits are set at 95% CL and only consider statistical uncertainties.

Chapter 10

Conclusion

10.1 Summary of the Analysis

Models that predict long-lived particles suggest solutions to outstanding problems with the Standard Model, making the search for LLP signatures a compelling avenue of experimental research. Presented in this thesis is one such search, which focused on the detection of a single displaced hadronic jet in ATLAS arising from the decay of one of a pair of hidden sector scalar particles within the ATLAS detector. This analysis used $140\,\text{fb}^{-1}$ of data, corresponding to the total physics-ready integrated luminosity received by ATLAS during Run 2 of the LHC.

Two benchmark models were used in this analysis, called the Hidden Sector ($H \to ss$) model and the Baryogenesis ($H \to \chi\chi$) model. Both models predict the production of a pair of scalar particles, via a Higgs Portal mechanism, which decay to SM fermions. With minimal constraints on scalar mass and proper lifetime, this analysis is sensitive to a broad number of LLP decay modes and proper lifetimes. The $H \to ss$ model decay modes include s decays to $\tau^+\tau^-$, $c\bar{c}$, $b\bar{b}$, and $t\bar{t}$, while the Baryogenesis model decay modes include $\tau^+\tau^-\nu$, cbs, and $b\bar{b}\nu$. The sensitive lifetimes range from $O(0.1)\,\text{m}$ to $O(100)\,\text{m}$ depending on the mass of the LLP. The requirement in this analysis that exactly one of the two LLPs must produce a displaced vertex improves sensitivity at higher and lower lifetimes compared to the published two-vertex analysis.

Data are selected using a dedicated Muon RoI trigger, which is seeded by L1 muon RoIs passing the `2MU10` p_T threshold. This trigger looks for clusters of three (four) muon RoIs in the barrel (endcap) region in order to accept the event. It was observed, in a comparison

of punch-through jets in multijet MC and data, that the data contained 24% (20%) more muon RoIs than MC in the barrel (endcap) region. This mismodeling factor was applied as a systematic uncertainty to the trigger efficiency.

In order to reconstruct the decay vertex location of the LLP's displaced hadronic jets, an analysis-specific tracklet-finding and reconstruction algorithm is employed. In a comparison of punch-through jets between multijet MC and data, it was found that MC contained 27% (9%) more tracklets than data in the barrel (endcap) region, with a relative scale factor of 0.73 (0.91). To account for this mismodeling, the reconstruction efficiency from signal MC was scaled by these scale factors. An alternative method of tracklet-by-tracklet reweighting was also investigated and the difference in scale factor between the two methods was found to be 11% (13%) in the barrel (endcap). This difference was applied as a systematic uncertainty on the rescaled reconstruction efficiency.

The main background for a displaced hadronic jet signature is punch-through jets that continue to shower into the MS. This background is mitigated by applying selection criteria to any reconstructed vertex requiring isolation with respect to jets from the calorimeter and tracks from the inner detector. The remaining background is estimated using an ABCD method with axes defined by the scores from a pair of neural networks (NNs). These neural networks are trained separately on non-overlapping sets of event features. The resulting ABCD plane was validated in a region orthogonal to the signal region, defined by a selection on $H_{\mathrm{T}}^{\mathrm{miss}}$ and was found to have a Pearson correlation of less than 2%. The amount of background entering the signal region was estimated for events with a barrel vertex and events with an endcap vertex, separately. Expected background contamination in the signal region was calculated to be $226 \pm 14 \pm 18$ ($46 \pm 2 \pm 2$) events in the barrel (endcaps), where the first uncertainty corresponds to the statistical uncertainty and the second to the systematic uncertainty. The analysis was unblinded after demonstrating the ABCD plane was reliable in the validation region. The observed numbers of events in the signal region were 235 (35) in the barrel (endcap) region, indicating no statistically significant excess.

Because signal MC samples are generated at fixed lifetime, a toy MC extrapolation procedure was utilized to estimate expected signal yields at higher and lower lifetimes. The trigger and reconstruction efficiencies for the truth-level LLPs were extracted from the signal MC

samples. Toy events, generated with the same conditions as the signal MC samples but only at truth-level, were used to rescale the LLP decay locations for different LLP proper decay lengths, $c\tau$. The trigger and reconstruction efficiencies were then used to determine whether a toy event would pass or fail the selection criteria. This process was validated by comparing the extrapolated yields between two samples that differ only in generated lifetime. Good agreement was observed for all samples. The percent difference between the total efficiency from the fully-simulated signal MC and the extrapolated efficiency at the same $c\tau$ was taken as a systematic uncertainty on the extrapolation yield for each sample.

Without an excess seen, limits on the process cross section were set. For each signal MC sample, a 95% confidence level (CL) limit was set using the CLs method with the simultaneous ABCD profile log-likelihood ratio as the test statistic. For the Hidden Sector samples with a SM Higgs mass, the upper limits on the branching fraction, B, for the $H \to ss$ process can be set. At the 95% CL, the lifetime exclusion ranges are given at $B = 0.1\%$, $B = 1\%$, and $B = 10\%$ of the ratio of cross sections $\sigma/\sigma_{\text{SM}}$. A comparison of the $B = 10\%$ exclusion range between this analysis and the prior analysis, which only used $36\,\text{fb}^{-1}$ of data from the first two years of Run 2 shows a marked improvement. For the 5 GeV scalar mass sample, the range $[0.03, 26.2]\,\text{m}$ is excluded at $B = 10\%$ in this analysis, whereas the prior range was $[0.04, 8.774]\,\text{m}$ [168]. This improvement is primarily due to increased statistics, though the results of this analysis also benefit from improved lifetime extrapolation methodologies, an improved understanding of the trigger and vertex reconstruction modeling in MC, and a more robust ABCD plane provided by the inclusion of the NN.

For the non-SM Higgs mass samples from the Hidden Sector model, the limits are set on the cross section times branching fraction of the $H \to ss$ process. The Baryogenesis samples could have had the limits placed on the branching fraction, but were calculated with respect to the cross section times branching fraction in order to be compared with prior results. Comparisons between this result and other ATLAS and CMS results can be found in [169].

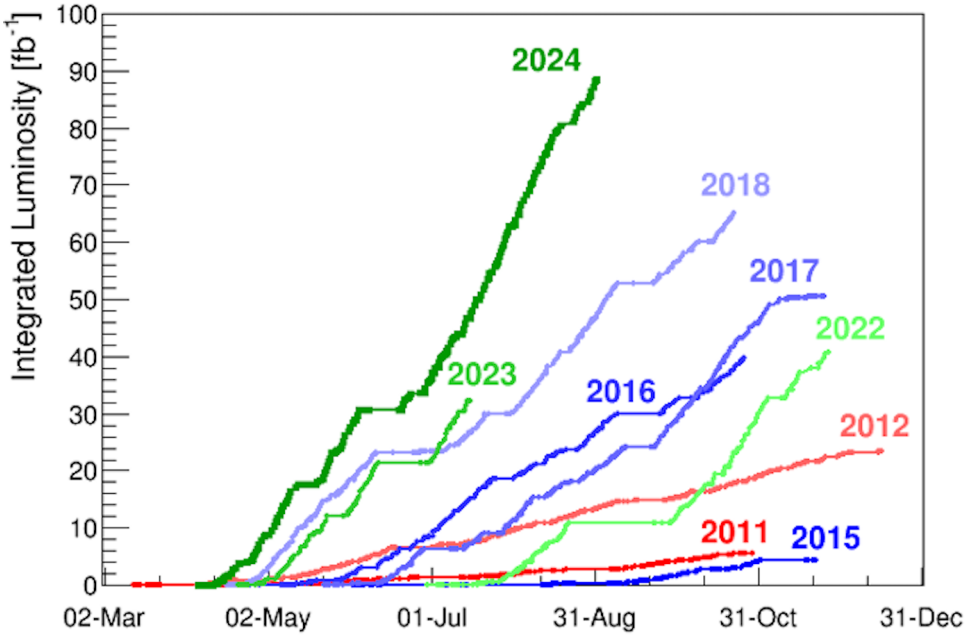

Figure 10.1: Integrated luminosity delivered to ATLAS by calendar year [170].

10.2 Future Work

Run 3 of the LHC will increase the total luminosity delivered to ATLAS, resulting in more statistics for analyses. As of the beginning of September in 2024, the LHC had already delivered a total integrated luminosity of 160 fb^{-1} to ATLAS [170]. The expected delivery by the end of Run 3 is 300 fb^{-1}, nearly double the delivered luminosity of Run 2 (159.8 fb^{-1}) [170]. Without any changes to the analysis, this increase in statistics would already represent a substantial improvement to sensitivity, especially when combined with current Run 2 results.

Improvements to aspects of the single MS vertex search could also be made for a future analysis using Run 3 data.

- **Neural Networks** - The NN model used in this analysis is a fairly simple multilayer perceptron (MLP) network. MLP architectures are dated, and more robust network architectures have been developed over the past several years which have a good chance of increasing background-signal separation, increasing signal statistics in the A-region of the ABCD planes, and yielding a higher sensitivity. While significant effort has

been made toward investigating new variables that could prove useful as NN input features, the inclusion of additional features may also yield some improvements in NN separation power.

- **Global Vertexing Algorithm** - The barrel and endcap fiducial regions exclude the pseudorapidity range $0.7 < |\eta| < 1.3$ due to the barrel and endcap having different vertex reconstruction algorithms. This restriction leads the rest of the analysis to treat the barrel and endcap separately as well. The development of a global algorithm would permit the inclusion of any vertices within this overlap region, the combination of the barrel and endcap ABCD planes, and the combination of the barrel and endcap trigger and vertex efficiencies for lifetime extrapolation. This would simplify the analysis greatly, increase the analysis coverage, and reduce statistical uncertainties by permitting the barrel and endcap statistics to be treated together. Due to the possibility of the same particle leaving tracks in both the barrel and endcap detectors, a robust duplicate detection algorithm would need to be developed to mitigate the chance of double-counting tracklets in the overlap region, which is likely to require considerable development effort and additional studies.

- **Better Understanding of MC Mismodeling** - The mismodeling of punch-through jets in the dijet MC, compared to data, introduces scale factors to the trigger and vertex efficiencies. These scale factors are responsible for fairly significant systematic uncertainties. Additionally, contributions from cosmic rays and cavern background are also not well modeled in MC simulation, and may have a nontrivial effect. To mitigate this contribution, more work is needed to understand the underlying cause of the mismodeling. The trigger efficiency calculated from dijet MC underestimates the number of muon RoIs, while the reconstruction efficiency is overestimated in MC, which comes from a higher reconstructed tracklet multiplicity. Understanding why there are fewer muon RoIs and the source of these extra tracklets could inform improvements to the MC modeling or a more efficient mitigation technique to reduce systematic contributions.

- **Improved Extrapolation Techniques** - While not a problem in this analysis, ad-

ditional statistics and reduced uncertainties may reveal a non-closure in the lifetime extrapolation procedure, meaning that two MC samples generated with the same Higgs and scalar masses, but different lifetimes, may no longer agree on expected event yields when extrapolated to higher and lower lifetimes. The vertex and trigger efficiencies are currently modeled as binned functions of LLP $L_{xy}\,(L_z)$ and LLP β. Increased signal selection efficiency, perhaps by improvements to the NNs, may permit a higher granularity in these binned functions, which would likely improve extrapolation agreement. Improvements to the extrapolation procedure could also decrease the systematic uncertainty applied to the limits, which comes from the difference in the total selection efficiency between that calculated directly from the full-sim signal MC and that returned by the lifetime extrapolation at the full-sim generated lifetime.

While not an option for Run 3, improvements to the LLP trigger could also result in higher signal sensitivity. The introduction of the New Small Wheel (NSW) during the Phase-I upgrades was accompanied by improvements to the L1 hardware-based trigger systems, introducing new information at the trigger level that was not available during Run 2. Some of this additional information could be leveraged to improve the LLP trigger to better target signal-like events. Considerable development would be needed in this direction, but taking advantage of new triggering technology unique to ATLAS post-Phase-I could prove to be a promising direction for an improved analysis.

REFERENCES

[1] Steven Weinberg. "A Model of Leptons". In: *Phys. Rev. Lett.* 19 (21 Nov. 1967), pp. 1264–1266. DOI: 10.1103/PhysRevLett.19.1264. URL: https://link.aps.org/doi/10.1103/PhysRevLett.19.1264.

[2] Abdus Salam. "Weak and Electromagnetic Interactions". In: *Conf. Proc. C* 680519 (1968), pp. 367–377. DOI: 10.1142/9789812795915_0034.

[3] Georges Aad et al. "Observation of a new particle in the search for the Standard Model Higgs boson with the ATLAS detector at the LHC. Observation of a new particle in the search for the Standard Model Higgs boson with the ATLAS detector at the LHC". In: *Phys. Lett. B* 716 (2012). Comments: 24 pages plus author list (38 pages total), 12 figures, 7 tables, revised author list, pp. 1–29. DOI: 10.1016/j.physletb.2012.08.020. arXiv: 1207.7214. URL: https://cds.cern.ch/record/1471031.

[4] Serguei Chatrchyan et al. "Observation of a new boson at a mass of 125 GeV with the CMS experiment at the LHC. Observation of a new boson at a mass of 125 GeV with the CMS experiment at the LHC". In: *Phys. Lett. B* 716 (2012), pp. 30–61. DOI: 10.1016/j.physletb.2012.08.021. arXiv: 1207.7235. URL: https://cds.cern.ch/record/1471016.

[5] M. C. Rodriguez. *The Minimal Supersymmetric Standard Model (MSSM) and General Singlet Extensions of the MSSM (GSEMSSM), a short review*. 2019. arXiv: 1911.13043 [hep-ph]. URL: https://arxiv.org/abs/1911.13043.

[6] JoAnne L Hewett et al. "Signatures of long-lived gluinos in split supersymmetry". In: *Journal of High Energy Physics* 2004.09 (Oct. 2004), pp. 070–070. ISSN: 1029-8479. DOI: 10.1088/1126-6708/2004/09/070. URL: http://dx.doi.org/10.1088/1126-6708/2004/09/070.

[7] G.F. Giudice and A. Romanino. "Erratum to: "Split supersymmetry" [Nucl. Phys. B 699 (2004) 65]". In: *Nuclear Physics B* 706.1–2 (Jan. 2005), p. 487. ISSN: 0550-3213. DOI: 10.1016/j.nuclphysb.2004.11.048. URL: http://dx.doi.org/10.1016/j.nuclphysb.2004.11.048.

[8] Matthew J. Strassler and Kathryn M. Zurek. "Echoes of a hidden valley at hadron colliders". In: *Physics Letters B* 651.5 (2007), pp. 374–379. ISSN: 0370-2693. DOI: https://doi.org/10.1016/j.physletb.2007.06.055. URL: https://www.sciencedirect.com/science/article/pii/S0370269307007721.

[9] Matthew J. Strassler and Kathryn M. Zurek. "Discovering the Higgs through highly-displaced vertices". In: *Physics Letters B* 661.4 (Mar. 2008), pp. 263–267. ISSN: 0370-2693. DOI: 10.1016/j.physletb.2008.02.008. URL: http://dx.doi.org/10.1016/j.physletb.2008.02.008.

[10] Giorgio Arcadi, Abdelhak Djouadi, and Martti Raidal. "Dark Matter through the Higgs portal". In: *Physics Reports* 842 (Feb. 2020), pp. 1–180. ISSN: 0370-1573. DOI: 10.1016/j.physrep.2019.11.003. URL: http://dx.doi.org/10.1016/j.physrep.2019.11.003.

[11] Gilly Elor et al. *New Ideas in Baryogenesis: A Snowmass White Paper*. 2022. arXiv: 2203.05010 [hep-ph]. URL: https://arxiv.org/abs/2203.05010.

[12] David E Morrissey and Michael J Ramsey-Musolf. "Electroweak baryogenesis". In: *New Journal of Physics* 14.12 (Dec. 2012), p. 125003. ISSN: 1367-2630. DOI: 10.1088/1367-2630/14/12/125003. URL: http://dx.doi.org/10.1088/1367-2630/14/12/125003.

[13] Lei Wang et al. "A Concise Review on Some Higgs-Related New Physics Models in Light of Current Experiments". In: *Universe* 9.4 (Apr. 2023), p. 178. ISSN: 2218-1997. DOI: 10.3390/universe9040178. URL: http://dx.doi.org/10.3390/universe9040178.

[14] Matthew J. Strassler. *On the Phenomenology of Hidden Valleys with Heavy Flavor*. 2008. arXiv: 0806.2385 [hep-ph]. URL: https://arxiv.org/abs/0806.2385.

[15] David Curtin et al. "Long-lived particles at the energy frontier: the MATHUSLA physics case". In: *Reports on Progress in Physics* 82.11 (Oct. 2019), p. 116201. ISSN: 1361-6633. DOI: 10.1088/1361-6633/ab28d6. URL: http://dx.doi.org/10.1088/1361-6633/ab28d6.

[16] Tao Han et al. "Phenomenology of hidden valleys at hadron colliders". In: *Journal of High Energy Physics* 2008.07 (July 2008), pp. 008–008. ISSN: 1029-8479. DOI: 10.1088/1126-6708/2008/07/008. URL: http://dx.doi.org/10.1088/1126-6708/2008/07/008.

[17] Cush. Public Domain. URL: https://en.wikipedia.org/wiki/File:Standard_Model_of_Elementary_Particles.svg.

[18] David Tong. *Gauge Theory*. 2018. URL: http://www.damtp.cam.ac.uk/user/tong/gaugetheory.html.

[19] Michael E. Peskin and Daniel V. Schroeder. *An Introduction to quantum field theory*. Reading, USA: Addison-Wesley, 1995. Chap. 3. ISBN: 978-0-201-50397-5, 978-0-429-50355-9, 978-0-429-49417-8. DOI: 10.1201/9780429503559.

[20] E. C. G. Sudarshan and R. E. Marshak. "THE NATURE OF THE FOUR-FERMION INTERACTION". In: *Current Science* 63.2 (1992), pp. 65–75. ISSN: 00113891. URL: http://www.jstor.org/stable/24095422 (visited on 10/16/2024).

[21] F. Halzen and Alan D. Martin. *QUARKS AND LEPTONS: AN INTRODUCTORY COURSE IN MODERN PARTICLE PHYSICS*. Wiley, 1984. ISBN: 978-0-471-88741-6.

[22] M.C. Gonzalez-Garcia and Michele Maltoni. "Phenomenology with massive neutrinos". In: *Physics Reports* 460.1–3 (Apr. 2008), pp. 1–129. ISSN: 0370-1573. DOI: 10.1016/j.physrep.2007.12.004. URL: http://dx.doi.org/10.1016/j.physrep.2007.12.004.

[23] L. Bergström. "Dark matter evidence, particle physics candidates and detection methods". In: *Annalen der Physik* 524.9–10 (Aug. 2012), pp. 479–496. ISSN: 1521-3889. DOI: 10.1002/andp.201200116. URL: http://dx.doi.org/10.1002/andp.201200116.

[24] Andrei D Sakharov. "Violation of CP invariance, C asymmetry, and baryon asymmetry of the universe". In: *Soviet Physics Uspekhi* 34.5 (May 1991), p. 392. DOI: 10.1070/PU1991v034n05ABEH002497. URL: https://dx.doi.org/10.1070/PU1991v034n05ABEH002497.

[25] Laurent Canetti, Marco Drewes, and Mikhail Shaposhnikov. "Matter and antimatter in the universe". In: *New Journal of Physics* 14.9 (Sept. 2012), p. 095012. ISSN: 1367-2630. DOI: 10.1088/1367-2630/14/9/095012. URL: http://dx.doi.org/10.1088/1367-2630/14/9/095012.

[26] Howard Georgi and S. L. Glashow. "Unity of All Elementary-Particle Forces". In: *Phys. Rev. Lett.* 32 (8 Feb. 1974), pp. 438–441. DOI: 10.1103/PhysRevLett.32.438. URL: https://link.aps.org/doi/10.1103/PhysRevLett.32.438.

[27] Assaf Shomer. *A pedagogical explanation for the non-renormalizability of gravity*. 2007. arXiv: 0709.3555 [hep-th]. URL: https://arxiv.org/abs/0709.3555.

[28] Steven Weinberg. "Photons and Gravitons in Perturbation Theory: Derivation of Maxwell's and Einstein's Equations". In: *Phys. Rev.* 138 (4B May 1965), B988–B1002. DOI: 10.1103/PhysRev.138.B988. URL: https://link.aps.org/doi/10.1103/PhysRev.138.B988.

[29] Benjamin Schulz. *Review on the quantization of gravity*. 2014. arXiv: 1409.7977 [gr-qc]. URL: https://arxiv.org/abs/1409.7977.

[30] C Csáki and P Tanedo. *Beyond the Standard Model*. en. 2015. DOI: 10.5170/CERN-2015-004.169. URL: http://cds.cern.ch/record/2119546.

[31] Roberto D. Peccei. "The Strong CP Problem and Axions". In: *Axions*. Springer Berlin Heidelberg, 2008, pp. 3–17. ISBN: 9783540735182. DOI: 10.1007/978-3-540-73518-2_1. URL: http://dx.doi.org/10.1007/978-3-540-73518-2_1.

[32] R. Aaij et al. "First measurement of the CP-violating phase in $B_s^0 \to J\psi(\to e^+e^-)\phi$ decays". In: *The European Physical Journal C* 81.11 (Nov. 2021). ISSN: 1434-6052. DOI: 10.1140/epjc/s10052-021-09711-7. URL: http://dx.doi.org/10.1140/epjc/s10052-021-09711-7.

[33] Particle Data Group. *Status of Higgs Boson Physics*. https://pdg.lbl.gov/2023/reviews/rpp2023-rev-higgs-boson.pdf. [Accessed 27-10-2024]. Aug. 2023.

[34] G. Aad et al. "Combination of searches for invisible decays of the Higgs boson using 139 fb^{-1} of proton-proton collision data at $\sqrt{s} = 13$ TeV collected with the ATLAS experiment". In: *Physics Letters B* 842 (July 2023). ISSN: 0370-2693. DOI: 10.1016/j.physletb.2023.137963. URL: http://dx.doi.org/10.1016/j.physletb.2023.137963.

[35] A. Tumasyan et al. "A search for decays of the Higgs boson to invisible particles in events with a top-antitop quark pair or a vector boson in proton-proton collisions at $\sqrt{s} = 13\,\text{TeV}$". In: *The European Physical Journal C* 83.10 (Oct. 2023). ISSN: 1434-6052. DOI: 10.1140/epjc/s10052-023-11952-7. URL: http://dx.doi.org/10.1140/epjc/s10052-023-11952-7.

[36] Robert Schabinger and James D. Wells. "Minimal spontaneously broken hidden sector and its impact on Higgs boson physics at the CERN Large Hadron Collider". In: *Physical Review D* 72.9 (Nov. 2005). ISSN: 1550-2368. DOI: 10.1103/physrevd.72.093007. URL: http://dx.doi.org/10.1103/PhysRevD.72.093007.

[37] David Curtin et al. "Exotic decays of the 125 GeV Higgs boson". In: *Physical Review D* 90.7 (Oct. 2014). ISSN: 1550-2368. DOI: 10.1103/physrevd.90.075004. URL: http://dx.doi.org/10.1103/PhysRevD.90.075004.

[38] Yanou Cui and Brian Shuve. "Probing baryogenesis with displaced vertices at the LHC". In: *Journal of High Energy Physics* 2015.2 (Feb. 2015). ISSN: 1029-8479. DOI: 10.1007/jhep02(2015)049. URL: http://dx.doi.org/10.1007/JHEP02(2015)049.

[39] A. D. Sakharov. "Violation of CP Invariance, C asymmetry, and baryon asymmetry of the universe". In: *Pisma Zh. Eksp. Teor. Fiz.* 5 (1967), pp. 32–35. DOI: 10.1070/PU1991v034n05ABEH002497.

[40] DONALD W. KERST. "HISTORICAL DEVELOPMENT OF THE BETATRON". In: *Nature* 157.3978 (Jan. 1946), pp. 90–95. ISSN: 1476-4687. DOI: 10.1038/157090a0. URL: https://doi.org/10.1038/157090a0.

[41] Sergio Tazzari. "Short History of Particle Accelerators". In: Presented at CERN CAS: Introduction to Accelerator Physics in Zakopane, Poland, 2006. URL: https://cas.web.cern.ch/sites/default/files/lectures/zakopane-2006/tazzari-history.pdf.

[42] *The Ring Cyclotron*. https://www.psi.ch/en/gfa/ring. [Accessed 29-05-2024].

[43] Lyndon R Evans and Philip Bryant. "LHC Machine". In: *JINST* 3 (2008). This report is an abridged version of the LHC Design Report (CERN-2004-003), S08001. DOI: 10.1088/1748-0221/3/08/S08001. URL: https://cds.cern.ch/record/1129806.

[44] Esma Mobs. "The CERN accelerator complex in 2019. Complexe des accélérateurs du CERN en 2019". In: (2019). General Photo. URL: https://cds.cern.ch/record/2684277.

[45] L Rossi. "Superconductivity: Its Role, Its Success and Its Setbacks in the Large Hadron Collider of CERN". In: *Supercond. Sci. Technol.* 23 (2010), p. 034001. DOI: 10.1088/0953-2048/23/3/034001. URL: https://cds.cern.ch/record/1235168.

[46] CERN. "Incident in sector 3-4 of the LHC – CERN Courier". In: (2008). [Accessed 30-05-2024].

[47] CERN. "LHC sets new record – accelerates beam to 3.5 TeV". In: (2010). [Accessed 30-05-2024]. URL: https://home.cern/news/press-release/cern/lhc-sets-new-record-accelerates-beam-35-tev.

[48] CERN. *LHC latest news*. https://lhc-commissioning.web.cern.ch/news-2015/LHC-latest-news.html. [Accessed 30-05-2024]. 2018.

[49] Cian O'Luanaigh. *Heavy metal: Refilling the lead source for the LHC*. https://home.cern/news/news/accelerators/heavy-metal-refilling-lead-source-lhc. [Accessed 24-10-2024]. Feb. 2013.

[50] *Overview of the status and developments on primary ion sources at CERN*. IPAC2011. 2011.

[51] CERN. *Linear accelerator 4 — home.cern*. https://home.cern/science/accelerators/linear-accelerator-4. [Accessed 24-05-2024].

[52] CERN. *The Proton Synchrotron Booster — home.cern*. https://home.cern/science/accelerators/proton-synchrotron-booster. [Accessed 24-05-2024].

[53] CERN. *The Proton Synchrotron — home.cern*. https://home.cern/science/accelerators/proton-synchrotron. [Accessed 24-05-2024].

[54] *Overview on CERN Test Beam Facilities and Plans for Tests for Non-Collider Experiments*. CERN. May 2009. URL: https://indico.cern.ch/event/51128/contributions/2032881/attachments/966402/1372336/test_beams_non-collider_Geschwendtner_200905.ppt.pdf.

[55] CERN. *The Super Proton Synchrotron — home.cern*. https://home.cern/science/accelerators/super-proton-synchrotron. [Accessed 24-05-2024].

[56] L Rossi. "Superconducting magnets for the LHC main lattice". In: *IEEE Trans. Appl. Supercond.* 14.2 (2004), pp. 153–158. DOI: 10.1109/TASC.2004.829031. URL: https://cds.cern.ch/record/732330.

[57] Oliver Sim Brüning et al. *LHC Design Report*. CERN Yellow Reports: Monographs. Geneva: CERN, 2004. DOI: 10.5170/CERN-2004-003-V-1. URL: https://cds.cern.ch/record/782076.

[58] Xabier C. Vidal and Ramon C Manzano. *Taking a closer look at LHC - RF cavities*. https://www.lhc-closer.es/taking_a_closer_look_at_lhc/0.rf_cavities. [Accessed 25-10-2024].

[59] Xabier C. Vidal and Ramon C Manzano. *Taking a closer look at LHC - Buckets and bunches*. https://www.lhc-closer.es/taking_a_closer_look_at_lhc/0.buckets_and_bunches. [Accessed 25-10-2024].

[60] K Aamodt et al. "The ALICE experiment at the CERN LHC. A Large Ion Collider Experiment". In: *JINST* 3 (2008). Also published by CERN Geneva in 2010, S08002. DOI: 10.1088/1748-0221/3/08/S08002. URL: http://cds.cern.ch/record/1129812.

[61] S Chatrchyan et al. "The CMS experiment at the CERN LHC. The Compact Muon Solenoid experiment". In: *JINST* 3 (2008). Also published by CERN Geneva in 2010, S08004. DOI: 10.1088/1748-0221/3/08/S08004. URL: http://cds.cern.ch/record/1129810.

[62] M Aleksa and M Diemoz. *Discussion on the electromagnetic calorimeters of ATLAS and CMS*. Tech. rep. Geneva: CERN, 2013. URL: https://cds.cern.ch/record/1547314.

[63] A Robichaud-Véronneau. *The ATLAS detector at the LHC*. Tech. rep. Geneva: CERN, 2009. URL: https://cds.cern.ch/record/1213517.

[64] A. Augusto Alves Jr. et al. "The LHCb Detector at the LHC". In: *JINST* 3 (2008). Also published by CERN Geneva in 2010, S08005. DOI: 10.1088/1748-0221/3/08/S08005. URL: https://cds.cern.ch/record/1129809.

[65] A. Airapetian et al. "ATLAS: Detector and physics performance technical design report. Volume 1". In: (May 1999).

[66] Joao Pequenao. "Computer generated image of the whole ATLAS detector". 2008. URL: https://cds.cern.ch/record/1095924.

[67] Joao Pequenao. "Computer generated image of the ATLAS inner detector". 2008. URL: https://cds.cern.ch/record/1095926.

[68] *ATLAS inner detector: Technical Design Report, 1*. Technical design report. ATLAS. Geneva: CERN, 1997. URL: https://cds.cern.ch/record/331063.

[69] The ATLAS TRT collaboration et al. "The ATLAS TRT end-cap detectors". In: *JINST* 3 (2008), P10003. DOI: 10.1088/1748-0221/3/10/P10003. URL: http://cds.cern.ch/record/1151338.

[70] A. Airapetian et al. *ATLAS detector and physics performance: Technical Design Report, 1*. Technical design report. ATLAS. Geneva: CERN, 1999. URL: https://cds.cern.ch/record/391176.

[71] *ATLAS liquid-argon calorimeter: Technical Design Report*. Technical design report. ATLAS. Geneva: CERN, 1996. DOI: 10.17181/CERN.FWRW.FOOQ. URL: https://cds.cern.ch/record/331061.

[72] Bernard Aubert et al. "Performance of the ATLAS Electromagnetic Calorimeter End-cap Module 0". In: *Nucl. Instrum. Methods Phys. Res. A* (Jan. 2003).

[73] Joao Pequenao. "Computer Generated image of the ATLAS calorimeter". 2008. URL: https://cds.cern.ch/record/1095927.

[74] Henric Wilkens et al. "The ATLAS Liquid Argon calorimeter: An overview". In: *Journal of Physics: Conference Series* 160.1 (Apr. 2009), p. 012043. DOI: 10.1088/1742-6596/160/1/012043. URL: https://dx.doi.org/10.1088/1742-6596/160/1/012043.

[75] *ATLAS tile calorimeter: Technical Design Report*. Technical design report. ATLAS. Geneva: CERN, 1996. DOI: 10.17181/CERN.JRBJ.7O28. URL: https://cds.cern.ch/record/331062.

[76] A Artamonov et al. "The ATLAS Forward Calorimeter". In: *JINST* 3 (2008), P02010. DOI: 10.1088/1748-0221/3/02/P02010. URL: https://cds.cern.ch/record/1094547.

[77] G Aad et al. "The ATLAS Experiment at the CERN Large Hadron Collider". In: *JINST* 3 (2008). Also published by CERN Geneva in 2010, S08003. DOI: 10.1088/1748-0221/3/08/S08003. URL: https://cds.cern.ch/record/1129811.

[78] P Adragna et al. "Testbeam Studies of Production Modules of the ATLAS Tile Calorimeter". In: *Nucl. Instrum. Methods Phys. Res., A* 606.3 (2009), pp. 362–394. DOI: 10.1016/j.nima.2009.04.009. URL: http://cds.cern.ch/record/1161354.

[79] L March. "Status of the ATLAS Liquid Argon Calorimeter and its performance after one year of LHC operation". In: (2011). URL: http://cds.cern.ch/record/1394598.

[80] Joao Pequenao. "Computer generated image of the ATLAS Muons subsystem". 2008. URL: https://cds.cern.ch/record/1095929.

[81] *ATLAS muon spectrometer: Technical Design Report*. Technical design report. ATLAS. Geneva: CERN, 1997. URL: https://cds.cern.ch/record/331068.

[82] Georges Aad et al. "Resolution of the ATLAS muon spectrometer monitored drift tubes in LHC Run 2". In: *JINST* 14.09 (2019), P09011. DOI: 10.1088/1748-0221/14/09/P09011. arXiv: 1906.12226. URL: https://cds.cern.ch/record/2680532.

[83] G. Aad et al. "Search for events with a pair of displaced vertices from long-lived neutral particles decaying into hadronic jets in the ATLAS muon spectrometer in pp collisions at $\sqrt{s} = 13\,TeV$". In: *Physical Review D* 106.3 (Aug. 2022). ISSN: 2470-0029. DOI: 10.1103/physrevd.106.032005. URL: http://dx.doi.org/10.1103/PhysRevD.106.032005.

[84] Georges Aad et al. "Luminosity determination in pp collisions at $\sqrt{s} = 13$ TeV using the ATLAS detector at the LHC. Luminosity determination in pp collisions at $\sqrt{s} = 13$ TeV using the ATLAS detector at the LHC". In: *Eur. Phys. J. C* 83.10 (2023), p. 982. DOI: 10.1140/epjc/s10052-023-11747-w. arXiv: 2212.09379. URL: https://cds.cern.ch/record/2844887.

[85] University of Massachusetts Amherst. "Physicists eager for new, high-energy Large Hadron Collider run". In: (June 2015). URL: www.sciencedaily.com/releases/2015/06/150603181744.htm.

[86] CERN. *LHC Schedule 2018*. Oct. 2018.

[87] Nicoletta Garelli. "Performance of the ATLAS Detector in Run-2". In: *EPJ Web Conf.* 164 (2017), p. 01021. DOI: 10.1051/epjconf/201716401021. URL: https://cds.cern.ch/record/2310929.

[88] Georges Aad et al. "ATLAS data quality operations and performance for 2015-2018 data-taking". In: *JINST* 15.04 (2020), P04003. DOI: 10.1088/1748-0221/15/04/P04003. arXiv: 1911.04632. URL: https://cds.cern.ch/record/2700249.

[89] G Avoni et al. "The new LUCID-2 detector for luminosity measurement and monitoring in ATLAS". In: *JINST* 13.07 (2018), P07017. DOI: 10.1088/1748-0221/13/07/P07017. URL: http://cds.cern.ch/record/2633501.

[90] Carla Sbarra. *The LUCID-2 Detector*. Tech. rep. Geneva: CERN, 2018. URL: https://cds.cern.ch/record/2649587.

[91] Vladislav Balagura. "Van der Meer scan luminosity measurement and beam–beam correction". In: *The European Physical Journal C* 81.1 (Jan. 2021). ISSN: 1434-6052. DOI: 10.1140/epjc/s10052-021-08837-y. URL: http://dx.doi.org/10.1140/epjc/s10052-021-08837-y.

[92] J. Alwall et al. "The automated computation of tree-level and next-to-leading order differential cross sections, and their matching to parton shower simulations". In: *JHEP* 07 (2014). Comments: 158 pages, 27 figures; a few references have been added, p. 079. DOI: 10.1007/JHEP07(2014)079. arXiv: 1405.0301. URL: https://cds.cern.ch/record/1699128.

[93] Torbjorn Sjostrand, Stephen Mrenna, and Peter Z. Skands. "A Brief Introduction to PYTHIA 8.1". In: *Comput. Phys. Commun.* 178 (2008), pp. 852–867. DOI: 10.1016/j.cpc.2008.01.036. arXiv: 0710.3820. URL: https://cds.cern.ch/record/1064095.

[94] The ATLAS Collaboration. *ATLAS Pythia 8 tunes to 7 TeV data*. Tech. rep. Geneva: CERN, 2014. URL: https://cds.cern.ch/record/1966419.

[95] Richard D. Ball et al. "Parton distributions with LHC data". In: *Nucl. Phys. B* 867 (2013). Comments: 53 pages, 30 figures, pp. 244–289. DOI: 10.1016/j.nuclphysb.2012.10.003. arXiv: 1207.1303. URL: https://cds.cern.ch/record/1460337.

[96] Richard D. Ball et al. "Parton distributions from high-precision collider data: NNPDF Collaboration". In: *The European Physical Journal C* 77.10 (Oct. 2017). ISSN: 1434-6052. DOI: 10.1140/epjc/s10052-017-5199-5. URL: http://dx.doi.org/10.1140/epjc/s10052-017-5199-5.

[97] S Agostinelli et al. "GEANT4–a simulation toolkit. GEANT4. A Simulation toolkit". In: *Nucl. Instrum. Methods Phys. Res., A* 506.3 (2003), pp. 250–303. DOI: 10.1016/S0168-9002(03)01368-8. URL: https://cds.cern.ch/record/602040.

[98] G. Aad et al. "The ATLAS Simulation Infrastructure". In: *The European Physical Journal C* 70.3 (Sept. 2010), pp. 823–874. ISSN: 1434-6052. DOI: 10.1140/epjc/s10052-010-1429-9. URL: http://dx.doi.org/10.1140/epjc/s10052-010-1429-9.

[99] P Calafiura et al. "The Athena Control Framework in Production, New Developments and Lessons Learned". In: (2005). DOI: 10.5170/CERN-2005-002.456. URL: https://cds.cern.ch/record/865624.

[100] G. Barrand et al. "GAUDI — A software architecture and framework for building HEP data processing applications". In: *Computer Physics Communications* 140.1 (2001). CHEP2000, pp. 45–55. ISSN: 0010-4655. DOI: https://doi.org/10.1016/S0010-4655(01)00254-5. URL: https://www.sciencedirect.com/science/article/pii/S0010465501002545.

[101] R Brun, F Rademakers, and S Panacek. "ROOT, an object oriented data analysis framework". In: (2000). URL: https://cds.cern.ch/record/491486.

[102] Javier Llorente Merino et al. *Multijet simulation for 13 TeV ATLAS Analyses*. Tech. rep. Geneva: CERN, 2018. URL: https://cds.cern.ch/record/2646017.

[103] *Identification of boosted, hadronically-decaying W and Z bosons in $\sqrt{s}$ = 13 TeV Monte Carlo Simulations for ATLAS*. Tech. rep. Geneva: CERN, 2015. URL: https://cds.cern.ch/record/2041461.

[104] Matthew Gignac. *Monte Carlo generators, and their usage/modeling in ATLAS*. Sept. 2019.

[105] Stephen Jiggins. "MPI@LHC Talk." In: (2016). URL: https://cds.cern.ch/record/2129370.

[106] ATLAS Outreach. "ATLAS Fact Sheet : To raise awareness of the ATLAS detector and collaboration on the LHC". 2010. DOI: 10.17181/CERN.1LN2.J772. URL: https://cds.cern.ch/record/1457044.

[107] *ApprovedPlotsDAQ AtlasPublic TWiki*. https://twiki.cern.ch/twiki/bin/view/AtlasPublic/ApprovedPlotsDAQ. [Accessed 28-09-2024].

[108] Georges Aad et al. "Operation of the ATLAS trigger system in Run 2". In: *JINST* 15.10 (2020), P10004. DOI: 10.1088/1748-0221/15/10/P10004. arXiv: 2007.12539. URL: https://cds.cern.ch/record/2725146.

[109] C Bernius. *The ATLAS Trigger Menu: Design and Performance*. Tech. rep. Geneva: CERN, 2012. URL: https://cds.cern.ch/record/1494548.

[110] *Trigger menu in 2018*. Tech. rep. All figures including auxiliary figures are available at https://atlas.web.cern.ch/Atlas/GROUPS/PHYSICS/PUBNOTES/ATL-DAQ-PUB-2019-001. Geneva: CERN, 2019. URL: https://cds.cern.ch/record/2693402.

[111] E F Eisenhandler. *ATLAS Level-1 Calorimeter Trigger Algorithms*. Tech. rep. Geneva: CERN, 2004. URL: https://cds.cern.ch/record/792528.

[112] Georges Aad et al. "Performance of the ATLAS muon triggers in Run 2". In: *JINST* 15 (2020), P09015. DOI: 10.1088/1748-0221/15/09/p09015. arXiv: 2004.13447. URL: https://cds.cern.ch/record/2716326.

[113] Rosa Simoniello. *The ATLAS Level-1 Topological Processor: from design to routine usage in Run-2*. Tech. rep. Geneva: CERN, 2019. DOI: 10.1109/NSSMIC.2018.8824280. URL: https://cds.cern.ch/record/2649959.

[114] ATLAS Collaboration. *Athena*. URL: https://doi.org/10.5281/zenodo.2641996.

[115] Georges Aad et al. "Triggers for displaced decays of long-lived neutral particles in the ATLAS detector. Triggers for displaced decays of long-lived neutral particles in the ATLAS detector". In: *JINST* 8 (2013), P07015. DOI: 10.1088/1748-0221/8/07/P07015. arXiv: 1305.2284. URL: https://cds.cern.ch/record/1546811.

[116] T Berger-Hryn'ova et al. *Physics Uses and Hardware Constraints of the L1 Topological Trigger*. Tech. rep. Geneva: CERN, 2014. URL: https://cds.cern.ch/record/1645921.

[117] M. Aaboud et al. "Performance of the ATLAS Transition Radiation Tracker in Run 1 of the LHC: Tracker properties". In: *Journal of Instrumentation* 12 (May 2017), P05002–P05002. DOI: 10.1088/1748-0221/12/05/P05002.

[118] Ahmet Bingül. "The ATLAS TRT and its Performance at LHC". In: *Journal of Physics: Conference Series* 347.1 (Feb. 2012), p. 012025. DOI: 10.1088/1742-6596/347/1/012025. URL: https://dx.doi.org/10.1088/1742-6596/347/1/012025.

[119] The ATLAS Collaboration et al. "A neural network clustering algorithm for the ATLAS silicon pixel detector. A neural network clustering algorithm for the ATLAS silicon pixel detector". In: *JINST* 9 (2014), P09009. DOI: 10.1088/1748-0221/9/09/P09009. arXiv: 1406.7690. URL: https://cds.cern.ch/record/1712337.

[120] Tracking CP. *ATLAS Tracking Software Tutorial*. https://atlassoftwaredocs.web.cern.ch/trackingTutorial/. [Accessed 13-07-2024]. July 2023.

[121] R. Frühwirth. "Application of Kalman filtering to track and vertex fitting". In: *Nuclear Instruments and Methods in Physics Research Section A: Accelerators, Spectrometers, Detectors and Associated Equipment* 262.2 (1987), pp. 444–450. ISSN: 0168-9002. DOI: https://doi.org/10.1016/0168-9002(87)90887-4. URL: https://www.sciencedirect.com/science/article/pii/0168900287908874.

[122] The ATLAS Collaboration et al. *Expected performance of the ATLAS experiment: detector, trigger and physics*. Geneva: CERN, 2009. URL: https://cds.cern.ch/record/1125884.

[123] *Vertex Reconstruction Performance of the ATLAS Detector at* $\sqrt{s} = 13$ *TeV*. Tech. rep. Geneva: CERN, 2015. URL: https://cds.cern.ch/record/2037717.

[124] Morad Aaboud et al. "Reconstruction of primary vertices at the ATLAS experiment in Run 1 proton–proton collisions at the LHC. Reconstruction of primary vertices at the ATLAS experiment in Run 1 proton-proton collisions at the LHC". In: *Eur. Phys. J. C* 77.5 (2017), p. 332. DOI: 10.1140/epjc/s10052-017-4887-5. arXiv: 1611.10235. URL: https://cds.cern.ch/record/2235651.

[125] Tim Robertson and J. D. Cryer. "An Iterative Procedure for Estimating the Mode". In: *Journal of the American Statistical Association* 69.348 (1974), pp. 1012–1016. DOI: 10.1080/01621459.1974.10480246. eprint: https://www.tandfonline.com/doi/pdf/10.1080/01621459.1974.10480246.

[126] Wolfgang Waltenberger, Rudolf Frühwirth, and Pascal Vanlaer. "Adaptive vertex fitting". In: *Journal of Physics G: Nuclear and Particle Physics* 34.12 (Nov. 2007), N343. DOI: 10.1088/0954-3899/34/12/N01. URL: https://dx.doi.org/10.1088/0954-3899/34/12/N01.

[127] G. Aad et al. "Topological cell clustering in the ATLAS calorimeters and its performance in LHC Run 1. Topological cell clustering in the ATLAS calorimeters and its performance in LHC Run 1". In: *Eur. Phys. J. C* 77 (2017), p. 490. DOI: 10.1140/epjc/s10052-017-5004-5. arXiv: 1603.02934. URL: https://cds.cern.ch/record/2138166.

[128] Stephen D. Ellis and Davison E. Soper. "Successive combination jet algorithm for hadron collisions". In: *Physical Review D* 48.7 (Oct. 1993), pp. 3160–3166. ISSN: 0556-2821. DOI: 10.1103/physrevd.48.3160. URL: http://dx.doi.org/10.1103/PhysRevD.48.3160.

[129] Matteo Cacciari, Gavin P Salam, and Gregory Soyez. "The anti-ktjet clustering algorithm". In: *Journal of High Energy Physics* 2008.04 (Apr. 2008), pp. 063–063. ISSN: 1029-8479. DOI: 10.1088/1126-6708/2008/04/063. URL: http://dx.doi.org/10.1088/1126-6708/2008/04/063.

[130] Alexis Romero et al. *Safety of Quark/Gluon Jet Classification*. 2021. arXiv: 2103.09103 [hep-ph]. URL: https://arxiv.org/abs/2103.09103.

[131] M. Aaboud et al. "Jet energy scale measurements and their systematic uncertainties in proton-proton collisions at $\sqrt{s} = 13$ TeV with the ATLAS detector. Jet energy scale measurements and their systematic uncertainties in proton-proton collisions at $\sqrt{s} = 13$ TeV with the ATLAS detector". In: *Phys. Rev. D* 96.7 (2017), p. 072002. DOI: 10.1103/PhysRevD.96.072002. arXiv: 1703.09665. URL: http://cds.cern.ch/record/2257300.

[132] Matteo Cacciari and Gavin P. Salam. "Pileup subtraction using jet areas". In: *Physics Letters B* 659.1 (2008), pp. 119–126. ISSN: 0370-2693. DOI: https://doi.org/10.1016/j.physletb.2007.09.077. URL: https://www.sciencedirect.com/science/article/pii/S0370269307011094.

[133] Georges Aad et al. "Jet energy measurement with the ATLAS detector in proton-proton collisions at $\sqrt{s} = 7$ TeV. Jet energy measurement with the ATLAS detector in proton-proton collisions at $\sqrt{s} = 7$ TeV". In: *Eur. Phys. J. C* 73 (2013), p. 2304. DOI: 10.1140/epjc/s10052-013-2304-2. arXiv: 1112.6426. URL: https://cds.cern.ch/record/1409965.

[134] ATLAS Collaboration. *Selection of jets produced in 13TeV proton-proton collisions with the ATLAS detector*. Tech. rep. Geneva: CERN, 2015. URL: https://cds.cern.ch/record/2037702.

[135] A. Hoecker et al. *TMVA - Toolkit for Multivariate Data Analysis*. 2009. arXiv: physics/0703039 [physics.data-an]. URL: https://arxiv.org/abs/physics/0703039.

[136] ATLAS Collaboration. *Tagging and suppression of pileup jets with the ATLAS detector*. Tech. rep. Geneva: CERN, 2014. URL: https://cds.cern.ch/record/1700870.

[137] ATLAS Collaboration. *Pile-up subtraction and suppression for jets in ATLAS*. Tech. rep. Geneva: CERN, 2013. URL: https://cds.cern.ch/record/1570994.

[138] Yu Him Justin Chiu. "The performance of the ATLAS missing transverse momentum high-level trigger in 2015 pp collisions at 13 TeV". Presented 01 Sep 2016. Victoria U., 2016. URL: https://cds.cern.ch/record/2219503.

[139] Morad Aaboud et al. "Performance of missing transverse momentum reconstruction with the ATLAS detector using proton-proton collisions at $\sqrt{s} = 13$ TeV". In: *Eur. Phys. J. C* 78.11 (2018), p. 903. DOI: 10.1140/epjc/s10052-018-6288-9. arXiv: 1802.08168. URL: https://cds.cern.ch/record/2305380.

[140] R Nicolaidou et al. "Muon identification procedure for the ATLAS detector at the LHC using Muonboy reconstruction package and tests of its performance using cosmic rays and single beam data". In: *Journal of Physics: Conference Series* 219.3 (Apr. 2010), p. 032052. DOI: 10.1088/1742-6596/219/3/032052. URL: https://dx.doi.org/10.1088/1742-6596/219/3/032052.

[141] M J Woudstra. "Precision of the ATLAS muon spectrometer". Presented on 4 Dec 2002. Amsterdam U., 2002. URL: https://cds.cern.ch/record/620198.

[142] P. J. Hendriks. "ATLAS muon reconstruction from a C++ perspective: a road to the Higgs". Award Date 26 April 2000. Universiteit van Amsterdam, 2000. URL: https://pure.uva.nl/ws/files/3065022/13290_Thesis.pdf.

[143] P. J. Hendricks. "ATLAS muon reconstruction from a C++ perspective: a road to the Higgs." [Accessed 22-12-2024]. 2000.

[144] ATLAS Collaboration. "Standalone vertex finding in the ATLAS muon spectrometer". In: *Journal of Instrumentation* 9.02 (Feb. 2014), P02001. ISSN: 1748-0221. DOI: 10.1088/1748-0221/9/02/P02001. URL: https://dx.doi.org/10.1088/1748-0221/9/02/P02001.

[145] M Biglietti, G Ciapetti, and D Ventura. *Stand Alone Vertex Finding in the ATLAS Muon Spectrometer*. Tech. rep. Geneva: CERN, 2011. URL: https://cds.cern.ch/record/1333393.

[146] Matthew J. Strassler and Kathryn M. Zurek. "Discovering the Higgs through highly-displaced vertices". In: *Physics Letters B* 661.4 (2008), pp. 263–267. ISSN: 0370-2693. DOI: https://doi.org/10.1016/j.physletb.2008.02.008. URL: https://www.sciencedirect.com/science/article/pii/S0370269308001846.

[147] Heather Russell. "Search for long-lived particles decaying in the muon spectrometer of the ATLAS detector at the LHC". Presented 02 Dec 2016. WUSTL, Seattle, 2016. URL: https://cds.cern.ch/record/2239318.

[148] G Ciapetti, H Lubatti, and D Ventura. *Standalone Vertex Finding in the ATLAS Muon Spectrometer*. Tech. rep. Geneva: CERN, 2012. URL: https://cds.cern.ch/record/1455664.

[149] M Boonekamp et al. *Cosmic Ray, Beam-Halo and Beam-Gas Rate Studies for ATLAS Commissioning*. Tech. rep. Geneva: CERN, 2004. URL: https://cds.cern.ch/record/719263.

[150] Suyong Choi and Hayoung Oh. *Improved Extrapolation Methods of Data-driven Background Estimation in High-Energy Physics*. 2021. arXiv: 1906.10831 [hep-ph]. URL: https://arxiv.org/abs/1906.10831.

[151] Will Buttinger. *Background Estimation with the ABCD Method*. https://twiki.cern.ch/twiki/pub/Main/ABCDMethod/ABCDGuide_draft18Oct18.pdf. [Accessed 28-06-2024]. Oct. 2018.

[152] Jeremy Jordan. *Neural networks: representation*. https://www.jeremyjordan.me/intro-to-neural-networks/. [Accessed 01-11-2024]. June 2017.

[153] Martín Abadi et al. *TensorFlow: Large-Scale Machine Learning on Heterogeneous Systems*. Software available from tensorflow.org. 2015. URL: https://www.tensorflow.org/.

[154] François Chollet et al. *Keras*. https://keras.io. 2015.

[155] I Longarini. "Beam-induced background identification with image vision techniques at ATLAS". In: *Nuovo Cimento C* 44.2-3 (2021), p. 53. DOI: 10.1393/ncc/i2021-21053-2. URL: https://cds.cern.ch/record/2791327.

[156] G. Aad et al. "Studies of the performance of the ATLAS detector using cosmic-ray muons. Studies of the performance of the ATLAS detector using cosmic-ray muons". In: *Eur. Phys. J. C* 71 (2011). Comments: 22 pages plus author list (33 pages total), 21 figures, 2 tables, p. 1593. DOI: 10.1140/epjc/s10052-011-1593-6. arXiv: 1011.6665. URL: https://cds.cern.ch/record/1311111.

[157] H. Ikeda et al. "A detailed test of the CsI(Tl) calorimeter for BELLE with photon beams of energy between 20 MeV and 5.4 GeV". In: *Nuclear Instruments and Methods in Physics Research Section A: Accelerators, Spectrometers, Detectors and Associated Equipment* 441.3 (2000), pp. 401–426. ISSN: 0168-9002. DOI: https://doi.org/10.1016/S0168-9002(99)00992-4. URL: https://www.sciencedirect.com/science/article/pii/S0168900299009924.

[158] F James and M Goossens. "MINUIT: Function Minimization and Error Analysis Reference Manual". In: (1998). CERN Program Library Long Writeups. URL: https://cds.cern.ch/record/2296388.

[159] CERN. *Chapter: Fitting Fistograms*. https://root.cern.ch/root/htmldoc/guides/users-guide/FittingHistograms.html. [Accessed 03-11-2024].

[160] Richard D. Ball et al. "Parton distributions for the LHC Run II". In: *JHEP* 04 (2015). Comments: 138 pages, 64 figures. Several typos in text and references corrected, one reference added, p. 040. DOI: 10.1007/JHEP04(2015)040. arXiv: 1410.8849. URL: https://cds.cern.ch/record/1966481.

[161] Jon Butterworth et al. "PDF4LHC recommendations for LHC Run II". In: *Journal of Physics G: Nuclear and Particle Physics* 43.2 (Jan. 2016), p. 023001. ISSN: 1361-6471. DOI: 10.1088/0954-3899/43/2/023001. URL: http://dx.doi.org/10.1088/0954-3899/43/2/023001.

[162] Glen Cowan et al. "Asymptotic formulae for likelihood-based tests of new physics". In: *The European Physical Journal C* 71.2 (Feb. 2011). ISSN: 1434-6052. DOI: 10.1140/epjc/s10052-011-1554-0. URL: http://dx.doi.org/10.1140/epjc/s10052-011-1554-0.

[163] ATLAS Statistics forum. *Frequentist Limit Recommendation*. Draft v1.1. URL: https://indico.cern.ch/event/126652/contributions/1343592/attachments/80222/115004/Frequentist_Limit_Recommendation.pdf.

[164] A L Read. "Presentation of search results: the CLs technique". In: *Journal of Physics G: Nuclear and Particle Physics* 28.10 (Sept. 2002), p. 2693. DOI: 10.1088/0954-3899/28/10/313. URL: https://dx.doi.org/10.1088/0954-3899/28/10/313.

[165] Hao Zhou. "Search for Long-Lived Particles Produced in Proton-Proton Collisions at $\sqrt{s}$ =13 TeV That Decay to Displaced Hadronic Jets Detected With the Muon Spectrometer in ATLAS". Presented 29 Jul 2021. University of Arizona, 2021. URL: https://cds.cern.ch/record/2779067.

[166] R.L. Workman et al. "Gauge and Higgs Bosons". In: *Prog.Theor.Exp.Phys.* 2022 (2022), p. 083C01. URL: https://pdg.lbl.gov/2022/tables/rpp2022-sum-gauge-higgs-bosons.pdf.

[167] Matthew Feickert, Lukas Heinrich, and Giordon Stark. *pyhf: pure-Python implementation of HistFactory with tensors and automatic differentiation*. 2022. arXiv: 2211.15838 [hep-ex]. URL: https://arxiv.org/abs/2211.15838.

[168] Morad Aaboud et al. "Search for long-lived particles produced in pp collisions at $\sqrt{s}$ = 13 TeV that decay into displaced hadronic jets in the ATLAS muon spectrometer". In: *Phys. Rev. D* 99 (2019). Submitted to Phys.Rev., p. 052005. DOI: 10.1103/PhysRevD.99.052005. arXiv: 1811.07370. URL: https://cds.cern.ch/record/2647833.

[169] ATLAS Collaboration and Louie Dartmoor Corpe. *Common ATLAS and CMS summary plots for Higgs boson mediated hidden sectors involving long-lived particles (Winter 2024-2025)*. Tech. rep. Common CMS and ATLAS Summary Plots for LLPs. Geneva: CERN, 2024. URL: https://cds.cern.ch/record/2920462.

[170] Rende Steerenberg. *Accelerator Report: LHC Run 3 achieves record-breaking integrated luminosity*. https://home.cern/news/news/accelerators/accelerator-report-lhc-run-3-achieves-record-breaking-integrated-luminosity. [Accessed 27-10-2024]. Sept. 2024.